

# Journal of Pharmaceutical Analysis

## EDITORIAL BOARD

### Editor-in-Chief

Langchong He  
Xi'an Jiaotong University, China

### Associate Editors

Bart De Spiegeleer  
*Ghent University, Belgium*  
Ian Sutherland  
*Brunel University, UK*  
Janusz Pawliszyn  
*University of Waterloo, Canada*  
Jin-Ming Lin  
*Tsinghua University, China*

Joghee Dharuman  
*KMCH College of Pharmacy, India*  
Kaishun Bi  
*Shenyang Pharmaceutical University, China*  
Paul R. Haddad  
*Australia*  
Stig Pedersen-Bjergaard  
*University of Oslo, Norway*

Su Zeng  
*Zhejiang University, China*  
Yifeng Chai  
*The Second Military Medical University, China*  
Zilin Chen  
*Wuhan University, China*

### Editorial Board

Alejandro Cifuentes  
*National Research Council of Spain (CSIC), Spain*  
Alexander Kurganov  
*Institute of petrochemical synthesis  
Russian Academy of sciences, Russia*  
Bing-Hua Yao  
*Xi'an University of Technology, China*  
Boryana Nikolova-Damyanova  
*Bulgarian Academy of Sciences, Bulgaria*  
Broeckhoven Ken  
*Vrije Universiteit Brussel, Belgium*  
Byeang Hyeon Kim  
*Pohang University of Science and Technology  
(POSTECH), Republic of Korea*  
Carolina Simó  
*Institute of Food Science Research, Spain*  
Chengxiao Zhang  
*Shaanxi Normal University, China*  
Chengzhi Huang  
*Southwest University, China*  
Dimitrios Tsikas  
*Hannover Medical School, Germany*  
George Qian Li  
*University of Sydney, Australia*  
Gerhard K. E. Scriba  
*Friedrich Schiller University Jena, Germany*  
Gongke Li  
*Sun Yat-sen University, China*  
Gosetti Fabio  
*University of Piemonte Orientale, Italy*  
Hidetoshi Arakawa  
*Showa University, Japan*  
Hsueh-Chia Chang  
*University of Notre Dame, USA*  
Jacques De Beer  
*Scientific Institute of Public Health, Belgium*

Jian-Bin Zheng  
*Northwest University, China*  
Jian-Zhong Lu  
*Fudan University, China*  
Jingkai Gu  
*Jilin University, China*  
John HT Luong  
*National Research Council Canada, Canada*  
Jun Haginaka  
*Mukogawa Women's University, Japan*  
Karine Faure  
*University of Lyon 1, France*  
Katsumi Uchiyama  
*Tokyo Metropolitan University, Japan*  
Koichi Otsuka  
*Kyoto University, Japan*  
Lingjun Li  
*University of Wisconsin-Madison, USA*  
Li-Xia Ding  
*National Institutes for Food and Drug Control, China*  
Massimo Morbidelli  
*ETH Zurich, Switzerland*  
Oliver J. Schmitz  
*University of Duisburg-Essen, Germany*  
Perry Wang  
*US Food and Drug Administration, USA*  
Pranav S. Shrivastav  
*Gujarat University, India*  
Pulok K. Mukherjee  
*Jadavpur University, India*  
Qiang Fu  
*Xi'an Jiaotong University, China*  
Ruin Moaddel  
*National Institute on Aging, USA*

Salvatore Fanali  
*Institute of Chemical Methodologies,  
Italian National Research Council – CNR, Italy*  
Sandra Furlanetto  
*University of Florence, Italy*  
Shaoping Li  
*University of Macau, China*  
Shigeo Suzuki  
*Kinki University, Japan*  
Shuangcheng Ma  
*National Institutes for Food and Drug Control, China*  
Sicen Wang  
*Xi'an Jiaotong University, China*  
Taijun Hang  
*China Pharmaceutical University, China*  
Tarek Belal  
*Alexandria University, Egypt*  
Toshimasa Toyo'oka  
*University of Shizuoka, Japan*  
Walter Jäger  
*University of Vienna, Austria*  
Xiangqun Zeng  
*Oakland University, USA*  
Xuan Wang  
*Peking University, China*  
Yanjiang Qiao  
*Beijing University of Chinese Medicine,  
China*  
Yoshinobu Baba  
*Nagoya University, Japan*  
Zhiguo Yu  
*Shenyang Pharmaceutical University,  
China*  
Zongwei Cai  
*Hong Kong Baptist University, China*

### Consulting editors

Jing Li  
*Wayne State University, USA*  
José Manuel Amigo  
*University of Copenhagen, Denmark*  
José Paulo Mota  
*Universidade Nova de Lisboa, Portugal*

June feng  
*Louisiana Tech University,  
USA*  
Raja Ghosh  
*McMaster University,  
Canada*

Youssef Daali  
*Geneva University,  
Switzerland*

### Editorial Office

**Managing Editor**  
Fen Qiu  
*Xi'an Jiaotong University, China*

**Executive Editors**  
Dongdong Zhang  
*Xi'an Jiaotong University, China*

Yanmin Zhang  
*Xi'an Jiaotong University, China*

Mengjie Wang  
*Xi'an Jiaotong University, China*

*Xi'an Jiaotong University;*  
76 Yanta West Road, Xi'an, 710061, China;  
Tel.: +86-29-82655433, +86-29-82655021;

E-mail: [jpa2011@126.com](mailto:jpa2011@126.com); [jpasubmit@126.com](mailto:jpasubmit@126.com); [jpa2011@xjtu.edu.cn](mailto:jpa2011@xjtu.edu.cn)



Contents lists available at ScienceDirect

## Journal of Pharmaceutical Analysis

journal homepage: [www.elsevier.com/locate/jpa](http://www.elsevier.com/locate/jpa)

## Review Paper

## Nanodiamonds with powerful ability for drug delivery and biomedical applications: Recent updates on in vivo study and patents

Swati Chauhan, Neha Jain, Upendra Nagaich\*

Department of Pharmaceutics, Amity Institute of Pharmacy, Amity University, Noida, U.P., India

## ARTICLE INFO

## Article history:

Received 28 February 2019

Received in revised form

21 September 2019

Accepted 25 September 2019

Available online 1 October 2019

## Keywords:

Nanomedicine

Biochemical application

Diamondoids

Surface functionalization

Drug targeting

## ABSTRACT

Nanodiamonds are novel nanosized carbon building blocks possessing varied fascinating mechanical, chemical, optical and biological properties, making them significant active moiety carriers for biomedical application. These are known as the most 'captivating' crystals attributed to their chemical inertness and unique properties posing them useful for variety of applications in biomedical era. Alongside, it becomes increasingly important to find, ascertain and circumvent the negative aspects associated with nanodiamonds. Surface modification or functionalization with biological molecules plays a significant role in managing the toxic behavior since nanodiamonds have tailorable surface chemistry. To take advantage of nanodiamond potential in drug delivery, focus has to be laid on its purity, surface chemistry and other considerations which may directly or indirectly affect drug adsorption on nanodiamond and drug release in biological environment. This review emphasizes on the basic properties, synthesis techniques, surface modification techniques, toxicity issues and biomedical applications of nanodiamonds. For the development of nanodiamonds as an effective dosage form, researchers are still engaged in the in-depth study of nanodiamonds and their effect on life interfaces.

© 2019 Xi'an Jiaotong University. Production and hosting by Elsevier B.V. This is an open access article under the CC BY-NC-ND license (<http://creativecommons.org/licenses/by-nc-nd/4.0/>).

## 1. Introduction

With the swift expansion in the field of nanoscience and nanotechnology, nanomaterials based on carbon have been a centre of attention ever since their innovation. Carbon-based nanomaterials include fullerene, carbon nanotubes, nanodiamonds and graphene. Their distinctive nature brands them to be used in many disciplines extending within material science, energy, environment, biology, pharmaceutical sciences and for drug delivery systems [1]. Diamond nanoparticles, also known as nanodiamonds (NDs), are single crystal diamonds consisting of carbon as the basic component with high physical and chemical properties. These are nanoscopic version of  $sp^3$  carbon, while other carbon nanotubes and fullerenes are of  $sp^2$  configuration. The average particle size of diamond nanoparticle is 4–5 nm (thousands of times smaller than human hair). On primary particle sizes basis, Shenderova and McGuire classified NDs into nanocrystalline particles (1 to  $\geq 150$  nm) and ultra-nanocrystalline particles (2–10 nm) as shown in Fig. 1.

NDs are famous as ultradisperse diamonds which have exclusive properties of diamond core viz. chemical inert core, prominent hardness and superior thermal conductivity [2]. There are several techniques for the synthesis of NDs viz. chemical vapor deposition, high temperature high pressure, and detonation of explosives [3]. The process of synthesis has been detailed in Section 3 of the paper. NDs are rapidly emerging as promising carriers for next-generation therapeutics and drug delivery. NDs exhibit tunable surface, excellent biocompatibility and large surface area for conjugation of molecules like drugs and genes for their intracellular and extracellular delivery. Additionally, fluorescence imparts a diagnostic feature to NDs, thus they can be utilized as image probes. Throughout the past couple of decades, many investigations have potentially added for the advancement of NDs, exploiting their numerous properties for biological applications [4]. On the contrary, there are several crucial concerns and challenges associated with these carbon-based nanocarriers for clinical application. The foremost challenge is toxicity of carbon-based nanocarriers viz. how their nature and mechanism affect the living cells. Therefore, an in-depth study is necessary to ascertain the mechanism of nanoparticle induced toxicity via in vivo and in vitro cytotoxicity studies. Moreover, short circulation half-life of nanoparticles causes their faster elimination via opsonization by phagocytes in human

Peer review under responsibility of Xi'an Jiaotong University.

\* Corresponding author.

E-mail address: [unagaich@amity.edu](mailto:unagaich@amity.edu) (U. Nagaich).

<https://doi.org/10.1016/j.jpha.2019.09.003>

2095-1779/© 2019 Xi'an Jiaotong University. Production and hosting by Elsevier B.V. This is an open access article under the CC BY-NC-ND license (<http://creativecommons.org/licenses/by-nc-nd/4.0/>).

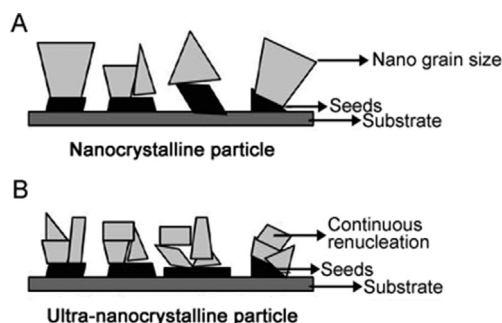


Fig. 1. Schematic representation of nanodiamond classification.

body, which makes them unsuitable for sustained drug delivery [5]. Thus, as a solution to this problem, surface functionalization, i.e., modification of surface by attaching ligands has emerged as a boon technique for making NDs best for delayed drug delivery.

Therefore, it is envisaged that NDs can serve as good drug carriers, image probes, or implant coatings in biological systems. However, developing future nanoscale devices and arrays that harness these nanoparticles will require unprecedented spatial control [6].

## 2. Unique structure and properties of NDs

The unique properties of NDs are attributed to the exclusive properties of diamonds and nanoparticles as shown in Fig. 2. Diamonds are the hardest known material and transparent electrical insulator. These consist of tetrahedral  $sp^3$  carbon atoms which form unique large crystals [7].

NDs are supposed to have core-shell structural design as they have diamond inner core ( $sp^3$  carbon atoms) and graphitic outer shell ( $sp^2$  carbon atoms) with hanging bonds ended with functional groups [8]. The accurate nature of the outer shell remains unclear, but two general models have emerged. One is an amorphous shell with significant  $sp^2$  carbon content and the other is a  $sp^2$  graphene-type sheet of a fullerene structure, giving rise to a structure described as 'bucky-diamond' [9]. The two types of bonds can be interchangeable viz. the stretched face of diamond is a graphene plane while the puckered graphene may become a diamond surface. This interchangeability allows NDs particles to act as flexible templates, particularly around the curved surface where electrons are unstable. These include a uniquely faceted truncated octahedral architecture that enables potent drug binding and dispersibility in water [10]. The surface mainly consists of carbon, phenols, pyrones and sulfonic acid as shown in Fig. 3. NDs also contain carboxylic

acid groups, anhydride, hydroxyl groups and epoxide groups but in smaller amount. Due to the presence of carboxylic groups, NDs suspensions are stable in water and have the capability of complexing with water soluble drugs like purvalanol A (drug for liver cancer), 4-hydroxytamoxifen (drug for breast cancer), and dexamethasone (an anti-inflammatory agent) [11].

Properly purified nanodiamond can have almost perfect crystalline structure with insignificant parts of non-diamond carbon. Furthermore, NDs have naturally occurring nitrogen-vacancy (N-V) centers or nitrogen impurities (as shown in Fig. 4), which can form complexes in the core of nanodiamond particles like peptides, and amines. NDs holding N-V centers provide fluorescence characteristic, and impart optical properties to NDs [12]. It is also known as fluorescent nanodiamond (FND), and has been utilized for bio-labeling agent.

Exploiting this fluorescence trait, it has been investigated that NDs complexes with doxorubicin significantly diminish the brain tumor by convection enhanced intracranial delivery. This indicates the possibility of using NDs to treat nervous system related diseases and injuries [13]. They absorb at 550–800 nm and emit bright fluorescence efficiently in the far-red region, without photoblinking and photobleaching, which is the key reason for application of NDs as cellular markers as a fluorescent probe for single particle tracking with the advantage of surface functionalization and non-cytotoxic nature of NDs [14]. N-V centers in NDs can also be formed in two steps, i.e., generation of vacancy by irradiation and then migration of atom through crystal lattice which is then trapped by foreign atom. There can be two types of charges on N-V center, i.e., neutral or negatively charged ones, which can easily be differentiated on the basis of their emission spectra. Negatively charged N-V centers are paramagnetic which upon optical pumping cause spin polarization. Spin polarization exhibits a long coherence time which has significant applications in diagnostics, particularly optical coherence tomography [6]. Optically, NDs reveal the largest optical band gap (5.4–5.6 eV at room temperature), and thus become a wide-band semiconductor. NDs robustly possess excellent electrical properties. An investigation on NDs showed that the aggregated NDs powder demonstrated a low dielectric loss tangent, indicating its good dielectric properties. Mechanically, NDs have high Young's modulus, thus making them strong and hard with elevated refractive index, electrical resistivity, and thermal conductivity. Maitra et al. synthesized poly (vinyl alcohol)-matrix (PVA) reinforced with nanodiamond particles (0.6 wt %) and characterized by nano-indentation technique for mechanical properties. The results displayed a noteworthy improvement in hardness and elastic modulus of PVA by small addition of NDs. The reason attributed to the increased covalent linkages between ND and PVA matrix [15]. Likewise, Gogotsi group produced multifunctional

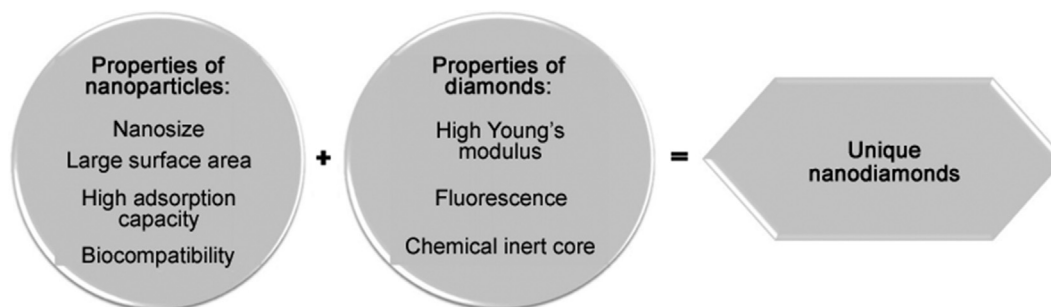


Fig. 2. Pictorial representation of properties of nanoparticles and diamonds.

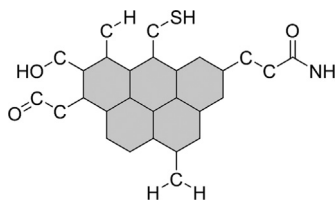


Fig. 3. Basic structure of nanodiamonds with surface functional groups.

bone scaffold materials with the help of poly ( $\alpha$ -lactic acid) (PLLA) and 1%–10% octadecylamine-functionalized nanodiamond (ND-ODA). The outcomes of mechanical testing displayed a 280% increase in the strain at failure and a 310% increase in fracture energy in tensile tests. Thus, an overall enhancement in mechanical properties of matrix was observed. The NDs have assured characteristics which concoct them a functional matter in several disciplines [16].

### 3. Synthesis of NDs

NDs were first formed in USSR in 1963 when detonation of carbon-based explosives resulted in formation of diamonds nanoparticles. NDs can also be formed by applying special techniques, principle and procedures like detonation technique, high-pressure high-temperature (HPHT), chemical vapor deposition (CVD) technique, ultrasonic synthesis, hydrothermal synthesis, ion and laser bombardment and electro-chemical synthesis [17]. The size, shape, surface structure (groups attached on surface like carboxyl and lactones) and quality of NDs are determined by the methods used in their production. There are several techniques for the synthesis of NDs viz CVD, HPHT and detonation technique. The properties of yielded NDs may vary from technique to technique. Detonation technique includes controlled explosion of carbon containing compounds which results in NDs of narrow size distribution having majorly round or oval shape. Detonated NDs have  $sp^2$  carbon on surface with functional groups and large surface area, which facilitates the attachment of drug molecules, thus proving an excellent drug carrier system. These types of NDs attain various drawbacks like presence of high number of impurities and lattice defects. Due to their small size and high impurities, these can keep stable fluorescent defects to a very less extent. Therefore they tend to be a poor candidate for sensing and labeling techniques. The smallest member of diamond family is diamondoid, which is obtained by applying the process of grinding. Diamondoids are extracted from crude oil. The lower diamondoids are known as adamantane. The resultant NDs are in more pure form and possess very few lattice defects than the detonated NDs. These have flattened surface like flakes having uniform structure with broad size distribution.

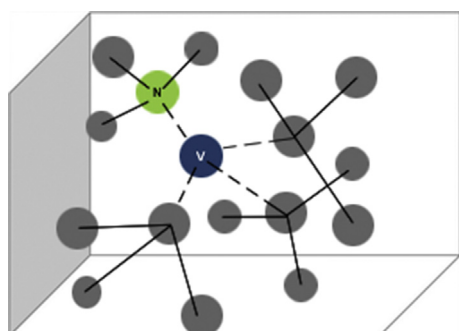


Fig. 4. Diagrammatic illustration of nitrogen-vacancy (N-V) centers in nanodiamonds.

Different sizes of NDs can be selected by centrifugation. Higher particles will settle down and the lower particles will remain in supernatant. Unlike the detonated NDs, these NDs possess stable defects with numerous colored centers. These stable defects result in fluorescence effect which is non-bleachable as compared to the fluorescence imparted by organic dyes. Negatively charged N-V centers are responsible for this stable fluorescence which can be exploited for biolabeling applications. These N-V centers are also responsible for imparting excellent spin properties to NDs, due to which they can react even in the presence of limited magnetic fields. This property can be utilized for sensor applications. NDs also have an excellent electrical property and thus can act as transducers in chemical sensing viz. hydrogen terminated diamond is surface conductive while boron doped diamond is a semiconductor.

Detonated NDs are formed by mixing two explosives, i.e., trinitrotoluene and hexogen (octogen), as shown in Fig. 5. By this procedure, average particles size of NDs can be obtained in the range of 4–5 nm. It is notable to mention the parameters to increase the yield of NDs, i.e., rapid cooling by increasing the quantity of coolant present in the system like gases (argon) and water, water base foams and ice [18]. The process of synthesis is depicted in Fig. 1. The resultant product obtained from detonation soot is a mixture of diamond particles (up to 75 wt %) with other carbon allotropes (25 wt %–85 wt %) and incombustible impurities (metals and oxides, 1 wt %–8 wt %), which has to be purified for the most applications. Another technique for nanodiamond synthesis is chemical vapor deposition (CVD). CVD is the common process used and includes techniques like hot filament chemical vapor deposition (HFCVD), microwave-plasma-assisted chemical vapor deposition (MWPCVD), and combustion flame chemical vapor deposition (CFCVD) for increased yield [19]. The process of CVD is clearly depicted in Fig. 5.

Neu et al. have introduced a process for the fabrication of high-quality, spatially isolated nano-diamonds on iridium via MWPCVD growth [20]. Tsugawa et al. developed a low-temperature and large-area nanodiamond coating method by MWPCVD sustained using surface [21]. Lin et al. used microwave plasma jet chemical vapor deposition system (MPJ-CVD) for synthesizing smooth ultrananocrystalline diamond (UNCD) films [22]. Ultrasonication is another technique for NDs preparation, utilizing high pressure and high temperature. The entire process of preparation via ultrasonic synthesis is mentioned in Fig. 6 [23]. The major concern with the nanodiamond synthesis is its yield and cost-effective production. Several researches have been conducted to obtain the cost-effective industrial production techniques.

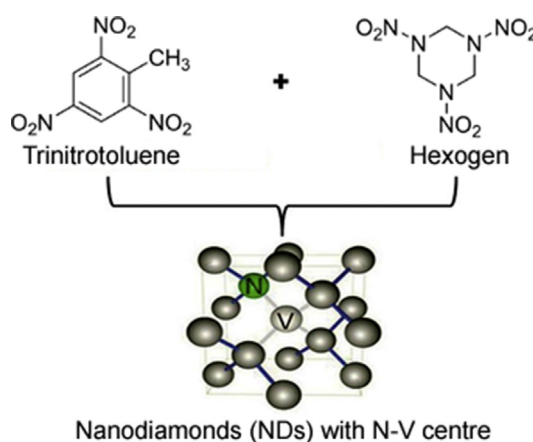


Fig. 5. Diagrammatic presentation of nanodiamonds synthesis via detonation technique.

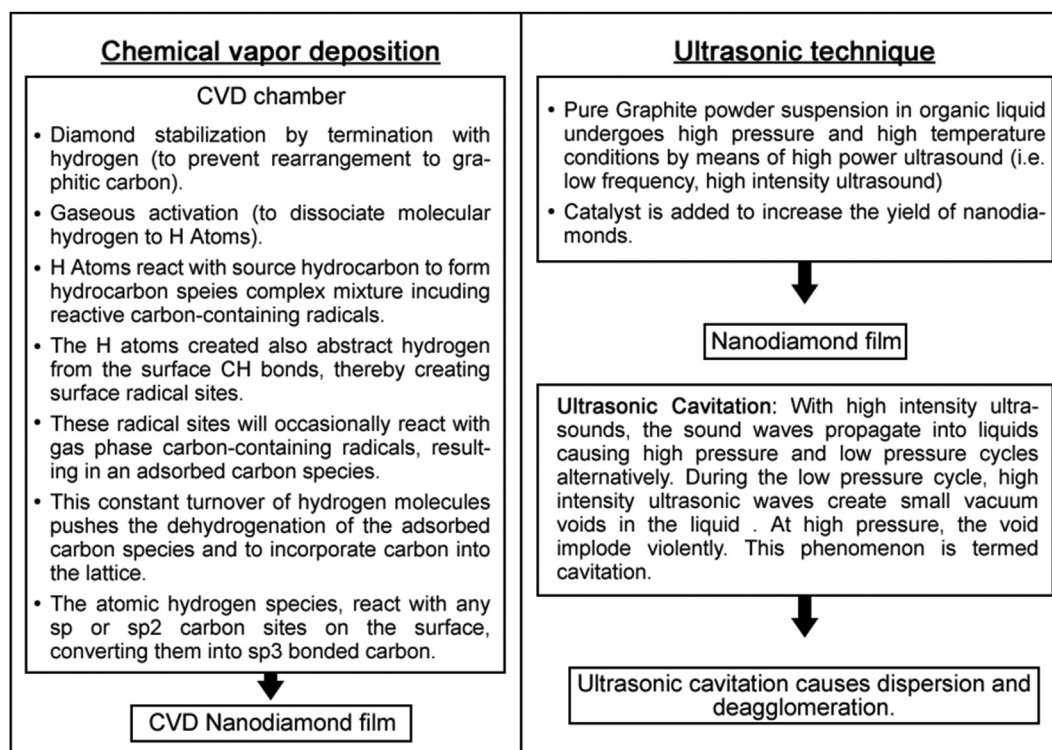


Fig. 6. Flowchart representation of nanodiamonds synthesis via chemical vapor deposition technique and ultrasonic technique.

Boudou et al. explored a fabrication technique for the production of fluorescent NDs with high yields. The process includes the conversion of diamond microcrystal powder obtained from ultrasonic method into aqueous concentrated colloidal dispersion of ultra-small nanoparticles (with a mean size less than 10 nm). The fabrication yield of NDs was higher than the previously reported microdiamonds. The results demonstrated an industrial cost-effective fabrication of fluorescent NDs with controlled properties [24].

#### 4. In vitro and in vivo cytotoxicity

NDs mediated drug delivery has drawn attention of scientists for secure and reliable transport of active moieties to the target site in a living system. However, for drug delivery significant toxicity is the major concern of these nano-carriers. Hence, it becomes obligatory to comprehend the in-depth knowledge of nanodiamond's biocompatibility via in vitro and in vivo studies [25]. In vitro cytotoxicity investigations are more simple, reproducible, more useful and cost-effective than in vivo studies in animal models. These tests are based on various cell functions like enzyme activity, cell proliferation, ATP (Adenosine triphosphate) production, and nucleotide uptake activity. Primarily, methyl tetrazolium (MTT) assays are very common in determining cell viability and proliferation [26]. Generally, it is a two-step process (as shown in Fig. 7). The first step involves reduction of yellow tetrazolium MTT (3-(4,5-dimethylthiazolyl-2)-2, 5-diphenyltetrazolium bromide) by metabolically active cells (by the action of dehydrogenase enzymes) to generate nicotinamide adenine dinucleotide (NADH) and nicotinamide adenine dinucleotide phosphate (NADPH) and insoluble formazan.

The second step involves solubilization of intracellular purple formazan which can be quantified by means of absorbance values spectrophotometrically. If the absorbance values are less than those

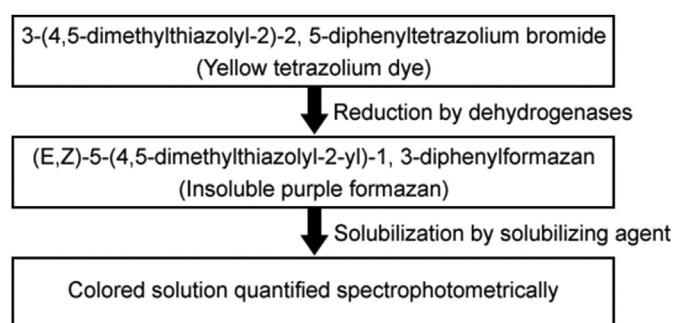


Fig. 7. In vitro cytotoxicity (MTT) assay for nanodiamonds.

of absorbance of control cells, there is reduction in rate of cell proliferation. Likewise, ATP assay is also known for its quick results and small sample cells. It is based on the assumption that live cells produce luminescence as it contains ATP inside and the level of luminescence will be proportional to ATP content of cells. It comprises cell lysis, which is followed by reaction between assay and ATP content of cell which finally generates luminescence. Photometer is used for the measurement of luminescence. NDs have also been estimated for in vitro cytotoxicity studies via MTT assay and ATP production assay [27]. The first reported toxicity of NDs at cellular level via MTT and ATP production assay was done by Schrand et al. The experiment turns out to be positive with no toxicity to cells with this size range and cell morphology remains unaffected after incubation with NDs. Further, they compared carbon-based nanomaterials (carbon black, carbon nanotubes, NDs) on neuroblastoma cells and macrophages. The results revealed the mildest toxic effect exhibited by NDs as compared to others [25]. Moreover, biocompatibility of NDs was also investigated on kidney cell culture by Yu et al. They explored the

localization of NDs within the cytoplasm of cells via fluorescent confocal microscopy and the outcomes showed less toxicity within the cells [28]. Supplementary to the above assays the toxicity or biocompatibility of NDs, reactive oxygen species (ROS) assay can also be performed. This assay is based on the generation of ROS by nanoparticle induced oxidative stress. Normally, ROS are produced as consequence of cellular redox/enzymatic reactions viz. metabolism and phagocytosis. In their further studies, Schrand et al. compared the ROS generation by carbon black and NDs via fluorescence intensity of dichlorofluorescein (DCF). The outcome revealed a lower level of ROS generation by NDs as compared to carbon black [29]. Additionally, Keremidarska et al. investigated the cytotoxicity of different sizes of NDs on two types of cell models, i.e., a human osteosarcoma cell line, MG63, and primary rat mesenchymal stem cells (rMSCs). Optical microscopy and proliferation assay were employed as assessing tools for cytotoxicity after 72 h of exposure to cells. NDs of small size were more toxic as they have shown elevated cell proliferation than those of higher size. Furthermore, genotoxicity studies have also become significant to envisage the effect of NDs at a chromosome level [30]. An investigation on TNF $\alpha$  and Bcl-x genes was done by Huang et al. by incubating acid treated NDs alongwith genes. The findings revealed no change in genes expression as compared to control. A significant biocompatibility was observed with HT-29 human colorectal adenocarcinoma cells by examining DNA fragmentation. A research on A549 lung cancer cells and 3T3-L1 embryonic fibroblasts revealed the non-cytotoxicity and significant viability of cells by incubating them with NDs for 10 days. Even, the cellular uptake of NDs did not lead to any interference in cell division and gene or protein expression [31]. Apart from in vitro cellular toxicity studies, animal models have also been used to study the effect of NDs on surrounding environment and thus, human health. Fig. 8 shows the different model organisms used for conducting in vivo study.

During manufacturing of NDs powder, some powder may spread in the surrounding air and may cause contamination due to its low density. This may also lead to pulmonary toxicity owing to respiration in that environment. To assess it, Yuan et al. performed the intratracheal instillation of NDs in mice and confirmed the low toxicity results via histopathological and ultrastructural investigations. Besides pulmonary toxicity and subcutaneous studies, a long-term toxicity study of NDs hydrosols was also performed via oral administration to mice. The aim was to study the effect of NDs on natural growth and reproducibility of mice via weight dynamics and production of offspring respectively. The experimental protocol includes water substitution by 0.002 wt%–0.05 wt% NDs hydrosols in mice regular diet. The results of weight dynamics displayed normal growth of internal organs viz. lungs, liver, kidneys and pancreas. Concurrently, healthy offsprings were observed, which indicates no loss in reproduction ability of mice [32]. The more detailed studies are shown in Table 1 [33–38].

## 5. Surface functionalization

Most of the commercially available NDs surface is found to be highly oxidized and carries numerous functional groups like hydroxyl, carboxyl, lactone and ketone. The presence of functional groups and sp<sup>2</sup> carbon directly affects the stability of NDs in a variety of media and leads to agglomeration. Moreover, NDs are thermodynamically unstable due to high surface energy. Thus, it becomes the need to alter the functional groups present on the surface of NDs. Surface functionalization involves modification in surface strategies of any compound (NDs), by attaching a variety of functional groups such as hydroxyl, carbonyl, carboxyl, anhydrides and lactones [39]. Surface functionalization also enhances the solubility in a variety of polar organic solvents and stability (by preventing agglomeration). However, as per the literature, scientists have explored significant mechanical and chemical techniques to reduce agglomeration and substitute functional group on their surface. Mechanical techniques comprise ultrasonic and ball milling. Apart from this, stirred media milling with ceramic beads followed by sonication has also emerged as a novel technology for the disintegration of NDs. Chemical technique involves nanodiamond powder heating in air at 400–430 °C so as to eliminate the sp<sup>2</sup> carbon impurities which may reduce the chances of agglomeration [40]. Osswald et al. highlighted the use of narrow temperature (400–430 °C) for maximum oxidation of sp<sup>2</sup> carbon with minimum wastage of diamond. NDs should be stable enough when their utilization is aimed for biological applications [41]. Alwani et al. formulated ND-gene complexes called diamoplexes for cervical cancer. Synthesis was done by covalent conjugation of lysine amino acid to carboxylated NDs surface generated through reoxidation in strong oxidizing acids. Results for particle size and zeta potential showed minimum sedimentation and good stability. The study concludes that functionalization of NDs with lysine maintains long term stability and also enables NDs to successfully interact with biological system [42]. Fluorination of NDs surface was done by Liu et al. Gaseous fluorine and hydrogen mixture reacted with NDs at 150–470 °C to produce a fluorinated NDs. Fluorinated NDs can further be functionalized with alkyl-lithium reagents, diamines and amino acids [43]. Bureson et al. aimed at the surface modification of NDs in a controlled manner so as to differentiate the influence of different functional groups on in vitro cellular response. Surface modification was done in hydro- and solvo-thermal conditions. The outcomes with in vitro cellular assays revealed no cellular toxicity with CO, OH, or NH-groups on the surface of the diamond particle [44]. Another successful targeted cellular interaction was explored by Krueger et al. They reduced all surface oxygen groups to hydroxyl by reacting borane in tetrahydrofuran (THF). Additionally, peptides synthesis was done by silane linker molecules to form an amine terminated surface [45]. These schemes are presented in Fig. 9. There are a variety of ligands utilized for the surface

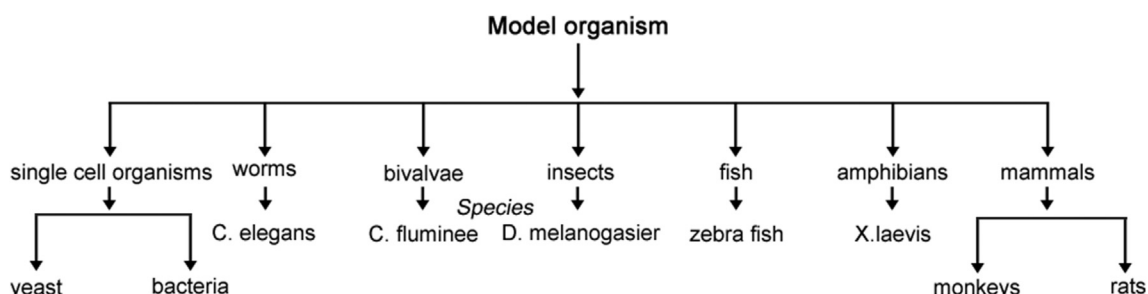


Fig. 8. Model organisms used for in vivo studies with nanodiamonds.

**Table 1**  
In vivo studies conducted with nanodiamonds.

S.No.	Parameter for biocompatibility	Observations based on parameters	Model organism	Nanodiamond type with size	In vivo study results
1.	Survival	1. Cytotoxicity and in vivo toxicity	1. Human embryonic kidney 293 (HEK293) cells 2. <i>Xenopus laevis</i> embryos	FND (4 nm)	Chemically surface functionalized (-OH, -NH <sub>2</sub> or -CO <sub>2</sub> H) ND related cytotoxicity and in vivo toxicity of ND were prepared. They used two model systems viz. human embryonic kidney 293 (HEK293) cells and <i>Xenopus laevis</i> embryos. The results of cell viability assays revealed that ND were not 1. cytotoxic to HEK293 cells at below 50 µg/mL ND 2. Having a potential embryotoxicity and teratogenicity for carboxylated ND-CO <sub>2</sub> H [40].
2.	Morphology	2. Mortality rate 1. Embryonic development 2. Histological examination	Bivalvae Zebrafish embryo  Cynomolgus monkey ( <i>Macaca fascicularis</i> ) Rat ( <i>Rattus norvegicus</i> ) Xenograft SCID mice	DND (4–6 nm) DND (100 nm)  DND ND-paclitaxel	100% mortality when exposed to ND solutions of 10 g/L [33]. A concentration dependent higher malformation induction after ND-COOH micro injection [34]. Some substantial abnormalities in monkey heart and liver at higher doses. Mild abnormalities at normal doses. No abnormal liver or kidney function histological changes. Preservation of anticancer activities on the induction of mitotic blockage and apoptosis [35].
3.	Biodistribution	Accumulation	Rat  Mice Rats and monkeys	NDS  FND ND	1. Radio labeled diamond nanoparticles gets accumulated majorly in lung, spleen and liver and finally gets excreted into the urinary tract. 2. An inflammatory response in the lungs and high dose- dependent retention of NDs in the lung [25]. NDs retention and accumulation in the macrophages present in the liver [9]. Accumulation in the axillary lymph nodes [36].
4.	Metabolism	1. Biochemical parameter 2. Oxidative stress markers	Murine	ND	1. Some histological alterations but no organ dysfunction. 2. Some changes in blood biochemical parameters affecting the liver function and lipid metabolism, but no signs of cell destruction [37]. Increased activity of glutathione S- transferase on 7 day and catalase on 14 day were observed respectively [38].

functionalization of NDs viz. carboxylic acid, fluorine, chlorine, lysine, and glutaraldehyde as stated in literature. Chemical modification of diamond surface is essential for diamond to be applied as potential biosensor or biochip or a substrate to immobilize biological molecules [46].

NDs can be used in various sectors including medical and non-medical. These are widely used as vehicle for drug delivery, in bio-imaging and cell tracking, skin care and hair implants, dental care, and many more. NDs tend to form agglomerates which may be useful in chromatography and drug delivery. The characteristics, such as photo stability, chemical non-reactivity, biocompatibility, and emission in the far-red bandwidth, make NDs an interesting candidate for noninvasive imaging [34]. These tiny gems possess a broad range of promising applications in drug delivery, bio-imaging and tissue engineering.

## 6. Biomedical applications of NDs

NDs exhibit special traits of nanoparticles and diamonds, which can widely be used in various fields viz. biomedical and imaging procedures. NDs are very prominent as targeted drug delivery system with increased drug efficacy and decreased toxicity level,

and thus can also be known as safer medication. Diamond containing structures will provide significant improvements in the diagnosis and treatment of medical conditions over the coming years. Diamond coatings have been applied to a number of medical devices in recent years, including temporal mandibular joint prostheses, heart valves, and micro electro-mechanical systems, microscale devices for sensing or drug delivery. Diamond nanowire based nucleic acid sensors have been developed. NDs are also used as targeted drug delivery vehicle for bone diseases and bone regeneration [47]. There are many potential biological and medical applications of NDs, including its use in biocompatible composites and implants, targeted drug delivery, components of biosensors and stable solid supports for the synthesis of peptides. But there are three main reported use of NDs, i.e., immobilization of proteins, as fluorescent markers for cell imaging and as a drug delivery vehicle.

### 6.1. NDs in imaging and therapy

The unique fluorescence properties of NDs have already been discussed. These properties could be explored further to obtain advantages; high quantum efficiency of NDs may result in bright fluorescence; NDs are photostable over longer periods which might help in long-term NDs tracking in cell; NDs have long time fluorescence and emission wavelength less than 690 nm that may contribute to high contrast imaging; photobleaching related to fluorophore can be avoided. The imaging and therapy utilizing nanodiamond helps in early diagnosis, intervention, and effective prevention. Imaging techniques are useful in determining the proper stage of the disease, follow-up after treatment and, as highlighted in recent times, in predicting prognosis [48]. Fu et al. examined the binding of positively charged NDs to negatively charged DNA by exploring a red fluorescent NDs (100 nm in size). Primarily, DNA molecules were labeled with TOTO-1 (nucleic acid stain) and then allowed to associate ionically with poly-L-lysine-coated carboxylated fluorescent NDs in a buffer medium (diluted solution). After this, the diluted solution was passed through micro

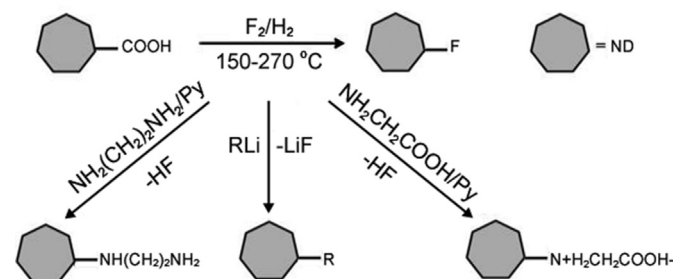


**Fig. 9.** Illustration of several schemes for the surface functionalization of nanodiamonds.

channel-combining technology and laser excitation at different wavelengths, DNA was discovered to interact with positively charged NDs via packing. This research reveals that interaction between biomolecules could be studied by single fluorescent nanodiamond [48]. Furthermore, another research group utilized fluorescent properties of NDs (100 nm red fluorescent NDs) to explore the uptake mechanism of transferring in HeLa cells. ND-transferrin complexes were made by linking NDs with transferrin via amide linkage [49]. In addition, Mohan et al. outlined the motion of free and bioconjugated red fluorescent NDs in *Caenorhabditis elegans* (worms). Worms were divested from *E. coli* and then given free NDs and dextran/albumin conjugated carboxylated NDs. After 12 h of administration, free NDs were localized in worm's intestinal tract with no absorption while bioconjugated NDs were captured up by intestinal cells of worms and remained there for 24 h [50]. Hsu et al. used fluorescent nanodiamond (FND) for the labeling and tracking of neuronal differentiation and neuron cells derived from embryonal carcinoma stem (ECS) cells [51]. Zurbuchen et al. had demonstrated a subcellular multimodal imaging technique which facilitates the localization of NDs having fluorescent N-V centers. Surface was functionalized to target specific locations which were observable by both optical and electron microscopies. The images of optical microscopy displayed NDs in vitro tracking and confirmed its uptake. Due to exclusive fluorescent property of NDs, these are utilized as biolabeling agent even for diagnosing diseases of the nervous system [52]. Huang et al. investigated the compatibility of NDs on neurons. The results revealed that NDs possess very low neuronal toxicity, except that it hinders the morphogenesis of neural cells [53].

#### 6.1.1. Disadvantages

Complications exist while the application of NDs from physics field to biomedical field. Methods used for characterizing NDs in dry state are hardly applicable for detecting NDs in living organisms such as cells [54].

Reineck et al. observed weak correlation between FND size and fluorescence brightness which may be due to surface interactions [55].

#### 6.2. Carrier for drug and peptide delivery

For the conjugation of active pharmaceutical ingredients, NDs are ideal candidate owing to their huge surface area and surface functionalities. A drug carrier is found to be suitable only in terms of its loading capacity, capability of protection from surrounding environment and inert nature. A prominent drug loading efficiency with less concentration of carrier is highly appreciated. Simultaneously, timely release of drug from the carrier is also of great significance for desired therapeutic effect. Huang et al. investigated the loading and release of a chemotherapeutic agent viz. doxorubicin hydrochloride (DOX) from NDs. The research was based on the concept of ionic interaction between carboxylic and hydroxylic groups present on the surface of NDs and amine group of DOX to form NDs-DOX loose cluster. In further studies, it was found that DOX was adsorbed on surface of NDs and also in the fissures of cluster. Additionally, cytotoxic studies of DOX-NDs on mouse macrophages and human colorectal cancer cells revealed a lower toxic effect with sustained release than free-DOX [56]. Apart from the large surface area for conjugation, NDs have also emerged as dispersibility enhancing agents of hydrophobic drugs [57]. There are certain chemotherapeutic moieties which have their solubilities in organic solvents that limit their parenteral administration viz. a liver cancer drug 'purvalanol A' [58] and a breast cancer moiety '4-hydroxytamoxifen' [59]. The characteristic of enhancing dispersibility in water is attributed to NDs' nature of adsorbing drug on

surfaces and retaining therapeutic effectiveness of the drug. The therapeutic activity of NDs formulations was confirmed by MTT assay. These outcomes revealed that NDs could play a significant role in formulation development of poor water-soluble drugs [60].

Enzyme immobilization is an attempt of technique which includes matrixing or engraving enzymes onto a polymer matrix and increasing the availability of enzymes to substrate. Immobilization of proteins on nanodiamond is much in use for drug delivery. Properties of having high colloidal stability and enterosorbent potential in aqueous and non-aqueous media allow NDs to be efficiently used for the targeted drug delivery [61]. But stability of the complexes is based on bonding of NDs with respective proteins. As concluded by Purtov et al. complexes obtained by covalent immobilization are more stable than non-specific absorption of proteins [62]. Researchers have proved the uptake of NDs by living cells. NDs can easily be complexed with any compound which can either be an antigen, an antibody or an immunoglobulin. Various researchers have shown their work on immobilization with NDs. Kossovsky et al used NDs coated with a disaccharide to immobilize an antigen, which was then directly injected into rabbits to elicit an immune response. The antigen carrier plays an important role in controlling the conformation of the antigen and exposing or shielding important functionalities; it is believed that NDs immobilization results in less distortion of the protein conformation allowing better binding by antibodies and hence, a stronger immune response [63]. Bondar et al. used detonation NDs for the separation of recombinant protein from *E. coli*. by physical adsorption of protein onto NDs particles [64]. Huang et al. described the immobilization of antibodies and bacterial binding on NDs [65]. Kong et al. used this principle to capture proteins for analysis by MS spectra [66,67]. Researcher have also demonstrated that NDs seeded electrodes can be bio-functionalized using previously published UV alkene surface chemistry of diamond films and used for pathogen detection. This is basically nano-structuring of biosensing electrodes with NDs for antibody immobilization [68].

Various researches have been carried out, which allow to consider the possibility of applying NDs as carriers to address deliveries of bioactive substances (i.e., drugs) to various biological targets (in vitro as well as in vivo). NDs have the potential to deliver the biological moieties into a single cell, or targeted cells; hence this technology is widely used in cancer treatment [69]. In cancer treatment, it is required to target the cancer cells, not the normal cell or tissue. Clusters of the NDs surround the drugs to ensure that they remain separated from healthy cells until they reach the cancer cells, where they are released. Therefore, it enables the whole amount of drug to reach the target site and the size of NDs enables kidney for their easy removal from the body without blocking other blood vessels [70].

Man et al. synthesized the daunorubicin - NDs conjugates for the treatment of chemoresistant leukemia which have the potential to improve treatment efficacy, especially towards resistant strains. Cell line studies on a K562 human myelogenous leukemia cell line with multidrug resistance and augmented daunorubicin exposure was carried out for efficacy enhancement demonstration. NDs enhanced the daunorubicin delivery to resistant cells [71]. NDs are used as a drug carrier mainly in any of the forms viz. NDs assemble on a chemical substrate to form a thin film, having interactions with a drug in two dimensions (forming spontaneous clusters also named as NDs hydrogel with low free energy in an aqueous solution), having interactions with a drug in three dimensions [16]. Nanostructured diamond (NSD) coatings or diamond like carbon coatings enhance the wear resistance and prevent leaching of metallic ions from orthopedic and dental implants into the body. NDs-based drug delivery against cancer is one of the most developed biomedical applications. Moreover, NDs also play a vital and

therapeutic role in tissue engineering and anti-microbial applications [19]. Toh and his research team describe a ND–mitoxantrone (MTX) complex that can be rapidly synthesized and mediate marked improvements in drug efficacy. This study concluded that ND–MTX complex markedly enhanced MTX retention and improved therapeutic efficacy in chemoresistant breast cancer cells [72]. Another research for improving therapeutic efficacy in chemoresistant cancer cell was done by reversibly bounding NDs to epirubicin by physical adsorption. This results in formation of nanodiamond–epirubicin drug complex. The results prove that NDs mediated drug delivery may serve as a powerful method for overcoming chemoresistance in cancer stem cells and markedly improving overall treatment against hepatic cancers [73]. NDs prove to be very efficient vehicle for drug delivery. A potential anti-cancer investigation has been conducted by researchers regarding the biomedical use of plant drug-functionalized NDs. Coupling of reduced NDs was done with 5,7-dimethoxycoumarin (citraopten, a plant secondary metabolite) to form a complex which shows its ability to reduce B16F10 tumor cell growth more effectively than treatment with the pure molecule. The ND–citraopten complex determines cell cycle arrest, morphological changes and alteration of mRNA levels of cytoskeletal related genes [74]. In the field of ocular drug delivery, NDs have been found significant application for the treatment of diseases like glaucoma. In this piece of work, researchers presented lysozyme-triggered release of timolol maleate loaded NDs and then embedding NDs onto contact lenses. They coated individual NDs with polyethyleneimine (PEI) and then cross-linked with an enzyme cleavable polysaccharide, chitosan, forming an NDs nanogel loaded with timolol maleate (TM). These NDs nanogels are then embedded within a poly-HEMA matrix and cast into contact lenses. The results revealed effective drug complexation and enzyme activation [75]. NDs are also excellent candidates for topical protection of skin from sun burn. They do not exhibit photo-catalytic activity which is the main factor of producing reactive oxygen species (ROS), resulting in the damaged skin. They exhibit the property of scattering by which they prevent UV B induced skin damage. Wu et al. evaluated the efficacy and safety of NDs in UV B protection using cell cultures and mouse models. Results revealed that NDs shielding efficiently decline 95% UV B radiation while direct exposure of UV B radiation to cultured keratinocyte and fibroblasts causes their death [76]. Lists of recent investigations are presented in Table 2 [77–79].

### 6.2.1. Advantages

NDs in their original form can be used for drug delivery, i.e., there is no need to apply the process of oxidative modification. This

can be due to attaining good water solubility even without any acidic treatment. This may result in minimum side effects.

NDs have strong affinity towards proteins and antibodies, thus forming more stable conjugates.

### 6.2.2. Disadvantages

Xing et al. demonstrated that genotoxicity can occur, while introducing the chemical groups onto NDs [80].

Due to smaller size of NDs, it is very difficult to evaluate their distribution through conventional microscopy method; hence, radionuclide tracer technique is used for detection. This technique involves use of radioactive materials, which can lead to toxicity, and is an expensive process [81].

The process of complexing nanodiamond with active moiety through covalent bonding is a complicated process and it is difficult to eliminate the toxic solvents used during synthesis. Moreover, the complex formed can not show slow-release function.

### 6.3. NDs in gene therapy

Gene therapy can be used in treatment of various life-threatening diseases, like cancer, heart disease and diabetes. NDs act as an emerging attractive tool for gene delivery, by which efficiency of gene therapy is much more increased. The technology requires both effective cellular uptake and cytosolic release of the gene. Taking green fluorescent protein gene as an example, Chu et al. demonstrated the successful cytosolic delivery and expression of such a gene using the prickly NDs as carrier [82]. Perevedentseva et al. provided evidence that lysine functionalization enables NDs to interact effectively with the biological system to be used for RNAi therapeutics [83]. Zhang et al. demonstrated NDs as viral vectors for in vitro gene delivery via surface immobilization with 800 Da polyethyleneimine and covalent conjugation in presence of amine groups. This approach represented an efficient avenue towards gene delivery via DNA functionalized NDs [84]. NDs have also been explored their potential in the delivery of small interfering RNAs. Liu et al. investigated the potential of small interfering RNAs (siRNA) loaded functionalized NDs with polymer polyethyleneimine (PEI) for its in vitro efficiency and cytotoxicity via simulation technique. The results showed to be highly effective for in vitro delivery with low cytotoxicity [85]. In addition, Alhaddad et al. elucidated the delivery of siRNA via cationic polymers viz. polyallylamine and polyethyleneimine coated diamond nanocrystals. They targeted Ewing sarcoma cells which were traceable for long time owing to their intrinsic fluorescence [86].

**Table 2**  
Recent investigations regarding Nanodiamonds for cancer therapy.

S.No.	Year	Methodology adopted for cancer investigation	In vitro and in vivo results
1.	2014	Cellular uptake studies of nanodiamond doxorubicin complex (NDDOX) via laser scanning confocal microscopy using HepG2 cells. In vivo survival rate comparison studies. Histopathology of tumor after treatment with NDDOX.	Slow and sustained drug release characteristics compared with free doxorubicin. Survival rate with NDDOX was four times greater than that free doxorubicin. Histopathological analysis revealed non-toxicity of NDs and NDDOX to kidney, liver, or spleen in contrast with the well-known toxic effects of free doxorubicin [77].
2.	2010	Nanodiamonds–paclitaxel conjugation for cancer therapy and evaluated by atomic force microscope and nuclear magnetic resonance spectroscopy.	Reduction in cell viability in the A549 human lung carcinoma cells. ND–paclitaxel was taken into lung cancer cells and was located in the microtubules and cytoplasm of A549 cells observed by flow cytometer analysis and confocal microscopy respectively. Tumor growth and formation of lung cancer cells were also blocked in xenograft SCID mice [78].
3.	2015	Self-assembled nanodiamond–lipid hybrid particles (NDLPs) were used for cell-targeted imaging and therapy of triple negative breast cancers.	Highly biocompatible particles providing cell-specific imaging, tumor retention of ND-complexes, preventing epirubicin toxicities and mediating regression of triple negative breast cancers [79].
4.	2014	Epirubicin was used to synthesize stable nanodiamond–drug complex.	Increased endocytic uptake and enhanced tumor cell retention. Improved impairment of secondary tumor formation [73].
5.	2015	Surface irradiated nanodiamonds (INDs) were grafted with polyethylene glycol (PEG) to improve its stability and circulation time in blood.	INDs accumulate in tumors and completely delineate the entire tumor within 10 h [38].

### 6.3.1. Advantages

NDs can act as versatile nanocarriers to deliver genes in biological systems with enhanced delivery efficiency and biocompatibility.

Efficiency of drug delivery can be increased to 70 times as compared to conventional gene delivery [84,87].

### 6.3.2. Disadvantages

More research is required so as to improve interaction with stem cells, bio-distribution and toxicity of NDs, thereby increasing their potential [88].

### 6.4. NDs as an antibacterial agent

Antimicrobial or antibacterial agents hinder/terminate the growth and reproduction of bacteria. NDs have been found to kill gram-positive and gram-negative bacteria. Wehling et al. showed that NDs can be an efficient antibacterial agent based on their surface composition. Their experiment proposed that the NDs possessing partially oxidized and negatively charged surfaces would have antibacterial property viz. acid anhydride group on surface [89]. Moreover, surface functionalization of NDs with protein molecules enhances the bactericidal property of NDs. In addition to the above-mentioned research, another group investigated the antibacterial activity of ultrafine nanodiamond against gram negative bacteria, i.e., *E. coli*. Functionalization of NDs surface was done with carboxyl group to form carboxylated nanodiamond (cND) and was kept in highly nutritious media. Upon scanning electron microscopy (SEM), the photomicrograph revealed that cND was attached to the bacterial cell wall surface leading to its destruction [90]. Surface functionalization of NDs with glycan (sugar coating) had also uncovered the bactericidal effect of NDs specifically for type 1 fimbriae-mediated *E. coli* adhesion. These have the potential in countering *E. coli* biofilm formation. NDs form covalent bond with molecules on cell walls or bind to intracellular components which inhibit vital enzymes and proteins, leading to a rapid collapse of the bacterial metabolism and finally cell death [91].

#### 6.4.1. Advantages

NDs act as a potent antibacterial agent by destroying bacterial barrier.

NDs have the potency to bind with several viruses like hepatitis B or C [92].

#### 6.4.2. Disadvantages

Continuous interaction with the cellulose dialysis membrane can result in the loss of reactive oxygen-groups and charges [93].

### 6.5. NDs in bone tissue engineering

Bone tissue engineering is a technique of creating biological substitutes to repair and replace the incomplete or absolute infected tissues. Therefore, the major challenge is to fabricate a scaffold which can provide strength comparable to natural bone [94]. Properties like high porosity, appropriate pore size, biocompatibility with adjacent tissue, biodegradability, ability to support adhesion, growth, and differentiation of osteogenic cells make NDs to act as a promising material for bone tissue engineering [95–97]. Zhang et al. fabricated a multifunctional fluorescent composite bone scaffold exploiting poly ( $\alpha$ -lactic acid) (PLLA) and octadecylamine-functionalized nanodiamond (ND-ODA) and observed that cell proliferation was not hampered by this scaffold [98]. Moreover, Yang et al. have used PND/polymer scaffold which supports osteoblast (bone-forming cell) growth and differentiation,

and also, enhances bio-mineralization and formation of bone like apatite on the scaffold in simulated body fluid (SBF). This concluded that these scaffolds are useful for a wide range of orthopedic regenerative engineering applications [99].

### 6.5.1. Disadvantages

It is not easy to design a biodegradable and bio-compatible scaffold attaining mechanical strength that of natural bone [95].

## 7. Limitations of NDs

Despite having diverse advantages and application, NDs also have some limitations which have to be overcome during their biomedical application; some of these are mentioned below:

- > Compared with standard organic dyes, the emission of an N-V center is low [83].
- > It is problematic to differentiate the particle from the background fluorescence, to overcome this problem diamonds containing many N-V centers are used. However, this requires larger diamonds; this larger size can lead to problems for some bio-applications.
- > Bound NDs might alter the structure and function of attached proteins [83,100].
- > The N-V centre in diamond is a promising candidate for a solid-state qubit. However, its charge state is known to be unstable, discharging from the qubit state NV<sup>-</sup> into the neutral state NVO under various circumstances [101].
- > The N-V center in nanodiamond has already been used as a fluorescence marker in biological systems. However, up to now there has been no analysis of the effect of the biological environment on the quantum dynamics of the N-V center; such considerations are critical to nano-biomagnetometry applications [23].
- > The conventional method use for synthesis of NDs requires high pressure and high temperature [101].

## 8. Patents on NDs

NDs have emerged as innovative formulation for drug delivery. Many researches are being carried out by using NDs for biological applications. Patents granted for drug delivery have been discussed in detail in Table 3 [102–111].

## 9. Conclusion

The extraordinary properties of NDs have enhanced the researchers' interest in diverse fields of applications. The sparkling and a style statement use of diamonds have been surmounted by their significant applications in diagnostics and drug delivery system. NDs' intrinsic structural integrity and involvement of synthetic techniques like disaggregation and functionalization have explored new horizons for biomedical applications. Still, many challenges like cellular fate, re-aggregation prevention, enhanced control on surface chemistry, and large volume manufacture of NDs are the issues of high concern. On the bright side, plethora of promising applications will drive the researchers in the biomedical field ahead. An advanced and better knowledge regarding the structure and surface chemistry will direct the investigators to achieve a significant control over properties and thus, their relevant applications. Thus, continual efforts in the development of NDs as diagnostic tool and as drug delivery system will be made to surpass the previously established carbon nanomaterials viz. nanotubes and fullerenes for biomedical applications.

**Table 3**  
Patents granted for Nanodiamonds as drug delivery system.

S.No.	Patent No./ Application No.	Title	Research work done
1.	US 20100129457A1	Nanodiamonds enhanced drugs	Efficacy of drugs like analgesics, cholesterol reducing drugs and other substances are increased by attaching them (covalently) and the functional groups to nanodiamond surface [102].
2.	US 8753614 B2	Nanodiamond UV protectant formulations	A cosmetic or sunscreen preparation comprising diamond nanoparticle in a physiologically compatible medium was prepared [103].
3.	US 9227089 B1	Skin treatment for promoting hair growth	Nanodiamond is used as a mineral carrier for infusing the blood product composition [104].
4.	US 20100305309 A1	Nanodiamond particle complexes	Soluble complexes of nanodiamond particles and therapeutic agents like insoluble therapeutics, anthracycline, tetracycline compounds, nucleic acids, proteins, etc were prepared [105].
5.	US 7294340 B2	Healthcare and cosmetic compositions containing nanodiamond	Compositions like deodorants, toothpastes, shampoos, antibiotics, dermal strips, DNA test strips, skin cleansers were explored [106].
6.	US 9248383 B2	Composite materials containing nanoparticles and their use in chromatography	Porous inorganic/organic hybrid particles were embedded with nanoparticles selected from oxides or nitrides [107]
7.	US 9283657 B2	Method of making a diamond particle suspension and method of making a polycrystalline diamond article therefrom	Polycrystalline diamond compact was formed using substantially homogeneous suspension of nanodiamond particles and microdiamond particles [108].
8.	US 8888736 B2	High shear application in medical therapy	Method comprising mixing a therapeutic gas or a therapeutic liquid or a combination thereof and a liquid carrier in a high shear device to produce a dispersion [109].
9.	US 8293216 B2	Cleaning oral care compositions	An oral care composition comprising a fused silica abrasive offering improved cleaning [110].
10.	US 7569205 B1	Nanodiamond fractional and the products thereof	Nanodiamonds were processed to fractionate the detonation nanodiamonds, forming a combination of detonation nanodiamonds and a solvent [111].

## Conflicts of interest

The authors declare that there are no conflicts of interest.

## Appendix A. Supplementary data

Supplementary data to this article can be found online at <https://doi.org/10.1016/j.jpha.2019.09.003>.

## References

- C. Cha, S.R. Shin, N. Docemeci, et al., Carbon based nanomaterials: multi functional materials for biomedical engineering, *ACS Nano* 7 (2013) 2891–2897.
- V. Georgakilas, J.A. Perman, J. Tucek, et al., Broad family of carbon nanomaterials: classification, chemistry, and applications of fullerenes, carbon dots, nanotubes, graphene, nanodiamonds, and combined superstructures, *Chem. Rev.* 115 (2015) 4744–4822.
- A. Chaudhary, J.O. Welch, R.B. Jackman, Electrical properties of mono-dispersed detonation nanodiamonds, *Appl. Phys. Lett.* 96 (2010) 242903.
- A.Y. Vul, A.T. Dideikin, A.E. Aleksenskii, et al., Detonation Nanodiamonds: Synthesis, Properties and Applications, *RSC Nanosci. Nanotechnol.* Royal Society of Chemistry, 2014, pp. 37–48.
- J. Tisler, G. Balasubramanian, B. Naydenov, et al., Fluorescence and spin properties of defects in single digit nanodiamonds, *ACS Nano* 3 (2009) 1959–1965.
- O.A. Williams, M. Nesladek, M. Daenen, et al., Growth, electronic properties and applications of nanodiamond, *Diam. Relat. Mater.* 17 (2008) 1080–1088.
- S. Kazi, A review article on nanodiamonds discussing their properties and applications, *Int. J. Pharm. Sci. Inven.* 3 (2014) 40–45.
- D. Slocombe, A. Porch, E. Bustarret, et al., Microwave properties of nanodiamond particles, *Appl. Phys. Lett.* 102 (2013) 244102.
- Y. Zhu, J. Li, W. Li, et al., The biocompatibility of nanodiamonds and their application in drug delivery systems, *Theranostics* (2012) 302–312.
- D. Ho, C.-H.K. Wang, E.K.-H. Chow, Nanodiamonds: the intersection of nanotechnology, drug development, and personalized medicine, *Sci. Adv.* 1 (2015) e1500439.
- R. Kaur, I. Badea, Nanodiamonds as novel nanomaterials for biomedical applications: drug delivery and imaging systems, *Int. J. Nanomed.* 8 (2013) 203–220.
- Y.Y. Hui, C.-L. Cheng, H.-C. Chang, Nanodiamonds for optical bioimaging, *J. Phys. D Appl. Phys.* 43 (2010) 374021.
- E. Perevedentseva, Y.C. Lin, M. Jani, et al., Biomedical applications of nanodiamonds in imaging and therapy, *Nanomedicine* 8 (2013) 2041–2060.
- Y.-R. Chang, H.Y. Lee, K. Chen, et al., Mass production and dynamic imaging of fluorescent nanodiamonds, *Nat. Nanotechnol.* 3 (2008) 284–288.
- U. Maitra, K.E. Prasad, U. Ramamurthy, et al., Mechanical properties of nanodiamond-reinforced polymer-matrix composites, *Solid State Commun.* 149 (2009) 1693–1697.
- V.N. Mochalin, O. Shenderova, D. Ho, et al., The properties and applications of nanodiamonds, *Nat. Nanotechnol.* 7 (2012) 11–23.
- B.I. Kharisov, O.V. Kharisova, L. Chavez-Guerrero, Synthesis techniques, properties, and applications of nanodiamonds, *Synthesis and Reactivity in Inorganic, Metal-Organic, and Nano-Metal Chemistry* 40 (2010) 84–101.
- V.V. Danilenko, On the history of the discovery of nanodiamond synthesis, *Phys. Solid State* 46 (2004) 595–599.
- W.-W. Zheng, Y.-H. Hsieh, Y.-C. Chiu, et al., Organic functionalization of ultradispersed nanodiamond: synthesis and applications, *J. Mater. Chem.* 19 (2009) 8432–8441.
- E. Neu, D. Steinmetz, J. Riedrich-Möller, et al., Single photon emission from silicon-vacancy color centres in chemical vapour deposition nano-diamonds on iridium, *New J. Phys.* 13 (2011) 025012.
- K. Tsugawa, M. Ishihara, J. Kim, et al., Large-area and low-temperature nanodiamond coating by microwave plasma chemical vapor deposition, *New Diam. Front. Carbon Technol.: Int. J. New Diam. Front. Carbon Relat. Mater.* 16 (2006) 337–346.
- C.-R. Lin, W.-H. Liao, D.-H. Wei, et al., Improvement on the synthesis technique of ultrananocrystalline diamond films by using microwave plasma jet chemical vapor deposition, *J. Cryst. Growth* 326 (2011) 212–217.
- L.T. Hall, C.D. Hill, J.H. Cole, et al., Monitoring ion-channel function in real time through quantum decoherence, *Proc. Natl. Acad. Sci. U.S.A.* 107 (2010) 18777–18782.
- J.-P. Boudou, P.A. Curmi, F. Jelezko, et al., High yield fabrication of fluorescent nanodiamonds, *Nanotechnology* 20 (2009) 359801.
- A.M. Schrand, H. Huang, C. Carlson, et al., Are diamond nanoparticles cytotoxic? *J. Phys. Chem. B* 111 (2007) 2–7.
- J. van Meerloo, G.J. Kaspers, J. Cloos, Cell sensitivity assays: the MTT assay, *Methods Mol. Biol.* 731 (2011) 237–245.
- P.-W. Sylvester, Optimization of the tetrazolium dye (MTT) colorimetric assay for cellular growth and viability, *Methods Mol. Biol.* 716 (2011) 157–168.
- S.-J. Yu, M.-W. Kang, H.-C. Chang, et al., Bright fluorescent nanodiamonds: no photobleaching and low cytotoxicity, *J. Am. Chem. Soc.* 127 (2005) 17604–17605.
- A.M. Schrand, L. Dai, J.J. Schlager, et al., Differential biocompatibility of carbon nanotubes and nanodiamonds, *Diam. Relat. Mater.* 16 (2007) 2118–2123.
- M. Keremidarska, A. Ganeva, D. Mitev, et al., Comparative study of cytotoxicity of detonation nanodiamond particles with an osteosarcoma cell line and primary mesenchymal stem cells, *Biotechnol. Biotechnol. Equip.* 28 (2014) 733–739.
- Y.-A. Huang, C.-W. Kao, K.-K. Liu, et al., The effect of fluorescent nanodiamonds on neuronal survival and morphogenesis, *Sci. Rep.* 4 (2014) 6919.
- Y. Yuan, X. Wang, G. Jia, et al., Pulmonary toxicity and translocation of nanodiamond in mice, *Diam. Relat. Mater.* 19 (2010) 291–299.
- A. Cid, A. Picado, J.B. Correia, et al., Oxidative stress and histological changes following exposure to diamond nanoparticles in the freshwater Asian clam *Corbicula fluminea* (Müller, 1774), *J. Hazard. Mater.* 284 (2015) 27–34.
- L. Marcon, F. Riquet, D. Vicogne, et al., Cellular and in vivo toxicity of

- functionalized nanodiamond in *Xenopus* embryos, *J. Mater. Chem.* 20 (2010) 8064.
- [35] K.K. Liu, W.W. Zheng, C.C. Wang, et al., Covalent linkage of nanodiamond-paclitaxel for drug delivery and cancer therapy, *Nanotechnology* 21 (2010) 315106.
- [36] V. Vijayanthimala, P.Y. Cheng, S.H. Yeh, et al., The long-term stability and biocompatibility of fluorescent nanodiamond as an *in vivo* contrast agent, *Biomaterials* 33 (2012) 7794–7802.
- [37] L.K. Moore, E.K. Chow, E. Osawa, et al., Diamond lipid hybrids enhance chemotherapeutic tolerance and mediate tumor regression, *Adv. Mater.* 25 (2013) 3532–3541.
- [38] A.A.M. Ali, H.R.H. Mohamed, Genotoxicity and oxidative stress induced by the orally administered nanosized nickel and cobalt oxides in male albino rats, *J. Basic Appl. Zool.* 2 (2019) 80.
- [39] K.B. Holt, Diamond at the nanoscale: applications of diamond nanoparticles from cellular biomarkers to quantum computing, *Philos. Trans. R. Soc. A Math. Phys. Eng. Sci.* 365 (2007) 2845–2861.
- [40] J.-Y. Raty, G. Galli, Ultradispersity of diamond at the nanoscale, *Nat. Mater.* 2 (2003) 792–795.
- [41] S. Osswald, G. Yushin, V. Mochalin, et al., Control of  $sp^2/sp^3$  carbon ratio and surface chemistry of nanodiamond powders by selective oxidation in air, *J. Am. Chem. Soc.* 128 (2006) 11635–11642.
- [42] S. Alwani, R. Kaur, D. Michel, et al., Lysine-functionalized nanodiamonds as gene carriers: development of stable colloidal dispersion for *in vitro* cellular uptake studies and siRNA delivery application, *Int. J. Nanomed.* 11 (2016) 687–702.
- [43] K. Liu, C. Cheng, C.C. Chang, et al., Biocompatible and detectable carboxylated nanodiamond on human cell, *Nanotechnology* 18 (2007) 325102.
- [44] T. Bursleson, N. Yusuf, A. Stanishevsky, Surface modification of nanodiamonds for biomedical application and analysis by infrared spectroscopy, *J. Ach. Mater. Manuf. Eng.* 37 (2009) 258–263.
- [45] A. Krueger, T. Boedeker, Deagglomeration and functionalisation of detonation nanodiamond with long alkyl chains, *Diam. Relat. Mater.* 17 (2008) 1367–1370.
- [46] L. Marcon, F. Riquet, D. Vicogne, et al., Cellular and *in vivo* toxicity of functionalized nanodiamond in *Xenopus* embryos, *J. Mater. Chem.* 20 (2010) 8064–8069.
- [47] A. Krueger, New carbon materials: biological applications of functionalized nanodiamond materials, *Chem. Eur. J.* 14 (2008) 1382–1390.
- [48] C.-C. Fu, H.-Y. Lee, K. Chen, et al., Characterization and application of single fluorescent nanodiamonds as cellular biomarkers, *Proc. Natl. Acad. Sci. U.S.A.* 104 (2007) 727–732.
- [49] V.Y. Dolmatov, Detonation synthesis ultradispersed diamonds: properties and applications, *Russ. Chem. Rev.* 70 (2001) 607–626.
- [50] N. Mohan, C.-S. Chen, H.-H. Hsieh, et al., *In vivo* imaging and toxicity assessments of fluorescent nanodiamonds in *Caenorhabditis elegans*, *Nano Lett.* 10 (2010) 3692–3699.
- [51] T.-C. Hsu, K.-K. Liu, H.-C. Chang, et al., Labeling of neuronal differentiation and neuron cells with biocompatible fluorescent nanodiamonds, *Sci. Rep.* 4 (2014) 5004.
- [52] M.A. Zurbuchen, M.P. Lake, S.A. Kohan, et al., Nanodiamond landmarks for subcellular multimodal optical and electron imaging, *Sci. Rep.* 3 (2013) 2668.
- [53] Y.-A. Huang, C.-W. Kao, K.-K. Liu, et al., The effect of fluorescent nanodiamonds on neuronal survival and morphogenesis, *Sci. Rep.* 4 (2014) 6919.
- [54] N. Prabhakar, J.M. Rosenholm, Nanodiamonds for advanced optical bio-imaging and beyond, *Curr. Opin. Colloid Interface Sci.* 39 (2019) 220–231.
- [55] P. Reineck, L.F. Trindade, J. Havlik, et al., Not all fluorescent nanodiamonds are created equal: a Comparative Study, *Part. Part. Syst. Charact.* 36 (2019) 1900009.
- [56] H. Huang, E. Pierstorff, E. Osawa, et al., Active nanodiamond hydrogels for chemotherapeutic delivery, *Nano Lett.* 7 (2007) 3305–3314.
- [57] M. Chen, E.D. Pierstorff, R. Lam, et al., Nanodiamond-mediated delivery of water-insoluble therapeutics, *ACS Nano* 3 (2009) 2016–2022.
- [58] A. Goga, D. Yang, A.D. Tward, et al., Inhibition of CDK1 as a potential therapy for tumors over-expressing MYC, *Nat. Med.* 13 (2007) 820–827.
- [59] S.G. Nayfield, J.E. Karp, L.G. Ford, et al., Potential role of tamoxifen in prevention of breast cancer, *J. Natl. Cancer Inst.* 83 (1991) 1450–1459.
- [60] B. Fisher, J.P. Costantino, D.L. Wickerham, et al., Tamoxifen for the prevention of breast cancer: current status of the national surgical adjuvant breast and bowel project p-1study, *J. Natl. Cancer Inst.* 97 (2005) 1652–1662.
- [61] S. Datta, L.R. Christena, Y.R.S. Rajaram, Enzyme immobilization: an overview on techniques and support materials, *3 Biotech* 3 (2012) 1–9.
- [62] K.V. Purtov, A.I. Petunin, A.E. Burov, et al., Nanodiamonds as carriers for address delivery of biologically active substances, *Nanoscale Res. Lett.* 5 (2010) 631–636.
- [63] N. Kossovsky, A. Gelman, H.J. Hnatyszyn, et al., Surface-modified diamond nanoparticles as antigen delivery vehicles, *Bioconjug. Chem.* 6 (1995) 507–511.
- [64] V.S. Bondar, I.O. Pozdnyakova, A.P. Puzyr, Applications of nanodiamonds for separation and purification of proteins, *Phys. Solid State* 46 (2004) 758–760.
- [65] T.S. Huang, Y. Tzeng, Y.K. Liu, et al., Immobilization of antibodies and bacterial binding on nanodiamond and carbon nanotubes for biosensor applications, *Diam. Relat. Mater.* 13 (2004) 1098–1102.
- [66] X.L. Kong, L.-C.L. Huang, C.-M. Hsu, et al., High-affinity capture of proteins by diamond nanoparticles for mass spectrometric analysis, *Anal. Chem.* 77 (2005) 259–265.
- [67] X. Kong, L.-C.L. Huang, S.-C.V. Liao, et al., Polylysine-coated diamond nanocrystals for MALDI-TOF mass analysis of DNA oligonucleotides, *Anal. Chem.* 77 (2005) 4273–4277.
- [68] W. Zhang, K. Patel, A. Schexnider, et al., Nanostructuring of biosensing electrodes with nanodiamonds for antibody immobilization, *ACS Nano* 8 (2014) 1419–1428.
- [69] A.D. Maynard, R.J. Aitken, T. Butz, et al., Safe handling of nanotechnology, *Nature* 444 (2006) 267–269.
- [70] M.S. Sachdeva, Drug targeting systems for cancer chemotherapy, *Expert Opin. Investig. Drugs* 7 (1998) 1849–1864.
- [71] H.B. Man, H. Kim, H.-J. Kim, et al., Synthesis of nanodiamond-daunorubicin conjugates to overcome multidrug chemoresistance in leukemia, *Nanomedicine* 10 (2014) 359–369.
- [72] T.-B. Toh, D.-K. Lee, W. Hou, et al., Nanodiamond–mitoxantrone complexes enhance drug retention in chemoresistant breast cancer cells, *Mol. Pharm.* 11 (2014) 2683–2691.
- [73] X. Wang, X.C. Low, W. Hou, et al., Epirubicin-adsorbed nanodiamonds kill chemoresistant hepatic cancer stem cells, *ACS Nano* 8 (2014) 12151–12166.
- [74] A. Gismondi, V. Nanni, G. Reina, et al., Nanodiamonds coupled with 5,7-dimethoxycoumarin, a plant bioactive metabolite, interfere with the mitotic process in B16F10 cells altering the actin organization, *Int. J. Nanomed.* 11 (2016) 557–574.
- [75] H.-J. Kim, K. Zhang, L. Moore, et al., Diamond nanogel-embedded contact lenses mediate lysozyme-dependent therapeutic release, *ACS Nano* 8 (2014) 2998–3005.
- [76] M.-S. Wu, D.-S. Sun, Y.-C. Lin, et al., Nanodiamonds protect skin from ultraviolet B-induced damage in mice, *J. Nanobiotechnol.* 13 (2015) 35.
- [77] Y. Li, Y. Tong, R. Cao, et al., *In vivo* enhancement of anticancer therapy using bare or chemotherapeutic drug-bearing nanodiamond particles, *Int. J. Nanomed.* 9 (2014) 1065–1082.
- [78] K.K. Liu, W.W. Zheng, C.C. Wang, et al., Covalent linkage of nanodiamond paclitaxel for drug delivery and cancer therapy, *Nanotechnology* 21 (2010) 315106.
- [79] T. Zhang, H. Cui, C. Fang, et al., Targeted nanodiamonds as phenotype specific photoacoustic contrast agents for breast cancer, *Nanomedicine* 10 (2015) 573–587.
- [80] Y. Xing, W. Xiong, L. Zhu, DNA damage in embryonic stem cells caused by nanodiamonds, *ACS Nano* 5 (2011) 2376–2384.
- [81] B. Kharisov, O. Kharisova, S. Berdonosov, Radioactive nanoparticles and their main applications: recent advances, *Recent Pat. Nanotechnol.* 8 (2014) 79–96.
- [82] Z. Chu, K. Miu, P. Lung, et al., Rapid endosomal escape of prickly nanodiamonds: implications for gene delivery, *Sci. Rep.* 5 (2015) 11661.
- [83] E.V. Perevedentseva, F.Y. Su, T.H. Su, et al., Laser-optical investigation of the effect of diamond nanoparticles on the structure and functional properties of proteins, *Quantum Electron.* 40 (2011) 1089–1093.
- [84] X.-Q. Zhang, M. Chen, R. Lam, et al., Polymer-functionalized nanodiamond platforms as vehicles for gene delivery, *ACS Nano* 3 (2009) 2609–2616.
- [85] Y.L. Liu, K.W. Sun, Protein functionalized nanodiamond arrays, *Nanoscale Res. Lett.* 5 (2010) 1045–1050.
- [86] A. Alhaddad, C. Durieu, G. Dantelle, et al., Influence of the internalization pathway on the efficacy of siRNA delivery by cationic fluorescent nanodiamonds in the ewing sarcoma cell model, *PLoS One* 7 (2012), e52207.
- [87] E.S. Khalid, Nanodiamond as a drug delivery system: applications and prospective, *J. Appl. Pharm. Sci.* 1 (2011) 29–39.
- [88] E.T. Sangiao, A.M. Holban, M.C. Gestal, Applications of nanodiamonds in the detection and therapy of infectious diseases, *Materials* 12 (2019) 1639.
- [89] J. Wehling, R. Dringen, R.N. Zare, et al., Bactericidal activity of partially oxidized nanodiamonds, *ACS Nano* 8 (2014) 6475–6483.
- [90] A. Chatterjee, E. Perevedentseva, M. Jani, et al., Antibacterial effect of ultra-fine nanodiamond against gram-negative bacteria *Escherichia coli*, *J. Biomed. Opt.* 20 (2015) 051014.
- [91] S. Szunerits, A. Barras, R. Boukherroub, Antibacterial applications of nanodiamonds, *Int. J. Environ. Res. Public Health* 13 (2016) 413.
- [92] E.T. Sangiao, A.M. Holban, M.C. Gestal, Applications of nanodiamonds in the detection and therapy of infectious diseases, *Materials* 12 (2019) 1639.
- [93] J. Wehling, R. Dringen, R.N. Zare, et al., Bactericidal activity of partially oxidized nanodiamonds, *ACS Nano* 8 (2014) 6475–6483.
- [94] M. Okamoto, Synthetic biopolymer/layered silicate nanocomposites for tissue engineering scaffolds, *Ceram. Nanocompos.* (2013) 548–581.
- [95] Y. Sun, Q. Yang, H. Wang, Synthesis and characterization of nanodiamond reinforced chitosan for bone tissue engineering, *J. Funct. Biomater.* 7 (2016) 27.
- [96] L. Gorausova, L. Bacakova, A. Kromka, et al., Nanodiamond as promising material for bone tissue engineering, *J. Nanosci. Nanotechnol.* 9 (2009) 3524–3534.
- [97] M. Okamoto, B. John, Synthetic biopolymer nanocomposites for tissue engineering scaffolds, *Prog. Polym. Sci.* 38 (2013) 1487–1503.
- [98] Q. Zhang, V.N. Mochalin, I. Neitzel, et al., Fluorescent PLLA-nanodiamond composites for bone tissue engineering, *Biomaterials* 32 (2011) 87–94.
- [99] L. Yang, T.J. Webster, Small and Bright: Nanodiamonds for Tissue Repair, Drug Delivery, and Biodetection IEEE Pulse, vol. 5, Institute of Electrical and Electronics Engineers, 2014, pp. 34–39.
- [100] B. Grotz, M.V. Hauf, M. Dankerl, et al., Charge state manipulation of qubits in

- diamond, Springer Nat. 3 (2012) 729.
- [101] A. Kumar, P. Lin, A. Xue, et al., Formation of nanodiamonds at near-ambient conditions via microplasma dissociation of ethanol vapour, Springer Nat. 4 (2013) 2618.
- [102] R. Ali, Nanodiamond Enhanced Drugs, US 20100129457 A1, 2010.
- [103] S. Olga, Nanodiamond UV Protectant Formulations, US 8753614 B2, 2014.
- [104] F. Joseph, Skin Treatment for Promoting Hair Growth, US 9227089 B1, 2016.
- [105] Ho Dean, Nanodiamond Particle Complexes, US 20100305309 A1, 2010.
- [106] S. Chien-Min, Healthcare and Cosmetic Compositions Containing Nanodiamond, US 7294340 B2, 2007.
- [107] D. Kevin, Composite Materials Containing Nanoparticles and Their Use in Chromatography, US 9248383 B2, 2016.
- [108] S. Chakraborty, Method of Making a Diamond Particle Suspension and Method of Making a Polycrystalline Diamond Article Therefrom, US 9283657 B2, 2016.
- [109] G. Rayford, High Shear Application in Medical Therapy, US 8888736 B2, 2014.
- [110] D. George, Cleaning Oral Care Compositions, US 8293216 B2, 2012.
- [111] H. Suzanne, Nanodiamond Fractional and the Products Thereof, US 7569205 B1, 2009.



## Original Article

# Karacolone, identified by network pharmacology, reduces degradation of the extracellular matrix in intervertebral disc degeneration via the NF- $\kappa$ B signaling pathway

Xiaoli Zhou <sup>a</sup>, Yingying Hong <sup>b</sup>, Yulin Zhan <sup>c,\*</sup>

<sup>a</sup> Department of Traditional Chinese Medicine, College of Medicine, Shanghai University of Traditional Chinese Medicine, Shanghai, 201203, China

<sup>b</sup> Department of Biology, School of Fisheries and Life Sciences, Shanghai Ocean University, Shanghai, 201306, China

<sup>c</sup> Orthopedics Department, Shanghai Sixth People's Hospital East Affiliated to Shanghai University of Medicine & Health Science, Shanghai, 201306, China

## ARTICLE INFO

## Article history:

Received 3 February 2019

Received in revised form

17 July 2019

Accepted 19 July 2019

Available online 26 July 2019

## Keywords:

Karacolone

Network pharmacology

Intervertebral disc degeneration

Extracellular matrix

Matrix metalloproteinases

## ABSTRACT

Karacolone is a compound found in the plant *Aconitum kusnezoffii* Reichb. Although *Aconitum kusnezoffii* Reichb is widely used for the treatment of pain, very few studies have been carried out on the use of karacolone due to its potential toxicity. In this study, we selected key matrix metalloproteinases (MMPs), collagen II, and aggrecan as targets due to their association with intervertebral disc degeneration (IDD). Using these targets, we then used network pharmacology to predict a series of molecules that might exert therapeutic effects on IDD. Of these molecules, karacolone was predicted to have the best effect. Tumor necrosis factor (TNF)- $\alpha$  is known to promote the degeneration of the extracellular matrix in IDD. We therefore applied different concentrations of karacolone (0, 1.25, or 12.88  $\mu$ M) along with 100 ng/mL TNF- $\alpha$  to rat nucleus pulposus cells and found that karacolone reduced the expression of MMP-14 in IDD by inhibiting the nuclear factor (NF)- $\kappa$ B pathway, while collagen II and aggrecan expression was increased. This suggested that extracellular matrix degradation was inhibited by karacolone ( $P < 0.05$ ). Our data therefore reveal a new clinical application of karacolone and provide support for the use of network pharmacology in predicting novel drugs.

© 2019 Xi'an Jiaotong University. Production and hosting by Elsevier B.V. All rights reserved. This is an open access article under the CC BY-NC-ND license (<http://creativecommons.org/licenses/by-nc-nd/4.0/>).

## 1. Introduction

Low back pain is an extremely common and frequently chronic disease. Indeed, according to a 2017 survey on the global burden of 354 diseases, low back pain was ranked in the top place in terms of the number of years that patients live with disability [1]. Many studies have suggested that low back pain is closely related to intervertebral disc degeneration (IDD) [2]. Although the precise mechanism underlying IDD is not fully understood, it is very apparent that degradation of the extracellular matrix (ECM) in the nucleus pulposus is one of the major characteristic changes. The main components of the ECM are collagen II and aggrecan. Collectively, these components allow the nucleus pulposus to retain water and therefore buffer and absorb pressure. In a healthy

disc, the synthesis and decomposition of the ECM are in equilibrium, predominantly due to the complex regulation of growth factors and catabolic cytokines. When the catabolic activity of the ECM exceeds its anabolic activity, there is a reduction in the relative content of collagen II and aggrecan, leading to water loss and the development of IDD [3]. Previous research has shown that tumor necrosis factor (TNF)- $\alpha$  promotes degradation of the ECM, and may initiate the initial production of matrix metalloproteinases (MMPs) [4].

MMPs are the main enzymes for degrading collagen and aggrecan. Higher expression levels of MMPs can be detected in degenerative intervertebral discs compared to normal discs [5]. One previous study in humans analyzed the relationship between different IDD grades and MMP-1 expression, and the results showed that MMP-1 expression was up-regulated with increasing degenerative grade [6]. Another study found up-regulated levels of MMP-2 in degenerative intervertebral discs after comparing the gene expression profiles of normal and degenerative intervertebral discs [7]. However, the MMP-3 gene can be expressed at high levels

Peer review under responsibility of Xi'an Jiaotong University.

\* Corresponding author.

E-mail address: [sd\\_zhanyl@sumhs.edu.cn](mailto:sd_zhanyl@sumhs.edu.cn) (Y. Zhan).

in degenerative intervertebral disc tissues in response to a wide range of different factors [8]. LeMaitre et al. [9] further showed that the expression of MMP-7 in chondrocyte-like cells of the nucleus pulposus increased with the aggravation of degeneration at the histological level. MMP-7 can degrade the major matrix molecules of the intervertebral disc, which is accompanied by the activation of many other proteases and cytokines, and it plays an important role in the degeneration of intervertebral discs. Although the levels of MMP-8 were shown not to be significantly up-regulated in degenerative IDD, MMP-8 expression gradually increased as the level of degeneration increased [10]. High MMP-10 expression has also been detected in the tissues of patients with symptomatic disc degeneration, which might represent the beginning of pain perception [11]. Other research has shown that MMP-12 is not only involved in degradation of the ECM in IDD but is also related to the activity of both cytokines and chemokines [12]. Li et al. [13] subsequently showed a positive correlation between levels of MMP-13 in degenerative intervertebral disc tissues and the degree of degeneration. In another study, Xu et al. [14] reported that while there was no significant difference in the expression of MMP-14 in intervertebral discs when compared between individuals of different ages, MMP-14 expression increased as the degree of degeneration increased. Most recently, Zhang et al. [15] showed that MMP-16 can degrade aggrecan and collagen II, thus leading to water loss and disc degeneration. Given the potential of MMP-14 as a marker for predicting IDD [16], we adopted this molecule as our main target in the experiments conducted as part of this study.

Currently, the treatment of IDD in clinical practice is still based on symptomatic therapies for single symptoms. While surgical treatment can be performed if the disease worsens, there remains no effective method to reverse or even delay the disease process. The precise regulation of specific biological targets may reverse the degradation of the ECM in IDD. Network pharmacology is a research method based on high-throughput omics analysis, use of interaction network databases, and virtual computing; this technique can be used to identify new drugs and determine the mechanistic actions of drugs. Network pharmacology analyzes the relationships between drugs and diseases in a systematic manner, and thus reveals the mechanisms of drugs acting upon the human body and allows us to predict new drugs with therapeutic effects from a database of compounds [17]. Two key databases can be used in network pharmacology. The first is the Connectivity Map Database, which contains the gene expression profiles of human cells in response to a large number of biologically active small molecules. The database can match a gene expression phenotype that is of interest to the user to microarray data on more than 1,300 small molecules. The output is a list of compounds with scores that represent correlations with the gene expression phenotype. These correlations range from high positive correlations (indicating similarity to the gene expression phenotype provided by the user) to high negative correlations (indicating the reverse of the gene expression phenotype provided by the user). Thus, a negative score may indicate a therapeutic effect [18]. The second database is the Traditional Chinese Medicine Systems Pharmacology (TCMSP) database, which features approximately 30,000 active molecules that can be found in Chinese herbal medicines. This database features important data on absorption, distribution, metabolism, and excretion (ADME)-related properties such as oral bioavailability, drug-likeness, and the half-life associated with oral administration in humans [19].

In this study, we selected key genes that are known to be related to ECM degradation during IDD as potential regulatory targets. We

then used a combination of network pharmacology and the concept of “disease-target-component-drug” to identify (using the Connectivity Map Database) potential therapeutic molecules for experimental validation and database screening (using the TCMSP database). In addition, we screened for the potential therapeutic molecules that can be sourced from traditional Chinese medicines, in the hope of laying a foundation for the exploration of combination therapy involving traditional Chinese medicine in the future.

## 2. Materials and methods

### 2.1. Target selection and drug screening

First, we identified members of the MMP family that are specifically up-regulated in IDD (MMP-1, -2, -3, -7, -8, -10, -12, -13, -14 and -16), and collagen II and aggrecan, which are both down-regulated in IDD, as specific drug targets. All of them were selected by searching the literature. A human protein interaction network was obtained from the Human Protein Reference Database, and Cytoscape 3.6.1 software (NRNB, CA, USA) was used to establish a protein interaction network. The Connectivity Map Database [18] was used to compare the gene expression profile of the disease (IDD) with the gene expression profiles of human cells in response to biologically active small molecules. The database allowed us to predict the effects of the molecules (in terms of their effects on human cells' gene expression profile) and obtain Connectivity Map scores for them. Molecules with negative scores were used as candidate therapeutic molecules, meaning that they were screened for in the TCMSP database [19] to identify molecules that can be sourced from Chinese herbal medicines. Given that oral bioavailability (OB) and drug-likeness (DL) are important indicators to assess the feasibility of using a molecule as a therapeutic drug, we established preset criteria ( $OB \geq 30.0$  and  $DL \geq 0.18$ ) to screen for the molecules in the TCMSP.

### 2.2. Reagents and antibodies

Karacolone (PLC $\geq$ 98% by high-performance liquid chromatography [HPLC]) was purchased from Shanghai Chengshao Biological (Shanghai, China). Anti-nuclear factor (NF)- $\kappa$ B p65 (acetyl K310) antibody and anti-NF- $\kappa$ B p65 (phospho S536) antibody were purchased from Abcam (Cambridge, MA, USA) while other antibodies were purchased from SAB (Baltimore, MD, USA). RPMI 1640 medium and fetal bovine serum (FBS) were purchased from BBI (Markham, CA, USA). Recombinant rat TNF- $\alpha$  was purchased from Sangon Biotech (Shanghai, China). Rat MMP-14 ELISA Kit, Rat Col II ELISA Kit and Rat Aggrecan ELISA Kit were purchased from Enzyme-linked Biotechnology (Shanghai, China).

### 2.3. Cell culture and identification

Primary culture nucleus pulposus cells, obtained from Sprague-Dawley rats, were purchased from Rothen Pharma Co., Ltd. (Shanghai, China). These cells were cultured at 37 °C in 5% CO<sub>2</sub>, and then grown to 90% confluence. The 3,3'-diaminobenzidine (DAB) method was used to identify nucleus pulposus cells. Slides of nucleus pulposus cells were prepared and fixed with 4% paraformaldehyde fix solution (BBI), sealed with goat serum (BBI), and incubated overnight at 4 °C with anti-collagen II rabbit antibody (diluted 1:200, SAB). The primary antibody was then washed off and horseradish peroxidase (HRP)-conjugated goat anti-rabbit IgG (BBI) was added, and the cells were incubated at room temperature

for 1 h. DAB was used for color development, and hematoxylin was used as a counterstain. Finally, neutral balsam mounting medium was used to seal the slides, which were then observed under an inverted microscope (Olympus Corporation, Tokyo, Japan). The nucleus pulposus cells of rats with collagen II positive rate >90% were used for the experiments.

#### 2.4. Cell counting kit 8 (CCK8)

Approximately  $5 \times 10^3$  nucleus pulposus cells were placed into each well of a 96-well cell culture plate with complete medium (90% RPMI 1640 medium and 10% FBS), exposed to different concentrations of karacoline (0.001, 0.010, 0.10, 1.0, 10.0, 100.0 and 1000.0  $\mu\text{M}$ ), and incubated for 24 h. The medium was then removed and replaced with 100  $\mu\text{L}$  complete medium and 10  $\mu\text{L}$  CCK8 solution; the cells were then incubated at 37 °C for 2 h. A blank group (complete medium only) and a control group (complete medium and nucleus pulposus cells) were prepared at the same time. The optical density (OD) at 450 nm was then determined using a microplate reader (BioTek Instruments Inc., Winooski, VT, USA). Cell survival rate was then calculated according to the following formula: Cell viability (%) = (OD treatment group - OD blank group)/(OD control group - OD blank group). The half maximal inhibitory concentration (IC<sub>50</sub>) value of karacoline regarding nucleus pulposus cells was calculated, and then the maximum dose without cytotoxicity was calculated. In addition, after adding different concentrations of TNF- $\alpha$  (50, 100, and 150 ng/mL), which promotes the degeneration of nucleus pulposus cells, cytotoxicity was detected at different time points (days 0, 1, 2, and 3) using the methodology described above.

#### 2.5. Real-time quantitative polymerase chain reaction (RT-qPCR)

Nucleus pulposus cells were incubated for 24 h with different concentrations of karacoline and 100 ng/mL TNF- $\alpha$ . Next, 1 mL total RNA extractor (Sangon Biotech) was used to lyse the cells, followed by incubation at room temperature for 10 min. Thereafter, 200  $\mu\text{L}$  chloroform was added and the cells were mixed with a vortexer for 15 s. They were then allowed to rest at room temperature for 3 min, and then centrifuged at 12,000 $\times g$  and 4 °C for 10 min. The upper water phase was placed into a clean centrifuge tube and the same amount of isopropanol was added. The samples were left at room temperature for 20 min and then centrifuged at 12,000 $\times g$  and 4 °C for 10 min. The supernatant was then discarded and 1 mL 75% ethanol was added to cause precipitation. The samples were then centrifuged again at 12,000 $\times g$  and 4 °C for 20 min and the supernatant was removed. The samples were then dried at room temperature for 5–10 min and 30–50  $\mu\text{L}$  RNase-free ddH<sub>2</sub>O was used to fully dissolve the resultant RNA.

The RNA was transcribed into complementary DNA using Super Moloney Murine Leukemia Virus (M-MuLV) Reverse Transcriptase (Diamond) and reverse transcription primers for the target genes (MMP-14, COL2A1 [which encodes collagen II], and ACAN [which encodes aggrecan]). Transcription was carried out at 50 °C for 30 min, then 80 °C for 15 min, followed by a cooling phase on ice. RT-qPCR was then performed by an MX3000P Real-Time Fluorescence Quantitative PCR System (Strata-gene, USA) using the following protocol: denaturation at 95 °C for 3 min and then 40 cycles of 95 °C for 12 s and 62 °C for 40 s. Glyceraldehyde 3-phosphate dehydrogenase (GAPDH) was used as an internal control. Primers for the amplification of target genes were designed and then pairs of primers were selected using BLAST in PubMed (Table 1).

**Table 1**  
Sequences of the primers used for qPCR.

Gene name	Primer sequences
MMP14	F:5'-ATGGAAGCAAGTCAGGGTCA-3' R:5'-ACCATCGCTCCTTGAAGACA-3'
COL2A1	F:5'-CTCATCCAGGGCTCCAATGA-3' R:5'-CCATGGGTGCAATGTCAACA-3'
ACAN	F:5'-GTTATCGCCACTTCCCGAC-3' R:5'-ATTGCAGGGAGTCCATCA-3'
GAPDH	F:5'-ACCACAGTCCATGCCATCAC-3' R:5'-TCCACCACCTGTGTGTA-3'

qPCR = Quantitative polymerase chain reaction; MMP14 = Matrix metalloproteinase 14; GAPDH = Glyceraldehyde-3-phosphate dehydrogenase.

#### 2.6. Enzyme-linked immunosorbent assay (ELISA)

ELISAs were performed using Rat MMP-14, Col II, and AGG ELISA Kits (Enzyme-linked Biotechnology, Shanghai, China). Nucleus pulposus cells were treated with different concentrations of karacoline (0, 1.25, or 12.88  $\mu\text{M}$ ) and 100 ng/mL TNF- $\alpha$  in complete medium (90% RPMI 1640 medium and 10% FBS) for 48 h. The mixture was then centrifuged at 300 $\times g$  for 20 min, and the supernatant was collected. Next, 50  $\mu\text{L}$  of standard substance at concentrations of 32, 16, 8, 4, 2, and 1 ng/mL were added to a microtiter plate. Thereafter, 50  $\mu\text{L}$  of each supernatant was added to other wells. With the exception of wells that were left as blanks, 100  $\mu\text{L}$  HRP labeled detection antibody was added to each of the wells (containing the standards or supernatants). The plates were then sealed with film and incubated at 37 °C for 60 min. The liquid in each well was then discarded and the plate was patted dry with absorbent paper. Each well was then filled with wash solution and allowed to stand for 1 min. The liquid was then discarded and the plate was patted dry with absorbent paper. This procedure was repeated five times. Next, 50  $\mu\text{L}$  substrate A and 50  $\mu\text{L}$  substrate B were added to each well and incubated in the dark at 37 °C for 15 min. Thereafter, 50  $\mu\text{L}$  stop solution was added to each well and the OD at 450 nm was determined (within 15 min) with a microplate reader (BioTek Instruments Inc., Winooski, VT, USA). To create a standard curve and obtain a linear regression equation, OD values were plotted on the x-axis and the concentration of the standard substance was plotted on the y-axis. The OD values of the supernatants were substituted into the equation to calculate the protein concentrations of MMP-14, collagen II, and aggrecan.

#### 2.7. Western blotting

To investigate proteins that are characteristic indicators of NF- $\kappa\text{B}$  pathway activation (p65, phospho-p65, and acetylated-p65), nucleus pulposus cells were treated with different concentrations of karacoline (0, 1.25, or 12.88  $\mu\text{M}$ ) and 100 ng/mL TNF- $\alpha$  for 24 h. To investigate the protein levels of MMP-14, collagen II, and aggrecan, different concentrations of karacoline (0, 1.25, or 12.88  $\mu\text{M}$ ) and 100 ng/mL TNF- $\alpha$  were added for 48 h. A Tissue or Cell Total Protein Extraction Kit (Sangon Biotech) was then used to extract total cell protein, and 10% sodium dodecyl sulfate polyacrylamide gel electrophoresis (SDS-PAGE) was used to separate 20  $\mu\text{L}$  total protein per well. After electrophoresis, the separated proteins were transferred to a polyvinylidene fluoride (PVDF) membrane and incubated overnight with the following primary antibodies: anti-aggrecan antibody (1:1000, SAB), anti-collagen II antibody (1:1000, SAB), anti-MMP-14 antibody (1:1000, SAB), anti-NF- $\kappa\text{B}$  p65 mouse

monoclonal antibody (1:1000, SAB), anti-NF-κB p65 (phospho S536) antibody (1:1000, Abcam), and anti-NF-κB p65 (acetyl K310) antibody (1:1000, Abcam). On the following day, the membranes were treated with HRP-conjugated goat anti-rabbit IgG (1:2000, Jackson, PA, USA), and chemiluminescence was assessed using SuperSignal West Pico Chemiluminescent Substrates (Pierce, WDC, USA). Finally, the membranes were exposed to X-ray films and the resultant films were photographed with the X-Omat BT Film (Kodak, NY, USA). Protein quantification was then performed

with a Gel-Pro Analyzer 4.0 (Media Cybernetics, WDC, USA), and bands with a positive response were quantified by densitometry and normalized against GAPDH.

2.8. Immunofluorescence

Microscope slides were placed in a 12-well cell culture plate and nucleus pulposus cells were placed on the slides at a density of  $2 \times 10^4$ /mL. The next day, the cells were treated with 100 ng/mL

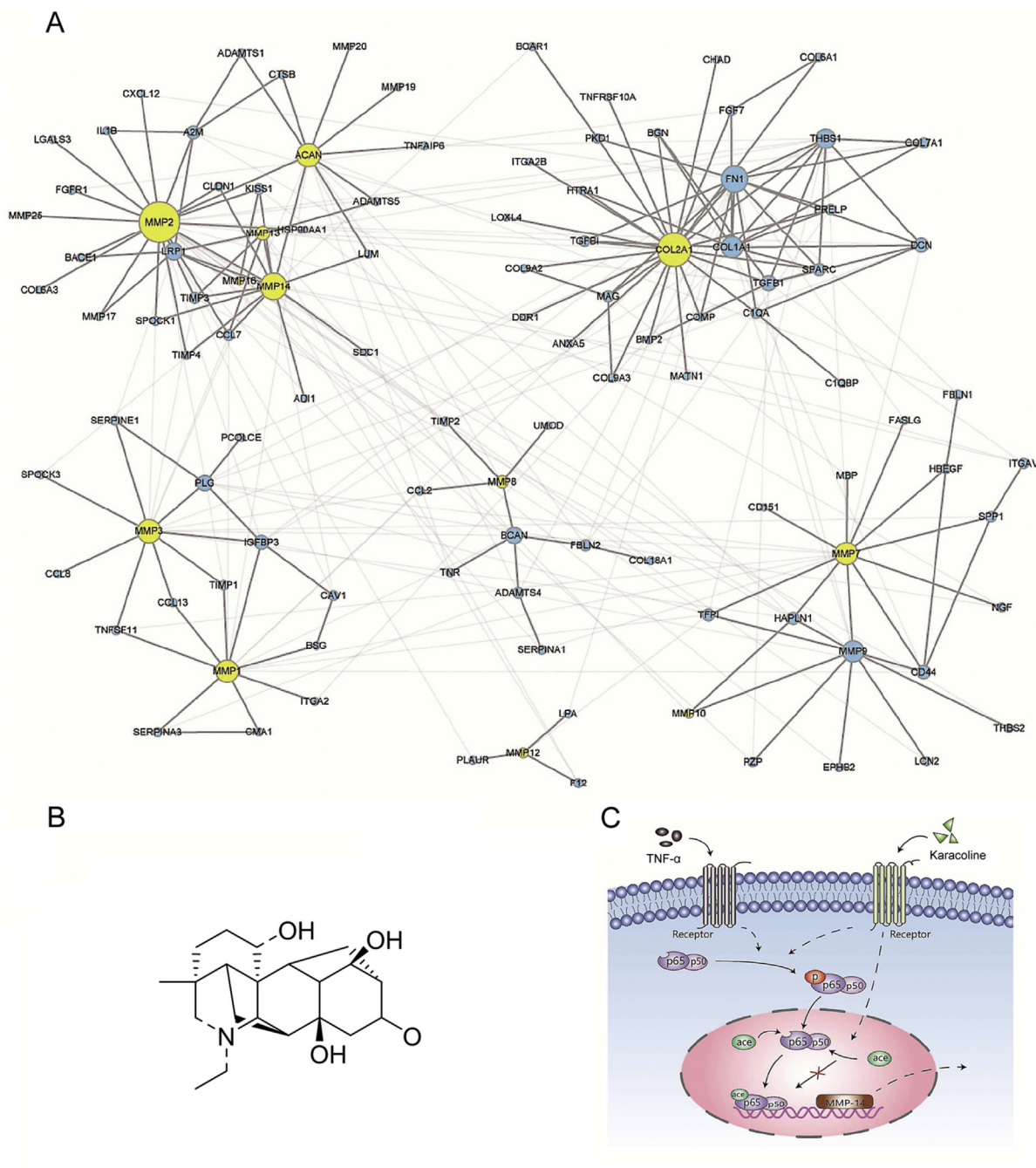


Fig. 1. (A) Protein interaction network of MMPs, collagen II and aggrecan. The size of each dot indicates how much it interacts with other proteins. (B) Molecular formula of karacoline. (C) Effect of karacoline on TNF-α-induced NF-κB signaling pathway activation.

TNF- $\alpha$ , 100 ng/mL TNF- $\alpha$  + 1.25  $\mu$ M karacoline, or 100 ng/mL TNF- $\alpha$  + 12.88  $\mu$ M karacoline. The slides were removed 4 days later and fixed with 4% paraformaldehyde for 15 min. The cells were treated with 0.5% Triton X-100 at room temperature for 20 min and then incubated with goat serum at room temperature for 1 h. The cells were then treated with anti-aggrecan antibody (1:200, SAB), anti-collagen II antibody (1:200, SAB), and anti-MMP-14 antibody (1:200, SAB) at 4 °C overnight. The cells were then incubated for 1 h at 37 °C with DyLight 549 goat anti-rabbit IgG antibody (Vector Laboratories, CA, USA) and then incubated with 4,6-diamidino-2-phenylindole (DAPI; BBI) for 5 min in the dark to stain the nuclei. The cells were then washed with phosphate-buffered saline plus Tween 20 (PBST; Sangon Biotech) and then dried. A sealing agent, containing a fluorescence quenching agent, was then applied and the images were observed and quantified under a fluorescence microscope.

### 2.9. Flow cytometry

Apoptosis was assessed using an Annexin V-Fluorescein Isothiocyanate (FITC) Apoptosis Detection Kit (BBI). Nucleus pulposus cells were added to a 6-well culture plate at a density of  $5 \times 10^4$ /mL and were then treated with the highest dose of karacoline without cytotoxicity (as demonstrated in a previous experiment) or twice the IC<sub>50</sub> dose of karacoline (also determined in a previous experiment) combined with 100 ng/mL TNF- $\alpha$  for 48 h. The cells were then washed with phosphate-buffered saline (PBS) and centrifuged at 300 $\times$ g for 5 min. The supernatant was then discarded and the cells were resuspended in 195  $\mu$ L  $1 \times$  binding buffer to obtain a cell density of  $5 \times 10^5$ /mL. Next, 5  $\mu$ L annexin V-FITC was added and incubated at room temperature in the dark for 10 min. Subsequently,  $1 \times$  binding buffer was used to wash the cells, which were then centrifuged at 300 $\times$ g for 5 min; the supernatant was discarded. Finally, the cells were resuspended in 190  $\mu$ L  $1 \times$  binding buffer, and 10  $\mu$ L propidium iodide was added to stain the nuclei red. Samples were immediately analyzed by flow cytometry (BD Biosciences, San Jose, CA, USA), each sample counts  $1 \times 10^4$  cells.

### 2.10. Statistical analysis

Quantity One (Bio-Rad Laboratories, CA, USA) was used for the grayscale analysis of the Western blotting results. GraphPad Prism 8 (GraphPad Software, CA, USA) was used for all other data analyses. Student's *t*-test was used for all pairwise comparisons, and differences were considered to be statistically significant if  $P < 0.05$ .

**Table 2**

Top 10 molecules that were identified using the Connectivity Map Database and then ranked by Connectivity Map score.

Molecule	Connectivity Map score	OB (%)	DL
Karacoline	-0.841	51.73	0.73
Tetrahydroalstonine	-0.775	32.42	0.81
Boldine	-0.702	31.18	0.51
Lysergol	-0.675	48.11	0.27
Papaverine	-0.652	64.04	0.38
Fisetin	-0.606	52.6	0.24
Lobelanidine	-0.577	60.53	0.32
Artemisinin	-0.572	49.88	0.31
Noscapine	-0.567	53.29	0.88
Podophyllotoxin	-0.536	59.94	0.86

OB = Oral bioavailability; DL = Drug-likeness.

## 3. Results

### 3.1. Targets and drugs for IDD

Compared with normal intervertebral discs, degenerative intervertebral discs exhibit greater expression levels of MMPs and lower expression levels of collagen II and aggrecan. These targets are central markers of IDD, and multiple proteins interact with them. Consequently, a protein interaction network can be obtained (Fig. 1A). In the network diagram, the size of each dot indicates the degree of protein interaction, so we can deduce that COL2A1 (which encodes collagen II), ACAN (which encodes aggrecan), and MMP-14 show high levels of probable interaction. Using the Connectivity Map and TCMSP databases, 15 molecules were identified and ranked by their Connectivity Map scores. The top 10 molecules are given in Table 2. Karacoline, which was ranked first in the list of 10 molecules, was selected for subsequent experimental verification (Fig. 1B). Given the role of TNF- $\alpha$  in IDD, and the fact that it can activate the NF- $\kappa$ B pathway to stimulate the secretion of MMP-14, karacoline was combined with TNF- $\alpha$  to verify whether karacoline could reverse the effects of TNF- $\alpha$  (Fig. 1C). The nucleus pulposus cells of rats with collagen II positive rate >90% were used for the experiments (Fig. 2A).

### 3.2. Effects of karacoline and TNF- $\alpha$ on the viability of nucleus pulposus cells

Our data showed that the high dose of karacoline was cytotoxic to nucleus pulposus cells. CCK8 assays were used to detect the cell viability of nucleus pulposus cells under different concentrations of karacoline. The IC<sub>50</sub> was calculated to be 6.444  $\mu$ M (Fig. 2B). The maximum dose of karacoline without cytotoxicity to nucleus pulposus cells was calculated to be 1.25  $\mu$ M. Using TNF- $\alpha$  at different concentrations, the CCK8 assay was performed again. The results demonstrated that 1.25  $\mu$ M karacoline antagonized the toxic effect of TNF- $\alpha$  on nucleus pulposus cells to some extent (Fig. 2C).

### 3.3. Karacoline reversed the expression of genes induced by TNF- $\alpha$

Nucleus pulposus cells were treated with 0, 1.25, or 12.88  $\mu$ M of karacoline and 100 ng/mL TNF- $\alpha$ , and qPCR was then performed. The data showed that TNF- $\alpha$  significantly up-regulated the expression of the MMP-14 gene, and down-regulated the expression of collagen II and aggrecan. Interestingly, karacoline reversed this effect. Both 1.25 and 12.88  $\mu$ M karacoline led to inhibition of MMP-14 gene expression, while the gene encoding collagen II was up-regulated ( $P < 0.05$ , Figs. 2D and F). Additionally, 1.25  $\mu$ M of karacoline increased the expression of aggrecan ( $P < 0.05$ , Fig. 2E).

### 3.4. Karacoline inhibited TNF- $\alpha$ -induced ECM degradation

Considering that ECM degradation is a key feature of IDD, we used a variety of methods to investigate the mechanisms involved. The outer surfaces of nucleus pulposus cells were treated with 100 ng/mL TNF- $\alpha$  with different concentrations of karacoline (0, 1.25, or 12.88  $\mu$ M), and the culture supernatant was then analyzed by ELISA. The results showed that TNF- $\alpha$  significantly decreased the secretion of collagen II and aggrecan in the supernatant. This situation was reversed by treatment with karacoline. Both 1.25 and 12.88  $\mu$ M karacoline increased the content of aggrecan in the supernatant, while 1.25  $\mu$ M karacoline also increased collagen II ( $P < 0.05$ , Figs. 3A and B). We also used western blotting to measure the intracellular content of collagen II and aggrecan proteins. Unfortunately, there were no statistically significant differences ( $P < 0.05$ , Figs. 3D and E). The immunofluorescence experiments

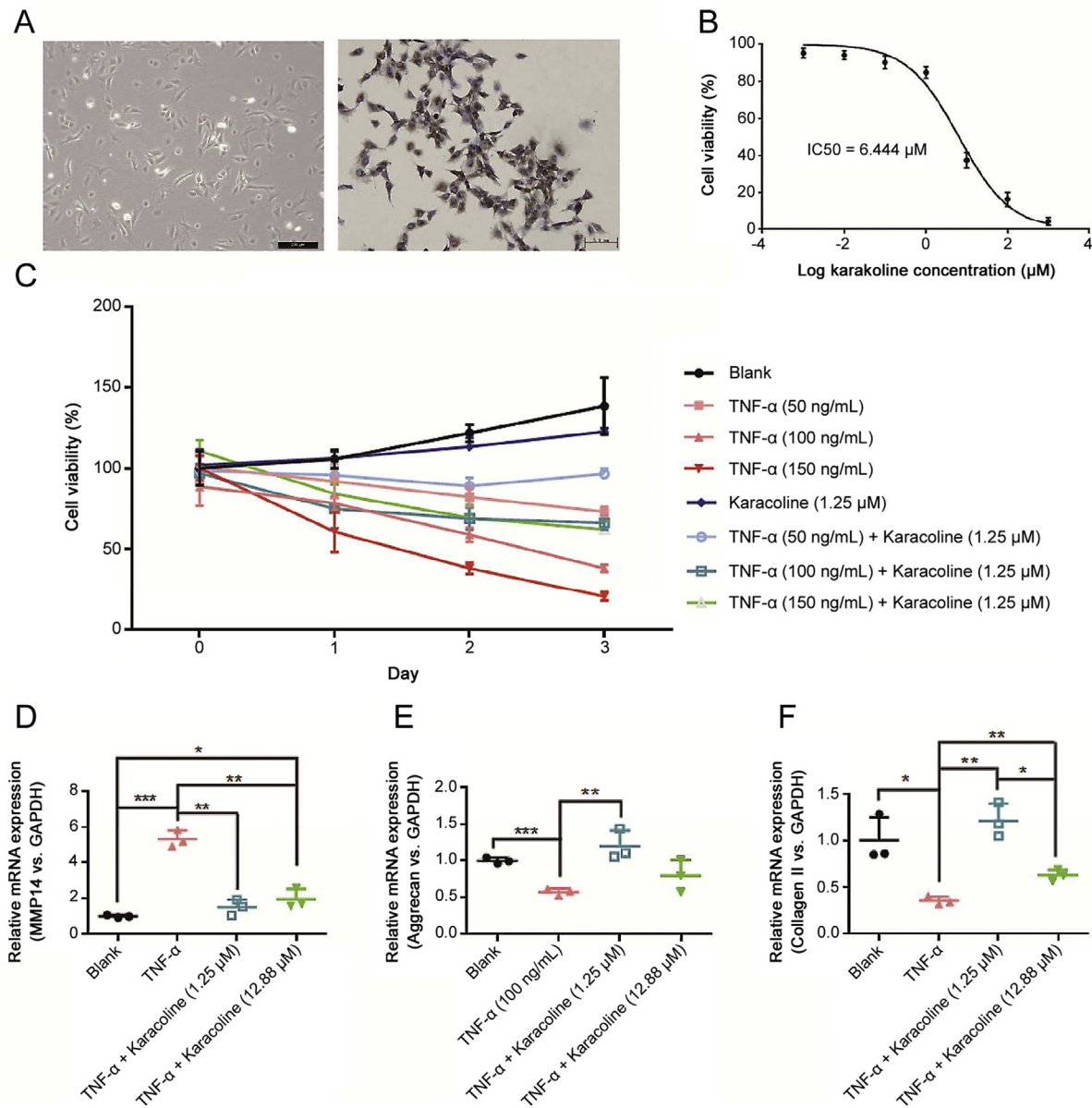


**Fig. 2.** (A) Immunohistochemical identification of rat nucleus pulposus cells. (B) Half maximal inhibitory concentration (IC<sub>50</sub>) of karacoline. (C) Cytotoxicity of karacoline at different concentrations of TNF- $\alpha$ . (D, E, F) Expression of MMP-14, aggrecan, and collagen II in rat nucleus pulposus cells treated with 0, 1.25, or 12.88  $\mu\text{M}$  karacoline and 100 ng/mL TNF- $\alpha$  (\* $P$  < 0.05, \*\* $P$  < 0.01, \*\*\* $P$  < 0.001).

clearly showed that compared with the TNF- $\alpha$ -only group, karacoline significantly increased the content of aggrecan and collagen II in the nucleus pulposus cells (Figs. 3F and G).

### 3.5. Karacoline inhibited TNF- $\alpha$ -induced NF- $\kappa$ B pathway activation and thereby reduced MMP-14 secretion

ELISA of culture supernatants indicated that 100 ng/mL TNF- $\alpha$  significantly increased the secretion of MMP-14 while the concentration of MMP-14 in the supernatant was reduced by 1.25  $\mu\text{M}$  karacoline ( $P$  < 0.05, Fig. 3C). Western blotting also confirmed that the expression of the MMP-14 protein in nucleus pulposus cells was significantly increased by the addition of 100 ng/mL TNF- $\alpha$ , but it was significantly reduced by 1.25  $\mu\text{M}$  karacoline ( $P$  < 0.05, Figs. 3D

and E). The same findings were also evident in our immunofluorescence data, which showed that when only 100 ng/mL TNF- $\alpha$  was added, the distribution of MMP-14 in nucleus pulposus cells increased, but this was decreased with the addition of 1.25, or 12.88  $\mu\text{M}$  karacoline (Fig. 3H). TNF- $\alpha$  can activate the NF- $\kappa$ B pathway to stimulate the secretion of MMP-14, so we hypothesized that karacoline could inhibit this effect. The levels of acetylated-p65 (characteristic indicators of NF- $\kappa$ B pathway activation) was increased when only 100 ng/mL TNF- $\alpha$  was added, but both 1.25 and 12.88  $\mu\text{M}$  karacoline could curb these effects. However, there was no significant difference in the levels of phospho-p65 between each group, suggesting that the NF- $\kappa$ B pathway was inhibited by karacoline, especially through its negative effects on p65 acetylation ( $P$  < 0.05, Figs. 3D and E).

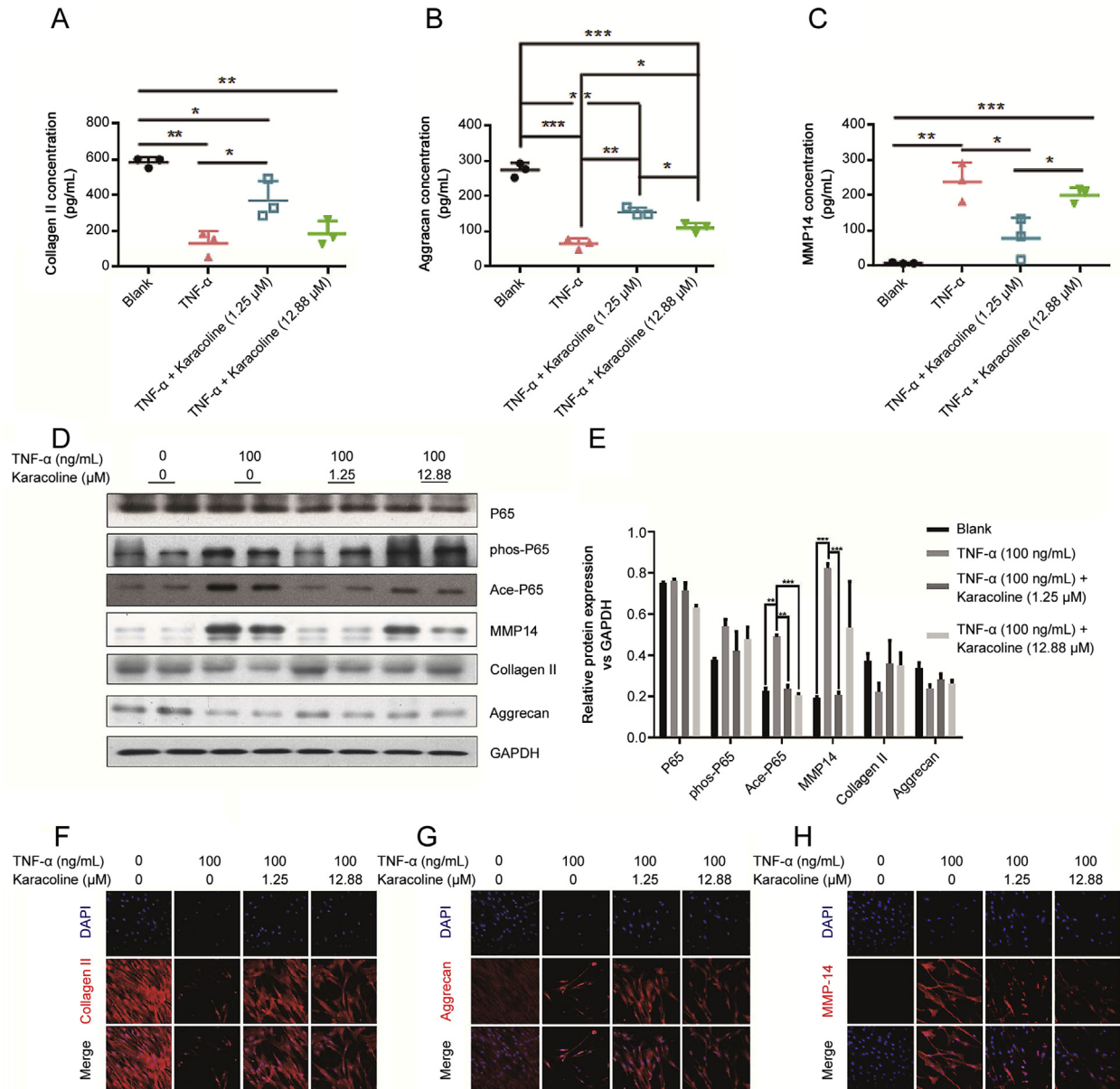


**Fig. 3.** (A, B, C) Secretion of collagen II, aggrecan, and MMP-14 in culture supernatant with 0, 1.25, or 12.88 μM karacoline and 100 ng/mL TNF-α (\* $P < 0.05$ , \*\* $P < 0.01$ , \*\*\* $P < 0.001$ ). (D) Western blotting results showing levels of phospho-p65, acetylated-p65, MMP-14, collagen II, and aggrecan in nucleus pulposus cells treated with 0, 1.25, or 12.88 μM karacoline and 100 ng/mL TNF-α. (E) Column analysis diagram of Western blotting results (\* $P < 0.05$ , \*\* $P < 0.01$ , \*\*\* $P < 0.001$ ). (F, G, H) Immunofluorescence of rat nucleus pulposus cells treated with 0, 1.25, or 12.88 μM karacoline and 100 ng/mL TNF-α.

### 3.6. Anti-apoptosis effect of karacoline on nucleus pulposus cells treated with TNF-α

A high concentration of karacoline was cytotoxic to nucleus pulposus cells, while TNF-α induced apoptosis of nucleus pulposus cells. Both 1.25 and 12.88 μM karacoline antagonized TNF-α-induced apoptosis (Fig. 4).

## 4. Discussion

The health and economic burden of IDD is significant. As such, a wide body of research has been carried out to investigate the factors that lead to the degradation of the ECM. Via these studies, the roles of many individual molecules have been elucidated. For

example, one study showed that streptozotocin-induced diabetic mice had disc degeneration and high expression levels of MMP-13 but also that a combined treatment of pentosan polysulfate and pyridoxine alleviated disc degeneration by reducing the expression of MMP-13 [20]. In another study, a specific inhibitor of NF-κB, BAY11-7082, was administered to human nucleus pulposus cells exposed to interleukin (IL)-1; the results showed that the gene expression of MMP-3, MMP-9, and MMP-13 were decreased, and also that the low expression of aggrecan and collagen II was reversed [21]. These studies confirmed the associations between MMPs, aggrecan, and collagen II. Our current study is the first to investigate the specific role of karacoline in IDD.

Karacoline is a natural herbal extract, which is mainly found in *Aconitum kusnezoffii* Reichb (a traditional Chinese herbal medicine).

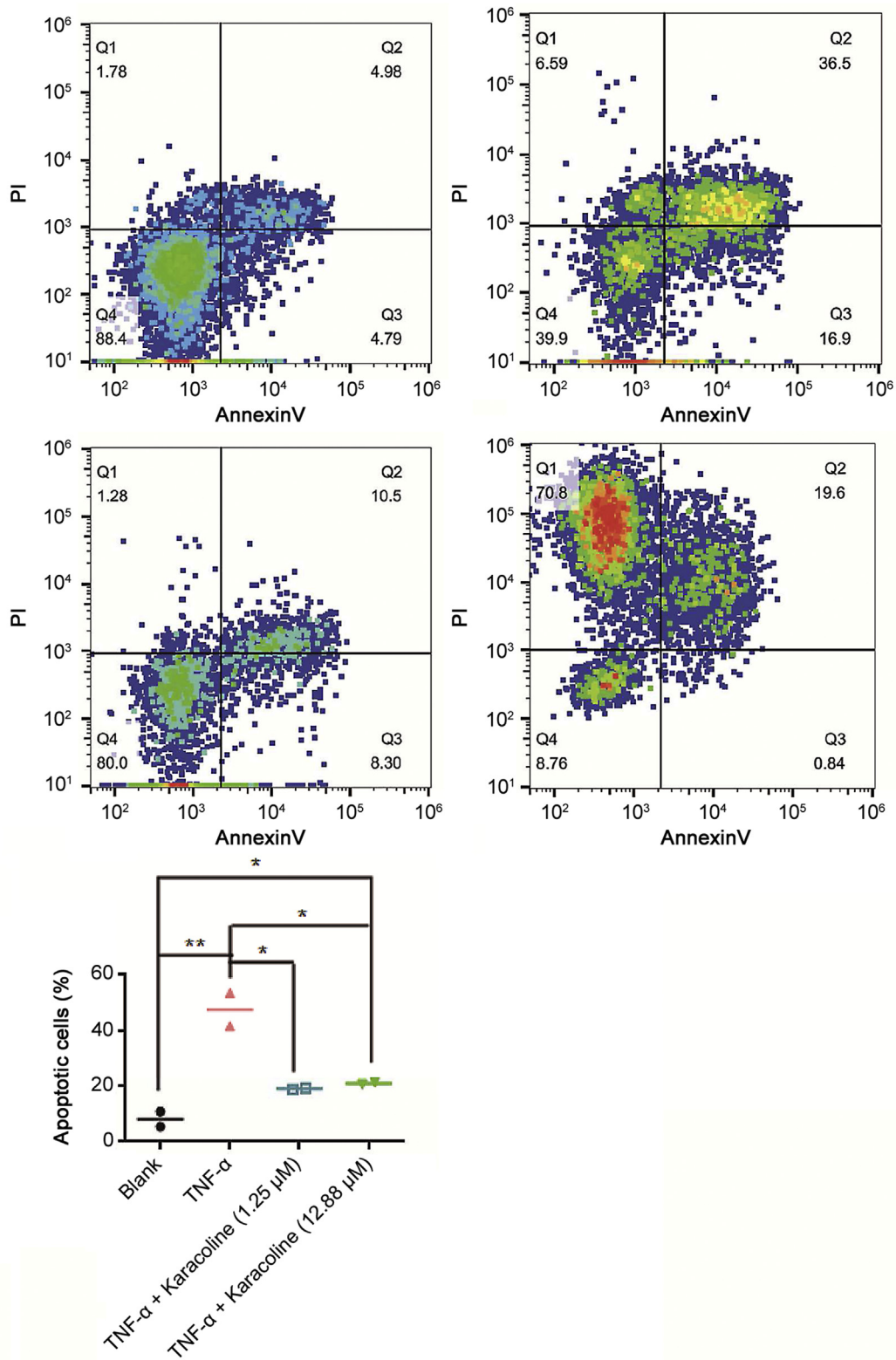


Fig. 4. Karacoline reduced TNF- $\alpha$ -induced apoptosis in rat nucleus pulposus cells.

The clinical application of *Aconitum kusnezoffii* Reichb has previously been limited because of its potential toxicity. However, due to its powerful analgesic effect, it is still widely used in the treatment of diseases associated with pain symptoms. The efficacy of this medicine is remarkable, and the key to its rational use is identifying the balance between efficacy and safety [22]. Similarly, the administration of karacoline must involve an appropriate dose. Our experiments showed that a low dose of karacoline was better than a high dose. In our experiment, we showed that karacoline effectively inhibited the activation of the NF- $\kappa$ B pathway and thereby reduced the production of MMP-14; this significantly reduced the degradation of the ECM.

Prior to this study, the potential role of karacoline in disease treatment had not been investigated; researchers have generally ignored this medicine because of its toxicity. Our analyses were innovative in this sense, because we initially used network pharmacology predictions to identify the potential role of karacoline in IDD treatment. Interestingly, our network predictions showed that karacoline was not the only important drug, as multiple other molecules were identified that are also worth exploring. This is not the first time that network pharmacology has been used to screen for drugs that could be used for the treatment of specific diseases. In terms of Western medicine compounds, a previous study compared the gene expression profiles of 100 diseases with the gene expression profiles in response to 164 drug compounds, which yielded predictions regarding their therapeutic potentials, many of which were shown to have entirely new indications. For example, an anti-ulcer drug, cimetidine, was predicted to be a candidate therapeutic agent for lung adenocarcinoma; this prediction was confirmed in vitro and in vivo using a mouse xenotransplantation model [23]. At present, the application of network pharmacology in Chinese herbal medicine is more focused on the further exploration of known medical compounds that can influence disease-related targets. For example, the plant-based combination therapy "*Astragalus-Angelica*" is used to treat traumatic brain injury; the target for this Chinese herbal medicine was first predicted by network pharmacology, and the accuracy of this prediction was then verified experimentally [24].

As described above, the value of this study lies not only in the discovery of single compounds, but also in the fact that multiple of these compounds can be mapped to traditional Chinese medicine combinations to create multi-target treatments. In fact, multi-target treatment is not a new concept. In the field of acquired immune deficiency syndrome (AIDS) treatment, combinations of drugs have been shown to be highly effective. For example, Atripla is marketed as a "cocktail therapy" for HIV infection and is composed of three drugs: efavirenz, emtricitabine, and tenofovir disoproxil fumarate. It remains a commonly used treatment for AIDS because it is tolerated well by patients and exhibits excellent efficacy [25]. In the field of cancer therapy, the combination of palbociclib and letrozole significantly increases the anti-tumor activity of palbociclib [26]. This demonstrates the advantage of multi-target combination therapy, which is an inherent strategy in traditional Chinese medicine. We can see that a single compound can exhibit good effects, but if multiple therapeutic compounds can be sourced from Chinese herbal medicine and administered as combination therapy, the efficacy may be much higher, which will be a key focus of our future research.

## Acknowledgments

This work was supported by the Pudong New Area Science and Technology Committee of Shanghai (Grant No. PKJ2015-Y08).

## Conflicts of interest

The authors declare that there are no conflicts of interest.

## Appendix A. Supplementary data

Supplementary data to this article can be found online at <https://doi.org/10.1016/j.jpba.2019.07.002>.

## References

- [1] S.L. James, D. Abate, K.H. Abate, et al., Global, regional, and national incidence, prevalence, and years lived with disability for 354 diseases and injuries for 195 countries and territories, 1990–2017: a systematic analysis for the Global Burden of Disease Study 2017, *Lancet* 392 (2018) 1789–1858.
- [2] K. Luoma, H. Riihimäki, R. Luukkonen, et al., Low back pain in relation to lumbar disc degeneration, *Spine* 25 (2000) 487–492.
- [3] A.M. Wang, P. Cao, A. Yee, et al., Detection of extracellular matrix degradation in intervertebral disc degeneration by diffusion magnetic resonance spectroscopy, *Magn. Reson. Med.* 73 (2015) 1703–1712.
- [4] C. Wang, X. Yu, Y. Yan, et al., Tumor necrosis factor- $\alpha$ : a key contributor to intervertebral disc degeneration, *Acta Biochim. Biophys. Sin.* 49 (2017) 1–13.
- [5] N.V. Vo, R.A. Hartman, T. Yurube, et al., Expression and regulation of metalloproteinases and their inhibitors in intervertebral disc aging and degeneration, *Spine J.* 13 (2013) 331–341.
- [6] H. Xu, Q. Mei, J. He, et al., Correlation of matrix metalloproteinases-1 and tissue inhibitor of metalloproteinases-1 with patient age and grade of lumbar disk herniation, *Cell Biochem. Biophys.* 69 (2014) 439–444.
- [7] Y. Tang, S. Wang, Y. Liu, et al., Microarray analysis of genes and gene functions in disc degeneration, *Exp. Ther. Med.* 7 (2014) 343–348.
- [8] H.V. Yuan, Y. Tang, Y.X. Liang, et al., Matrix metalloproteinase-3 and vitamin d receptor genetic polymorphisms, and their interactions with occupational exposure in lumbar disc degeneration, *J. Occup. Health* 52 (2010) 23–30.
- [9] C.L. LeMaitre, A.J. Freemont, J.A. Hoyland, Human disc degeneration is associated with increased MMP 7 expression, *Biotech. Histochem.* 81 (2006) 4–6.
- [10] B. Bachmeier, A. Nerlich, N. Mittermaier, et al., Matrix metalloproteinase expression levels suggest distinct enzyme roles during lumbar disc herniation and degeneration, *Eur. Spine J.* 18 (2009) 1573–1586.
- [11] S.M. Richardson, P. Doyle, B.M. Minogue, et al., Increased expression of matrix metalloproteinase-10, nerve growth factor and substance p in the painful degenerate intervertebral disc, *Arthritis Res. Ther.* 11 (2009) R216.
- [12] H.E. Gruber, J.A. Ingram, M.D. Cox, et al., Matrix metalloproteinase-12 immunolocalization in the degenerating human intervertebral disc and sand rat spine: biologic implications, *Exp. Mol. Pathol.* 97 (2014) 1–5.
- [13] H.R. Li, Q. Cui, Z.Y. Dong, et al., Downregulation of miR-27b is involved in Loss of Type II collagen by directly targeting matrix metalloproteinase 13 (MMP13) in human intervertebral disc degeneration, *Spine* 41 (2016) E116–E123.
- [14] H. Xu, Q. Mei, B. Xu, et al., Expression of matrix metalloproteinases is positively related to the severity of disc degeneration and growing age in the east Asian lumbar disc herniation patients, *Cell Biochem. Biophys.* 70 (2014) 1219–1225.
- [15] W.L. Zhang, Y.F. Chen, H.Z. Meng, et al., Role of miR-155 in the regulation of MMP-16 expression in intervertebral disc degeneration, *J. Orthop. Res.* 35 (2017) 1323–1334.
- [16] J. Zhang, X. Sun, J. Liu, et al., The role of matrix metalloproteinase 14 polymorphisms in susceptibility to intervertebral disc degeneration in the Chinese Han population, *Arch. Med. Sci.* 11 (2015) 801–806.
- [17] B. Chen, A.J. Butte, Network medicine in disease analysis and therapeutics, *Clin. Pharmacol. Ther.* 94 (2013) 627–629.
- [18] J. Lamb, E.D. Crawford, D. Peck, et al., The Connectivity Map: using gene-expression signatures to connect small molecules, genes, and disease, *Science* 313 (2006) 1929–1935.
- [19] J. Ru, P. Li, J. Wang, et al., TCMSP: a database of systems pharmacology for drug discovery from herbal medicines, *J. Cheminf.* 6 (2014) 13, <https://doi.org/10.1186/1758-2946-6-13>.
- [20] S. Illien-Junger, F. Grosjean, D.M. Laudier, et al., Combined anti-inflammatory and anti-age drug treatments have a protective effect on intervertebral discs in mice with diabetes, *PLoS One* 8 (2013), e64302.
- [21] Z. Sun, S. Zhao, C. Liu, et al., Effects of nuclear factor kappa B signaling pathway in human intervertebral disc degeneration, *Spine* 40 (2015) 224–232.
- [22] Z. Sui, Q. Li, L. Zhu, et al., An integrative investigation of the toxicity of *Aconiti kusnezoffii* radix and the attenuation effect of its processed drug using a UHPLC-Q-TOF based rat serum and urine metabolomics strategy, *J. Pharm. Biomed. Anal.* 145 (2017) 240–247.
- [23] M. Sirota, J.T. Dudley, J. Kim, et al., Discovery and preclinical validation of drug indications using compendia of public gene expression data, *Sci. Transl. Med.*

- 3 (2011) 96ra77.
- [24] G. Xie, W. Peng, P. Li, et al., A network pharmacology analysis to explore the effect of on traumatic brain injury, *BioMed Res. Int.* 2018 (2018) 3951783.
- [25] E. Deeks, C. Perry, Efavirenz/emtricitabine/tenofovir disoproxil fumarate single-tablet regimen (Atripla®): a review of its use in the management of HIV infection, *Drugs* 70 (2010) 2315–2338.
- [26] B. Warth, P. Raffeiner, A. Granados, et al., Metabolomics reveals that dietary xenoestrogens alter cellular metabolism induced by palbociclib/letrozole combination cancer therapy, *Cell. Chem. Biol.* 25 (2018) 1–10.



## Original Article

## Comparing different domains of analysis for the characterisation of N-glycans on monoclonal antibodies

Sara Carillo <sup>a,1</sup>, Raquel Pérez-Robles <sup>b,1</sup>, Craig Jakes <sup>a,c</sup>, Meire Ribeiro da Silva <sup>a</sup>, Silvia Millán Martín <sup>a</sup>, Amy Farrell <sup>a</sup>, Natalia Navas <sup>b</sup>, Jonathan Bones <sup>a,c,\*</sup><sup>a</sup> Characterisation and Comparability Laboratory, NIBRT – the National Institute for Bioprocessing Research and Training, Foster Avenue, Mount Merrion, Blackrock, Co. Dublin, A94 X099, Ireland<sup>b</sup> Department of Analytical Chemistry, Biohealth Research Institute (ibs.GRANADA), University of Granada, Granada, Spain<sup>c</sup> School of Chemical and Bioprocess Engineering, University College Dublin, Belfield, Dublin 4, D04 V1W8, Ireland

## ARTICLE INFO

## Article history:

Received 10 August 2019

Received in revised form

27 November 2019

Accepted 28 November 2019

Available online 29 November 2019

## Keywords:

N-Glycans

Biopharmaceuticals

Monoclonal antibodies

Intact mass analysis

Mass spectrometry

Native mass spectrometry

Glycan analysis

Peptide mapping

Glycopeptide analysis

## ABSTRACT

With the size of the biopharmaceutical market exponentially increasing, there is an aligned growth in the importance of data-rich analyses, not only to assess drug product safety but also to assist drug development driven by the deeper understanding of structure/function relationships. In monoclonal antibodies, many functions are regulated by N-glycans present in the constant region of the heavy chains and their mechanisms of action are not completely known. The importance of their function focuses analytical research efforts on the development of robust, accurate and fast methods to support drug development and quality control. Released N-glycan analysis is considered as the gold standard for glycosylation characterisation; however, it is not the only method for quantitative analysis of glycoform heterogeneity. In this study, ten different analytical workflows for N-glycan analysis were compared using four monoclonal antibodies. While observing good comparability between the quantitative results generated, it was possible to appreciate the advantages and disadvantages of each technique and to summarise all the observations to guide the choice of the most appropriate analytical workflow according to application and the desired depth of data generated.

© 2019 Xi'an Jiaotong University. Production and hosting by Elsevier B.V. This is an open access article under the CC BY-NC-ND license (<http://creativecommons.org/licenses/by-nc-nd/4.0/>).

## 1. Introduction

Therapeutic monoclonal antibodies (mAbs) are a major class of biopharmaceuticals that have been used as autoimmune and oncology therapeutics [1]. Over the last decade, three to five new mAb products have been approved annually in Europe and/or the US [2]. The market for mAbs is expected to continue to grow over the coming years with over 300 mAb candidates currently in development [2,3]. Chinese hamster ovary (CHO) cells are the most commonly used expression system for mAbs, as they have the ability to produce human-like post-translational modifications, thereby reducing the potential for adverse reactions in humans [4].

Moreover, the use of CHO cell lines for over 30 years has established a history of product safety, efficacy and improvements in cell engineering, leading to high product titre and the capacity to adapt their growth in adhesion and suspension cell cultures [5]. Glycosylation, the most prominent post-translational modification (PTM), occurs in endoplasmic reticulum and Golgi apparatus [4]. Glycans can be attached to either the mAb heavy chain constant region (N-glycans) or serine or threonine (O-glycans) with the former being the most prominent [6]. N-glycans are classified into three main groups, i.e. oligomannose glycans, complex glycans and hybrid glycans. The N-glycans on mAbs produced in CHO cells are mainly asialylated core fucosylated complex glycans [7].

Glycosylation significantly impacts the stability and function of mAbs, including mediation of antibody-dependent cell-mediated cytotoxicity (ADCC) and complement dependent cytotoxicity (CDC) [7]. N-glycosylation stabilizes the structure of an mAb; therefore, deglycosylation renders mAbs thermally less stable, more susceptible to unfolding [8] and prone to aggregation [9]. Afucosylation of mAb N-glycans can result in increased binding affinity of mAbs to

Peer review under responsibility of Xi'an Jiaotong University.

\* Corresponding author at: Characterisation and Comparability Laboratory, NIBRT – The National Institute for Bioprocessing Research and Training, Foster Avenue, Mount Merrion, Blackrock, Co. Dublin, A94 X099, Ireland.

E-mail address: [jonathan.bones@nibrt.ie](mailto:jonathan.bones@nibrt.ie) (J. Bones).

<sup>1</sup> These authors contributed equally to this work.

<https://doi.org/10.1016/j.jpha.2019.11.008>

2095-1779/© 2019 Xi'an Jiaotong University. Production and hosting by Elsevier B.V. This is an open access article under the CC BY-NC-ND license (<http://creativecommons.org/licenses/by-nc-nd/4.0/>).

receptors present on the surface of leukocyte effector cells, which can enhance ADCC [10,11]. Several studies have suggested that terminal sialic acid residues on glycans mediate anti-inflammatory responses, reduce ADCC in vivo [12] and inhibit allergic reaction [13]. Galactosylation does not affect ADCC; however, the presence of galactose residues on N-glycans may lead to an increase in CDC [14,15] or anti-inflammatory activity [16]. High-mannose N-glycans have been shown to correlate with accelerated clearance of mAbs from the blood, decreasing circulating half-life of the drugs [17–19]. Therefore, control of the glycosylation pattern is required to ensure adherence to lot release specifications [20]. Characterisation of the glycosylation present on mAbs is a regulatory requirement not only for lot release but also for new drug applications and biosimilar approval [21], as reported in International Council for Harmonization (ICH) guideline Q6B. European Medicines Agency guidelines suggest that particular attention should be paid to their degree of mannosylation, galactosylation, fucosylation and sialylation and that distribution of the main glycan structures should be determined [4].

Different strategies can be applied to analyse the N-glycan moieties [22] with the gold standard workflow involving enzymatic release of oligosaccharides from the protein and chemical derivatisation with a label used for the detection technique of choice [23]. The most common separation techniques to analyse released N-glycans are capillary electrophoresis and liquid chromatography (LC) coupled to fluorescent detection and/or high resolution mass spectrometry (HR-MS). N-glycans can also be analysed as glycopeptides after mAb proteolysis (e.g. tryptic digest), glycopeptide enrichment and LC-MS/MS analysis, obtaining in-depth data on the glycoforms present on the protein as well as site-specific information. These two approaches require high levels of expertise and training for both sample preparation and LC-MS data acquisition and analysis, to ensure method robustness. Due to the recent advances in LC-MS technologies and the improvements in high resolution mass spectrometry of proteins, other analytical routes for determining N-glycan profiles are now available. These include characterisation of the glycoforms at intact protein level, using denaturing or native conditions, sometimes supported by top-down data, as well as the analysis of mAbs subunits via LC-MS [4,24–27].

Intact mass analysis and top-down approaches facilitate the analysis of glycosylation with minimal sample preparation and represent rapid methods for the determination of glycoform profiles. However, if a more detailed analysis is required, it is necessary to produce a complementary glycan map because the intact protein glycan profile may not enable the detection of low abundant glycans [4]. Middle-up analysis is applied to mAbs after digestion with a proteolytic enzyme such as IdeS protease and allows the study of individual domains yielding region specific N-glycan profiles [28,29].

Intact and subunit analysis for the determination of N-glycans relies on HR-MS analysis that is essential to distinguish near-isobaric species generated by the intrinsic heterogeneity present on monoclonal antibodies. This heterogeneity arises not only at the N-glycan level but is also due to the presence of other PTMs, such as methionine and tryptophan oxidation, asparagine and glutamine conversion to succinimide intermediates, deamidation or C-term lysine truncation.

Here, we performed an extensive Fc-glycosylation analysis comparison using ten different methods to quantitatively characterize the N-glycan profiles from biotherapeutics, i.e., bevacizumab (BEV), infliximab (INF), rituximab (RIT) and trastuzumab (TRA). The four mAbs were studied across different domains of analysis: intact mass analysis using denatured and native conditions, reduced mAb (heavy/light chain analysis), intact Fc region (gingipain digestion),

single chain Fc analysis (IdeS digested subunits), tryptic digestion based peptide mapping and released N-glycan analysis. Due to its wide acceptance, hydrophilic interaction liquid chromatography (HILIC) of N-glycans after labelling with anthranilic acid (2-AA) or 2-aminobenzamide (2-AB) was used as a reference method. The ten methods were compared in terms of depth of information achieved, level of expertise and instrumentation required for sample preparation and data analysis, relevance of the data obtained as well as suitability for structural characterisation or batch-to-batch comparison to assist the choice of the most suitable technique for N-glycan analysis.

## 2. Materials and methods

### 2.1. Chemicals and reagents

Rituximab, bevacizumab, infliximab and trastuzumab drug products were kindly provided by the Hospital Pharmacy Unit of the University Hospital of San Cecilio in Granada, Spain.

LC-MS grade solvents (0.1% (v/v) formic acid in water, 0.1% (v/v) formic acid in acetonitrile, formic acid, acetonitrile, water) were sourced from Fisher Scientific. TCEP and guanidine-HCl were obtained from Pierce. IdeS (immunoglobulin-degrading enzyme of *Streptococcus pyogenes*) (FabRICATOR™) and kgp (Lys-gingipain) (GingisKHAN™) were purchased from Genovis. SMART Digest™ kit, magnetic resin option was obtained from Thermo Scientific and PNGase F (CarboClip®) was obtained from Asparia Glycomics (Gipuzkoa, Spain). All other reagents were purchased from Sigma-Aldrich (Arklow, Ireland).

### 2.2. Analytical instrumentation

All LC-MS analyses were performed using a Vanquish™ Flex Quaternary UHPLC (Thermo Scientific, Germering, Germany) and a Q Exactive™ Plus Hybrid Quadrupole Orbitrap MS instrument with extended mass BioPharma Option, equipped with an Ion Max source with a HESI-II probe (Thermo Scientific, Bremen, Germany). All data were acquired using Thermo Scientific™ Xcalibur™ software 4.0.

### 2.3. Intact mass analysis under native conditions

For mAb analysis using native intact MS, 10 µg of mAb sample was injected onto a MAbPac™ SEC-1 column, 5 µm, 300 Å, 4.0 mm × 300 mm (Thermo Scientific™, Cat# 074696) under isocratic conditions of 50 mM ammonium acetate buffer at 300 µL/min for 20 min. The column temperature was at 30 °C. The MS method consisted of full positive polarity MS scans only at 17,500 resolution setting (defined at  $m/z$  200) with the mass range set to 2500–8000  $m/z$  and automatic gain control (AGC) target value of  $3.0 \times 10^6$  with a maximum injection time of 200 ms and 10 microscans. In-source collision induced dissociation (CID) was set to 150 eV. Runs were performed in HMR mode. MS instrumental tune parameters were set as follows: spray voltage was 3.6 kV, sheath gas flow rate was 20 arbitrary units (AU), auxiliary gas flow rate was 5 AU, capillary temperature was 275 °C, probe heater temperature was 275 °C and S-lens RF voltage set to 200 V.

### 2.4. Intact mass analysis under denaturing conditions

For mAb analysis under denaturing conditions, 10 µg of each mAb was injected onto a MAbPac™ RP column, 4 µm, 2.1 mm × 50 mm (Thermo Scientific, Cat# 088648). The analysis was performed using a binary gradient of 0.1% (v/v) formic acid in water (A) and 0.1% (v/v) formic acid in acetonitrile (B). Gradient

conditions were as follows: 25% B increased to 45% B in 2.5 min with a further increase to 80% B in 0.5 min with a 1 min isocratic hold. Initial conditions were restored in 0.2 min and held for an additional 3.8 min to ensure column re-equilibration. The column temperature was maintained at 70 °C throughout and flow rate was sustained at 300  $\mu\text{L}/\text{min}$ . The MS method consisted of full positive polarity MS scans only at 17,500 resolution setting (defined at  $m/z$  200) with the mass range set to 1500–4500  $m/z$  and AGC target value of  $3.0 \times 10^6$  with a maximum injection time of 100 ms and 10 microscans. In-source CID was set to 100 eV. Analysis was performed using protein mode. MS instrumental tune parameters were set as follows: spray voltage was 3.8 kV, sheath gas flow rate was 35 AU, auxiliary gas flow rate was 10 AU, capillary temperature was 275 °C, probe heater temperature was 175 °C and S-lens RF voltage set to 80 V.

### 2.5. Analysis of reduced mAb

MABs were treated with 50 mM tris(2-carboxyethyl)phosphine) (TCEP) in 4 M guanidine-HCl, for 45 min at room temperature then diluted to 100 ng/ $\mu\text{L}$  in water. 2  $\mu\text{L}$  of mAb was injected onto a MAbPac RP column, 4  $\mu\text{m}$ , 2.1 mm  $\times$  50 mm (Thermo Scientific, Cat# 088648) and analysis was performed using a binary gradient of 0.1% (v/v) formic acid in water (A) and 0.1% (v/v) formic acid in acetonitrile (B). Gradient conditions were as follows: 28% B initially for 1 min, increased to 40% B in 15 min with a further increase to 80% B in 1 min and a final 1 min isocratic hold. Initial conditions were restored in 0.5 min and held for an additional 9.8 min to ensure column re-equilibration. The column temperature was maintained at 80 °C throughout and flow rate was maintained at 300  $\mu\text{L}/\text{min}$ .

The MS method consisted of full positive polarity MS scans only at 17,500 resolution setting for heavy chain analysis and 140,000 for light chain analysis (defined at  $m/z$  200) with the mass range set to 600–2400  $m/z$  and AGC target value of  $3.0 \times 10^6$  with a maximum injection time of 200 ms and 10 microscans. In-source CID was set to 0 eV. Analysis was performed using protein mode. MS instrumental tune parameters were set as follows: spray voltage was 3.8 kV, sheath gas flow rate was 25 AU, auxiliary gas flow rate was 10 AU, capillary temperature was 320 °C, probe heater temperature was 150 °C and S-lens RF voltage set to 60 V.

### 2.6. Middle up analysis of mAbs

For each mAb, two populations of mAb sub-units were analysed, one prepared following treatment with IdeS and the other with kgp.

For IdeS digestion, 40  $\mu\text{g}$  of each mAb was combined with 0.5  $\mu\text{L}$  of the enzymatic digestion solution (67 units/ $\mu\text{L}$  in Optima grade water) and incubated at 37 °C for 2 h at 500 rpm. Reduction of disulphide bonds was achieved by incubation in 4 M guanidine hydrochloride and 50 mM TCEP for 45 min at 56 °C. Following incubation, samples were reduced to dryness *via* vacuum centrifugation and reconstituted in 0.1% formic acid (1  $\mu\text{g}/\mu\text{L}$ ) prior of LC-MS analysis. For kgp digestion, 50  $\mu\text{g}$  of each mAb was treated as recommended by the vendor and incubated for 2 h at 37 °C.

LC-MS analysis of mAb sub-units was performed on a MABPac RP column, 4  $\mu\text{m}$ , 2.1 mm  $\times$  100 mm (Thermo Scientific, Cat# 088648). The mobile phases were 0.1% formic acid in water (90/10, v/v, mobile phase A) and 0.1% formic acid in ACN/water (90/10, v/v, mobile phase B). The LC gradient profile was as follows: 25% B for 1 min, then increased to 45% B in 15 min; % B was kept constant for 1 min, then a wash step at 80% B was performed for 2 min before restoring initial conditions and column re-equilibration was performed 6 min. Total runtime was 25 min. The column temperature

was maintained at 80 °C throughout and flow rate was sustained at 300  $\mu\text{L}/\text{min}$ . For the kgp digest, the same column was employed, using 0.1% formic acid in water (A) and 0.1% formic acid in acetonitrile (B) as mobile phases. For Fc and Fab regions separation, the gradient was 20% B for 2 min, then increased to 45% B in 14 min and further increased at 80% B in 1 min, held for an additional minute and starting conditions restored in 0.5 min and held for 6.5 min. The MS method for both analyses consisted of full positive polarity MS scans only at 140,000 or 35,000 resolution setting (defined at  $m/z$  200), for IdeS and kgp digest respectively, with the mass range set to 600–2400  $m/z$  and AGC target value of  $3.0 \times 10^6$  with a maximum injection time of 200 ms and 5 microscans. In-source CID was set to 0 eV. The analysis was performed in protein mode. MS instrumental tune parameters were set as follows: spray voltage was 3.8 kV, sheath gas flow rate was 25 AU, auxiliary gas flow rate was 10 AU, capillary temperature was 320 °C, probe heater temperature was 150 °C and S-lens RF voltage set to 60 V.

### 2.7. Peptide mapping

Samples were diluted to 2 mg/mL in water. For each sample digest, sample and SMART Digest buffer were added to each lane of a KingFisher Deepwell 96-well plate as outlined in Table S1. Trypsin Bead “wash buffer” was prepared by diluting SMART Digest buffer 1:4 (v/v) in water. Bead buffer was neat SMART Digest buffer. Digestion was performed using Kingfisher Duo Prime Purification System with BindIt™ software (version 4.0). Samples were incubated for 45 min at 70 °C at a medium mixing speed (to prevent sedimentation of beads), with post digestion cooling to 10 °C. Following digestion, disulphide bond reduction was performed with 10 mM DTT for 30 min at 37 °C and subsequent alkylation with 20 mM IA (iodoacetamide) in darkness for 30 min. The reaction was quenched with 15  $\mu\text{L}$  of 100 mM DTT followed by 15  $\mu\text{L}$  10% TFA (final concentration 11 mM DTT and 1% TFA). The tryptic peptides were separated and monitored by LC-MS/MS analysis using an Acclaim Vanquish C18, 2.2  $\mu\text{m}$ , 2.1 mm  $\times$  250 mm (Thermo Scientific, Cat#074812-V).

Analysis was performed using a binary gradient of 0.1% (v/v) formic acid in water (A) and 0.1% (v/v) formic acid in acetonitrile (B). Gradient conditions were as follows: 2% B increased to 40% B in 45 min with a further increase to 80% B in 1 min with 4 min isocratic hold. Initial conditions were restored in 0.5 min and held for an additional 15 min to ensure column re-equilibration. The column temperature was maintained at 25 °C throughout and flow rate was sustained at 300  $\mu\text{L}/\text{min}$ . The MS method consisted of full positive polarity MS scans at 70,000 resolution setting (at  $m/z$  200) with the mass range set to 200–2000  $m/z$  and AGC target value of  $3.0 \times 10^6$  with a maximum injection time of 100 ms and one microscan. In-source CID was set to 0 eV. MS<sup>2</sup> settings were as follows: a resolution setting of 17,500 (at  $m/z$  200), AGC target value of  $1.0 \times 10^5$ , isolation window set to 2.0  $m/z$ , signal intensity threshold of  $1.0 \times 10^4$ , normalized collision energy set to 28, top 5 precursors selected for fragmentation and dynamic exclusion set to 7 s.

MS instrumental tune parameters were set as follows: spray voltage was 3.8 kV, sheath gas flow rate was 25 AU, auxiliary gas flow rate was 10 AU, capillary temperature was 320 °C, probe heater temperature was 150 °C and S-lens RF voltage set to 60 V.

Glycopeptides identification and quantitation was performed using BioPharma Finder 3.0 software using Full MS and MS/MS data, mass deviation of 5 ppm and minimum confidence of 95%.

### 2.8. N-glycan release and labelling

N-glycans from 200  $\mu\text{g}$  of each mAb were released and labelled

as reported previously [30]. All the samples were reconstituted in the starting gradient conditions and analysed on an Accucore 150-Amide-HILIC 2.1 mm × 150 mm (Thermo Scientific) column using both fluorescence and MS detection.

Analysis was performed using a binary gradient of 50 mM ammonium formate, pH 4.4 (A) and acetonitrile (B). Gradient conditions were as follows: 72% B decreased to 45% B in 40 min

with a further decrease to 40% B in 2.5 min with 0.5 min isocratic hold. Initial conditions were restored in 0.1 min and held for an additional 1.9 min to ensure column re-equilibration. The column temperature was maintained at 50 °C throughout and flow rate was sustained at 400 μL/min. Fluorescence detection was acquired using the following settings:  $\lambda_{\text{ex/em}} = 330/420$  nm for 2-AB and  $\lambda_{\text{ex/em}} = 350/425$  nm for 2-AA. The MS method consisted

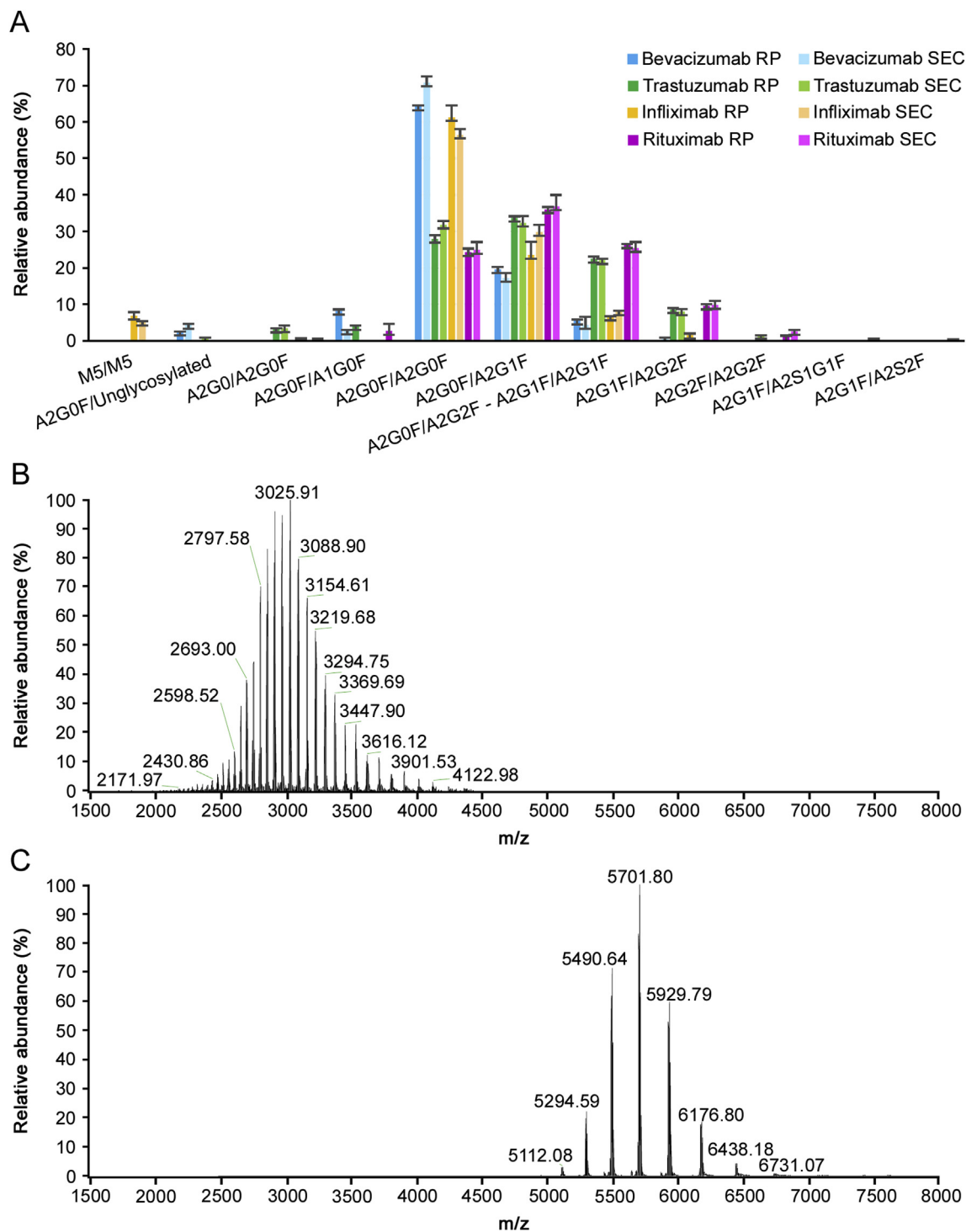


**Fig. 1.** (A) N-glycan profiles of bevacizumab (blue), trastuzumab (green), infliximab (orange) and rituximab (pink) drug products analysed *via* intact mass analysis in denaturing (dark colour shade) and native (light colour shade) conditions. Relative abundancies were calculated on the basis of MS signal intensities obtained after raw data deconvolution and averaged on triplicate analysis. Comparison of intact protein mass spectrometry in denaturing (B) and native (C) conditions.

of full MS scans in negative polarity mode at 70,000 resolution setting (defined at  $m/z$  200) with the mass range set to 380–2000  $m/z$  and AGC target value of  $3.0 \times 10^6$  with a maximum injection time of 50 ms and one microscan. In-source CID was set to 20.0 eV. MS instrumental tune parameters were set as follows: spray voltage was 3.5 kV, sheath gas flow rate was 50 AU, auxiliary gas flow rate was 13 AU, capillary temperature was 320 °C, probe heater temperature was 400 °C and S-lens RF voltage set to 50 V.

## 2.9. Data processing

Released N-glycan analysis was performed using Xcalibur QualBrowser 4.0 for signal integration and availing of GlycoWork Bench for correct glycoform identification. All other data processing, quantitation and identification were performed on BioPharma Finder 3.0 software (Thermo Scientific) using the parameters summarized in Tables S2 and S3.

**Table 1**

Experimental mass for the intact mAbs in native and denatured conditions. The relative abundances of proteoforms are also reported. Experimental mass, mass accuracy and relative abundance were calculated as average of triplicate analysis. Theoretical masses were calculated considering 2 C-term lysine clipping and 16 disulphide bonds unless stated otherwise.

mAbs	Analysis	Modifications/Glycoforms associated	Experimental mass (Da)	Theoretical average mass (Da)	Mass difference (ppm)	Relative abundance (%)
BEV	Denatured conditions	A2G0F/unglycosylated	147752.6	147751.9	4.7	2.5
		A2G0F/A1G0F	148995.5	148994.0	10.1	8.2
		A2G0F/A2G0F	149198.0	149197.6	2.7	64.0
		A2G0F/A2G1F	149359.9	149359.7	1.3	19.5
		A2G0F/A2G2F or A2G1F/A2G1F	149521.6	149521.8	1.3	5.5
BEV	Native conditions	A2G0F/unglycosylated	147751.8	147751.9	0.7	4.3
		A2G0F/A1G0F	148991.1	148994.0	19.5	2.9
		A2G0F/A2G0F	149195.6	149197.6	13.4	70.8
		A2G0F/A2G1F	149361.7	149359.7	13.4	17.2
		A2G0F/A2G2F or A2G1F/A2G1F	149524.5	149521.8	18.1	4.3
TRA	Denatured conditions	A2G1F/A2G2F	149685.7	149684.0	11.4	0.5
		A1G0F/A2G0F	147852.5	147853.4	6.3	4.0
		A2G0/A2G0F	147911.7	147910.4	8.7	3.4
		A2G0F/A2G0F	148058.6	148056.6	13.6	27.9
		A2G0F/A2G1F	148219.2	148218.7	3.4	33.7
TRA	Native conditions	A2G0F/A2G2F or A2G1F/A2G1F	148380.1	148380.8	5.0	22.5
		A2G1F/A2G2F	148541.9	148543.0	7.3	8.6
		A2G0F/unglycosylated	146611.6	146610.9	4.7	0.8
		A2G0/A2G0F	147910.7	147910.4	1.7	3.4
		A2G0F/A2G0F	148058.1	148056.6	10.1	31.8
INF	Denatured conditions	A2G0F/A2G1F	148220.5	148218.7	11.9	32.3
		A2G0F/A2G2F or A2G1F/A2G1F	148382.3	148380.8	9.8	22.1
		A2G1F/A2G2F	148544.8	148543.0	12.0	8.0
		A2G2F/A2G2F	148704.4	148705.1	4.7	1.5
		1x C-term K, M5/M5	148185.6	148184.2	9.4	1.4
INF	Native conditions	2x C-term K, M5/M5	148313.1	148312.4	4.5	5.6
		A2G0F/A2G0F	148514.4	148512.6	12.4	21.6
		1x C-term K, A2G0F/A2G0F	148643.4	148640.7	17.8	12.0
		A2G0F/A2G1F	148677.7	148674.7	20.2	5.7
		2x C-term K, A2G0F/A2G0F	148770.4	148768.9	10.2	27.7
RIT	Denatured conditions	2x C-term K, A2G0F/A2G1F	148932.4	148931.1	8.8	17.8
		2x C-term K, A2G0F/A2G2F or A2G1F/A2G1F	149094.6	149093.2	9.3	6.6
		2x C-term K, A2G1F/A2G2F	149255.9	149255.3	3.5	1.6
		M5/M5	148058.3	148056.1	15.3	1.2
		2x C-term K, M5/M5	148314.1	148312.4	11.6	3.9
RIT	Native conditions	A2G0/A2G0F	148367.4	148366.4	6.4	0.6
		A2G0F/A2G0F	148512.9	148512.6	2.0	19.1
		1x C-term K, A2G0F/A2G0F	148643.0	148640.7	15.4	10.0
		A2G0F/A2G1F	148678.0	148674.7	22.2	10.5
		2x C-term K, A2G0F/A2G0F	148770.0	148768.9	7.4	27.4
RIT	Denatured conditions	2x C-term K, A2G0F/A2G1F	148932.0	148931.1	6.7	19.3
		2x C-term K, A2G0F/A2G2F or A2G1F/A2G1F	149094.1	149093.2	6.0	8.0
		A1G0F/A2G0F	146873.1	146872.1	6.6	2.7
		A2G0F/A2G0F	147077.8	147075.3	17.0	24.3
		A2G0F/A2G1F	147238.2	147237.5	4.5	36.0
RIT	Native conditions	A2G0F/A2G2F or A2G1F/A2G1F	147400.9	147399.6	8.4	26.4
		A2G1F/A2G2F	147562.3	147561.8	3.5	9.6
		A2G2F/A2G2F	147724.2	147723.9	2.1	1.0
		A2G0/A2G0F	146927.4	146929.2	12.5	0.3
		A2G0F/A2G0F	147078.4	147075.3	20.8	24.9
RIT	Denatured conditions	A2G0F/A2G1F	147240.1	147237.5	17.5	36.7
		A2G0F/A2G2F or A2G1F/A2G1F	147403.0	147399.6	22.8	25.4
		A2G1F/A2G2F	147563.8	147561.8	14.0	9.8
		A2G2F/A2G2F	147722.5	147723.9	9.7	2.6
		A2G2F/A2S1G1F	148019.1	148015.2	26.8	0.2
RIT	Denatured conditions	A2G2F/A2S2F	148308.2	148306.4	11.9	0.1

**Table 2**  
Proteoforms obtained after heavy chain analysis on the 4 monoclonal antibodies analysed. Average experimental masses on triplicate analysis were reported together with theoretical average masses and average mass accuracies for each proteoform. Relative abundances were calculated based on the MS signal intensities in the triplicate analysis. Masses were calculated accounting for C-term lysine clipping unless stated otherwise.

mAbs	Modifications/Glycoforms	Experimental mass (Da)	Theoretical average mass (Da)	Mass difference (ppm)	Relative abundance (%)	
BEV	Unglycosylated	49718.8	49718.7	1.3	1.5	
	A1G0F	50961.2	50960.8	6.7	2.1	
	A2G0	51017.5	51017.9	7.1	0.4	
	A2G0F	51163.8	51164.0	5.0	82.0	
	A2G1	51180.0	51180.0	1.3	1.4	
	A2G1F	51325.9	51326.2	4.8	12.0	
	A2G2F	51488.3	51488.3	1.3	0.4	
	A2S1G1F	51746.2	51745.6	12.1	0.2	
	TRA	M5	50372.6	50373.2	12.5	0.7
		A1G0F	50398.3	50398.3	1.3	0.6
A2G0		50455.0	50455.3	6.8	3.9	
A2G0F		50601.2	50601.5	6.1	51.0	
A2G1		50617.4	50617.5	1.6	0.6	
A2G1F		50763.3	50763.6	6.5	38.1	
A2G2F		50925.3	50925.8	8.2	5.1	
INF	M5	50605.5	50605.4	3.4	1.2	
	1x C-term lysine, M5	50734.1	50733.5	10.1	2.1	
	A1G0F	50758.2	50758.6	7.4	1.3	
	A2G0	50815.3	50815.7	7.2	1.1	
	A2G0F	50833.5	50833.6	1.8	17.8	
	1x C-term lysine, A2G0F	50962.0	50961.8	4.5	48.2	
	A2G1F	50995.3	50995.8	8.6	11.3	
	1x C-term lysine, A2G1F	51123.3	51123.9	12.3	16.2	
	A2G2F	51158.4	51157.9	9.4	0.8	
	RIT	Gln- > Pyro-Glu, A2G0F	50513.9	50514.3	8.1	46.2
Gln- > Pyro-Glu, A2G1F		50676.1	50676.4	7.0	46.4	
Gln- > Pyro-Glu, A2G2F		50838.1	50838.6	9.9	7.4	

### 3. Results and discussion

#### 3.1. Intact mass analysis

Intact mass analysis was performed on the four mAbs using both denaturing and native conditions. Excellent MS data quality allowed achievement of mass accuracies  $\leq 10$  ppm for the majority of mAb proteoforms. In particular, proteoforms containing C-term lysine truncation, N-terminal pyro-Glu formation and Fc N-glycosylation were considered. The N-glycan profiles resulting for the four mAbs are presented in Fig. 1 and Table 1.

Both intact mass analyses using native or denaturing conditions show comparable N-glycan quantitative results (Figs. 1A, S1-S4, Table S4) and allow minimum sample preparation, rapid analysis and data processing (see Table 2). Nevertheless, some minor differences could be observed between the two techniques as some low abundant species (<3%) can be identified only using native conditions, due to the greater spatial spectral resolution obtained with native MS (Figs. 1B–C). In particular, sialylated species were detected only when using native conditions, while they were not revealed in any other analysis at the intact or subunit level. However, the shift of the charge envelope to higher mass ranges generates spectra in a region of reduced resolution, causing a small decrease in the average mass accuracy (7.9 ppm in denatured mode vs. 11.9 ppm in native mode) [31]. Since intact mass analysis returns the mass of the N-glycoforms present on both heavy chains, it is possible that this analysis will return an underestimated or overestimated value for some N-glycans. As an example, it is not possible to distinguish between proteoforms presenting A2G1F N-glycans on both chains or presenting one A2G0F and one A2G2F.

#### 3.2. Reduced mAb/Heavy chain analysis

Intact analysis of reduced mAb allows monitoring N-glycan abundance without the complexity caused by the presence of

glycans on the two chains. Analysed mAbs were reduced with TCEP in HCl-Guanidine 8 M and injected for LC-MS analysis after a relatively quick and easy sample preparation. The MS acquisition is performed with different settings for heavy chain and light chain due to the differences in molecular masses and the requirement for different instrument settings [32]. Heavy chain spectra showed a reduced complexity that enabled identification of a greater number of features, including lower abundant glycoforms with respect to the intact mass analysis level (Tables 2 and S5) as well as an improved overall mass accuracy (average  $\Delta = 6.4$  ppm) determination due to the lower mass of the fragment analysed.

#### 3.3. Fc region

The four mAbs presented in this study were digested with gingipain enzyme, which allowed the hydrolysis of the heavy chain above the hinge region. As a consequence, disulphide bonds remaining in place in the hinge region preserved both scFc (single

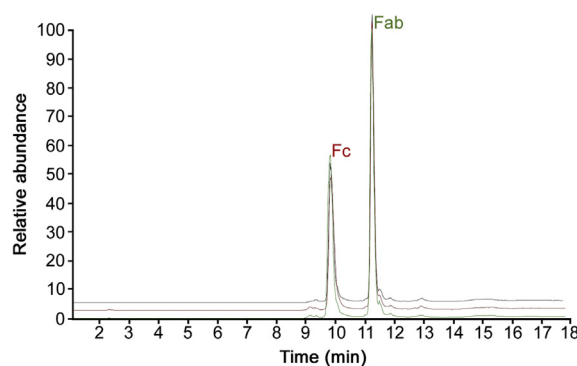


**Fig. 2.** Base Peak Chromatograms (BPCs) of the RP-MS analysis performed in triplicate on Fc region from trastuzumab drug product after digestion with gingipain.

**Table 3**

N-glycan analysis performed for the 4 mAbs analysed on the Fc region after digestion with gingipain. Experimental average masses are reported as well as theoretical average masses and average mass accuracies based on triplicate analysis. The relative abundances of fragments are also shown and were based on MS signal intensities averaged on triplicate analysis. Both C-term lysine loss and 6 disulphide bonds were considered in the calculation of the theoretical average mass unless stated otherwise.

mAbs	Modifications/Glycoforms associated	Experimental mass (Da)	Theoretical average mass (Da)	Mass difference (ppm, $n = 3$ )	Relative abundance (% , $n = 3$ )
BEV	A2G0F/A2G0	53148.2	53149.3	20.7	4.1
	A2G0F/A2G0F	53294.8	53295.4	11.4	61.7
	A2G0F/A2G1F	53456.9	53457.6	12.3	20.6
	A2G1F/A2G1F or A2G0F/A2G2F	53620.3	53619.7	11.1	11.2
	A2G1F/A2G2F	53782.7	53781.8	16.6	2.4
TRA	A2G0/A2G0F	53149.4	53149.3	1.7	6.4
	A2G0F/A2G0F	53294.8	53295.4	10.9	27.3
	A2G0F/A2G1F	53457.2	53457.6	7.4	33.1
	A2G1F/A2G1F or A2G0F/A2G2F	53619.3	53619.7	7.7	24.1
	A2G1F/A2G2F	53781.4	53781.8	7.5	8.9
INF	A2G2F/A2G2F	53943.3	53944.0	13.5	0.2
	1x No C-term K A1G0F/A1G0F	52950.7	52953.1	45.1	0.6
	A2G0F/A1G0F	53028.0	53028.1	1.1	0.2
	A2G0F/A2G0F	53231.3	53231.3	0.1	27.7
	1x C-term K, A2G0F/A2G0F	53358.5	53359.5	18.5	8.7
	A2G0F/A2G1F	53393.2	53393.4	3.7	21.9
	A1G0M5/A2G0F	53464.3	53463.5	13.7	0.3
	2x C-term K, A2G0F/A2G0F	53487.3	53487.6	6.1	9.7
	1x C-term K, A2G0F/A2G1F	53521.5	53521.6	1.4	7.2
	A2G0F/A2G2F or A2G1F/A2G1F	53555.5	53555.6	1.1	10.8
	2x C-term K, A2G0F/A2G1F	53649.6	53649.8	4.1	5.3
	1x No C-term K A1G0M5/A2G2F	53658.6	53658.7	2.3	0.1
	1x C-term K, A2G0F/A2G2F or A2G1F/A2G1F	53682.9	53683.8	15.1	2.7
	A2Sg1G0F/A2G0F	53700.1	53699.8	5.6	0.2
	A2G1F/A2G2F	53718.3	53717.7	9.9	1.0
	2x C-term K, A2G0F/A2G2F or A2G1F/A2G1F	53811.8	53811.9	2.5	1.3
	1x C-term K, A2G2/A2G2F	53862.1	53861.9	3.1	1.2
A2Sg1G1F/A2G0F	53862.7	53862.8	3.4	0.7	
2x C-term K, A2G1F/A2G2F	53973.1	53974.1	17.9	0.3	
A2Sg1G1F/A2G1F	54024.8	54025.0	3.9	0.1	
RIT	Gln- > Pyro-Glu, A2G0/A2G0F	53085.5	53085.2	7.0	0.4
	Gln- > Pyro-Glu, A2G1F/A2G1F	53555.3	53555.6	5.9	27.5
	Gln- > Pyro-Glu, A2G1F/A2G2F	53717.5	53717.7	4.3	11.3
	Gln- > Pyro-Glu, A2G0F/A2G0F	53230.9	53231.3	7.5	25.3
	Gln- > Pyro-Glu, A2G2F/A2G2F	53880.3	53879.9	8.9	1.0
	Gln- > Pyro-Glu, A2G0F/A2G1F	53393.1	53393.4	6.8	34.5

**Table 4**

scFc analysis via RP-HRMS. Average experimental masses were determined based on triplicate analysis, as well as mass accuracies and relative abundancies. C-term lysine clipping was considered in the theoretical mass calculation unless indicated otherwise.

mAbs	Modifications/Glycoforms	Experimental mass (Da)	Theoretical monoisotopic mass (Da)	Mass difference (ppm)	Relative abundance (%)
BEV	Unglycosylated	23775.974	23775.930	1.9	1.4
	A2G0F	25220.485	25220.463	0.8	84.9
	A2G1F	25382.504	25382.516	0.5	10.3
	A1G0F	25018.436	25017.380	2.3	1.9
TRA	A2G0	25074.482	25074.410	2.9	1.5
	A2G0	25074.431	25074.405	1.0	4.3
	A2G0F	25220.513	25220.463	2.0	52.0
	A2G1F	25382.581	25382.516	2.6	36.2
	A1G0F	25017.445	25017.380	2.6	1.8
INF	M5	24992.715	24992.350	14.6	1.6
	A2G2F	25544.569	25544.569	0.0	4.1
	M5	24960.391	24960.380	0.4	1.6
	A1G0F	24985.423	24985.412	0.4	2.4
	1x C-term lysine, M5	25088.477	25088.475	0.1	1.8
	1x C-term lysine, A2G0F	25316.594	25316.586	0.3	38.6
	1x C-term lysine, A2G1	25332.552	25332.581	1.1	1.4
	1x C-term lysine, A2G0	25170.536	25170.528	0.3	3.0
	A2G0F	25188.488	25188.487	0.0	30.2
	A2G1F	25350.558	25350.544	0.6	10.9
RIT	1x C-term lysine, A2G1F	25478.629	25478.639	0.4	10.1
	A2G0F	25188.541	25188.491	2.0	44.2
	A2G1F	25350.583	25350.544	1.5	48.3
	A2G2F	25512.604	25512.597	0.3	7.5

chain Fc), reducing the complexity of the associated mass spectra while keeping intact the information present at the same time on both chains (Figs. 2 and S5). MS data were acquired with higher resolution settings than intact mass spectra, allowing the confident

identification of a larger number of Fc variants (Tables 3 and S6), especially for more complex drug products such as infliximab, which presents, on top of the almost equally distributed C-term lysine variants, a greater variety of the N-glycans present at the

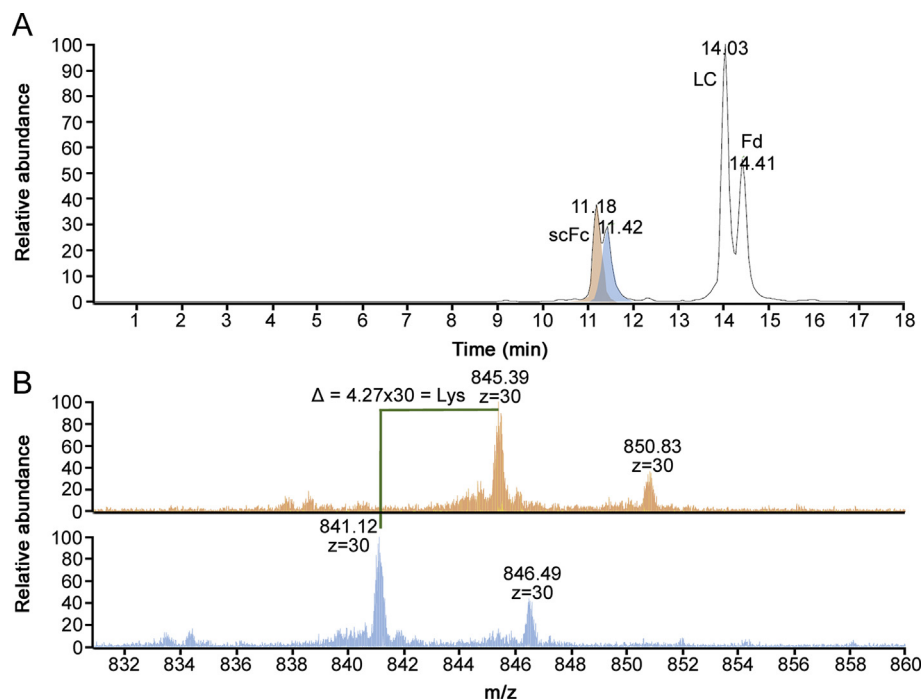


**Fig. 3.** (A) BPC for RP-MS analysis of the IdeS digested infliximab drug product. (B) Zoom of charge state +30 for scFc peaks containing (top) and missing (down) C-term lysine.

glycosylation site of both heavy chains. This type of analysis presents similar ambiguity found in intact mass analysis where it is not possible to distinguish between two isobaric species having different N-glycan distribution.

### 3.4. IdeS digestion

IdeS digestion is a widely used enzymatic tool to obtain subunits of the monoclonal antibody in a molecular mass range where high resolution mass spectrometry is readily available. IdeS cleaves monoclonal antibodies below the hinge region, driving the formation of two identical scFc regions. If HR-MS data are needed for Fab region as well, a reduction step facilitates the generation of a free light chain and the Fd region, both with the same mass range of approximately 25 kDa, making it possible to apply the same tuning parameters for data acquisition, as well as high mass resolution settings, returning isotopically resolved data that enable to obtain monoisotopic mass information. The data analysis permitted the identification of subunit proteoforms with average mass accuracy  $\leq 2$  ppm (Tables 4 and S7, Figs. S6–9). Moreover, reverse phase separation of the subunits is able to separate proteoforms containing other types of modifications, such as C-term lysine truncation, reducing the complexity of MS signal identification for near isobaric variants arising from the combination of N-glycan and lysine presence/absence (Fig. 3).

### 3.5. Peptide mapping

Peptide mapping analysis is a comprehensive tool for protein characterisation using proteolysis of the biopharmaceutical followed by LC-MS/MS analysis of the peptides. Peptide mapping is widely used in biopharmaceutical analysis to verify the primary sequence and determine the types and locations of PTMs present. The higher sensitivity of peptide mapping, together with the availability of MS/MS data, provides accurate information on the N-glycans present as well as site-specific information if multiple glycosylation sites are

present on the protein. Peptide mapping analysis has demanding sample preparation that requires multiple steps and analyst expertise to ensure reproducibility. MS/MS data analysis, although

**Table 5**

N-glycan abundancies for the 4 analysed mAbs obtained through peptide mapping analysis via LC-MS/MS. Abundancies are expressed as % respect to the total abundance of the peptide EEQYNSTYR and/or TKPREEQYNSTYR containing 1 miscleavage and were calculated on triplicate independent sample preparations.

Glycoform	% Relative abundance (n = 3)			
	Bevacizumab	Trastuzumab	Infliximab	Rituximab
A1G0	0.84	2.30	2.47	0.34
A1G0F	6.61	6.98	8.78	5.06
A1G0M4	–	–	1.70	–
A1G0M5	–	–	3.87	–
A1G0M5F	–	–	1.83	–
A1G1	–	0.59	–	–
A1G1F	0.76	2.18	3.91	1.80
A1G1M5	–	–	1.36	–
A1G1M5F	–	–	0.52	–
A1S1	–	0.09	–	–
A1S1F	–	0.40	–	0.21
A1S1M5 (A1Sg1M4F)	–	–	0.51	–
A1Sg1	–	–	0.32	–
A1Sg1F	–	–	2.10	–
A2G0	2.33	5.38	1.66	1.61
A2G0F	74.86	39.88	44.86	40.77
A2G1	–	1.94	0.37	0.63
A2G1F	10.77	32.28	18.60	39.80
A2G2	–	0.16	–	–
A2G2F	0.73	5.19	2.40	7.51
A2S1G0F	–	0.44	–	0.48
A2S1G1F	–	0.65	–	1.00
A2S2F	–	0.23	–	0.48
A3G1F	–	0.16	–	0.16
A2Sg1G0F	–	–	0.76	–
M3	–	0.16	–	–
M4	–	0.15	0.09	–
M5	0.87	2.87	7.33	1.45
M6	–	0.20	0.12	0.29
Unglycosylated	5.35	1.44	0.39	1.34

improved by modern software tools, requires experienced analysts. For these reasons, this technique is not yet considered suitable for a regulated environment, even though it is an established gold standard during product development and many research efforts are directed towards standardisation and simplification of the peptide mapping workflow to facilitate its introduction into quality control laboratories [33]. Analysis performed on the four mAbs returned a higher number of N-glycoforms than with any other technique, reaching abundancies  $\leq 0.1\%$  (Tables 5 and S8), obtained setting a mass accuracy threshold of 5 ppm during data analysis. Glycopeptides separation could resolve isomers like A2G1F and A2G1'F (Fig. 4A) enabling their quantitation, although MS/MS data did not provide fingerprint spectra to distinguish the two glycoforms (Fig. 4B). Performing peptide mapping analysis without knowledge of pre-existing information from released N-glycans may mislead glycopeptide identification, for example the identification of a low abundant glycan in infliximab as A1S1M5 (Table 5). It is known that infliximab drug product is characterized by the presence of N-glycolyl neuraminic acid (NeuG) and that there is the possibility of isobaric N-glycans where N-acetyl neuraminic acid (NeuA) and one galactose are substituted by NeuG and one fucose. The low abundance of this glycan and the absence of MS/MS data relative to the loss of sialic acid or fucose (data not shown) caused the software to incorrectly assign the glycopeptide, which could be

avoided by providing a molecule specific N-glycan database relative to the drug product as determined using released N-glycan analysis.

### 3.6. Released N-glycan

Released N-glycan analysis is the most established technique for N-glycan profiling of glycoproteins. In this study, we evaluated (Tables S9–S10) the performance, in terms of relative quantitation of the N-glycans when labelling the sample with two of the mainly used labels (2-AA and 2-AB) and compared the relative quantitation results obtained using MS (Tables S9 and S11, Fig. 5A) and fluorescence (FLR) signal integration (Tables S10 and S12, Fig. 5B). The results show good comparability of the sample preparation performed with the two different labels and with the two detection techniques (Fig. 5), while the overall mass accuracy was lower than 2 ppm.

### 3.7. Evaluation of the different approaches for N-glycan analysis

While assessing comparability of the quantitative results obtained across the different techniques, a number of factors which may drive the analyst to the choice of the right technique were evaluated (Fig. 6), such as the time of the analysis from sample

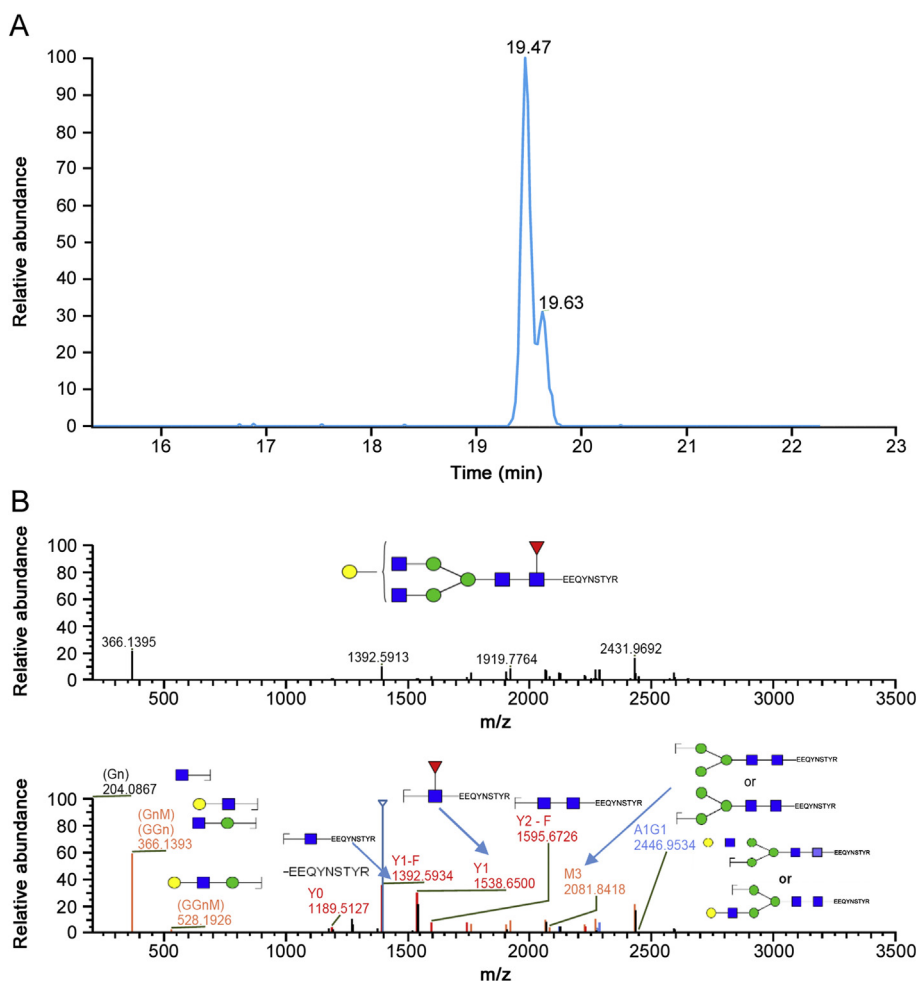


**Fig. 4.** Extracted Ion Chromatogram (XIC) of the glycopeptide carrying A2G1F N-glycan from the peptide mapping analysis of rituximab drug product (A) and relative MS/MS spectrum (B).

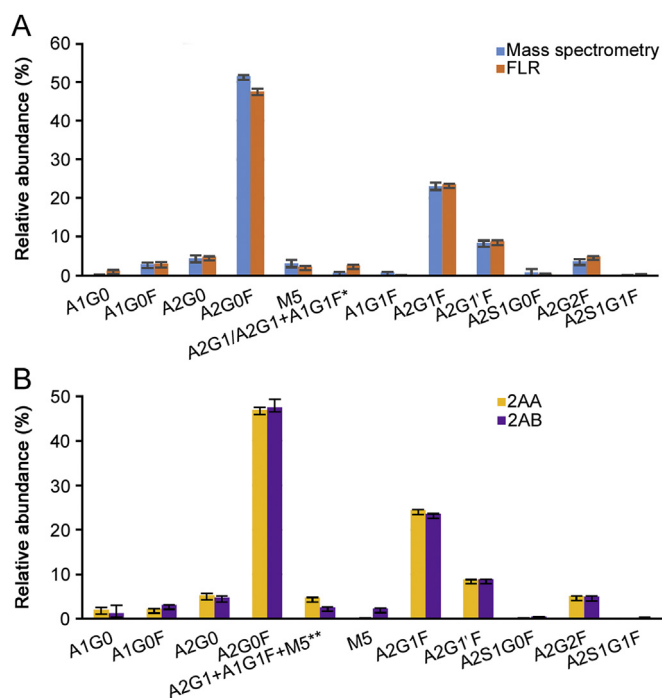


**Fig. 5.** (A) Comparison of released 2-AB labelled N-glycan from trastuzumab drug product. Quantitation was obtained integrating fluorescence trace (orange) and MS signals from each N-glycan (blue). Quantitation is based on triplicate sample preparation. \*In 2-AB trace coeluting A2G1 and A1G1F N-glycans were quantified as a single peak. (B) Comparison of released N-glycan from trastuzumab drug product. Quantitation was obtained from fluorescence trace after labelling with 2-AA (yellow) and 2-AB (purple). Quantitation is based on triplicate sample preparation. \*\*In 2-AB labelled N-glycans M5 elutes at a different retention time, and relative percentage is only relative to coeluting A2G1 and A1G1F species.

preparation to final data analysis report, the depth of structural identification obtained on the glycoforms with each technique, data quality, accuracy and robustness of the results, sensitivity of the technique, the amount of sample required and the need of expertise to perform both sample preparation and data analysis.

Workflows using the information retained at intact or subunits level will require little or no sample preparation, making it ideal for routine analysis to assure robustness of the analysis; nevertheless, the structural details obtained in this way are limited to the most abundant glycoforms (Fig. 7) and they do not provide structural details on the glycans; isomers relative abundance cannot be assessed as well as ambiguity between some glycoforms when the analysis is carried on both heavy chains at the same time (intact, gingipain digest) or with other PTMs such as glycation. N-glycan

analysis at intact level is also strongly dependent on sample heterogeneity; when other PTMs strongly influence the complexity of the mass spectra at intact level or there is an intrinsic complexity of N-glycan profiles, the use of tools to simplify the data is strongly recommended and the analysis of subunits can be helpful, as for infliximab drug product analysed in this study.

Sample complexity and N-glycan abundance are also strictly related to robustness of the analysis; while generally low %RSD values were obtained, the presence of near-isobaric species or of very low abundant species returned higher values (Tables S4-S8, S11-S12).

While providing excellent data quality and additional structural information, workflows such as peptide mapping and the analysis of released N-glycans require more time and need for trained analysts. These analyses are not yet robust enough to assure reproducibility across analysts and laboratories as they require multiple steps for the sample preparation and a high degree of expertise for the data analysis without or with little support from bioinformatics tools. In particular, it was possible to appreciate a marked difference in the quantitative analysis in terms of %RSD values between released N-glycan and peptide mapping analysis (Tables S8, S11, S12). Released N-glycan involved a number of non-automated steps for sample preparation while data processing required efforts in terms of manual integration of the obtained chromatograms as there are few software tools that guarantee a fully automated analysis of fluorescently labelled N-glycans. On the contrary, the possibility to fully automate trypsin digestion and the data analysis fully integrated into bioinformatics tools is probably the main reason for the difference of reproducibility between the two techniques. Even if efforts towards standardisation and automatization of these methods are being made to transfer them into the QC laboratories [33], a high level of knowledge in the MS data interpretation is still required.

#### 4. Conclusion

N-glycan analysis of biopharmaceuticals is a major critical attribute influencing many functions of the drug product [4,34,35]. Their assessment is required from ICH Q6B to assure biologics safety and stability and it constitutes important criteria to assess biosimilarity between originator and newly developed drugs. Although released N-glycan analysis is considered as the gold standard, N-glycan heterogeneity on the monoclonal antibodies can be assessed through several analytical workflows.

In this study, we compared N-glycan analysis and quantitation obtained through ten different methods on four different commercially available monoclonal antibodies.

While assessing good comparability of the quantitative data obtained with these techniques, several advantages and disadvantages were proved.

Recently, an interlaboratory study was published on the analysis of NIST standard mAb glycosylation [36]. The results highlighted the lack of standardisation of analytical methods for N-glycan identification and quantitation. De Leoz et al. obtained 103 different reports with a range of N-glycans identified spanning 4 to 48 structures. This variability was surely affected by the analytical workflow applied, but proved to be mainly dependent on laboratory skills. Since the experiments reported herein were performed in the same laboratory, from analysts with similar skills and using the same equipment, the variability seen in quantitative results can solely be dependent on the workflow and it was possible to appreciate the differences between more direct or automated methods, such as intact analysis or glycopeptides analysis, and more lengthy and laborious techniques, such as released N-glycan analysis. Furthermore, the choice of the analytical workflow can

	Time	Structural identification	Data quality	Sensitivity	Sample amount	Need of expertise
Intact mass RP	Green	Orange	Yellow	Yellow	Yellow	Yellow
Intact mass SEC	Green	Orange	Yellow	Yellow	Yellow	Yellow
Fc region	Green	Orange	Yellow	Yellow	Yellow	Yellow
Reduced (HC)	Green	Orange	Yellow	Yellow	Yellow	Yellow
IdeS subunits	Green	Orange	Yellow	Yellow	Yellow	Yellow
Peptide mapping	Orange	Green	Yellow	Yellow	Yellow	Yellow
N-glycan 2AB FLR	Red	Yellow	Green	Green	Yellow	Yellow
N-glycan 2AA FLR	Red	Yellow	Green	Green	Yellow	Yellow
N-glycan 2AB MS	Red	Green	Green	Green	Yellow	Yellow
N-glycan 2AA MS	Red	Green	Green	Green	Yellow	Yellow

**Fig. 6.** Heat map of the factors leading to the choice of the right technique for N-glycan analysis.

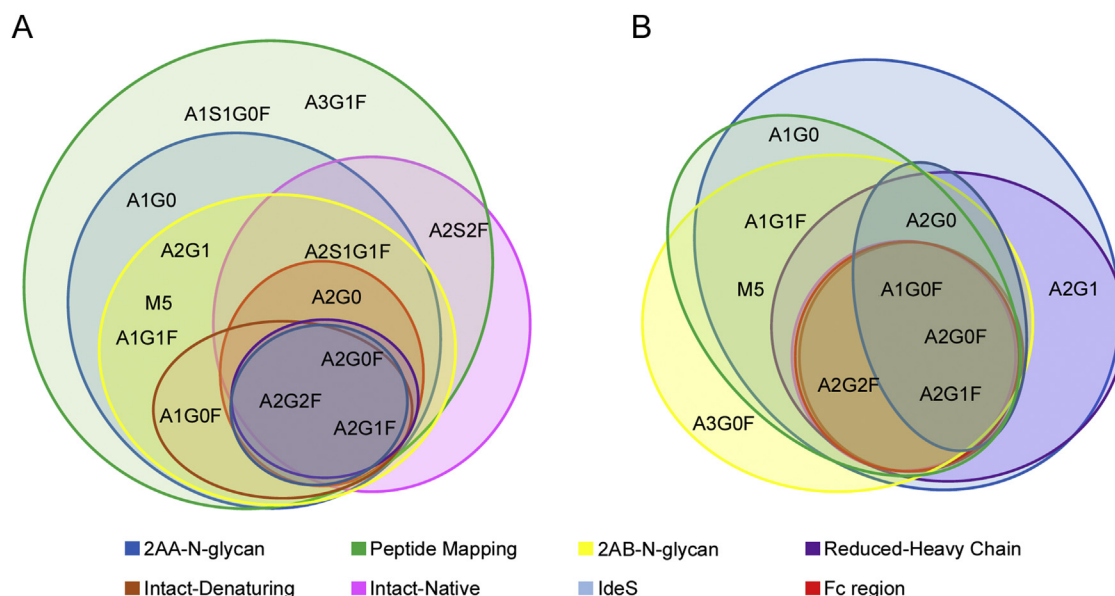


Fig. 7. Venn Diagram of the N-glycans quantified through 8 different workflows on rituximab (A) and bevacizumab (B) drug products.

strongly impact the in-depth of structural features detected.

It should also be considered that biopharmaceuticals analysis occurs at different stages of the bioprocess, from early development to lot-to-lot comparison for batch release and there is usually a stronger need for structural details during drug development than in the later stages. It is possible in this way to use the technique of choice according to the specific application and information required, justifying the lack of standardisation for this critical workflow. All the consideration provided in this study, while remaining strongly sample dependent, can surely constitute a guide for the choice of the most appropriate technique for N-glycan analysis of biopharmaceuticals.

### Acknowledgments

The authors gratefully acknowledge funding from Science Foundation Ireland under Grant Number 13/CDA/2196 and collaborators from Thermo Fisher Scientific for instrument access.

### Conflicts of interest

The authors declare that there are no conflicts of interest.

### Appendix A. Supplementary data

Supplementary data to this article can be found online at <https://doi.org/10.1016/j.jpha.2019.11.008>.

### References

- [1] Z. Elgundi, M. Reslan, E. Cruz, et al., The state-of-play and future of antibody therapeutics, *Adv. Drug Deliv. Rev.* 122 (2017) 2–19.
- [2] D.M. Ecker, S.D. Jones, H.L. Levine, The therapeutic monoclonal antibody market, *mAbs* 7 (2015) 9–14.
- [3] H. Kaplon, J.M. Reichert, Antibodies to watch in 2018, *mAbs* 10 (2018) 183–203.
- [4] A. Planinc, J. Bones, B. Dejaeger, et al., Glycan characterization of biopharmaceuticals: updates and perspectives, *Anal. Chim. Acta* 921 (2016) 13–27.
- [5] J.Y. Kim, Y.-G. Kim, G.M. Lee, CHO cells in biotechnology for production of recombinant proteins: current state and further potential, *Appl. Microbiol. Biotechnol.* 93 (2012) 917–930.
- [6] P. Hossler, S.F. Khattak, Z.J. Li, Optimal and consistent protein glycosylation in mammalian cell culture, *Glycobiology* 19 (2009) 936–949.
- [7] L. Liu, Antibody glycosylation and its impact on the pharmacokinetics and pharmacodynamics of monoclonal antibodies and Fc-fusion proteins, *J. Pharm. Sci.* 104 (2015) 1866–1884.
- [8] F. Higel, A. Seidl, F. Sorgel, et al., N-glycosylation heterogeneity and the influence on structure, function and pharmacokinetics of monoclonal antibodies and Fc fusion proteins, *Eur. J. Pharm. Biopharm.* 100 (2016) 94–100.
- [9] K. Zheng, C. Bantog, R. Bayer, The impact of glycosylation on monoclonal antibody conformation and stability, *mAbs* 3 (2011) 568–576.
- [10] S. Matsumiya, Y. Yamaguchi, J. Saito, et al., Structural comparison of fucosylated and nonfucosylated Fc fragments of human immunoglobulin G1, *J. Mol. Biol.* 368 (2007) 767–779.
- [11] R. Upton, L. Bell, C. Guy, et al., Orthogonal assessment of biotherapeutic glycosylation: a case study correlating N-glycan core afucosylation of herceptin with mechanism of action, *Anal. Chem.* 88 (2016) 10259–10265.
- [12] Y. Kaneko, F. Nimmerjahn, J.V. Ravetch, Anti-inflammatory activity of immunoglobulin G resulting from Fc sialylation, *Science* 313 (2006) 670–673.
- [13] A. Epp, J. Hobusch, Y.C. Bartsch, et al., Sialylation of IgG antibodies inhibits IgG-mediated allergic reactions, *J. Allergy Clin. Immunol.* 141 (2018) 399–402 e398.
- [14] T.S. Raju, R.E. Jordan, Galactosylation variations in marketed therapeutic antibodies, *mAbs* 4 (2012) 385–391.
- [15] M. Thomann, K. Reckermann, D. Reusch, et al., Fc-galactosylation modulates antibody-dependent cellular cytotoxicity of therapeutic antibodies, *Mol. Immunol.* 73 (2016) 69–75.
- [16] C.M. Karsten, M.K. Pandey, J. Figge, et al., Anti-inflammatory activity of IgG1 mediated by Fc galactosylation and association of FcγRIIIb and dectin-1, *Nat. Med.* 18 (2012) 1401–1406.
- [17] T.A. Bowden, K. Baruah, C.H. Coles, et al., Chemical and structural analysis of an antibody folding intermediate trapped during glycan biosynthesis, *J. Am. Chem. Soc.* 134 (2012) 17554–17563.
- [18] A.M. Goetze, Y.D. Liu, Z. Zhang, et al., High-mannose glycans on the Fc region of therapeutic IgG antibodies increase serum clearance in humans, *Glycobiology* 21 (2011) 949–959.
- [19] Y.D. Liu, G.C. Flynn, Effect of high mannose glycan pairing on IgG antibody clearance, *Biologicals* 44 (2016) 163–169.
- [20] S. Sha, C. Agarabi, K. Brorson, et al., N-Glycosylation design and control of therapeutic monoclonal antibodies, *Trends Biotechnol.* 34 (2016) 835–846.
- [21] B.L. Duivelshof, W. Jiskoot, A. Beck, et al., Glycosylation of biosimilars: recent advances in analytical characterization and clinical implications, *Anal. Chim. Acta* 1089 (2019) 1–18.
- [22] A. Beck, E. Wagner-Rousset, D. Ayoub, et al., Characterization of therapeutic antibodies and related products, *Anal. Chem.* 85 (2013) 715–736.
- [23] X. Yang, M.G. Bartlett, Glycan analysis for protein therapeutics, *J. Chromatogr. B* 1120 (2019) 29–40.
- [24] P. Liu, X. Zhu, W. Wu, et al., Subunit mass analysis for monitoring multiple attributes of monoclonal antibodies, *Rapid Commun. Mass Spectrom.* 33 (2019) 31–40.
- [25] E. Largy, F. Cantais, G. Van Vyncht, et al., Orthogonal liquid chromatography–mass spectrometry methods for the comprehensive characterization of therapeutic glycoproteins, from released glycans to intact protein level, *J. Chromatogr. A* 1498 (2017) 128–146.

- [26] T. Wohlschlager, K. Scheffler, I.C. Forstenlehner, et al., Native mass spectrometry combined with enzymatic dissection unravels glycoform heterogeneity of biopharmaceuticals, *Nat. Commun.* 9 (2018) 1713.
- [27] V. D'Atri, L. Nováková, S. Fekete, et al., Orthogonal middle-up approaches for characterization of the glycan heterogeneity of etanercept by hydrophilic interaction chromatography coupled to high-resolution mass spectrometry, *Anal. Chem.* 91 (2019) 873–880.
- [28] D. Reusch, M. Habberger, D. Falck, et al., Comparison of methods for the analysis of therapeutic immunoglobulin G Fc-glycosylation profiles-Part 2: mass spectrometric methods, *mAbs* 7 (2015) 732–742.
- [29] D. Reusch, M. Habberger, B. Maier, et al., Comparison of methods for the analysis of therapeutic immunoglobulin G Fc-glycosylation profiles-part 1: separation-based methods, *mAbs* 7 (2015) 167–179.
- [30] S. Carillo, S. Mittermayr, A. Farrell, et al., Glycosylation analysis of therapeutic glycoproteins produced in CHO cells, in: P. Meleady (Ed.), *Heterologous Protein Production in CHO Cells: Methods and Protocols*, Springer New York, New York, NY, 2017, pp. 227–241.
- [31] M. Tassi, J. De Vos, S. Chatterjee, et al., Advances in native high-performance liquid chromatography and intact mass spectrometry for the characterization of biopharmaceutical products, *J. Sep. Sci.* 41 (2018) 125–144.
- [32] A. Farrell, S. Carillo, K. Scheffler, et al., Monoclonal antibody sequence assessment using a hybrid quadrupole-Orbitrap mass spectrometer, *Anal. Methods* 10 (2018) 3100–3109.
- [33] R.S. Rogers, M. Abernathy, D.D. Richardson, et al., A view on the importance of “Multi-Attribute Method” for measuring purity of biopharmaceuticals and improving overall control strategy, *AAPS J.* 20 (2017) 7.
- [34] S. Iida, R. Kuni-Kamochi, K. Mori, et al., Two mechanisms of the enhanced antibody-dependent cellular cytotoxicity (ADCC) efficacy of non-fucosylated therapeutic antibodies in human blood, *BMC Cancer* 9 (2009) 58.
- [35] T.T. Wang, IgG Fc glycosylation in human immunity, in: J.V. Ravetch, F. Nimmerjahn (Eds.), *Fc Mediated Activity of Antibodies: Structural and Functional Diversity*, Springer International Publishing, Cham, 2019, pp. 63–75.
- [36] M.L.A. De Leoz, D.L. Duewer, A. Fung, et al., NIST interlaboratory study on glycosylation analysis of monoclonal antibodies: comparison of results from diverse analytical methods, *Mol. Cell. Proteomics* (2019), <https://doi.org/10.1074/mcp.RA119.001677>. In press.



Contents lists available at ScienceDirect

## Journal of Pharmaceutical Analysis

journal homepage: [www.elsevier.com/locate/jpa](http://www.elsevier.com/locate/jpa)

## Original Article

Rapid identification of chemical profile in Gandou decoction by UPLC-Q-TOF-MS<sup>E</sup> coupled with novel informatics UNIFI platformLi Xu <sup>a</sup>, Yi Liu <sup>a,c</sup>, Hongfei Wu <sup>b</sup>, Huan Wu <sup>b</sup>, Xiaochuang Liu <sup>b</sup>, An Zhou <sup>a,b,\*</sup><sup>a</sup> The Experimental Research Center, Anhui University of Chinese Medicine, Hefei 230038, China<sup>b</sup> Anhui Province Key Laboratory of Chinese Medicinal Formula, Hefei 230012, China<sup>c</sup> Waters Corporation (China), Shanghai 201206, China

## ARTICLE INFO

## Article history:

Received 26 December 2018

Received in revised form

7 May 2019

Accepted 10 May 2019

Available online 15 May 2019

## Keywords:

Gandou decoction

UPLC-Q-TOF-MS<sup>E</sup>

UNIFI informatics platform

Chemical constituents

## ABSTRACT

Gandou decoction (GDD), a well-known traditional Chinese medicine (TCM) formula, has been widely used for decades to treat Wilson's disease (WD) in China due to its remarkable clinical effects. However, the chemical constituents of GDD still remain unclear because of their complexity. In this work, a reliable and sensitive strategy based on ultra-performance liquid chromatography coupled with quadrupole time-of-flight tandem mass spectrometry (UPLC-Q-TOF-MS<sup>E</sup>) and UNIFI informatics platform was applied to investigate the chemical components in GDD. In total, 96 compounds including anthraquinones, alkaloids, protostane triterpenoids, flavonoids, triterpenoid saponins, tannins, curcuminoids, etc. were identified or tentatively characterized from GDD by comparing their retention time, accurate mass within 5 ppm error and MS<sup>E</sup> fragmentation patterns. Among them, eleven compounds were confirmed unambiguously with reference standards. Representative compounds in different chemical structure types were analyzed in fragmentation patterns and characteristic ions. Moreover, to better understand the chemical contribution of individual herbs to the whole decoction, the corresponding each herb in GDD was also detected. This study developed a rapid method for characterizing the chemical constituents in GDD, which could not only be used for chemical standardization and quality control, but also be helpful for further research of GDD in vivo.

© 2019 Xi'an Jiaotong University. Production and hosting by Elsevier B.V. All rights reserved. This is an open access article under the CC BY-NC-ND license (<http://creativecommons.org/licenses/by-nc-nd/4.0/>).

## 1. Introduction

Traditional Chinese medicines (TCM) have been extensively used for the prevention and treatment of complex and chronic diseases in China [1,2]. TCM formulae, combination of medicinal plants or animal materials, collectively exert therapeutic actions by complex interactions among multiple components from different herbal medicines. Based on TCM theories, these constituents in formulae could play a multi-target, synergistic and harmless therapeutic role [3]. As the components in TCM are rather complicated, it is difficult to separate and identify multiple chemical constituents. Therefore, developing a rapid and reliable method for elucidating the composition of TCM is necessary.

Wilson's disease (WD), also known as hepatolenticular

degeneration, is an autosomal recessive genetic disorder of copper metabolism caused by ATP7B gene mutation [4,5]. Excessive copper accumulation in patients suffering from WD leads to liver disease, neurological disorder, K-F rings, and osteoporosis [6]. Currently, there are several chelating agents such as D-penicillamine, dimercaptosuccinic acid, trientine, and tetrathiomolybdate for medical therapy [7]. Although Western conventional medications are highly effective, prevalent, and low-priced, a number of side effects have been observed with chelation therapy [8]. Gandou decoction (GDD), a classical TCM formula, has been used in clinics to treat WD for decades in China [9,10]. It is composed of six crude drugs, i.e., *Rheum palmatum* L. (Da-Huang), *Coptis chinensis* Franch. (Huang-Lian), *Curcuma longa* L. (Jiang-Huang), *Lysimachia christinae* Hance (Jin-Qian-Cao), *Alisma orientale* (Sam.) Juzep. (Ze-Xie) and *Panax notoginseng* (Burk.) F. H. Chen (San-Qi). The clinical studies have been proven that GDD can promote urinary copper excretion, ameliorate liver function and improve the patient's clinical symptoms [7,11]. Furthermore, GDD appears to be safe, effective, and well tolerated and has fewer adverse effects than Western conventional medications [12]. In our previous studies, we investigated

Peer review under responsibility of Xi'an Jiaotong University.

\* Corresponding author at: the Experimental Research Center, Anhui University of Chinese Medicine, Hefei 230038, China.

E-mail address: [anzhou@ahcm.edu.cn](mailto:anzhou@ahcm.edu.cn) (A. Zhou).

<https://doi.org/10.1016/j.jpha.2019.05.003>

2095-1779/© 2019 Xi'an Jiaotong University. Production and hosting by Elsevier B.V. All rights reserved. This is an open access article under the CC BY-NC-ND license (<http://creativecommons.org/licenses/by-nc-nd/4.0/>).

the therapeutic effect and serum metabolic profiling of GDD in copper-laden rats. It was found that GDD could reduce the hepatic copper accumulation, and improve liver pathological characteristics by restoring the impaired lipid metabolism, amino metabolism and glucose metabolism [13]. However, due to multi-component systems of TCM, the chemical constituents of GDD still remain unclear. Therefore, a systematic chemical profiling research of GDD is in an urgent need.

In recent years, UPLC-Q-TOF-MS<sup>E</sup> (where E represents collision energy) has provided a powerful approach for the efficient separation and structural characterization of TCM with the advantage of its high resolution, sensitivity and accuracy [14]. Q-TOF-MS<sup>E</sup> capable of simultaneously acquiring accurate mass precursor ion in MS full scan and fragment ions in MS<sup>E</sup> high-energy scan increased the credibility of analysis results [15,16]. Additionally, UNIFI software from Waters Corporation is a versatile and automated data processing platform. The software incorporates scientific library into a streamlined workflow to integrate data acquisition, library searching, MS fragment matching and report generation, which alleviates the workload from massive MS data and realizes rapid analysis of chemical components [17]. This high throughput strategy was innovatively used for screening and identification of chemical components in herbal medicines [18,19] and TCM formulae [20]. In the present study, an integrative strategy based on UPLC-Q-TOF-MS<sup>E</sup> coupled with UNIFI informatics platform has been applied to reveal the chemical profile of GDD. The aim of this study is to develop an analytical method for elucidating the material basis of GDD and provide valuable information for the quality control and in vivo analysis.

## 2. Material and methods

### 2.1. Materials and reagents

*Rheum palmatum* L., *Coptis chinensis* Franch., *Curcuma longa* L., *Lysimachia christinae* Hance, *Alisma orientale* (Sam.) Juzep. and *Panax notoginseng* (Burk.) F. H. Chen were purchased from Beijing Tongrentang Co., Ltd. (Hefei, China) and authenticated by Doctor Rongchun Han (College of Pharmacy, Anhui University of Chinese Medicine, Hefei, China). All voucher specimens were deposited at the authors' laboratory. The reference standards, including berberine hydrochloride, phycion, emodin, alisol B 23-acetate, quercetin and notoginsenoside R<sub>1</sub>, were obtained from the National Institutes for Food and Drug Control (Beijing, China). Chrysophanol, rhein, aloe-emodin and kaempferide were obtained from Beina Chuanglian Biotechnology Research Institute (Beijing, China). Curcumin was isolated in our laboratory with a purity of more than 98% by HPLC, and its structure and molecular weight have been identified by using several spectral analyses and MS, respectively. Acetonitrile and methanol (LC-MS grade) were purchased from TEDIA (Fairfield, USA). Formic acid was obtained from Tianjin Guangfu Fine Chemical Research Institute (Tianjin, China). Ultrapure water was purified using a Milli-Q water purification system (Millipore, Billerica, MA, USA).

### 2.2. Standards and sample preparation

GDD consisted of six ingredients, including *Rheum palmatum* L. (20.0 g), *Coptis chinensis* Franch (20.0 g), *Curcuma longa* L. (20.0 g), *Lysimachia christinae* Hance (24.0 g), *Alisma orientale* (Sam.) Juzep. (24.0 g) and *Panax notoginseng* (Burk.) F. H. Chen (3.0 g). They were mixed together and immersed in 0.8 L distilled water (1:8, w/v) for 0.5 h. Afterwards, they were decocted twice by extracting and refluxing for 1 h each time. Finally, the two extractions were combined and concentrated to 1.0 g crude drug per milliliter, and

then the solution was freeze-dried and stored in a vacuum desiccator before use. The accurately weighed 1.0 g freeze-dried powder was dispersed in 30 mL methanol and ultrasonicated in a water bath for 30 min to prepare solutions. The individual preparation of six herbs was carried out according to the same procedures as that of GDD. An aliquot of 5  $\mu$ L filtrate was injected into the UPLC-Q-TOF-MS<sup>E</sup> system for analysis after filtered through 0.22  $\mu$ m filter membrane.

11 reference standards were dissolved in methanol. Before qualitative analysis, they were mixed together to make reasonable concentration and filtered through 0.22  $\mu$ m filter membrane.

### 2.3. Chromatography and mass spectrometry conditions

Chromatographic analysis was performed using a Waters Acuity<sup>TM</sup> UPLC system (Waters Corporation, Milford, USA). Chromatographic separation was carried out at 30 °C, using an Agilent Eclipse Plus C18 RRHD column (2.1 mm  $\times$  100 mm, 1.8  $\mu$ m) with mobile phases A (0.1% formic acid in water) and B (acetonitrile). The flow rate was set at 0.3 mL/min. The gradient profile was as follows: 0–1 min, 10%–10% B; 1–4 min, 10%–20% B; 4–10 min, 20%–30% B; 10–15 min, 30%–40% B; 15–18 min, 40%–50% B; 18–23 min, 50%–75% B; 23–25 min, 75%–85% B; 25–27 min, 85%–100% B.

Mass spectrometric detection was carried out on Waters Xevo G2 Q-TOF mass spectrometer (Waters Corporation, Milford, USA) equipped with an ESI source. The full scan data were acquired from 50 to 1200 Da, using a capillary voltage of 3.0 kV for positive ion mode and –2.5 kV for negative ion mode, sampling cone voltage of 40 V for positive ion mode and 50 V for negative ion mode, extraction cone voltage of 4.0 V, source temperature of 120 °C (ESI<sup>+</sup>) or 110 °C (ESI<sup>–</sup>), cone gas flow of 50 L/h, desolvation gas (N<sub>2</sub>) flow of 600 L/h and desolvation gas temperature of 350 °C. The collision voltage was set as 6.0 eV for low-energy scan and 20–80 eV for high-energy scan. Data were centroided and mass was corrected during acquisition using an external reference (LockSpray<sup>TM</sup>) consisting of a 200  $\mu$ g/mL solution of leucine-enkephalin infused at a flow rate of 10  $\mu$ L/min via a lockspray interface, generating a realtime reference ion of [M+H]<sup>+</sup> (*m/z* 556.2771) in positive ion mode and [M–H]<sup>–</sup> (*m/z* 554.2615) in negative ion mode to ensure accurate MS analysis. All data collected in centroid mode were obtained and used to calculate the accurate mass and composition of relative target ions with MassLynx<sup>TM</sup> V4.1 software (Waters).

### 2.4. Establishment of a chemical compounds library of GDD

The systematic information on chemical compounds isolated from the six individual herbs in GDD was collected and sorted out by retrieving databases such as China Journals of Full-text database (CNKI), Medline, PubMed, Web of Science and ChemSpider. A self-building library of chemical compounds was established by UNIFI software, including compound name, molecular formula, chemical structure, and accurate molecular mass. Among them, the information of 356 compounds is listed in Table S1.

### 2.5. Data analysis by UNIFI platform

All MS data analysis was processed on the platform of UNIFI software. Minimum peak area of 200 was set for 2D peak detection. The peaks intensity of high energy over 80 counts and the peak intensity of low energy over 200 counts were the selected parameters in 3D peak detection. A margin of error up to 5 ppm for identified compounds was allowed and the matching compounds would be generated predicted fragments from structure. We selected positive adducts including H<sup>+</sup>, Na<sup>+</sup> and negative adducts

containing  $\text{HCOO}^-$  and  $\text{H}^-$ . They were allowed cross adduct combinations.

### 3. Results and discussion

#### 3.1. Identification and characterization of chemical compounds

The high resolution MS data of GDD were quickly acquired by UPLC-Q-TOF-MS<sup>E</sup> method. The base peak intensity (BPI) chromatograms of GDD in positive and negative ion modes are depicted in Fig. 1. The UNIFI screening platform was utilized to process and analyze the MS data, and then automatically matched the fragment information. After further manual verification, a total of 96 compounds were identified or tentatively characterized in GDD, including 21 anthraquinones, 14 alkaloids, 17 protostane triterpenoids, 10 flavonoids, 8 triterpenoid saponins, 10 tannins, 4 curcuminoids and 12 others. The detailed MS information of these components is summarized in Table 1. Meanwhile, the chemical structures were confirmed based on accurate mass, MS<sup>E</sup> data and related literatures. The structures of main chemical constituents in GDD are shown in Fig. 2.

#### 3.2. Analysis of GDD by UPLC-Q-TOF-MS<sup>E</sup>

##### 3.2.1. Anthraquinones

21 anthraquinones were detected from GDD and were also the major bioactive constituents of *Rheum palmatum* L. In this study, 6 free anthraquinones, 13 anthraquinone glycosides and 2 anthrones were determined based on MS database-matching. Anthraquinones have a characteristic fragmentation behavior with successive or simultaneous losses of CO, OH, CH<sub>3</sub> and CO<sub>2</sub> [21,22]. Peaks 64, 65, 76, 83 and 86 were exactly identified as aloe emodin, rhein, emodin, chrysophanol and physcion by comparing retention time

and fragmentation patterns with reference standards. Rhein, the main anthraquinone in GDD, was used to characterize the fragmentation pathways (Fig. 3). Rhein showed quasi-molecular ion  $[\text{M}-\text{H}]^-$  at  $m/z$  283.0256 in negative ion mode, and yielded fragment ions at  $m/z$  239.0356 and 211.0403 by losses of CO<sub>2</sub> and CO, respectively. And then, the ion at  $m/z$  211.0403 could further lose one molecule of CO to generate ion at  $m/z$  183.0439. Aloe emodin and emodin were isomers with the same  $[\text{M}-\text{H}]^-$  ion at  $m/z$  269. In high energy MS<sup>E</sup> spectra, emodin revealed  $[\text{M}-\text{H}-\text{CO}]^-$  ion at  $m/z$  241.0507 and  $[\text{M}-\text{H}-\text{CO}-\text{O}]^-$  ion at  $m/z$  225.0559, while aloe emodin could be differentiated by the characteristic ion  $[\text{M}-\text{H}-\text{CHO}]^-$  at  $m/z$  240.0421. Physcion showed  $[\text{M}-\text{H}]^-$  ion at  $m/z$  283.0619, and the obvious fragments ions at  $m/z$  255.0315  $[\text{M}-\text{H}-\text{CO}]^-$  and 240.0359  $[\text{M}-\text{H}-\text{CO}-\text{CH}_3]^-$  were further obtained. Chrysophanol showed  $[\text{M}-\text{H}]^-$  ion at  $m/z$  253.0515, only one product ion at  $m/z$  225.0545  $[\text{M}-\text{H}-\text{CO}]^-$ .

For anthraquinone glycosides, aglycone ions were identified based on the MS fragmentation behaviors of free anthraquinones. Peak 47 exhibited  $[\text{M}-\text{H}]^-$  ion at  $m/z$  415.1045, which generated an  $[\text{M}-\text{H}-162\text{Da}]^-$  ion at  $m/z$  253.0515 by eliminating the glucose residue. The further loss of CO was in accordance with the characteristic ion at  $m/z$  225.0563 of chrysophanol. Thus, peak 47 was assigned as chrysophanol-1-*O*- $\beta$ -D-glc. Based on these fragmentation patterns, peaks 15, 17, 32, 35, 44, 45, 46, 47, 48, 51, 52, 53, and 60 were inferred as anthraquinones glycosides. In addition, anthrones are an important type of anthraquinone. Sennosides usually gave a significant ion at  $m/z$  386 which originated from C-10–C-10' cleavage. Peak 27 showed  $[\text{M}-\text{H}]^-$  ion at  $m/z$  861.1908, which first produced ions at  $m/z$  699.1358 and 655.1880 by sequential loss of terminal glucose residue and CO<sub>2</sub>, followed by the cleavage of C-10 and C-10' forming  $[\text{M}-\text{H}-\text{Glc}-\text{CO}_2-\text{C}_{15}\text{H}_9\text{O}_5]^-$  ion at  $m/z$  386.1002. Its structure was identified as sennoside A or B. These two isomers were not distinguished from each other only by their MS spectra. Similarly, peak 25 displayed the same fragmentation patterns as peak 27, so it was presumed as sennoside C or D.

##### 3.2.2. Alkaloids

A total of 14 alkaloids were identified in positive ion mode and came from *Coptis chinensis* Franch, including protoberberine alkaloids, apomorphine alkaloids, and tetrahydroprotoberberine alkaloids. As reported in the literature, the neutral losses like the methyl radical (CH<sub>3</sub>·), hydrogen radical (H·) and CO are the main fragment patterns of protoberberine alkaloids due to the successive cleavage of substituted methoxyl or methylenedioxy groups on the A- and D-rings [23]. Peak 39 was unequivocally identified as berberine by contrast with a reference standard. The MS spectrum and possible fragmentation pathways of berberine are depicted in Fig. 4. Taking berberine as an example, it produced fragment ions at  $m/z$  321.0983  $[\text{M}-\text{CH}_3]^+$ , 320.0918  $[\text{M}-\text{CH}_3-\text{H}]^+$ , 306.0763  $[\text{M}-2\text{CH}_3]^+$ , 292.0969  $[\text{M}-\text{CH}_3-\text{H}-\text{CO}]^+$  and 278.0813  $[\text{M}-2\text{CH}_3-\text{CO}]^+$ . Peak 40 showed  $[\text{M}]^+$  ion at  $m/z$  352.1538 and yielded characteristic ions at  $m/z$  337.1430  $[\text{M}-\text{CH}_3]^+$ , 336.0983  $[\text{M}-\text{CH}_3-\text{H}]^+$ , 322.1068  $[\text{M}-2\text{CH}_3]^+$  and 308.1275  $[\text{M}-\text{CH}_3-\text{H}-\text{CO}]^+$ , which indicated that it was presumed as palmatine. Likewise, the other peaks 31, 33, 34, 38 and 67 could be tentatively identified as coptisine, jatrorrhizine, epi-berberine, worenine and 8-oxoberberine, respectively.

Peak 10 gave  $[\text{M}]^+$  ion at  $m/z$  342.1701 with a molecular formula C<sub>20</sub>H<sub>24</sub>NO<sub>4</sub>. The predominant ions appeared at  $m/z$  297.1123  $[\text{M}-(\text{CH}_3)_2\text{NH}]^+$ , 282.0876  $[\text{M}-(\text{CH}_3)_2\text{NH}-\text{CH}_3]^+$ , 265.0861  $[\text{M}-(\text{CH}_3)_2\text{NH}-\text{CH}_3\text{OH}]^+$ , and 237.0908  $[\text{M}-(\text{CH}_3)_2\text{NH}-\text{CH}_3\text{OH}-\text{CO}]^+$ , which is consistent with the common structure of apomorphine alkaloids. Thus, peak 10 was considered as magnoflorine. Analogously, peaks 8 and 11 were deemed as isocorydine and isoboldine. Additionally, the tetrahydroprotoberberine alkaloids have retro-Diels-Alder (RDA) reaction, resulting in the cleavage of the

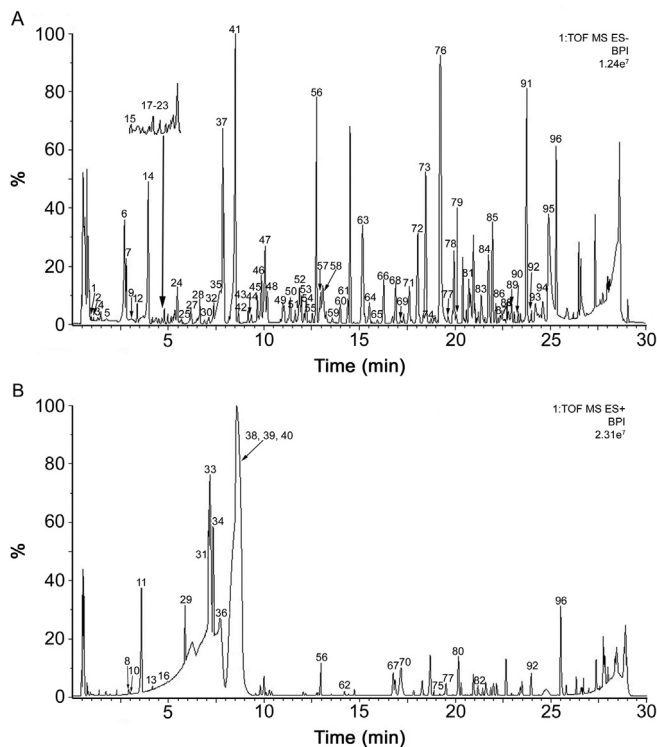


Fig. 1. The base peak intensity (BPI) chromatograms of GDD from UPLC-Q-TOF-MS<sup>E</sup> analysis. (A) Negative scan; (B) Positive scan.

**Table 1**  
Identification of chemical constituents of GDD by UPLC-Q-TOF-MS<sup>E</sup>.

No.	t <sub>R</sub> (min)	Identification	Neutral mass (Da)	Formular	Observed neutral mass (Da)	Experimental mass (m/z)	Error (ppm)	MS and MS <sup>E</sup> data (+ or -) (m/z)	Source
1	0.98	Gallic acid-O-glc	332.0743	C <sub>13</sub> H <sub>16</sub> O <sub>10</sub>	332.0743	331.0669	-0.5	331.0669[M-H] <sup>-</sup>	a
2	1.05	Gallic acid	170.0215	C <sub>7</sub> H <sub>6</sub> O <sub>5</sub>	170.0214	169.0141	-0.8	169.0141[M-H-Glc] <sup>-</sup>	a
3	1.39	Progallin A	198.0528	C <sub>9</sub> H <sub>10</sub> O <sub>5</sub>	198.0528	197.0455	-0.7	125.0244[M-H-CO <sub>2</sub> ] <sup>-</sup>	a
4	1.50	(+)-Catechin-5-O-β-D-glc	452.1319	C <sub>21</sub> H <sub>24</sub> O <sub>11</sub>	452.1318	451.1245	-0.7	197.0455[M-H] <sup>-</sup>	a
5	1.71	Procyanidin B	578.1424	C <sub>30</sub> H <sub>26</sub> O <sub>12</sub>	578.1432	577.1359	1.4	124.0455[M-H-2CH <sub>2</sub> -COOH] <sup>-</sup>	a
6	2.71	Chlorogenic acid	354.0951	C <sub>16</sub> H <sub>18</sub> O <sub>9</sub>	354.0962	353.0889	3.1	451.1245[M-H] <sup>-</sup>	b,d
7	2.82	(-)-Epicatechin	290.0790	C <sub>15</sub> H <sub>14</sub> O <sub>6</sub>	290.0797	289.0724	2.3	289.0717[M-H-Glc] <sup>-</sup>	a
8	3.16	Isocorydine	341.1627	C <sub>20</sub> H <sub>23</sub> NO <sub>4</sub>	341.1628	342.1707	0.1	289.0712[M-H-catechin] <sup>-</sup>	b
9	3.19	Procyanidin B-O-gallate	730.1534	C <sub>37</sub> H <sub>30</sub> O <sub>16</sub>	730.1544	729.1471	1.3	353.0889[M-H] <sup>-</sup>	a
10	3.20	Magnoflorine	342.1705	C <sub>20</sub> H <sub>24</sub> NO <sub>4</sub>	342.1730	342.1701	-1.2	191.0899[M-C <sub>9</sub> H <sub>6</sub> O <sub>3</sub> ] <sup>-</sup>	b
11	3.42	Isoboldine	327.1471	C <sub>19</sub> H <sub>21</sub> NO <sub>4</sub>	327.1479	328.1552	2.7	289.0724[M-H] <sup>-</sup>	b
12	3.79	Isovitexin	432.1056	C <sub>21</sub> H <sub>20</sub> O <sub>10</sub>	432.1065	477.1047	1.8	245.0821[M-H-CO <sub>2</sub> ] <sup>-</sup>	d
13	4.75	Tetradehydroscoulerine	322.1079	C <sub>19</sub> H <sub>16</sub> NO <sub>4</sub>	322.1055	322.1052	-6.6	245.0821[M-H-CO <sub>2</sub> ] <sup>-</sup>	b
14	4.79	Procyanidin B-5,3,3'-di-O-gallate	882.1643	C <sub>44</sub> H <sub>34</sub> O <sub>20</sub>	882.1685	881.1612	4.8	296.1132[M+H-CH <sub>3</sub> -CH <sub>3</sub> O] <sup>+</sup>	a
15	4.86	Emodin-8-O-β-D-glc	432.1056	C <sub>21</sub> H <sub>20</sub> O <sub>10</sub>	432.1065	431.0992	1.9	729.1471[M-H] <sup>-</sup>	a
16	4.88	Rutin	610.1534	C <sub>27</sub> H <sub>30</sub> O <sub>16</sub>	610.1555	609.1483	3.6	577.1350[M-H-gallate] <sup>-</sup>	a,d
17	5.09	Rhein-1-O-β-D-glc	446.0849	C <sub>21</sub> H <sub>18</sub> O <sub>11</sub>	446.0860	445.0787	2.4	342.1701[M] <sup>+</sup>	a
18	5.11	Isolindleyin or lindleyin	478.1475	C <sub>23</sub> H <sub>26</sub> O <sub>11</sub>	478.1483	477.1410	1.7	297.1123[M-(CH <sub>3</sub> ) <sub>2</sub> NH] <sup>+</sup>	d
19	5.14	(+)-Catechin-3-O-gallate	442.0900	C <sub>22</sub> H <sub>18</sub> O <sub>10</sub>	442.0910	441.0838	2.4	282.0876[M-(CH <sub>3</sub> ) <sub>2</sub> NH-CH <sub>3</sub> ] <sup>+</sup>	a
								265.0861[M-(CH <sub>3</sub> ) <sub>2</sub> NH-CH <sub>3</sub> OH] <sup>+</sup>	
								237.0908[M-(CH <sub>3</sub> ) <sub>2</sub> NH-CH <sub>3</sub> OH-CO] <sup>+</sup>	
								328.1552[M+H] <sup>+</sup>	
								297.1123[M+H-CH <sub>3</sub> O] <sup>+</sup>	
								477.1047[M+HCOO] <sup>-</sup>	
								431.0982[M-H] <sup>-</sup>	
								311.0567[M-H-CO <sub>2</sub> -C <sub>3</sub> H <sub>8</sub> O <sub>2</sub> ] <sup>-</sup>	
								322.1052[M] <sup>+</sup>	
								307.0839[M-CH <sub>3</sub> ] <sup>+</sup>	
								279.0511[M-CH <sub>3</sub> -CO] <sup>+</sup>	
								881.1612[M-H] <sup>-</sup>	
								729.1471[M-H-gallate] <sup>-</sup>	
								711.0735[M-H-gallate-H <sub>2</sub> O] <sup>-</sup>	
								559.1341[M-H-2gallate-H <sub>2</sub> O] <sup>-</sup>	
								431.0992[M-H] <sup>-</sup>	
								269.0461[M-H-Glc] <sup>-</sup>	
								241.0493[M-H-Glc-CO] <sup>-</sup>	
								225.0554[M-H-Glc-CO-O] <sup>-</sup>	
								609.1483[M-H] <sup>-</sup>	
								463.0815[M-H-Rha] <sup>-</sup>	
								301.0487[M-H-Rha-Glc] <sup>-</sup>	
								445.0787[M-H] <sup>-</sup>	
								283.0256[M-H-Glc] <sup>-</sup>	
								239.0356[M-H-Glc-CO <sub>2</sub> ] <sup>-</sup>	
								211.0403[M-H-Glc-CO <sub>2</sub> -CO] <sup>-</sup>	
								477.1410[M-H] <sup>-</sup>	
								313.0552[M-H-C <sub>10</sub> H <sub>12</sub> O <sub>2</sub> ] <sup>-</sup>	
								169.0145[M-H-C <sub>16</sub> H <sub>20</sub> O <sub>6</sub> ] <sup>-</sup>	
								441.0838[M-H] <sup>-</sup>	
								289.0722[M-H-C <sub>7</sub> H <sub>4</sub> O <sub>4</sub> ] <sup>-</sup>	
								165.1245[M-H-C <sub>14</sub> H <sub>12</sub> O <sub>6</sub> ] <sup>-</sup>	

20	5.20	Ferulic acid- <i>O</i> - $\beta$ -D-glc	356.1107	C <sub>16</sub> H <sub>20</sub> O <sub>9</sub>	356.1113	355.1040	1.5	355.1040[M-H] <sup>-</sup>	d
21	5.25	Isoquercitrin	464.0955	C <sub>21</sub> H <sub>20</sub> O <sub>12</sub>	464.0972	463.0899	3.7	193.1033[M-H-Glc] <sup>-</sup> 463.0899[M-H] <sup>-</sup>	d
22	5.45	Isolindleyin or lindleyin	478.1475	C <sub>23</sub> H <sub>26</sub> O <sub>11</sub>	478.1482	477.1408	1.6	301.0038[M-H-C <sub>6</sub> H <sub>10</sub> O <sub>5</sub> ] <sup>-</sup> 477.1408[M-H] <sup>-</sup>	a
23	5.61	Kaempferol-3- <i>O</i> -rutinoside	594.1585	C <sub>27</sub> H <sub>30</sub> O <sub>15</sub>	594.1599	593.1521	1.6	313.0551[M-H-C <sub>10</sub> H <sub>12</sub> O <sub>2</sub> ] <sup>-</sup> 169.0144[M-H-C <sub>16</sub> H <sub>20</sub> O <sub>6</sub> ] <sup>-</sup> 593.1521[M-H] <sup>-</sup>	d
24	5.65	Resveratrol-4'- <i>O</i> - $\beta$ -D-(2''- <i>O</i> -galloyl)-glc	542.1424	C <sub>27</sub> H <sub>26</sub> O <sub>12</sub>	542.1431	541.1333	1.2	447.1591[M-H-Rha] <sup>-</sup> 285.0832[M-H-Rha-Glc] <sup>-</sup>	a
25	5.70	Senoside C or D	848.2164	C <sub>42</sub> H <sub>40</sub> O <sub>19</sub>	848.2177	847.2104	1.5	541.1333[M-H] <sup>-</sup> 313.0555[M-H-Res-H <sub>2</sub> O] <sup>-</sup>	a
26	5.89	Tetrahydropalmatine	355.1784	C <sub>21</sub> H <sub>25</sub> NO <sub>4</sub>	355.1792	356.1865	2.4	847.2104[M-H] <sup>-</sup> 685.1557[M-H-Glc] <sup>-</sup>	b
27	6.24	Senoside A or B	862.1956	C <sub>42</sub> H <sub>38</sub> O <sub>20</sub>	862.1981	861.1908	2.8	356.1865[M+H] <sup>+</sup> 192.1019[M+H-C <sub>10</sub> H <sub>12</sub> O <sub>2</sub> ] <sup>+</sup> 861.1908[M-H] <sup>-</sup>	a
28	6.36	Homoorientin	448.1006	C <sub>21</sub> H <sub>20</sub> O <sub>11</sub>	448.1000	447.0927	-1.2	699.1358[M-H-Glc] <sup>-</sup> 655.1880[M-H-Glc-CO <sub>2</sub> ] <sup>-</sup> 386.1002[M-H-Glc-CO <sub>2</sub> -C <sub>15</sub> H <sub>9</sub> O <sub>5</sub> ] <sup>-</sup>	d
29	6.52	Thalifendine	322.1079	C <sub>19</sub> H <sub>16</sub> NO <sub>4</sub>	322.1069	322.1082	-0.4	447.0927[M-H] <sup>-</sup> 322.1082[M] <sup>+</sup>	b
30	6.94	Hesperetin-5- <i>O</i> -glc	464.1319	C <sub>22</sub> H <sub>24</sub> O <sub>11</sub>	464.1313	463.1240	1.5	279.0889[M-CH <sub>3</sub> -CO] <sup>+</sup> 463.1240[M-H] <sup>-</sup>	d
31	7.01	Coptisine	320.0923	C <sub>19</sub> H <sub>14</sub> NO <sub>4</sub>	320.0921	320.0921	0.6	301.1131[M-H-Glc] <sup>-</sup> 320.0921[M] <sup>+</sup>	b
32	7.08	Rhein-8- <i>O</i> - $\beta$ -D-(6''- <i>O</i> -acetyl)-glc	488.0955	C <sub>23</sub> H <sub>20</sub> O <sub>12</sub>	488.0949	487.0876	1.5	292.0970[M-CO] <sup>+</sup> 487.0876[M-H] <sup>-</sup>	a
33	7.15	Jatrorrhizine	338.1392	C <sub>20</sub> H <sub>20</sub> NO <sub>4</sub>	338.1384	338.1384	2.4	283.0246[M-H-acetyl-Glc] <sup>-</sup> 239.0347[M-H-acetyl-Glc-CO <sub>2</sub> ] <sup>-</sup>	b
34	7.35	Epiberberine	336.1236	C <sub>20</sub> H <sub>18</sub> NO <sub>4</sub>	336.1250	336.1250	-4.2	338.1384[M] <sup>+</sup> 322.0997[M-CH <sub>3</sub> -H] <sup>+</sup> 308.1309[M-2CH <sub>3</sub> ] <sup>+</sup> 336.1250[M] <sup>+</sup>	b
35	7.47	Aloe emodin-8- <i>O</i> - $\beta$ -D-glc	432.1056	C <sub>21</sub> H <sub>20</sub> O <sub>10</sub>	432.1068	431.0992	0.8	320.0935[M-CH <sub>3</sub> -H] <sup>+</sup> 292.1314[M-CH <sub>3</sub> -H-CO] <sup>+</sup> 431.0992[M-H] <sup>-</sup>	a
36	7.48	Tetrahydroberberine	339.1471	C <sub>20</sub> H <sub>21</sub> NO <sub>4</sub>	339.1466	340.1544	-1.4	269.0385[M-H-Glc] <sup>-</sup> 225.0562[M-H-Glc-CO <sub>2</sub> ] <sup>-</sup>	b
37 <sup>s</sup>	7.72	Notoginsenoside R <sub>1</sub>	932.5345	C <sub>47</sub> H <sub>80</sub> O <sub>18</sub>	932.5372	977.5354	2.8	340.1544[M+H] <sup>+</sup> 176.0705[M+H-C <sub>10</sub> H <sub>12</sub> O <sub>2</sub> ] <sup>+</sup> 977.5354[M+HCOO] <sup>-</sup>	f
38	8.09	Worenine	334.1079	C <sub>20</sub> H <sub>16</sub> NO <sub>4</sub>	334.1080	334.1080	-0.3	931.5297[M-H] <sup>-</sup> 799.4856[M-H-Xyl] <sup>-</sup> 637.4314[M-H-Xyl-Glc] <sup>-</sup> 475.3782[M-H-Xyl-2Glc] <sup>-</sup>	b
39 <sup>s</sup>	8.46	Berberine	336.1236	C <sub>20</sub> H <sub>18</sub> NO <sub>4</sub>	336.1230	336.1231	1.8	334.1080[M] <sup>+</sup> 320.1093[M-CH <sub>2</sub> ] <sup>+</sup> 318.1092[M-CH <sub>2</sub> -2H] <sup>+</sup> 292.0969[M-CH <sub>2</sub> -CO] <sup>+</sup>	b
40	8.51	Palmatine	352.1549	C <sub>21</sub> H <sub>22</sub> NO <sub>4</sub>	352.1543	352.1538	-1.7	336.1231[M] <sup>+</sup> 321.0983[M-CH <sub>3</sub> ] <sup>+</sup> 320.0918[M-CH <sub>3</sub> -H] <sup>+</sup> 306.0763[M-2CH <sub>3</sub> ] <sup>+</sup> 292.0969[M-CH <sub>3</sub> -H-CO] <sup>+</sup> 278.0813[M-2CH <sub>3</sub> -CO] <sup>+</sup>	b
								352.1538[M] <sup>+</sup> 337.1430[M-CH <sub>3</sub> ] <sup>+</sup> 336.0983[M-CH <sub>3</sub> -H] <sup>+</sup> 322.1068 [M-2CH <sub>3</sub> ] <sup>+</sup> 308.1275 [M-CH <sub>3</sub> -H-CO] <sup>+</sup>	

Table 1 (continued)

No.	t <sub>R</sub> (min)	Identification	Neutral mass (Da)	Formular	Observed neutral mass (Da)	Experimental mass (m/z)	Error (ppm)	MS and MS <sup>E</sup> data (+ or -) (m/z)	Source
41	8.53	Ginsenoside Rg <sub>1</sub>	800.4922	C <sub>42</sub> H <sub>72</sub> O <sub>14</sub>	800.4939	845.4921	2.0	845.4921[M+HCOO] <sup>-</sup> 799.4863[M-H] <sup>-</sup> 637.4321[M-H-Glc] <sup>-</sup> 475.3784[M-H-2Glc] <sup>-</sup>	f
42	9.23	Kaempferol	286.0477	C <sub>15</sub> H <sub>10</sub> O <sub>6</sub>	286.0479	285.0406	0.7	285.0406[M-H] <sup>-</sup> 229.0451[M-H-C <sub>2</sub> O <sub>2</sub> ] <sup>-</sup> 169.0141[M-H-C <sub>3</sub> O <sub>5</sub> ] <sup>-</sup>	a,d
43 <sup>g</sup>	9.46	Quercetin	302.0427	C <sub>15</sub> H <sub>10</sub> O <sub>7</sub>	302.0432	301.0360	2.0	301.0360[M-H] <sup>-</sup> 151.0451[M-H-C <sub>8</sub> H <sub>6</sub> O <sub>3</sub> ] <sup>-</sup> 121.0431[M-H-C <sub>8</sub> H <sub>6</sub> O <sub>3</sub> -CH <sub>2</sub> O] <sup>-</sup> 107.0162[M-H-C <sub>8</sub> H <sub>6</sub> O <sub>3</sub> -CH <sub>2</sub> O-CH <sub>2</sub> ] <sup>-</sup>	d
44	9.61	Aloin	418.1264	C <sub>21</sub> H <sub>22</sub> O <sub>9</sub>	418.1267	417.1195	0.8	417.1195[M-H] <sup>-</sup> 255.0666[M-H-Glc] <sup>-</sup> 227.0718[M-H-Glc-CO] <sup>-</sup>	a
45	9.76	Aloe emodin-1-O-β-D-glc	432.1056	C <sub>21</sub> H <sub>20</sub> O <sub>10</sub>	432.1068	431.0995	2.7	431.0995[M-H] <sup>-</sup> 269.0452[M-H-Glc] <sup>-</sup> 225.0562[M-H-Glc-CO <sub>2</sub> ] <sup>-</sup>	a
46	9.91	Aloe emodin-ω-O-β-D-glc	432.1056	C <sub>21</sub> H <sub>20</sub> O <sub>10</sub>	432.1068	431.0995	2.7	431.0995[M-H] <sup>-</sup> 269.0463[M-H-Glc] <sup>-</sup> 225.0560[M-H-Glc-CO <sub>2</sub> ] <sup>-</sup>	a
47	10.09	Chrysophanol-1-O-β-D-glc	416.1107	C <sub>21</sub> H <sub>20</sub> O <sub>9</sub>	416.1118	415.1045	2.6	415.1045[M-H] <sup>-</sup> 253.0515[M-H-Glc] <sup>-</sup> 225.0563[M-H-Glc-CO] <sup>-</sup>	a
48	10.91	Aloe emodin-8-(6"-O-malonyl)-glc	518.1060	C <sub>24</sub> H <sub>22</sub> O <sub>13</sub>	518.1076	517.1003	3.1	517.1003[M-H] <sup>-</sup> 473.1097[M-H-CO <sub>2</sub> ] <sup>-</sup> 269.0463[M-H-malonyl-Glc] <sup>-</sup>	a
49	10.95	Calebin-A	384.1209	C <sub>21</sub> H <sub>20</sub> O <sub>7</sub>	384.1211	429.1193	0.5	429.1193[M+HCOO] <sup>-</sup>	c
50	11.16	Naringenin	272.0685	C <sub>15</sub> H <sub>12</sub> O <sub>5</sub>	272.0689	271.0616	1.5	271.0616[M-H] <sup>-</sup> 151.0665[M-H-C <sub>8</sub> H <sub>8</sub> O] <sup>-</sup>	d
51	11.25	Aloe emodin-8-O-β-D-(6"-O-acetyl)-glc	474.1162	C <sub>23</sub> H <sub>22</sub> O <sub>11</sub>	474.1169	473.1096	1.5	473.1096[M-H] <sup>-</sup> 269.0451[M-H-acetyl-Glc] <sup>-</sup> 240.0410[M-H-acetyl-Glc-CHO] <sup>-</sup>	a
52	11.77	Physcion-8-O-β-D-glc	446.1213	C <sub>22</sub> H <sub>22</sub> O <sub>10</sub>	446.1219	445.1146	1.3	445.1146[M-H] <sup>-</sup> 283.0617[M-H-Glc] <sup>-</sup> 240.0433[M-H-Glc-CO-CH <sub>3</sub> ] <sup>-</sup>	a
53	11.85	Chrysophanol-8-O-β-D-(6"-O-acetyl)-glc	458.1213	C <sub>23</sub> H <sub>22</sub> O <sub>10</sub>	458.1221	457.1148	1.8	457.1148[M-H] <sup>-</sup> 253.0511[M-H-acetyl-Glc] <sup>-</sup> 225.0561[M-H-acetyl-Glc-CO] <sup>-</sup>	a
54	12.18	Notoginsenoside R <sub>2</sub>	770.4816	C <sub>41</sub> H <sub>70</sub> O <sub>13</sub>	770.4843	815.4825	3.3	815.4825[M+HCOO] <sup>-</sup> 769.4768[M-H] <sup>-</sup> 637.4335[M-H-Xyl] <sup>-</sup> 475.3786[M-H-Xyl-Glc] <sup>-</sup>	f
55	12.53	Ginsenoside Rb <sub>1</sub>	1108.6029	C <sub>54</sub> H <sub>92</sub> O <sub>23</sub>	1108.6105	1107.5967	6.6	1107.5967[M-H] <sup>-</sup> 945.5469[M-H-Glc] <sup>-</sup> 783.4917[M-H-2Glc] <sup>-</sup> 621.4361[M-H-3Glc] <sup>-</sup> 459.3824[M-H-4Glc] <sup>-</sup>	f
56	12.69	Cyclocurcumin	368.1260	C <sub>21</sub> H <sub>20</sub> O <sub>6</sub>	368.1258	367.1186	-0.4	367.1186[M-H] <sup>-</sup> 175.0401[M-H-C <sub>11</sub> H <sub>12</sub> O <sub>3</sub> ] <sup>-</sup>	c
57	12.74	Ginsenoside Rg <sub>2</sub>	784.4973	C <sub>42</sub> H <sub>72</sub> O <sub>13</sub>	784.4999	829.4982	3.2	829.4982[M+HCOO] <sup>-</sup> 783.4922[M-H] <sup>-</sup> 637.4326[M-H-Rha] <sup>-</sup> 475.3789[M-H-Rha-Glc] <sup>-</sup>	f

58	12.94	Ginsenoside Rh <sub>1</sub>	638.4394	C <sub>36</sub> H <sub>62</sub> O <sub>9</sub>	638.4414	683.4382	2.9	683.4382[M+HCOO] <sup>-</sup> 637.4321[M-H] <sup>-</sup>	f
59	13.18	6-Methyl-rhein	298.0477	C <sub>16</sub> H <sub>10</sub> O <sub>6</sub>	298.0481	297.0408	1.1	475.3784[M-H-Glc] <sup>-</sup> 297.0408[M-H] <sup>-</sup>	a
60	13.21	Physcion-8-O-β-D-(6"-O-acetyl)-glc	488.1319	C <sub>24</sub> H <sub>24</sub> O <sub>11</sub>	488.1323	487.1250	0.8	283.0251[M-H-CH <sub>2</sub> ] <sup>-</sup> 239.0358[M-H-CH <sub>2</sub> -CO <sub>2</sub> ] <sup>-</sup> 487.1250[M-H] <sup>-</sup>	a
61	13.51	Orientalol A	254.1882	C <sub>15</sub> H <sub>26</sub> O <sub>3</sub>	254.1907	299.1889	8.3	283.0615[M-H-acetyl-Glc] <sup>-</sup> 255.0317[M-H-acetyl-Glc-CO] <sup>-</sup> 240.0432[M-H-acetyl-Glc-CO-CH <sub>3</sub> ] <sup>-</sup>	c
62	14.13	16-Oxo-alisol A	504.3451	C <sub>30</sub> H <sub>48</sub> O <sub>6</sub>	504.3474	505.3223	4.3	299.1889[M+HCOO] <sup>-</sup> 253.1905[M-H] <sup>-</sup>	e
63	14.41	Ginsenoside Rd	946.5501	C <sub>48</sub> H <sub>82</sub> O <sub>18</sub>	946.5581	991.5563	8.0	505.3223[M+H] <sup>+</sup> 487.3327[M+H-H <sub>2</sub> O] <sup>+</sup> 469.3285[M+H-2H <sub>2</sub> O] <sup>+</sup> 451.3318[M+H-3H <sub>2</sub> O] <sup>+</sup> 415.2824[M+H-C <sub>4</sub> H <sub>10</sub> O <sub>2</sub> ] <sup>+</sup> 397.2783[M+H-C <sub>4</sub> H <sub>10</sub> O <sub>2</sub> -H <sub>2</sub> O] <sup>+</sup>	f
64 <sup>s</sup>	14.52	Aloe emodin	270.0528	C <sub>15</sub> H <sub>10</sub> O <sub>5</sub>	270.0536	269.0462	3.0	991.5563[M+HCOO] <sup>-</sup> 945.5563[M-H] <sup>-</sup> 783.4939[M-H-Glc] <sup>-</sup> 621.4398[M-H-2Glc] <sup>-</sup> 459.3851[M-H-3Glc] <sup>-</sup>	a
65 <sup>s</sup>	15.30	Rhein	284.0321	C <sub>15</sub> H <sub>8</sub> O <sub>6</sub>	284.0332	283.0256	4.0	269.0462[M-H] <sup>-</sup> 240.0421[M-H-CHO] <sup>-</sup> 211.0410[M-H-2CHO] <sup>-</sup>	a
66	16.01	Notoginsenoside R <sub>3</sub>	962.5450	C <sub>48</sub> H <sub>82</sub> O <sub>19</sub>	962.5491	961.5418	4.2	283.0256[M-H] <sup>-</sup> 239.0356[M-H-CO <sub>2</sub> ] <sup>-</sup> 211.0403[M-H-CO <sub>2</sub> -CO] <sup>-</sup> 183.0439[M-H-CO <sub>2</sub> -CO-CO] <sup>-</sup>	f
67	16.70	8-Oxoberberine	351.1107	C <sub>20</sub> H <sub>17</sub> NO <sub>5</sub>	351.1108	352.1181	0.4	961.5418[M-H] <sup>-</sup> 799.4889[M-H-Glc] <sup>-</sup> 637.4360[M-H-2Glc] <sup>-</sup> 475.3817[M-H-3Glc] <sup>-</sup>	b
68	16.72	Alisol I	454.3447	C <sub>30</sub> H <sub>46</sub> O <sub>3</sub>	454.3460	455.3526	2.6	352.1181[M+H] <sup>+</sup> 337.0948[M+H-CH <sub>3</sub> ] <sup>+</sup> 294.0764[M+H-2CH <sub>3</sub> -CO] <sup>+</sup>	e
69	17.05	Alisol C	486.3345	C <sub>30</sub> H <sub>46</sub> O <sub>5</sub>	486.3368	487.3418	4.2	455.3526[M+H] <sup>+</sup> 383.2943[M+H-C <sub>4</sub> H <sub>8</sub> O] <sup>+</sup>	e
70	17.24	Ar-turmerone	216.1514	C <sub>15</sub> H <sub>20</sub> O	216.1516	217.1588	0.7	487.3418[M+H] <sup>+</sup> 469.3265[M+H-H <sub>2</sub> O] <sup>+</sup> 451.3215[M+H-2H <sub>2</sub> O] <sup>+</sup> 415.2841[M+H-C <sub>4</sub> H <sub>8</sub> O] <sup>+</sup> 397.2746[M+H-C <sub>4</sub> H <sub>10</sub> O <sub>2</sub> ] <sup>+</sup>	c
71 <sup>s</sup>	17.34	Kaempferide	300.0634	C <sub>16</sub> H <sub>12</sub> O <sub>6</sub>	300.0628	299.0553	-2.1	217.1588[M+H] <sup>+</sup> 120.0935[M+H-C <sub>6</sub> H <sub>9</sub> O] <sup>+</sup> 92.06212[M+H-C <sub>8</sub> H <sub>13</sub> O] <sup>+</sup>	d
72	17.46	Bisdemethoxycurcumin	308.1049	C <sub>19</sub> H <sub>16</sub> O <sub>4</sub>	308.1058	307.0984	2.9	299.0553[M-H] <sup>-</sup> 284.0489[M-H-CH <sub>3</sub> ] <sup>-</sup>	c
73	17.93	Demethoxycurcumin	338.1154	C <sub>20</sub> H <sub>18</sub> O <sub>5</sub>	338.1161	337.1088	2.0	307.0984[M-H] <sup>-</sup> 187.0406[M-H-C <sub>8</sub> H <sub>8</sub> O] <sup>-</sup>	c
74 <sup>s</sup>	18.38	Curcumin	368.1260	C <sub>21</sub> H <sub>20</sub> O <sub>6</sub>	368.1260	367.1192	-0.1	337.1088[M-H] <sup>-</sup> 217.0508[M-H-C <sub>8</sub> H <sub>8</sub> O] <sup>-</sup>	c
75	18.94	Alisol M 23-acetate	488.3502	C <sub>30</sub> H <sub>48</sub> O <sub>5</sub>	488.3497	489.3480	-0.8	367.1192[M-H] <sup>-</sup> 217.0524[M-H-C <sub>9</sub> H <sub>10</sub> O <sub>2</sub> ] <sup>-</sup>	e
								489.3480[M+H] <sup>+</sup> 471.2696[M+H-H <sub>2</sub> O] <sup>+</sup>	

(continued on next page)

Table 1 (continued)

No.	t <sub>R</sub> (min)	Identification	Neutral mass (Da)	Formular	Observed neutral mass (Da)	Experimental mass (m/z)	Error (ppm)	MS and MS <sup>E</sup> data (+ or -) (m/z)	Source
76 <sup>§</sup>	19.25	Emodin	270.0528	C <sub>15</sub> H <sub>10</sub> O <sub>5</sub>	270.0533	269.0460	1.7	269.0460[M-H] <sup>-</sup> 241.0507[M-H-CO] <sup>-</sup> 225.0559[M-H-CO-O] <sup>-</sup>	a
77	19.54	Bisabolone oxide A	236.1776	C <sub>15</sub> H <sub>24</sub> O <sub>2</sub>	236.1776	237.1850	0.5	237.1850[M+H] <sup>+</sup>	c
78	19.65	Alisol C 23-acetate	528.3451	C <sub>32</sub> H <sub>48</sub> O <sub>6</sub>	528.3453	529.3535	1.0	529.3535[M+H] <sup>+</sup> 511.3415[M+H-H <sub>2</sub> O] <sup>+</sup> 469.3456[M+H-HAc] <sup>+</sup>	e
79	19.71	Alisol F	488.3502	C <sub>30</sub> H <sub>48</sub> O <sub>5</sub>	488.3497	511.3391	-1.4	511.3391[M+Na] <sup>+</sup> 471.2696[M+H-H <sub>2</sub> O] <sup>+</sup> 453.2687[M+H-2H <sub>2</sub> O] <sup>+</sup> 399.3129[M+H-C <sub>4</sub> H <sub>10</sub> O <sub>2</sub> ] <sup>+</sup> 381.3091[M+H-C <sub>4</sub> H <sub>10</sub> O <sub>2</sub> -H <sub>2</sub> O] <sup>+</sup>	e
80	20.04	Alisol L 23-acetate	510.3345	C <sub>32</sub> H <sub>46</sub> O <sub>5</sub>	510.3350	511.3418	1.0	511.3418[M+H] <sup>+</sup> 451.3201[M+H-HAc] <sup>+</sup> 397.2739[M+H-C <sub>6</sub> H <sub>10</sub> O <sub>2</sub> ] <sup>+</sup>	e
81	20.59	Procyanidin	594.1373	C <sub>30</sub> H <sub>26</sub> O <sub>13</sub>	594.1382	593.1309	0.8	593.1309[M-H] <sup>-</sup>	a
82	21.39	Neolisol A	488.3502	C <sub>30</sub> H <sub>48</sub> O <sub>5</sub>	488.3505	489.3572	2.5	489.3572[M+H] <sup>+</sup> 471.3571[M+H-H <sub>2</sub> O] <sup>+</sup>	e
83 <sup>§</sup>	21.71	Chrysophanol	254.0579	C <sub>15</sub> H <sub>10</sub> O <sub>4</sub>	254.0579	253.0515	3.3	253.0515[M-H] <sup>-</sup> 225.0545[M-H-CO] <sup>-</sup>	a
84	21.72	16,23-Oxido alisol B	470.3396	C <sub>30</sub> H <sub>46</sub> O <sub>4</sub>	470.3395	493.3287	-0.2	493.3287[M+Na] <sup>+</sup> 453.3362[M+H-H <sub>2</sub> O] <sup>+</sup> 339.2686[M+H-C <sub>6</sub> H <sub>10</sub> O <sub>2</sub> -H <sub>2</sub> O] <sup>+</sup>	e
85	22.56	Gingerdione	292.1675	C <sub>17</sub> H <sub>24</sub> O <sub>4</sub>	292.1679	337.1661	1.4	337.1661[M+HCOO] <sup>-</sup> 291.1629[M-H] <sup>-</sup>	c
86 <sup>§</sup>	22.80	Physcion	284.0685	C <sub>16</sub> H <sub>12</sub> O <sub>5</sub>	284.0692	283.0619	2.5	283.0619[M-H] <sup>-</sup> 255.0315[M-H-CO] <sup>-</sup> 240.0359[M-H-CO-CH <sub>3</sub> ] <sup>-</sup>	a
87	22.90	Alisol A 23-acetate	532.3764	C <sub>32</sub> H <sub>52</sub> O <sub>6</sub>	532.3767	555.3749	0.6	555.3749[M+Na] <sup>+</sup> 515.3516[M+H-H <sub>2</sub> O] <sup>+</sup> 383.2797[M+H-C <sub>6</sub> H <sub>12</sub> O <sub>3</sub> -H <sub>2</sub> O] <sup>+</sup>	e
88	23.05	11-Deoxy-alisol C	470.3396	C <sub>30</sub> H <sub>46</sub> O <sub>4</sub>	470.3398	471.3380	0.3	471.3380[M+H] <sup>+</sup> 453.3515[M+H-H <sub>2</sub> O] <sup>+</sup> 399.2874[M+H-C <sub>4</sub> H <sub>8</sub> O] <sup>+</sup>	e
89	23.32	Stearic acid	284.2715	C <sub>18</sub> H <sub>36</sub> O <sub>2</sub>	284.2717	283.2645	0.7	283.2645[M-H] <sup>-</sup>	d
90	23.54	Alisol A	490.3658	C <sub>30</sub> H <sub>50</sub> O <sub>5</sub>	490.3678	491.3661	3.8	491.3661[M+H] <sup>+</sup> 473.3515[M+H-H <sub>2</sub> O] <sup>+</sup> 455.3621[M+H-2H <sub>2</sub> O] <sup>+</sup> 437.3415[M+H-3H <sub>2</sub> O] <sup>+</sup> 383.2973[M+H-H <sub>2</sub> O-C <sub>4</sub> H <sub>10</sub> O <sub>2</sub> ] <sup>+</sup>	e
91	23.79	Alisol B	472.3553	C <sub>30</sub> H <sub>48</sub> O <sub>4</sub>	472.3558	473.3622	-0.7	473.3622[M+H] <sup>+</sup> 455.3515[M+H-H <sub>2</sub> O] <sup>+</sup> 437.3521[M+H-2H <sub>2</sub> O] <sup>+</sup> 383.2943[M+H-H <sub>2</sub> O-C <sub>4</sub> H <sub>8</sub> O] <sup>+</sup>	e
92	23.93	Alisol L	468.3240	C <sub>30</sub> H <sub>44</sub> O <sub>4</sub>	468.3238	469.3310	-0.4	469.3310[M+H] <sup>+</sup> 451.3188[M+H-H <sub>2</sub> O] <sup>+</sup> 397.2745[M+H-C <sub>4</sub> H <sub>8</sub> O] <sup>+</sup>	e
93	24.47	Alisol O	512.3502	C <sub>32</sub> H <sub>48</sub> O <sub>5</sub>	512.3492	513.3581	0.3	513.3581[M+H] <sup>+</sup> 495.3475[M+H-H <sub>2</sub> O] <sup>+</sup> 453.3413[M+H-HAc] <sup>+</sup> 435.3628[M+H-HAc-H <sub>2</sub> O] <sup>+</sup>	e
94	24.65	Linolenic acid	278.2246	C <sub>18</sub> H <sub>30</sub> O <sub>2</sub>	278.2245	277.2164	-1.4	277.2164[M-H] <sup>-</sup>	a,d
95	25.28	Alisol A 24-acetate	532.3764	C <sub>32</sub> H <sub>52</sub> O <sub>6</sub>	532.3761	555.3748	1.5	555.3748[M+Na] <sup>+</sup> 515.3516[M+H-H <sub>2</sub> O] <sup>+</sup> 497.3472[M+H-2H <sub>2</sub> O] <sup>+</sup> 383.2797[M+H-C <sub>6</sub> H <sub>12</sub> O <sub>3</sub> -H <sub>2</sub> O] <sup>+</sup>	e

96 <sup>g</sup>	25.38	Alisol B 23-acetate	514.3658	C <sub>32</sub> H <sub>50</sub> O <sub>5</sub>	514.3661	537.3554	0.5	537.3554[M+Na] <sup>+</sup> 515.3735[M+H] <sup>+</sup> 497.3629[M+H-H <sub>2</sub> O] <sup>+</sup> 479.3508[M+H-2H <sub>2</sub> O] <sup>+</sup> 437.3415[M+H-H <sub>2</sub> O-HAc] <sup>+</sup> 383.2688[M+H-C <sub>6</sub> H <sub>12</sub> O <sub>3</sub> ] <sup>+</sup>	e
-----------------	-------	---------------------	----------	--	----------	----------	-----	--	---

Glc: glucose; Rha: rhamnose; Xyl: xylose; Res: resveratrol.

<sup>a</sup> *Rheum palmatum* L.

<sup>b</sup> *Coptis chinensis* Franch.

<sup>c</sup> *Curcuma longa* L.

<sup>d</sup> *Lysimachia christinae* Hance.

<sup>e</sup> *Alisma orientale* (Sam.) Juzep.

<sup>f</sup> *Panax notoginseng* (Burk.) F. H. Chen.

<sup>g</sup> Identified by comparison with reference standards.

terminal chain, such as -CH<sub>3</sub>. Peak 26 gave a protonated ion at  $m/z$  356.1865. The fragment ions at  $m/z$  192.1019 and 165.0893 were attributed to RDA cleavage at C- and B-rings. By further loss of a methyl radical, two obtained ions generated characteristic ions at  $m/z$  177.0774 and 150.0663, respectively. Therefore, peak 26 was tentatively identified as tetrahydropalmatine.

### 3.2.3. Protostane triterpenoids

17 protostane triterpenoids in GDD originated from *Alisma orientale* (Sam.) Juzep. Protostane triterpenoids showed [M+H]<sup>+</sup> ion, adduct [M+Na]<sup>+</sup> ion in positive ion mode and all possess a tetracyclic carbon skeleton. During the collision-induced dissociation (CID) process, the hydrogen rearrangement at C-23-OH resulting in C-23–C-24 bond dissociation was proposed as a characteristic CID fragmentation pathway, which can be used to further distinguish certain positional isomers containing the acetyl unit at the C-23 or C-24 position [23,24]. Such compounds usually occurred successive losses of H<sub>2</sub>O, acetic acid group (HAc, 60 Da) and other complex groups such as C<sub>4</sub>H<sub>8</sub>O (72 Da), C<sub>4</sub>H<sub>10</sub>O<sub>2</sub> (90 Da) and C<sub>6</sub>H<sub>12</sub>O<sub>3</sub> (132 Da). Peaks 96 was exactly identified as alisol B 23-acetate based on retention time and fragment behavior of reference standard. The high energy MS<sup>E</sup> spectra and the proposed fragment pathway of alisol B 23-acetate are depicted in Fig. 5. Alisol B 23-acetate showed [M+H]<sup>+</sup> and [M+Na]<sup>+</sup> ions at  $m/z$  515.3735 and 537.3554, which underwent several dehydrations or deacetylations to form fragment ions at  $m/z$  497.3629 [M + H-H<sub>2</sub>O]<sup>+</sup>, 479.3508 [M + H-2H<sub>2</sub>O]<sup>+</sup>, and 437.3415 [M + H-H<sub>2</sub>O-HAc]<sup>+</sup>, and then dissociation of the C-23–C-24 bond and loss of H<sub>2</sub>O gave rise to [M + H-C<sub>6</sub>H<sub>12</sub>O<sub>3</sub>]<sup>+</sup> ion at  $m/z$  383.2688. Peaks 87, 91, and 95 showed the similar fragmentation behavior to alisol B 23-acetate, and were identified as alisol A 23-acetate, alisol B, and alisol A 24-acetate, respectively.

Peak 92 had a protonated ion [M+H]<sup>+</sup> at  $m/z$  469.3310 with a molecular formula of C<sub>30</sub>H<sub>44</sub>O<sub>4</sub>, and formed characteristic ions at 451.3188 [M + H-H<sub>2</sub>O]<sup>+</sup> and  $m/z$  397.2745 [M + H-C<sub>4</sub>H<sub>8</sub>O]<sup>+</sup> through 23-OH dehydration and C-23–C-24 dissociation. Thus, it was assigned as Alisol L. Owing to similar cleavage patterns by loss of C<sub>4</sub>H<sub>8</sub>O, peaks 69 and 88 were deduced to be alisol C and 11-deoxy- Alisol C, respectively. Peak 62 exhibited [M+H]<sup>+</sup> ion at  $m/z$  505.3223. Three typical dehydration ions at  $m/z$  487.3327, 469.3285 and 451.3318 were generated from the hydroxyl groups. The dissociation of the C-23–C-24 bond via hydrogen rearrangement at C-23-OH produced diagnostic ion at  $m/z$  415.2824 [M + H-C<sub>4</sub>H<sub>10</sub>O<sub>2</sub>]<sup>+</sup>, with further loss of H<sub>2</sub>O generating an ion at  $m/z$  397.2783 [M + H-C<sub>4</sub>H<sub>10</sub>O<sub>2</sub>-H<sub>2</sub>O]<sup>+</sup>, so peak 62 was tentatively identified as 16-oxo- alisol A. Peak 90, 14Da less than that of 16-oxo- alisol A and similar to 16-oxo- alisol A, was further confirmed as alisol A.

### 3.2.4. Flavonoids

Ten flavones and their glycosides have been screened and identified in GDD using the UNIFI workflow. It is well known that the main MS behavior of flavone aglycones was RDA fragmentation pathway and losses of small molecules and/or radicals like CH<sub>3</sub>, CO and CO<sub>2</sub> [25]. For flavones glycosides, the cleavage at glycosidic linkages could happen in both positive and negative ion modes, and 162 Da (Glc), 146 Da (Rha) and 308 Da (rutinoside) were the characteristic neutral loss of flavonoid-O-glycosides. The fragment ions with low  $m/z$  were the same as that of their aglycones. Among them, peaks 43 and 71 were ascertained to be quercetin and kaempferide by contrast with reference standards. Here we took quercetin and kaempferide as examples to describe the fragment patterns of these components. Quercetin displayed a deprotonated ion at  $m/z$  301.0360 with a molecular formula of C<sub>15</sub>H<sub>10</sub>O<sub>7</sub>, and the ions at  $m/z$  151.0451 [M-H-C<sub>8</sub>H<sub>6</sub>O<sub>3</sub>]<sup>-</sup>, 121.0431 [M-H-C<sub>8</sub>H<sub>6</sub>O<sub>3</sub>-

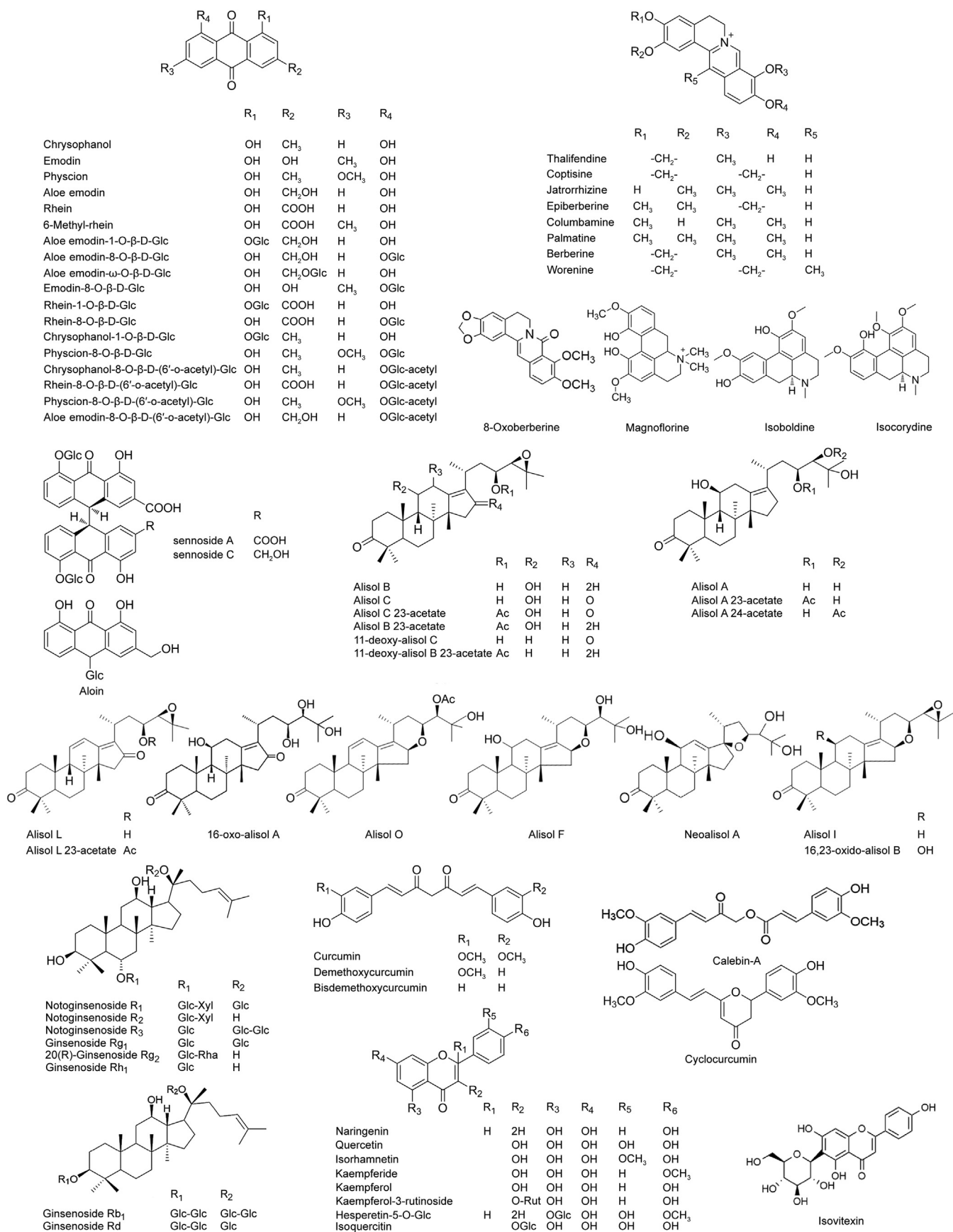


Fig. 2. Chemical structures of compounds identified in GDD.

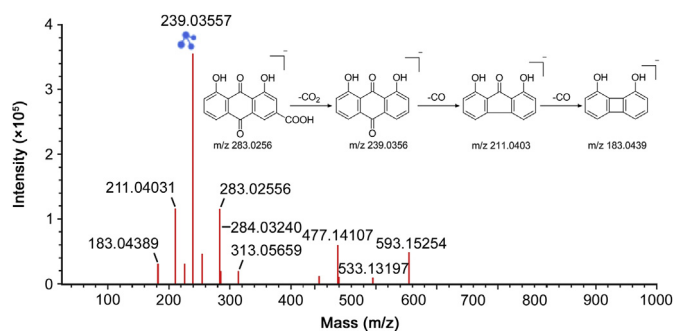


Fig. 3. The MS spectra and fragmentation pathway of rhein in negative ion mode.

$\text{CH}_2\text{O}]^-$  and  $107.0162 [\text{M}-\text{H}-\text{C}_8\text{H}_6\text{O}_3-\text{CH}_2\text{O}-\text{CH}_2]^-$  resulted from RDA cleavage. Kaempferide, with the parent ion  $[\text{M}-\text{H}]^-$  at  $m/z$  299.0553, exhibited a diagnostic ion  $[\text{M}-\text{H}-\text{CH}_3]^-$  at  $m/z$  284.0489 and RDA cleavage ion at  $m/z$  151.0055.

Peak 42 presented  $[\text{M}-\text{H}]^-$  ion at  $m/z$  285.0406, which was 14 Da less than that of kaempferide, showing the similar fragment pathways as kaempferide. It was presumed as kaempferol. Peak 23 displayed  $[\text{M}-\text{H}]^-$  ion at  $m/z$  593.1521 and produced predominant fragment ions at 447.1591  $[\text{M}-\text{H}-\text{Rha}]^-$ , 285.0832  $[\text{M}-\text{H}-\text{Rha}-\text{Glc}]^-$  due to successive losses of glycoside fragments. Meanwhile, the ion at  $m/z$  285.0832 further generated the characteristic ions identical to those of kaempferol, so the structure of this compound was considered as kaempferol-3-*O*-rutinoside. Analogously, peaks 16 and 30 were identified as rutin and hesperetin-5-*O*-glc, respectively.

### 3.2.5. Triterpenoid saponins

Eight triterpenoid saponins were detected from *Panax notoginseng* (Burk.) F. H. Chen in negative ion mode. These compounds offered the intense deprotonated ion  $[\text{M}-\text{H}]^-$  and adduct ion  $[\text{M} + \text{HCOO}]^-$ . The primary fragmentation pattern of triterpenoid saponins was the successive losses of glycosidic unit at the site of C-20, C-3 or C-6 of ginsenosides until the formation of  $[\text{Aglycon}-\text{H}]^-$  ions. The species and amount of glycosyl groups were observed from MS data, in which the mass differences of 162Da, 132Da and 146Da indicated the presence of glucose (Glc), xylose (Xyl), and rhamnose (Rha), respectively [26]. Peak 37 was definitely identified as notoginsenoside R<sub>1</sub> with a reference standard. To facilitate characterization of these ginsenosides, the MS fragmentation pattern of notoginsenoside R<sub>1</sub> is investigated in detail (Fig. 6). Notoginsenoside R<sub>1</sub> gave  $[\text{M}-\text{H}]^-$  ion at  $m/z$  931.5297 and  $[\text{M} + \text{HCOO}]^-$  ion at  $m/z$  977.5354, along with three major fragment ions at  $m/z$  799.4856  $[\text{M}-\text{H}-\text{Xyl}]^-$ , 637.4314  $[\text{M}-\text{H}-\text{Xyl}-\text{Glc}]^-$ , and 475.3782  $[\text{M}-\text{H}-\text{Xyl}-2\text{Glc}]^-$  observed in high energy MS<sup>E</sup> spectra. Peak 55 showed deprotonated ion  $[\text{M}-\text{H}]^-$  at  $m/z$  1107.5967 with a molecular formula of C<sub>54</sub>H<sub>92</sub>O<sub>23</sub>. The fragment ion at  $m/z$  459.3824  $[\text{M}-\text{H}-4\text{Glc}]^-$  represented glycosidic cleavage by loss of four glucose residues. Hence, it was tentatively characterized as ginsenoside Rb<sub>1</sub>.

Peak 41 displayed  $[\text{M}-\text{H}]^-$  and  $[\text{M} + \text{HCOO}]^-$  ions at  $m/z$  799.4863 and 845.4921, respectively, and produced fragment ion at  $m/z$  475.3784 by loss of two glucose residues. Thus, it was tentatively assigned to be ginsenoside Rg<sub>1</sub>. Peak 54 showed deprotonated ion at  $m/z$  769.4768. The fragment ions at  $m/z$  637.4335  $[\text{M}-\text{H}-\text{Xyl}]^-$  and 475.3786  $[\text{M}-\text{H}-\text{Xyl}-\text{Glc}]^-$  corresponded to successive neutral losses of xylose residue and glucose residue, indicating that peak 54 was notoginsenoside R<sub>2</sub>. Peak 57 gave  $[\text{M}-\text{H}]^-$

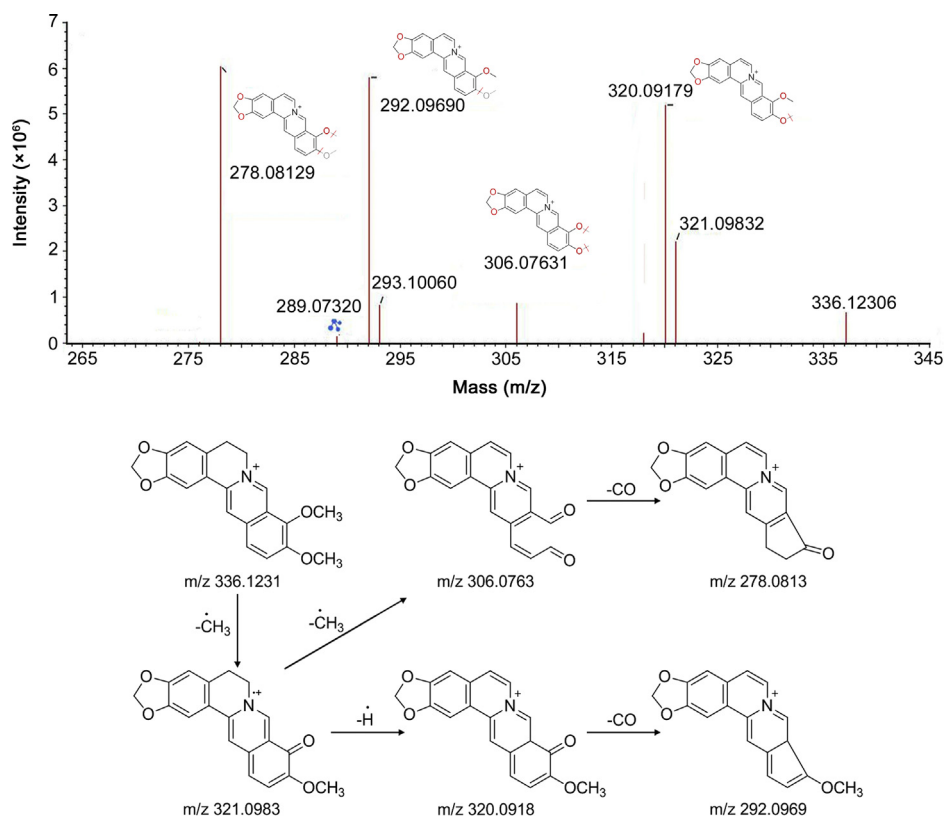


Fig. 4. The MS spectra and fragmentation pathway of berberine in positive ion mode.

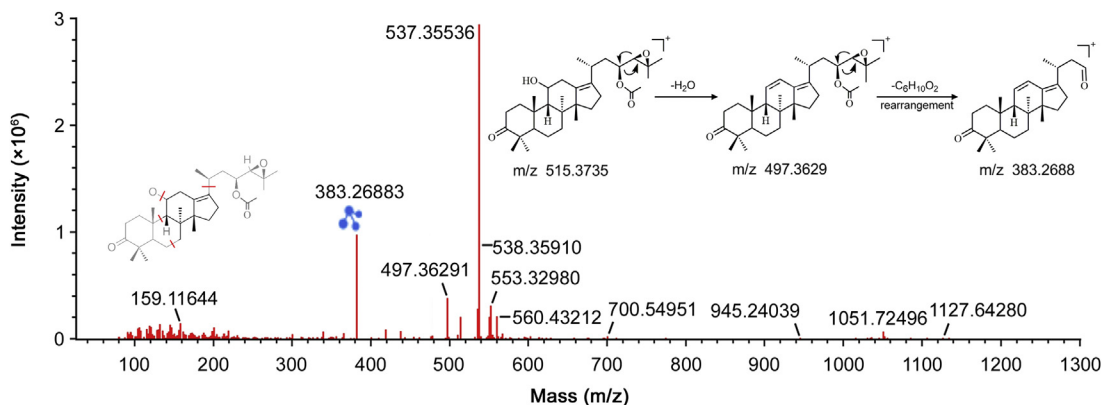


Fig. 5. The MS spectra and fragmentation pathway of alisol B 23-acetate in positive ion mode.

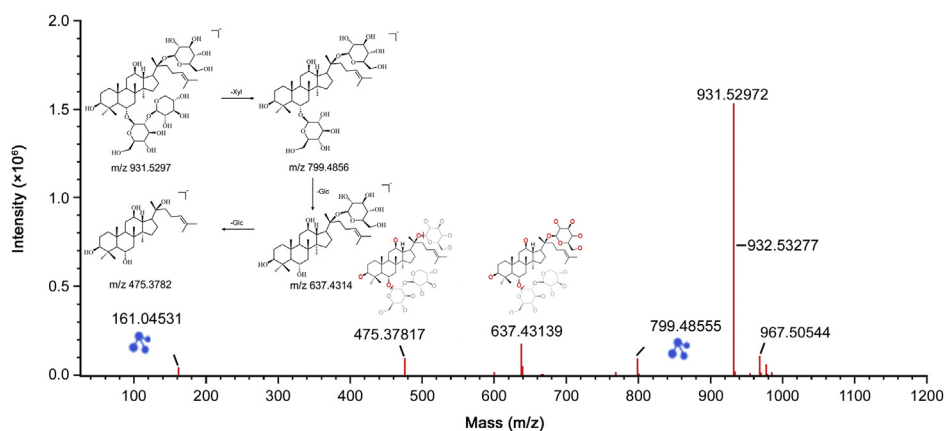


Fig. 6. The MS spectra and fragmentation pathway of notoginsenoside R<sub>1</sub> in negative ion mode.

at  $m/z$  783.4922, which further fragmented into  $m/z$  637.4326  $[M-H-Rha]^-$  and  $m/z$  475.3789  $[M-H-Rha-Glc]^-$ , so their fragment ions suggested that it was ginsenoside Rg<sub>2</sub>. According to the cleavage of glycosidic linkages discussed above, peaks 58, 63 and 66 were tentatively identified as ginsenoside Rh<sub>1</sub>, ginsenoside Rd, and notoginsenoside R<sub>3</sub>, respectively.

### 3.2.6. Others

Four curcuminoids were recognized as the major active components in *Curcuma longa* L. Peak 74 was unambiguously identified as curcumin by comparison with a reference standard. Curcumin was taken as an example, which gave precursor ion at  $m/z$  367.1192  $[M-H]^-$  and diagnostic ion at  $m/z$  217.0524  $[M-H-C_9H_{10}O_2]^-$  in negative ion mode. Analogously, peaks 56, 72 and 73 were identified as cyclocurcumin, bisdemethoxycurcumin and demethoxycurcumin, respectively. The fragmentation behaviors were in accordance with those previously reported in the literature [27].

In addition, there are small amounts of tannins in GDD, of which 10 components were identified as tannins or acylglucosides by comparing with the data in library. Peak 2 showed  $[M-H]^-$  ion at  $m/z$  169.0141 as base peak, and fragment ion of  $m/z$  125.0244 corresponding to the loss of CO<sub>2</sub> residues. So it was tentatively identified as gallic acid. Peak 5 gave  $[M-H]^-$  ion at  $m/z$  577.1359 with a molecule formula of C<sub>30</sub>H<sub>26</sub>O<sub>12</sub>, which yielded characteristic ions at  $m/z$  425.0873  $[M-H-C_7H_4O_4]^-$ , 407.0763  $[M-H-C_7H_4O_4-H_2O]^-$  and 289.0712  $[M-H-catechin]^-$ . Thus, it was tentatively deduced to be procyanidin B. Peak 9 exhibited  $[M-H]^-$  ion at  $m/z$  729.1471 and fragment ion at  $m/z$  577.1350  $[M-H-gallate]^-$ , suggesting that it

had an additional gallate than procyanidin B. It was tentatively identified as procyanidin B-*O*-gallate. Based on the similar fragment pattern, peaks 1, 4 and 19 were determined as gallic acid-*O*-glc, (+)-catechin-5-*O*- $\beta$ -D-glc and (+)-catechin-3-*O*-gallate by matching the data in library, respectively.

### 3.3. Contribution of individual herbs to GDD

The established method was subsequently applied to analyze individual herbal decoctions by UPLC-Q-TOF-MS<sup>E</sup>, and the relative sources of 96 compounds were also correspondingly confirmed. In summary, 37 components were from *Rheum palmatum* L., 15 components were from *Coptis chinensis* Franch., 9 components came from *Curcuma longa* L., 15 components were from *Lysimachia christinae* Hance, 17 components were from *Alisma orientale* (Sam.) Juzep. and 8 triterpenoid saponins were from *Panax notoginseng* (Burk.) F. H. Chen. The BPI chromatograms of six individual herbs in positive and negative ion modes are shown in Fig. 7. But each individual herb undoubtedly contributed to chemical components in GDD. Therefore, different sources and multiple types of pharmacodynamic components can exert better therapeutic effect through synergism or complementation.

## 4. Conclusion

In this study, an integrative strategy based on UPLC-Q-TOF-MS<sup>E</sup> coupled with UNIFI informatics platform was applied for chemical profile analysis of GDD. To the best of our knowledge, it was the first

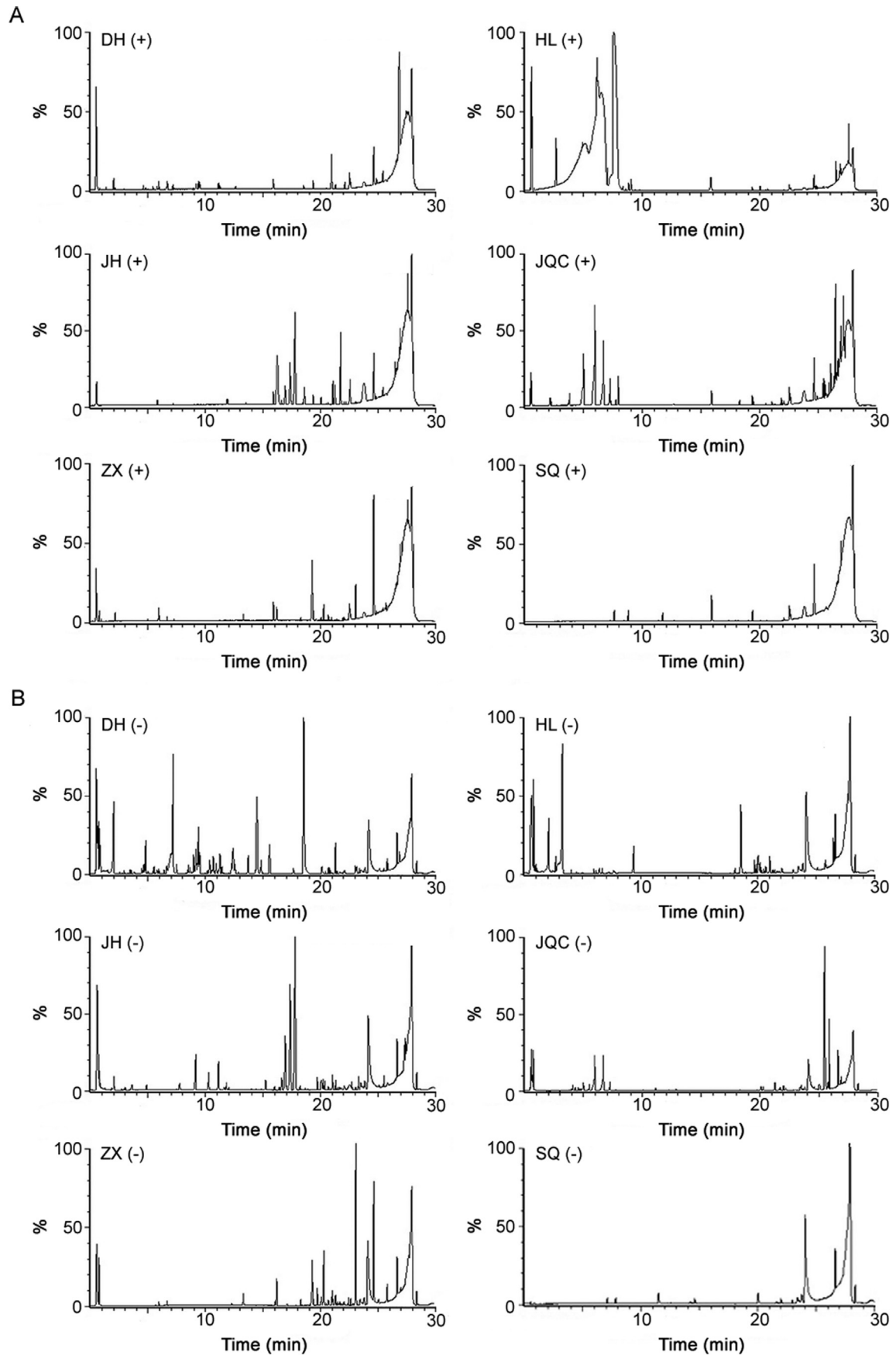


**Fig. 7.** The base peak intensity (BPI) chromatograms of six individual herbs in positive (A) and negative (B) ion modes. DH = *Rheum palmatum* L., HL = *Coptis chinensis* Franch., JH = *Curcuma longa* L., JQC = *Lysimachia christinae* Hance, ZX = *Alisma orientale* (Sam.) Juzep. and SQ = *Panax notoginseng* (Burk.) F. H. Chen.

time to reveal the constituents in GDD comprehensively. By comparison with retention time, accurate mass, fragmentation behavior, a total of 96 compounds were identified or tentatively characterized from GDD, including anthraquinones, alkaloids, protostane triterpenoids, flavonoids, triterpenoid saponins, tannins, curcuminoids and other compounds. Additionally, the ESI-MS fragmentation patterns of representative compounds in different chemical structure types were investigated. Most of the high response constitutions in individual herbs were also detected in GDD. This approach provided a rapid method for high throughput screening and characterization of constituents, and would be available in other TCM formulae analysis. What is more, the results could supply valuable information for the quality control and further study of GDD *in vivo*.

Moreover, we found that most of the compounds have abundant phenolic hydroxyl, especially the anthraquinones, curcumin and flavonoids. The structures of these compounds tend to be easily chelated by copper ions. Therefore, it is speculated that natural small molecules in GDD that could selectively chelate copper are able to form stable complexes to promote copper excretion. These molecules with properties would serve as a promising alternative to current treatments. This work has great guiding significance in further research and application of GDD in clinical treatment.

### Acknowledgments

This research was supported by the National Natural Science Foundation of China (No: 81872976, 81873038, 81303245), Key Project of the National Science Fund of Anhui Province (No: KJ2016A398), Key Project Foundation of Oversea Visiting and Research for the Excellent Young and Middle-aged Faculties in Universities of Anhui Province (No: gxgwx2018042), and Primary Research & Development Plan of Anhui Province (No: 201904a07020051).

### Conflicts of interest

The authors declare that there are no conflicts of interest.

### Appendix A. Supplementary data

Supplementary data to this article can be found online at <https://doi.org/10.1016/j.jpha.2019.05.003>.

### References

- [1] R. Stone, Lifting the veil on traditional Chinese medicine, *Science* 319 (2008) 709–710.
- [2] F. Cheung, TCM: made in China, *Nature* 480 (2011) S82–S83.
- [3] X.L. Zhao, X.Z. Zhang, L.Q. Di, et al., Exploration of thoughts and methods in study on material base of traditional Chinese medicinal herbs prescriptions, *World Sci. Technol.* 11 (2009) 488–492.
- [4] A. Ala, A.P. Walker, K. Ashkan, et al., Wilson's disease, *Lancet* 369 (2007) 397–408.
- [5] M.L. Schilsky, A century for progress in the diagnosis of Wilson disease, *J. Trace Elem. Med. Biol.* 28 (2014) 492–494.
- [6] E.A. Roberts, M.L. Schilsky, Diagnosis and treatment of Wilson disease: an update, *Hepatology* 47 (2008) 2089–2111.
- [7] J. Liu, J. Luan, X. Zhou, et al., Epidemiology, diagnosis, and treatment of Wilson's disease, *Intractable Rare Dis. Res.* 6 (2017) 249–255.
- [8] W.J. Li, C. Chen, Z.F. You, et al., Current drug managements of Wilson's disease: from west to east, *Curr. Neuropharmacol.* 14 (2016) 322–325.
- [9] B.C. Xue, R.M. Yang, J.Y. Hu, Effect of Gandou Decoction IV combined with short-term decoppering therapy with sodium dimercapto-sulphonate on serum indexes of hepatic fibrosis in patients with Wilson's disease, *Chin. J. Integr. Med.* 27 (2007) 785–788.
- [10] J. Zhang, J.Y. Hu, X.F. Ma, et al., Effect of Gandou Decoction combined with decoppering therapy on quality of life in patients with Wilson's disease: a prospective study of 135 cases, *J. Anhui Univ. Chin. Med.* 34 (2015) 14–16.
- [11] Y. Liu, M.M. Cheng, J.J. Dong, et al., Intestinal absorptive characteristics of ingredients from ethanol extracts of Gandou decoction by rat everted intestinal sac models, *China J. Chin. Mater. Med.* 42 (2017) 2571–2576.
- [12] Y. Wang, C.L. Xie, D.L. Fu, et al., Clinical efficacy and safety of Chinese herbal medicine for Wilson's disease: a systematic review of 9 randomized controlled trials, *Complement. Ther. Med.* 20 (2012) 143–154.
- [13] M. Cheng, H. Wu, H. Wu, et al., Metabolic profiling of copper-laden Hepatolenticular degeneration model rats and the interventional effects of Gandou Decoction using UPLC-Q-TOF/MS, *J. Pharm. Biomed. Anal.* 164 (2019) 187–195.
- [14] C.J. Wang, Y.Q. Jiang, D.H. Liu, et al., Characterization of phloroglucinol derivatives and diterpenes in *Euphorbia ebracteolata* Hayata by utilizing ultra-performance liquid chromatography/quadrupole time-of-flight mass spectrometry, *J. Pharm. Anal.* 3 (2013) 292–297.
- [15] L. Bao, X. Bao, P. Li, et al., Chemical profiling of *Malva verticillata* L. by UPLC-Q-TOF-MS<sup>E</sup> and their antioxidant activity *in vitro*, *J. Pharm. Biomed. Anal.* 150 (2018) 420–426.
- [16] M. Fan, K. Qin, F. Ding, et al., Identification and differentiation of major components in three different "Sheng-ma" crude drug species by UPLC/Q-TOF-MS, *Acta Pharm. Sin. B* 7 (2017) 185–192.
- [17] L. Deng, A.M. Shi, H.Z. Liu, et al., Identification of chemical ingredients of peanut stems and leaves extracts using UPLC-QTOF-MS coupled with novel informatics UNIFI platform, *J. Mass Spectrom.* 51 (2016) 1157–1167.
- [18] P.P. Liu, G.S. Shan, F. Zhang, et al., Metabolomics analysis and rapid identification of changes in chemical ingredients in crude and processed *Astragali Radix* by UPLC-QTOF-MS combined with novel informatics UNIFI platform, *Chin. J. Nat. Med.* 16 (2018) 714–720.
- [19] X. Gao, Y. Ma, Z. Wang, et al., Identification of anti-inflammatory active ingredients from *Tumuxiang* by ultra-performance liquid chromatography/quadrupole time-of-flight-MS<sup>E</sup>, *Biomed. Chromatogr.* 32 (2018) e4179.
- [20] J.F. Tang, W.X. Li, X.J. Tan, et al., A novel and improved UHPLC-QTOF/MS method for the rapid analysis of the chemical constituents of *Danhong* injection, *Anal. Methods* 8 (2016) 2904–2914.
- [21] H. Zhu, R. Yin, F. Han, et al., Characterization of chemical constituents in *Zhi-Zi-Da-Huang* decoction by ultra high performance liquid chromatography coupled with quadrupole time-of-flight mass spectrometry, *J. Sep. Sci.* 37 (2014) 3489–3496.
- [22] H.Y. Zhao, M.X. Fan, X. Wu, et al., Chemical profiling of the Chinese herb formula *Xiao-Cheng-Qi* Decoction using liquid chromatography coupled with electrospray ionization mass spectrometry, *J. Chromatogr. Sci.* 51 (2013) 273–285.
- [23] Q. Liu, Z. Jiao, Y. Liu, et al., Chemical profiling of *San-Huang* decoction by UPLC-ESI-Q-TOF-MS, *J. Pharm. Biomed. Anal.* 131 (2016) 20–32.
- [24] W. Zhao, X. Huang, X. Li, et al., Qualitative and quantitative analysis of major triterpenoids in *Alismatis Rhizoma* by high performance liquid chromatography/diode-array detector/quadrupole-time-of-flight mass spectrometry and ultra-performance liquid chromatography/triple quadrupole mass spectrometry, *Molecules* 20 (2015) 13958–13981.
- [25] S. Wang, L. Chen, J. Leng, et al., Fragment ion diagnostic strategies for the comprehensive identification of chemical profile of *Gui-Zhi-Tang* by integrating high-resolution MS, multiple-stage MS and UV information, *J. Pharm. Biomed. Anal.* 98 (2014) 22–35.
- [26] L. Xu, L.H. Mu, J. Peng, et al., UPLC-Q-TOF-MS<sup>E</sup> analysis of the constituents of *Ding-Zhi-Xiao-Wan*, a traditional Chinese antidepressant, in normal and depressive rats, *J. Chromatogr. B Anal. Technol. Biomed. Life Sci.* 1026 (2016) 36–42.
- [27] K. Ashraf, M. Mujeeb, A. Ahmad, et al., Determination of curcuminoids in *Curcuma longa* Linn. by UPLC/Q-TOF-MS: an application in turmeric cultivation, *J. Chromatogr. Sci.* 53 (2015) 1346–1352.



## Original Article

GC-NICI-MS analysis of acetazolamide and other sulfonamide (R-SO<sub>2</sub>-NH<sub>2</sub>) drugs as pentafluorobenzyl derivatives [R-SO<sub>2</sub>-N(PFB)<sub>2</sub>] and quantification of pharmacological acetazolamide in human urineOlga Begou<sup>a, b, c, 1</sup>, Kathrin Drabert<sup>a, 1</sup>, Georgios Theodoridis<sup>b, c</sup>, Dimitrios Tsikas<sup>a, \*</sup><sup>a</sup> Institute of Toxicology, Core Unit Proteomics, Hannover Medical School, Carl-Neuberg-Strasse 1, D-30625, Hannover, Germany<sup>b</sup> Department of Chemistry, Aristotle University of Thessaloniki, 54124, Thessaloniki, Greece<sup>c</sup> BIOMIC\_AUTH, Center for Interdisciplinary Research and Innovation (CIRI-AUTH), Balkan Center, 10th Km Thessaloniki-Thermi Rd, P.O. Box 8318, GR 57001, Thessaloniki, Greece

## ARTICLE INFO

## Article history:

Received 2 August 2019

Received in revised form

19 November 2019

Accepted 22 November 2019

Available online 28 November 2019

## Keywords:

Acetazolamide  
Derivatization  
Quantification  
Sulfonamides  
Validation

## ABSTRACT

Acetazolamide (molecular mass (MM), 222) belongs to the class of sulfonamides (R-SO<sub>2</sub>-NH<sub>2</sub>) and is one of the strongest pharmacological inhibitors of carbonic anhydrase activity. Acetazolamide is excreted unchanged in the urine. Here, we report on the development, validation and biomedical application of a stable-isotope dilution GC-MS method for the reliable quantitative determination of acetazolamide in human urine. The method is based on evaporation to dryness of 50 μL urine aliquots, base-catalyzed derivatization of acetazolamide (d<sub>0</sub>-AZM) and its internal standard [*acetylo*-<sup>2</sup>H<sub>3</sub>]acetazolamide (d<sub>3</sub>-AZM) in 30 vol% pentafluorobenzyl (PFB) bromide in acetonitrile (60 min, 30 °C), reconstitution in toluene (200 μL) and injection of 1-μL aliquots. The negative-ion chemical ionization (NICI) mass spectra (methane) of the PFB derivatives contained several intense ions including [M]<sup>-</sup> at *m/z* 581 for d<sub>0</sub>-AZM and *m/z* 584 for d<sub>3</sub>-AZM, suggesting derivatization of their sulfonamide groups to form *N,N*-dipentafluorobenzyl derivatives (R-SO<sub>2</sub>-N(PFB)<sub>2</sub>), i.e., d<sub>0</sub>-AZM-(PFB)<sub>2</sub> and d<sub>3</sub>-AZM-(PFB)<sub>2</sub>, respectively. Quantification was performed by selected-ion monitoring of *m/z* 581 and 83 for d<sub>0</sub>-AZM-(PFB)<sub>2</sub> and *m/z* 584 and 86 for d<sub>3</sub>-AZM-(PFB)<sub>2</sub>. The limits of detection and quantitation of the method were determined to be 300 fmol (67 pg) and 1 μM of acetazolamide, respectively. Intra- and inter-assay precision and accuracy for acetazolamide in human urine samples in pharmacologically relevant concentration ranges were determined to be 0.3%–4.2% and 95.3%–109%, respectively. The method was applied to measure urinary acetazolamide excretion after ingestion of a 250 mg acetazolamide-containing tablet (Acemit®) by a healthy volunteer. Among other tested sulfonamide drugs, methazolamide (MM, 236) was also found to form a *N,N*-dipentafluorobenzyl derivative, whereas dorzolamide (MM, 324) was hardly detectable. No GC-MS peaks were obtained from the PFB bromide derivatization of hydrochlorothiazide (MM, 298), xipamide (MM, 355), indapamide and metholazone (MM, 366 each) or brinzolamide (MM, 384). We demonstrate for the first time that sulfonamide drugs can be derivatized with PFB bromide and quantitated by GC-MS. Sulfonamides with MM larger than 236 are likely to be derivatized by PFB bromide but to lack thermal stability.

© 2019 Xi'an Jiaotong University. Production and hosting by Elsevier B.V. This is an open access article under the CC BY-NC-ND license (<http://creativecommons.org/licenses/by-nc-nd/4.0/>).

## 1. Introduction

Acetazolamide (*N*-(5-sulfamoyl-1,3,4-thiadiazol-2-yl)acetamide, MM 222.25; CAS number 216665-38-2; see Fig. S1) is one of

the oldest therapeutically used diuretic drugs. Acetazolamide is a strong inhibitor of carbonic anhydrase (CA) which catalyzes the reversible reaction between CO<sub>2</sub> and H<sub>2</sub>O to form bicarbonate and protons (CO<sub>2</sub> + H<sub>2</sub>O ↔ HCO<sub>3</sub><sup>-</sup> + H<sup>+</sup>) [1]. Acetazolamide and other sulfonamide (R-SO<sub>2</sub>-NH<sub>2</sub>) drugs (see Fig. S1) are widely used for the treatment of glaucoma, mountain sickness, sleep apnea, epilepsy and hypertension [1]. The pharmacological action of acetazolamide and relatives in several organs such as eyes, brain and kidney is based on the inhibition of CA activity. In glaucoma and epilepsy,

Peer review under responsibility of Xi'an Jiaotong University.

\* Corresponding author.

E-mail address: [tsikas.dimitros@mh-hannover.de](mailto:tsikas.dimitros@mh-hannover.de) (D. Tsikas).<sup>1</sup> These authors contributed equally to this work and are both first authors.

inhibition of CA activity by acetazolamide results in reduction of intraocular and cerebral pressure. Inhibition of CA activity in the kidney results in enhanced excretion of  $\text{HCO}_3^-$  and inorganic nitrite ( $\text{NO}_2^-$ ) [2,3]. Acetazolamide-induced loss of nitrite may be of particular importance because  $\text{NO}_2^-$  is considered an abundant reservoir of the endogenous potent vasodilator nitric oxide (NO). The urinary nitrate-to-nitrite molar ratio, i.e.,  $U_{\text{NO}_3^-/\text{R}}$ , may be a useful measure of renal CA-dependent reabsorption of urinary nitrite in humans [4]. Besides its therapeutic use, acetazolamide gained importance as a potential performance-enhancing drug in sport doping [5].

Several analytical methods based on liquid chromatography (LC) [6–12] and gas chromatography (GC) [13–21] have been reported for the determination of acetazolamide and related sulfonamides in various biological samples including plasma and urine. For GC analysis, sulfonamides such as acetazolamide require conversion of their sulfonamide group to thermally stable and volatile derivatives. The amine group of the sulfonamide group of acetazolamide and many other sulfonamides is the only functional group that is accessible for chemical derivatization. Methylation of the amine group of sulfonamides has been often performed using methyl iodide (iodomethane,  $\text{CH}_3\text{I}$ ) [13–19]. Silylation of the amine group of sulfonamides for GC has also been reported [20,21].

Pentafluorobenzyl (PFB) bromide (PFB-Br) is a versatile derivatization reagent in chromatography (GC, LC) and mass spectrometry (MS) [22]. It can be used for the derivatization of nucleophilic substances and inorganic and organic anions both in aqueous phase such as plasma and urine and in anhydrous organic solvents such as acetonitrile [2,23–25]. Analogous to the derivatization of amine groups such as those in creatinine with PFB-Br [24], we assumed that PFB-Br may be useful as a derivatization reagent for the amine group of acetazolamide and other sulfonamides in GC-based analytical methods. The reaction of  $\text{R-SO}_2\text{-NH}_2$  with PFB-Br may lead to the formation of mono-PFB derivatives ( $\text{R-SO}_2\text{-NHPFB}$ ) and di-PFB derivatives ( $\text{R-SO}_2\text{-N(PFB)}_2$ ). To the best of our knowledge, the derivatization of acetazolamide or other sulfonamides with PFB-Br has not been reported thus far.

In the present work, we demonstrate that PFB-Br is useful for the *N*-alkylation of the sulfonamide group of acetazolamide representing the group of sulfonamides. We found that the derivatization of acetazolamide is best performed in anhydrous acetonitrile using *N,N*-diisopropylethylamine (i.e., Hünig base) as the catalyst under very mild conditions (30 °C) (Fig. S1). As acetazolamide is excreted in the urine without metabolization, we developed and validated a GC-MS method for the quantitative determination of acetazolamide in human urine using commercially available [*acetylo*- $^2\text{H}_3$ ]acetazolamide as the internal standard (IS). Negative-ion chemical ionization (NICI) of the PFB derivative of acetazolamide provided the lowest limit of detection (LOD) thus far reported for acetazolamide. We also tested the utility of PFB-Br for the derivatization of other sulfonamide drugs. The applicability of the method in clinical-pharmacologic settings was demonstrated upon ingestion of a 250 mg acetazolamide tablet by a healthy volunteer.

## 2. Experimental

### 2.1. Materials and chemicals

[*acetylo*- $^2\text{H}_3$ ]Acetazolamide ( $\text{d}_3$ -AZM; declared amount, 1 mg) was obtained from Hycultec (Beutelsbach, Germany) and was diluted in dimethyl sulfoxide (DMSO) in the original flask. The chemical and isotopic purity of  $\text{d}_3$ -AZM had not been declared by the supplier. 2,3,4,5,6-Pentafluorobenzyl bromide, *N,N*-diisopropylethylamine, pentafluoropropionic anhydride (PFPA, >99%),

2,3,4,5,6-pentafluorobenzoyl chloride (>99%), unlabeled acetazolamide ( $\text{d}_0$ -AZM; >99%) and all the other sulfonamides (>98%) used in the present study were obtained from Sigma-Aldrich (Darmstadt, Germany). DMSO and acetonitrile (GC grade; dried over molsieve) were purchased from Merck (Darmstadt, Germany). Toluene (p.a.) was purchased from Baker (Deventer, The Netherlands). The silylation reagent *N,O*-bis(trimethylsilyl)trifluoroacetamide (BSTFA, >99%) was obtained from Macherey-Nagel (Düren, Germany).

### 2.2. Safety considerations

PFB-Br and PFPA are corrosive. PFB-Br is an eye irritant. Inhalation and contact with skin and eyes should be avoided. All work should be performed in a well-ventilated fume hood.

### 2.3. Preparation of calibration standards

Acetazolamide is freely soluble in DMSO. Solutions and dilutions of acetazolamide and all other sulfonamides were prepared in DMSO. Stock solutions of  $\text{d}_0$ -AZM (100 mM) and  $\text{d}_3$ -AZM (50 mM) and their working dilutions (each 10 mM) were stored at 8 °C and –18 °C, respectively.

### 2.4. Biological samples and preparation of urine samples

Acetazolamide-free urine samples used in method development and validation were obtained from healthy volunteers after informed consent. These volunteers did not ingest acetazolamide at least two weeks before. Samples (1 mL aliquots) were kept frozen at –18 °C until analysis. Prior to sample derivatization, urine samples were thawed and centrifuged (3350×g, 5 min).

In quantitative analyses, 50  $\mu\text{L}$  aliquots of the clear urine supernatants were placed in 1.8 mL glass vials and 5  $\mu\text{L}$  aliquots of a 10 mM solution of  $\text{d}_3$ -AZM in DMSO were added. Urine and DMSO were evaporated to dryness under a stream of nitrogen gas. To remove effectively remaining water, ethanol (100  $\mu\text{L}$ ) was added, the vials were vortex-mixed for about 10 s and then ethanol was evaporated to dryness under a stream of nitrogen gas.

### 2.5. Derivatization procedure with PFB-Br in water-free phase

Solid residues were dissolved in anhydrous acetonitrile (100  $\mu\text{L}$ ). Then, 10  $\mu\text{L}$  of *N,N*-diisopropylethylamine and 10  $\mu\text{L}$  of 30 vol% PFB-Br in anhydrous acetonitrile were added, the glass vials were tightly sealed and vortex-mixed for about 10 s. Subsequently, the samples were heated for 60 min at 30 °C on a thermostatic block model MBT250-4 from Kleinfeld Labortechnik (Gehrden, Germany). After cooling to room temperature the samples were evaporated again to dryness under a stream of nitrogen gas and the residues were reconstituted with 200  $\mu\text{L}$  aliquots of toluene and vortexed for 2 min. Clear and particle-free aliquots (about 180  $\mu\text{L}$ ) of the toluene phases were transferred into 1.8 mL autosampler glass vials equipped with 200  $\mu\text{L}$  microinserts for GC-MS analysis as described below.

### 2.6. Validation of the method

The GC-MS method was validated for acetazolamide in urine samples donated by three healthy humans. Pharmacologically relevant concentrations ranges (0–1000  $\mu\text{M}$  acetazolamide) were used. Validation experiments included linearity, accuracy (recovery, %) and precision (RSD, %). For the sake of clarity, the validation experiments are described in detail in the sections Results and Discussion.

## 2.7. GC-MS conditions

GC-MS analyses were performed on a single-quadrupole mass spectrometer model ISQ directly interfaced with a Trace 1310 series gas chromatograph equipped with an autosampler AS 1310 from ThermoFisher (Dreieich, Germany). The gas chromatograph was equipped with a 15 m long fused-silica capillary column Optima 17 (0.25 mm I.D., 0.25  $\mu$ m film thickness) from Macherey-Nagel (Düren, Germany). In quantitative analyses, the following oven temperature program was used with helium (at a constant flow rate of 1 mL/min) as the carrier gas: 1.0 min at 90 °C, then increased to 250 °C at a rate of 35 °C/min and to 320 °C at a rate of 35 °C/min, respectively. The column was held at 320 °C for 6 min. Interface, injector and ion-source were kept constant at 260 °C, 200 °C and 250 °C, respectively. Electron energy was set to 70 eV and electron current to 50  $\mu$ A. Methane (2.4 mL/min) was used as the reagent gas for NICI. Aliquots (1  $\mu$ L from the toluene phase) were injected in the splitless mode by means of the autosampler. Quantification of acetazolamide was performed in the NICI mode by selected-ion monitoring (SIM) the ions with  $m/z$  581 and  $m/z$  83 for  $d_0$ -AZM and  $m/z$  584 and  $m/z$  86 for  $d_3$ -AZM (IS) with a dwell-time of 50 ms for each ion. The electron multiplier voltage was set to 2025 V. Deviations from the conditions described above are mentioned in the sections Results and Discussion.

## 2.8. Data analysis and presentation

If not otherwise specified, quantitative analyses were performed in triplicate. Unpaired *t*-test was used to check statistical significance. Values are presented as mean  $\pm$  SD.

## 3. Results

### 3.1. Testing derivatization methods for acetazolamide

Acetazolamide (Fig. S1) and methazolamide have a single functional group that is accessible to chemical derivatization. This is the amine group of the sulfonamide functionality; other sulfonamides such as dorzolamide possess additional derivatizable functional groups. We tested the utility of several derivatization agents for acetazolamide representing the group of sulfonamide drugs for GC-NICI-MS analysis. These derivatization reagents included pentafluorobenzyl bromide (PFB-Br), pentafluorobenzoyl chloride (PFBzoyl-Cl) and pentafluoropropionic anhydride (PFPA). Previously, we found these reagents to be useful for amine groups-containing substances such as creatinine [24], dimethylamine (DMA) [26] and amino acids [27], respectively.

We also tested BSTFA, which is a versatile reagent for different functionalities including hydroxyl and amine groups. In our tests, BSTFA was found to be not suitable, because derivatization (60 min, 60 °C) resulted in loss of the acetyl group in  $d_0$ -AZM and  $d_3$ -AZM, thus not allowing quantitative analysis of acetazolamide (data not shown). Procedures previously reported for the derivatization of methyl esters of amino acids [27] revealed that PFPA is not useful for the derivatization of acetazolamide (data not shown). By using a previously reported procedure for the extractive derivatization of urinary DMA with PFBzoyl-Cl [26], acetazolamide could also not be derivatized (data not shown).

PFB-Br is a versatile derivatization reagent in nucleophilic substitution reactions [22]. Its utility in GC-MS has been demonstrated for different classes of substances in aqueous and anhydrous systems [22]. We found that acetazolamide cannot be derivatized in aqueous buffered solutions including phosphate and Tris buffer of neutral pH value and in human urine (pH range, 5.5–7.8) (data not shown). In contrast, acetazolamide was found to be readily

derivatized with PFB-Br in anhydrous acetonitrile using *N,N*-diisopropylethylamine as the base catalyst under very mild conditions and short derivatization times as has been reported for carboxylic acids including prostaglandins [28], i.e., warming the derivatization mixture for 60 min at 30 °C. Higher derivatization temperatures tested (i.e., 40 °C, 50 °C, 60 °C) were found to provide yellow-to-brownish colored derivatization solutions, most likely due to decomposition reactions (data not shown). For these reasons we selected PFB-Br derivatization of acetazolamide in anhydrous acetonitrile and tested the utility of this derivatization for methazolamide and other sulfonamide drugs.

### 3.2. GC-NICI-MS characterization of the PFB derivatives of sulfonamides

Each 50 nmol of  $d_0$ -AZM and  $d_3$ -AZM were mixed, derivatized with PFB-Br (60 min, 30 °C), the sample was evaporated to dryness and the residue was reconstituted with toluene as described in Experimental section. The appearance of the originally clear and colorless solution did not change upon derivatization. GC-NICI-MS mass spectra were obtained by injecting 1  $\mu$ L aliquots of the toluene phases (180  $\mu$ L) each corresponding to 250 pmol of  $d_0$ -AZM and  $d_3$ -AZM (assuming quantitative derivatization). GC-NICI-MS analysis of the sample in scan mode resulted in few GC peaks. The mass spectrum obtained from the GC peak of the PFB derivatives of the mixture of  $d_0$ -AZM and  $d_3$ -AZM eluting at about 8.35 min is shown in Fig. 1. It contains five pairs of ions differing by 3 Da each, most likely due to the presence of the intact acetyl groups in the PFB derivatives of  $d_0$ -AZM and  $d_3$ -AZM.

The largest anions at  $m/z$  581 and  $m/z$  584 in the mass spectrum can be assigned to the *N,N*-dipentafluorobenzyl derivatives of  $d_0$ -AZM (R-SO<sub>2</sub>-N(PFB)<sub>2</sub>; molecular mass, 582) and  $d_3$ -AZM (R( $d_3$ )-SO<sub>2</sub>-N(PFB)<sub>2</sub>; molecular mass, 585), respectively. The ions  $m/z$  375 and  $m/z$  357 are common to the  $d_0$ -AZM and  $d_3$ -AZM derivatives and are likely produced from breaking of the derivatized sulfonamide groups. Presumably,  $m/z$  357 derives from  $m/z$  375 by loss of a water molecule (H<sub>2</sub>O, 18 Da). The ion  $m/z$  167 is also common to  $d_0$ -AZM and  $d_3$ -AZM and is due to [C<sub>6</sub>F<sub>5</sub>]<sup>-</sup>. The ions  $m/z$  83 and  $m/z$  86 carry each one acetyl group and their structures are likely to be [CH<sub>3</sub>CO-N-CN]<sup>-</sup> and [CD<sub>3</sub>CO-N-CN]<sup>-</sup>, respectively. The most intense and common ion in the mass spectra of  $d_0$ -AZM-(PFB)<sub>2</sub> and  $d_3$ -AZM-(PFB)<sub>2</sub> is  $m/z$  58 and is likely to be the negatively charged thioethene epoxide [(CH=CH)S]<sup>-</sup>.

It is worth mentioning that the retention time of the PFB ester-methoxime (MO)-trimethylsilyl (TMS) ether derivative of prostaglandin E<sub>2</sub> (i.e., PGE<sub>2</sub>-PFB-MO-(TMS)<sub>2</sub>; molecular mass, 705) under the same GC-MS conditions was 8.32 min. This observation indicates that the C<sub>34</sub>-species PGE<sub>2</sub>-PFB-MO-(TMS)<sub>2</sub> is as volatile as the C<sub>18</sub>-species  $d_0$ -AZM-(PFB)<sub>2</sub> and  $d_3$ -AZM-(PFB)<sub>2</sub>, presumably because of its two TMS ether functionalities.

The mass spectrum obtained from the GC peak of the PFB derivative of methazolamide (retention time, 7.8 min) is shown in Fig. 2. The ions at  $m/z$  357 and  $m/z$  375 in this mass spectrum indicate that dorzolamide reacts with PFB-Br to form the *N,N*-dipentafluorobenzyl derivative R-SO<sub>2</sub>-N(PFB)<sub>2</sub> (molecular mass, 596) analogous to acetazolamide. However, the R-SO<sub>2</sub>-N(PFB)<sub>2</sub> derivative of methazolamide ionizes quite differently than the R-SO<sub>2</sub>-N(PFB)<sub>2</sub> derivative of acetazolamide. The intense ion at  $m/z$  415 is likely to be due to [M-PFB]<sup>-</sup>. The most intense ion at  $m/z$  220 in the mass spectrum of the *N,N*-dipentafluorobenzyl derivative of methazolamide is likely to be due to [M-NH(PFB)<sub>2</sub>]<sup>-</sup> which is absent in the mass spectrum of *N,N*-dipentafluorobenzyl derivative of acetazolamide. The reason for this disparity could be the formation of the electrically neutral [M-NH(PFB)<sub>2</sub>] or radical species [M-NH(PFB)<sub>2</sub>]<sup>•</sup>. A likely explanation of the remarkable differences in

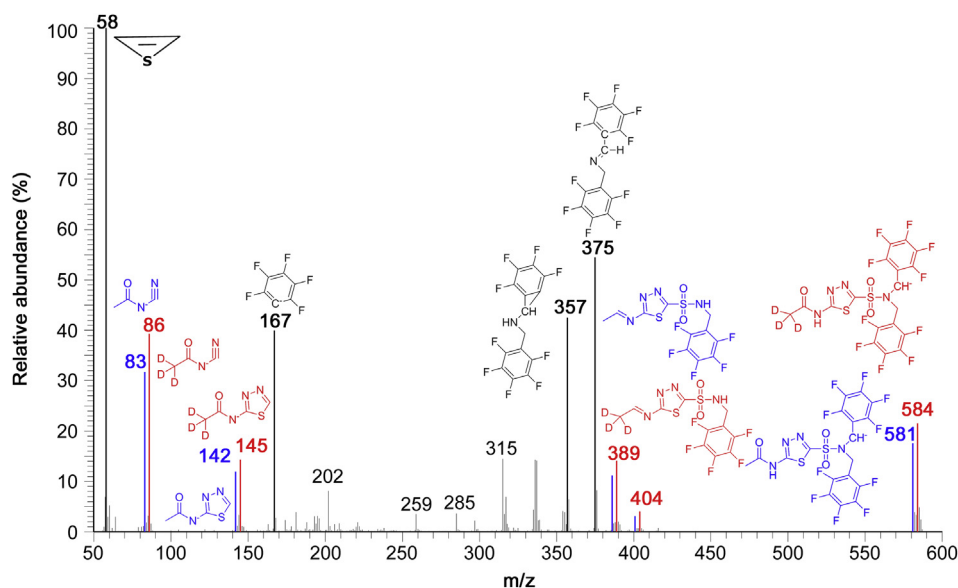


**Fig. 1.** GC-NICI-MS spectrum obtained from a mixture containing each about 250 pmol of unlabeled acetazolamide ( $d_0$ -AZM) and  $[acetylo-^2H_3]$ -acetazolamide ( $d_3$ -AZM) as pentafluorobenzyl (PFB) derivatives eluting at about 8.35 min. Inserts indicate the proposed structures for the anions of the PFB derivatives of  $d_0$ -AZM and  $d_3$ -AZM. Mass fragments differing by 3 Da are shown in blue and red. For simplicity the charge of the anions is not indicated.

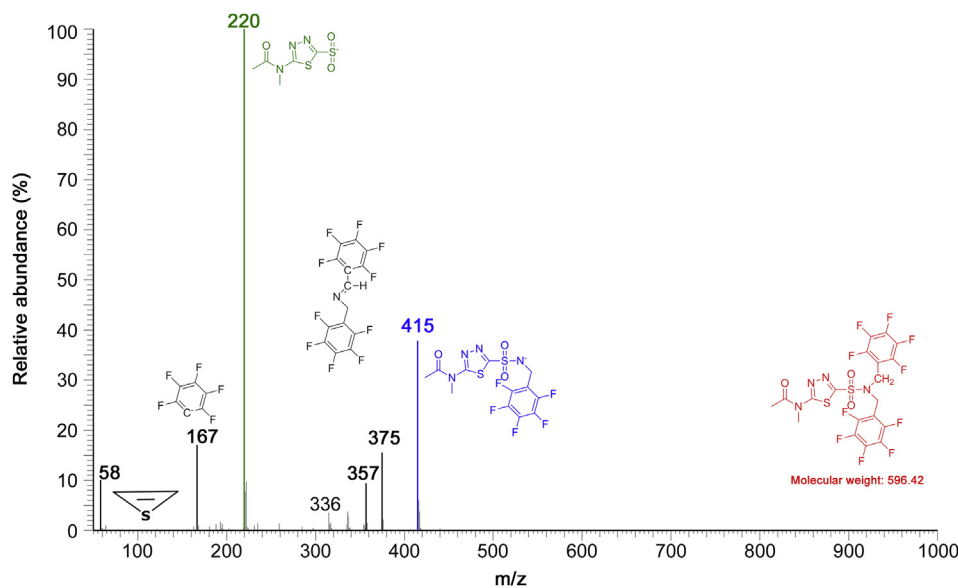


**Fig. 2.** GC-NICI-MS spectrum obtained from unlabeled methazolamide (about 250 pmol) as pentafluorobenzyl derivative eluting at about 7.8 min. Inserts indicate the proposed structures for the PFB derivative of methazolamide and of mass fragments.

the NICI mass spectra of the  $N,N$ -dipentafluorobenzyl derivatives of the structurally closely acetazolamide and methazolamide and the shorter retention time of the methazolamide derivative could be the methyl group on the amidic N atom of methazolamide. This methyl group makes the derivative more lipophilic, volatile, presumably more stable, and influences the NICI as well (see Fig. S2).

The mass spectrum obtained from the GC peak of the PFB derivative of dorzolamide (retention time, 10.2 min) is shown in Fig. S3. The ions at  $m/z$  357 and  $m/z$  375 in this mass spectrum indicate that dorzolamide reacts with PFB-Br to form the  $N,N$ -dipentafluorobenzyl derivative  $R-SO_2-N(PFB)_2$  (molecular mass, 684) analogous to acetazolamide and methazolamide. Yet, in contrast to the mass spectra of the PFB derivatives of acetazolamide and methazolamide, the NICI mass spectrum of the dorzolamide

derivative does not contain the anion at  $m/z$  58 ( $[(CH=CH)S]^-$ ). This could be due to the lack of the thiadiazole structure in dorzolamide.

### 3.3. GC-NICI-MS characterization and standardization of $[acetylo-^2H_3]$ acetazolamide ( $d_3$ -AZM)

Declared amounts of commercially available stable-isotope labelled analogs, especially of those delivered in very small, not (accurately) weighable amounts, may differ from those obtained experimentally. The chemical and isotopic purity of the  $d_3$ -AZM used in our study had not been declared by the supplier and was, therefore, determined experimentally as follows.

Aliquots (5  $\mu$ L) of separate 10 mM solutions of  $d_3$ -AZM and  $d_0$ -AZM in DMSO were derivatized and analyzed separately. Aliquots

(1  $\mu\text{L}$ ) of the toluene phases assuming to contain 250 pmol of  $\text{d}_3$ -AZM or  $\text{d}_0$ -AZM were injected on three different days each in triplicate per day and SIM of  $m/z$  581,  $m/z$  584,  $m/z$  83 and  $m/z$  86 was performed. The peak area ratio (PAR) values for  $\text{d}_3$ -AZM in the absence of synthetic  $\text{d}_0$ -AZM were determined to be (mean  $\pm$  SD,  $n = 9$ )  $0.00257 \pm 0.001$  for the PAR  $m/z$  581 to  $m/z$  584 and  $0.00477 \pm 0.002$  for the PAR  $m/z$  83 to  $m/z$  86. These data indicate an isotopic purity of the commercially available  $\text{d}_3$ -AZM preparation of about 99.7% at  $^2\text{H}$  and no appreciable contribution of  $\text{d}_0$ -AZM to  $\text{d}_3$ -AZM in the commercially available  $\text{d}_3$ -AZM. The PAR values for  $\text{d}_0$ -AZM in the absence of  $\text{d}_3$ -AZM were determined to be (mean  $\pm$  SD,  $n = 9$ )  $0.0233 \pm 0.001$  for the PAR  $m/z$  584 to  $m/z$  581 and  $0.00122 \pm 0.0007$  for the PAR  $m/z$  86 to  $m/z$  83, indicating no appreciable contribution of  $\text{d}_3$ -AZM to  $\text{d}_0$ -AZM.

The standardization procedure of  $\text{d}_3$ -AZM and the linearity of the method were performed in matrix-free samples, i.e., by using solutions of  $\text{d}_3$ -AZM (10 mM) and  $\text{d}_0$ -AZM (10 mM) in DMSO. Standard curves were prepared on three different days by derivatizing mixtures containing a fixed amount of  $\text{d}_3$ -AZM (50 nmol; 5  $\mu\text{L}$ ) and different amounts of  $\text{d}_0$ -AZM (0 nmol, 0  $\mu\text{L}$ ; 40 nmol, 4  $\mu\text{L}$ ; 80 nmol, 8  $\mu\text{L}$ ; 120 nmol, 12  $\mu\text{L}$ ; 160 nmol, 16  $\mu\text{L}$ ; 200 nmol, 20  $\mu\text{L}$ ) and by analyzing the samples by GC-MS in the SIM mode:  $m/z$  83,  $m/z$  86,  $m/z$  581 and  $m/z$  584 each a dwell-time of 50 ms. Triplicate injections were performed for each concentration point. The concentration of  $\text{d}_3$ -AZM in the toluene phases (each 200  $\mu\text{L}$ ) was considered (assuming quantitative derivatization and extraction) to be 250  $\mu\text{M}$ . The concentrations of  $\text{d}_0$ -AZM in the toluene phases (each 200  $\mu\text{L}$ ) were considered (assuming quantitative derivatization and extraction) to be 0, 200, 400, 600, 800 and 1000  $\mu\text{M}$ . These concentrations were chosen in order to simulate pharmacologically relevant concentrations for acetazolamide in human urine.

Linear regression analysis between the PAR of  $m/z$  581 to  $m/z$  584 ( $y_1$ ) measured on three days and the nominal acetazolamide concentration ( $x_1$ ) yielded the regression equation  $y_1 = 0.0581(\pm 0.016) + 0.0031(\pm 0.00003)x_1$  ( $r = 0.997$ ). Linear regression analysis between the PAR of  $m/z$  83 to  $m/z$  86 ( $y_2$ ) measured and the nominal acetazolamide concentration derivatized ( $x_2$ ) yielded the regression equation  $y_2 = 0.1024(\pm 0.0190) + 0.0028(\pm 0.00003)x_2$  ( $r = 0.994$ ). The reciprocal slope values of the regression equations provide the concentration of the internal standard  $\text{d}_3$ -AZM. In this experiment, the  $\text{d}_3$ -AZM concentration was calculated to be 323  $\mu\text{M}$  using the PAR of  $m/z$  581 to  $m/z$  584, and 357  $\mu\text{M}$  using the PAR of  $m/z$  83 to  $m/z$  86. Both values differ from the nominal  $\text{d}_3$ -AZM concentration of 250  $\mu\text{M}$  considering the delivered amount of  $\text{d}_3$ -AZM. The concentration of the internal standard was corrected using the experimentally observed data. Accuracy and precision data obtained using the PAR of  $m/z$  581 to  $m/z$  584 (corrected  $\text{d}_3$ -AZM concentration, 323  $\mu\text{M}$ ) and the PAR of  $m/z$  83 to  $m/z$  86 (corrected  $\text{d}_3$ -AZM concentration, 357  $\mu\text{M}$ ) are summarized in Table S1. GC-MS chromatograms from the analysis of acetazolamide (at 600  $\mu\text{M}$ ) in DMSO and urine are shown in Fig. S4.

Linear regression analysis between the corresponding PAR values of  $m/z$  83 to  $m/z$  86 ( $y$ ) and the PAR values of  $m/z$  581 to  $m/z$  584 ( $x$ ) resulted in the regression equation  $y = 0.05(\pm 0.02) + 0.913(\pm 0.009)x$  ( $r = 0.995$ ). The slope value of this regression equation is very close to the ratio of the corrected concentrations of  $\text{d}_3$ -AZM, i.e.,  $323/357 = 0.905$ . In method validation experiments and in quantitative analyses of acetazolamide in urine samples, the above mentioned corrected  $\text{d}_3$ -AZM concentrations were used.

The retention time of the  $\text{R-SO}_2\text{-N(PFB)}_2$  derivatives in the standardization experiment described above was determined to be (mean  $\pm$  SD,  $n = 124$ )  $8.33 \pm 0.008$  min (RSD, 0.09%) for  $\text{d}_3$ -AZM and  $8.35 \pm 0.007$  min (RSD, 0.09%) for  $\text{d}_0$ -AZM (paired  $t$ -test,  $P < 0.0001$ ). The ratio of the retention times of  $\text{d}_0$ -AZM and  $\text{d}_3$ -AZM

was calculated to be (mean  $\pm$  SD)  $1.002 \pm 0.001$  (RSD, 0.1%), indicating a highly reproducible GC behaviour of the  $\text{R-SO}_2\text{-N(PFB)}_2$  derivatives of AZM. The PFB derivative of  $\text{d}_3$ -AZM eluted constantly in front of the PFB derivative of  $\text{d}_0$ -AZM, indicating an interaction of the acetyl groups of the PFB derivatives of  $\text{d}_3$ -AZM and  $\text{d}_0$ -AZM with the stationary phase of the GC column.

### 3.4. Accuracy and precision of the method for urinary acetazolamide

Method validation was performed using urine samples from three healthy volunteers. Native urine samples were used without dilution, yet centrifugation was performed to remove solid material. Aliquots (50  $\mu\text{L}$ ) of clear supernatants were used throughout. The internal standard  $\text{d}_3$ -AZM was added to urine samples at a final added concentration to cover a pharmacologically relevant concentration range (0–1000  $\mu\text{M}$ ). The method was validated on three days in triplicate for each concentration using the SIM of  $m/z$  83,  $m/z$  86,  $m/z$  581 and  $m/z$  584.  $\text{d}_0$ -AZM was calculated by multiplying the PAR of  $m/z$  581 to  $m/z$  584 with the  $\text{d}_3$ -AZM concentration of 323  $\mu\text{M}$  and the PAR of  $m/z$  83 to  $m/z$  86 with the  $\text{d}_3$ -AZM concentration of 357  $\mu\text{M}$  (see above). The results from the validation of the GC-MS method for acetazolamide in the human urine samples from three healthy subjects are summarized collectively in Table 1. In the urine samples spiked with  $\text{d}_3$ -AZM only, the concentration of  $\text{d}_0$ -AZM was determined to be around 1  $\mu\text{M}$ , likely originating from unlabeled acetazolamide ( $\text{d}_0$ -AZM) present in the commercially available  $\text{d}_3$ -AZM preparation (see above). The PAR values ( $y$ ) were linear in the entire concentration range of added AZM ( $x$ ). Precision (RSD) ranged between 5.3% and 12.9% for the spiked urine samples. Accuracy (recovery) ranged between 97.8% and 109.1% for AZM added to the urine samples. These data indicate that the GC-MS method is precise and accurate for the measurement of AZM in human urine.

### 3.5. Limit of detection (LOD) of the method for acetazolamide

For the determination of the LOD value of the GC-MS method, 50 nmol of  $\text{d}_0$ -AZM and 50 nmol of  $\text{d}_3$ -AZM (each 5  $\mu\text{L}$  of two separate 10 mM solutions in DMSO) were combined and derivatized as described above. The residue was reconstituted in 200  $\mu\text{L}$  toluene aliquots corresponding to an amount of 250 pmol per 1  $\mu\text{L}$ . Subsequently, serial 1:1-dilutions (by volume) with toluene were performed to construct samples containing 125, 62.5, 31.3, 15.6, 7.8, 3.9 pmol per 1  $\mu\text{L}$  toluene. Each 1  $\mu\text{L}$  of the samples was injected in triplicate and analyzed by SIM of  $m/z$  83,  $m/z$  86,  $m/z$  581 and  $m/z$  584.

The PAR values of  $m/z$  581 to  $m/z$  584 and of  $m/z$  83 to  $m/z$  86 were determined to be (mean  $\pm$  SD,  $n = 21$ )  $0.745 \pm 0.011$  and  $0.797 \pm 0.035$  ( $P < 0.0001$ , Wilcoxon test), respectively. The ratio of the signal-to-noise ( $S/N$ ) value of the peak areas of  $m/z$  581 and  $m/z$  584 was determined to be (mean  $\pm$  SD,  $n = 21$ )  $1.33 \pm 1.43$ . The  $S/N$  values of the peak areas of  $m/z$  83 and  $m/z$  86 was calculated to be (mean  $\pm$  SD,  $n = 21$ )  $1.16 \pm 0.57$ . The  $S/N$  values of  $m/z$  581,  $m/z$  584,  $m/z$  83 and  $m/z$  86 were correlated with the injected amounts of  $\text{d}_0$ -AZM and  $\text{d}_3$ -AZM derivatives ( $P < 0.0001$  for all). The corresponding Spearman correlation coefficients were 0.948, 0.916, 0.940 and 0.918. Linear regression analysis between the  $S/N$  values of  $m/z$  581,  $m/z$  584,  $m/z$  83 and  $m/z$  86 ( $y$ ) and the injected amounts of  $\text{d}_0$ -AZM and  $\text{d}_3$ -AZM ( $x$ , pmol) resulted in the regression equations  $y = -395 + 53x$  ( $r = 0.944$ ),  $y = 601 + 30x$  ( $r = 0.633$ ),  $y = 68 + 2.1x$  ( $r = 0.876$ ), and  $y = 83 + 1.98x$  ( $r = 0.813$ ), respectively.

The  $S/N$  values of the lowest injected amount (each 3.9 pmol of  $\text{d}_0$ -AZM and  $\text{d}_3$ -AZM) were determined to be  $38.7 \pm 3.2$  (RSD, 8.3%) for  $m/z$  581,  $41.0 \pm 8.0$  (RSD, 19.5%) for  $m/z$  584,  $18.3 \pm 4.55$  (RSD,

**Table 1**  
Inter- and intra-day GC-MS validation data for acetazolamide in urine samples of three healthy volunteers (1, 2, 3) using SIM of  $m/z$  581, 584, 83 and 86.

Sample	PAR 581/584			PAR 83/86		
	Urine 1	Urine 2	Urine 3	Urine 1	Urine 2	Urine 3
Day 1	$y = 0.094 + 0.00332x$ $r^2 = 0.9907$	$y = 0.066 + 0.00321x$ $r^2 = 0.9977$	$y = 0.0084 + 0.00341x$ $r^2 = 0.9952$	$y = 0.064 + 0.00313x$ $r^2 = 0.9916$	$y = 0.166 + 0.00276x$ $r^2 = 0.9773$	$y = -0.058 + 0.0033x$ $r^2 = 0.9953$
Day 2	$y = -0.055 + 0.00427x$ $r^2 = 0.9992$	$y = 0.041 + 0.00383x$ $r^2 = 0.9987$	$y = -0.018 + 0.00403x$ $r^2 = 0.9994$	$y = -0.054 + 0.00401x$ $r^2 = 0.9966$	$y = 0.102 + 0.00346x$ $r^2 = 0.9887$	$y = -0.058 + 0.00408x$ $r^2 = 0.9876$
Day 3	$y = 0.088 + 0.00365x$ $r^2 = 0.989$	$y = 0.060 + 0.00357x$ $r^2 = 0.9988$	$y = 0.074 + 0.00362x$ $r^2 = 0.9848$	$y = 0.125 + 0.00326x$ $r^2 = 0.9693$	$y = 0.167 + 0.0032x$ $r^2 = 0.968$	$y = 0.133 + 0.00319x$ $r^2 = 0.9652$
All days	$y = 0.049 + 0.00369x$ $r^2 = 0.9968$ 1/slope = 271 $\mu\text{M}$ $y = 0.032 + 0.00368x$ , $r^2 = 0.9993$ 1/slope = 272 $\mu\text{M}$ $d_3$ -AZM	$y = 0.056 + 0.00354x$ $r^2 = 0.9992$ 1/slope = 283 $\mu\text{M}$	$y = 0.009 + 0.0038x$ $r^2 = 0.9999$ 1/slope = 262 $\mu\text{M}$	$y = 0.051 + 0.0034x$ $r^2 = 0.9971$ $y = 0.067 + 0.00336x$ , $r^2 = 0.9944$ 1/slope = 298 $\mu\text{M}$ $d_3$ -AZM	$y = 0.145 + 0.0031x$ $r^2 = 0.9821$ 1/slope = 319 $\mu\text{M}$	$y = 0.006 + 0.0035x$ $r^2 = 0.9959$ 1/slope = 284 $\mu\text{M}$
AZM ( $\mu\text{M}$ )	AZM measured ( $\mu\text{M}$ ) (mean $\pm$ SD, $n = 9$ )	Precision (RSD, %)	Recovery (%)	AZM measured ( $\mu\text{M}$ ) (mean $\pm$ SD, $n = 9$ )	Precision (RSD, %)	Recovery (%)
0	1.11 $\pm$ 0.69	62.0	not applicable	1.7 $\pm$ 0.9	52.0	not applicable
200	206 $\pm$ 18	8.8	102.4	215 $\pm$ 22	10.4	106.7
400	417 $\pm$ 28	6.7	104.0	426 $\pm$ 26	6.1	106.1
600	626 $\pm$ 33	5.3	104.1	656 $\pm$ 64	9.7	109.1
800	803 $\pm$ 66	8.2	100.2	845 $\pm$ 104	12.3	105.4
1000	1002 $\pm$ 103	10.3	100.1	980 $\pm$ 127	12.9	97.8

24.6%) for  $m/z$  83, and  $14.7 \pm 6.7$  (RSD, 45%) for  $m/z$  86. These data indicate that SIM of  $m/z$  581 and  $m/z$  584 is associated with a higher precision compared to SIM of  $m/z$  83 and  $m/z$  86 for very low AZM concentrations. Extrapolation of the mean  $S/N$  value of 39 to an  $S/N$  value of 3 (for  $m/z$  581) yields an LOD value of about 0.3 pmol (300 fmol, 67 pg) for the  $d_0$ -AZM derivative (SIM of  $m/z$  581,  $m/z$  584,  $m/z$  83 and  $m/z$  86; 50 ms dwell-time for each ion).

### 3.6. Limit of quantitation (LOQ) for acetazolamide in human urine

The LOQ of the method for urinary acetazolamide was determined in the same urine samples (each three 50  $\mu\text{L}$  aliquots) used in the method validation. In this experiment, urine samples were spiked with  $d_0$ -AZM to reach final added concentrations of 0, 25, 50, 100, 150 and 200  $\mu\text{M}$ . The concentration of  $d_3$ -AZM added to the urine samples was 250  $\mu\text{M}$ . Each toluene extract was injected three times and SIM of  $m/z$  581,  $m/z$  584,  $m/z$  83 and  $m/z$  86 with 50 ms dwell-time for each ion was performed.

Plotting the PAR of  $m/z$  581 to  $m/z$  584 ( $y_1$ ) versus the concentration of  $d_0$ -AZM added to urine ( $x_1$ ,  $\mu\text{M}$ ) yielded the regression equation  $y_1 = 0.018 + 0.00381x_1$  ( $r = 0.9983$ ). Plotting the PAR of  $m/z$  83 to  $m/z$  86 ( $y_2$ ) versus the concentration of  $d_0$ -AZM added to urine ( $x_2$ ,  $\mu\text{M}$ ) yielded the regression equation  $y_2 = 0.018 + 0.0035x_1$  ( $r = 0.9943$ ). The reciprocal slope values correspond to  $d_3$ -AZM concentrations of 262  $\mu\text{M}$  and 283  $\mu\text{M}$ , respectively, which are close to the nominal concentration of 250  $\mu\text{M}$ . Acetazolamide was determined in the urine samples of this experiment with a precision ranging between 1.9% and 7%, and with a recovery ranging between 101% and 120%. The lowest added  $d_0$ -AZM concentration of 25  $\mu\text{M}$  was determined with a precision of 5% (using  $m/z$  581 and  $m/z$  584) and 7% (using  $m/z$  83 and  $m/z$  86). The corresponding recovery values were 120.5% and 120%. These data suggest that the LOQ value for acetazolamide in 50  $\mu\text{L}$  aliquots human urine samples is 25  $\mu\text{M}$  or lower using SIM of  $m/z$  581,  $m/z$  584,  $m/z$  83 and  $m/z$  86. The results of this experiment are summarized in Table 2.

### 3.7. Stability of PFB derivatives of acetazolamide in toluene

The stability of the PFB derivatives of  $d_0$ -AZM and  $d_3$ -AZM in toluene extracts from 50  $\mu\text{L}$  aliquots of a human urine sample

spiked with 0, 250, 500, 750 and 1000  $\mu\text{M}$  of  $d_0$ -AZM and with the fixed concentration of 250  $\mu\text{M}$  of  $d_3$ -AZM (see above) were analyzed immediately after sample work up and after storage at room temperature (about 18  $^\circ\text{C}$ ) for 21 days.

Linear regression analysis between the PAR values of  $m/z$  581 to  $m/z$  584 ( $y_1$ ) and  $d_0$ -AZM concentration in urine ( $x_1$ ) resulted in the regression equations  $y_1 = 0.074 + 0.0036x_1$  ( $r = 0.9950$ ) for day 1 and  $y_1 = -0.006 + 0.0039x_1$  ( $r = 0.9969$ ) for day 21. Linear regression analysis between the PAR values of  $m/z$  83 to  $m/z$  86 ( $y_2$ ) and the  $d_0$ -AZM concentration in urine ( $x_2$ ) resulted in the regression equations  $y_2 = 0.135 + 0.0034x_2$  ( $r = 0.9877$ ) for day 1 and  $y_2 = 0.011 + 0.0037x_2$  ( $r = 0.9965$ ) for day 21. Considering the data of all samples of this experiment, the peak area (arbitrary unit, a.u.) of the  $d_3$ -AZM derivative ( $m/z$  584) decreased by a mean factor of 2.6 (mean  $\pm$  SEM; from 7,186,105  $\pm$  71,508 a.u. on day 1 to 2,807,011  $\pm$  98,903 a.u. on day 21). The corresponding values for the peak area of  $m/z$  86 decreased by a mean factor of 1.5 (mean  $\pm$  SEM; from 4,379,094  $\pm$  86,864 a.u. to 3,001,832  $\pm$  183,046 a.u.). The PAR of  $m/z$  86 to  $m/z$  584 was (mean  $\pm$  SEM) 0.586  $\pm$  0.022 on day 1 (PAR<sub>1d</sub>) and 1.096  $\pm$  0.039 on day 21 (PAR<sub>21d</sub>), resulting in a PAR<sub>21d</sub>/PAR<sub>1d</sub> ratio of 1.94  $\pm$  0.16. These data indicate that the PFB derivatives of  $d_0$ -AZM (from urine samples spiked with 0–1000  $\mu\text{M}$   $d_0$ -AZM) and  $d_3$ -AZM (from the same urine samples spiked at 250  $\mu\text{M}$ ) in toluene are relatively stable when stored for 21 days at 18  $^\circ\text{C}$ .

### 3.8. Biomedical application

We tested the usefulness of our GC-MS method in the setting of a pilot study. One healthy volunteer (female, 29 years of age, 70 kg), being an author of this article, ingested 250 mg acetazolamide (one tablet Acemit® from medphano, Germany). Before (time zero) and after (up to 5 h) drug administration urine samples were collected in polypropylene bottles pre-cooled in an ice bath. The pH of the urine samples was measured, the urine specimens were aliquoted, and the samples were analyzed for nitrate, nitrite and creatinine with previously reported GC-MS methods after acidification by using a 20 vol % acetic acid solution to remove  $\text{CO}_2/\text{NaHCO}_3/\text{Na}_2\text{CO}_3$  [2,3]. The urinary concentration of acetazolamide was measured in 50  $\mu\text{L}$  aliquots as described in this article by SIM of  $m/z$  581,  $m/z$  584,  $m/z$  83 and  $m/z$  86. The concentration of the internal standard was

**Table 2**

Results of the experiment performed to determine the LOQ of the GC-MS method for acetazolamide (AZM) in human urine.

Added AZM ( $\mu\text{M}$ )	PAR 581/584	Measured AZM ( $\mu\text{M}$ )	Precision (RSD, %)	Recovery (%)	PAR 83/86	Measured AZM ( $\mu\text{M}$ )	Precision (RSD, %)	Recovery (%)
0	$0.006 \pm 0.004$	$1.57 \pm 1.05$	66.9	not applicable	$0.008 \pm 0.002$	$2.26 \pm 0.57$	25.2	not applicable
25	$0.121 \pm 0.006$	$31.7 \pm 1.57$	5.0	120.5	$0.114 \pm 0.008$	$32.3 \pm 2.26$	7.0	120
50	$0.217 \pm 0.007$	$56.9 \pm 1.83$	3.2	110.7	$0.200 \pm 0.004$	$56.6 \pm 1.13$	2.0	108.7
100	$0.396 \pm 0.010$	$103.8 \pm 2.62$	2.5	102.2	$0.367 \pm 0.019$	$103.9 \pm 5.4$	5.2	101.6
150	$0.593 \pm 0.011$	$155.4 \pm 2.88$	1.9	102.6	$0.550 \pm 0.015$	$155.7 \pm 4.2$	2.7	102.3
200	$0.777 \pm 0.019$	$203.6 \pm 5.0$	2.5	101.0	$0.723 \pm 0.047$	$204.6 \pm 13.3$	6.5	101.2

250  $\mu\text{M}$  in all urine samples. Urinary excretion of nitrate, nitrite, creatinine and acetazolamide was corrected for urinary creatinine excretion and the creatinine-corrected excretion rates are expressed as  $\mu\text{mol}$  analyte per  $\text{mmol}$  creatine ( $\mu\text{mol}/\text{mmol}$ ).

After a lag-time of about 0.5 h, the creatinine-corrected excretion of acetazolamide increased almost linearly within the subsequent 1.5 h to reach the value 96  $\mu\text{mol}/\text{mmol}$ , which remained almost unchanged for the next 3 h (Fig. 3A). SIM of  $m/z$  581 and  $m/z$  584, and SIM of  $m/z$  83 and  $m/z$  86 resulted in closely correlating acetazolamide concentrations using urine volumes of 50  $\mu\text{L}$  ( $r = 0.929$ ). Similar results were also obtained by using urine volumes of 40, 30, 20, 10 and 5  $\mu\text{L}$  from this study (Fig. S5). The creatinine-corrected excretion rates of nitrite and nitrate increased in parallel to reach their maximum values about 1 h after acetazolamide ingestion (Fig. 3B). The pH value of the urine samples collected in this experiment increased from 7.10 before acetazolamide ingestion to 7.65 after 1.5 h (Fig. 3C). The highest concentration of acetazolamide measured in the urine samples of this experiment was 278  $\mu\text{M}$ . GC-MS chromatograms from analyses of urine samples from this experiment are shown in Fig. 4. The acetazolamide concentrations in the urine samples measured in the present study are in agreement with previously reported data using other analytical methods such as HPLC [7,8,29,30], indicating a relatively constant and long-lasting excretion of acetazolamide. The acetazolamide concentrations in blood of humans ingested acetazolamide have also been reported to be relatively constant for many hours upon acetazolamide ingestion at therapeutic doses [31,32].

The results with respect to urinary excretion of nitrite and nitrate collaborate with our previous observations, indicating reversible acetazolamide-dependent inhibition of nitrite and nitrate reabsorption in the kidney [2,3].

#### 4. Discussion

The sulfonamide group ( $\text{R-SO}_2\text{-NH}_2$ ) is common to many classes of drugs. Acetazolamide is one of the oldest and structurally simplest and still therapeutically used sulfonamide drugs, administered for the treatment of many diseases [1], but also used as a potential performance-enhancing drug in sport doping [5]. We have recently shown that acetazolamide ingested at therapeutic doses by healthy subjects enhanced excretion of  $\text{HCO}_3^-$  and inorganic nitrite ( $\text{NO}_2^-$ ) in urine [2–4], most likely by inhibiting nitrite-dependent renal CA activity and by additional not yet well understood mechanisms. This newly recognized pharmacological action of acetazolamide may be of particular importance, since  $\text{NO}_2^-$  is considered an abundant reservoir of NO, one of the strongest endogenous vasodilators. In order to better understand the effects of acetazolamide on nitrite excretion in vivo in humans, reliable analytical methods for the quantitative measurement of acetazolamide in urine are required.

Nowadays, liquid chromatography-tandem mass spectrometry (LC-MS/MS) is one of the most efficient analytical techniques used to measure numerous analytes in biological samples, commonly

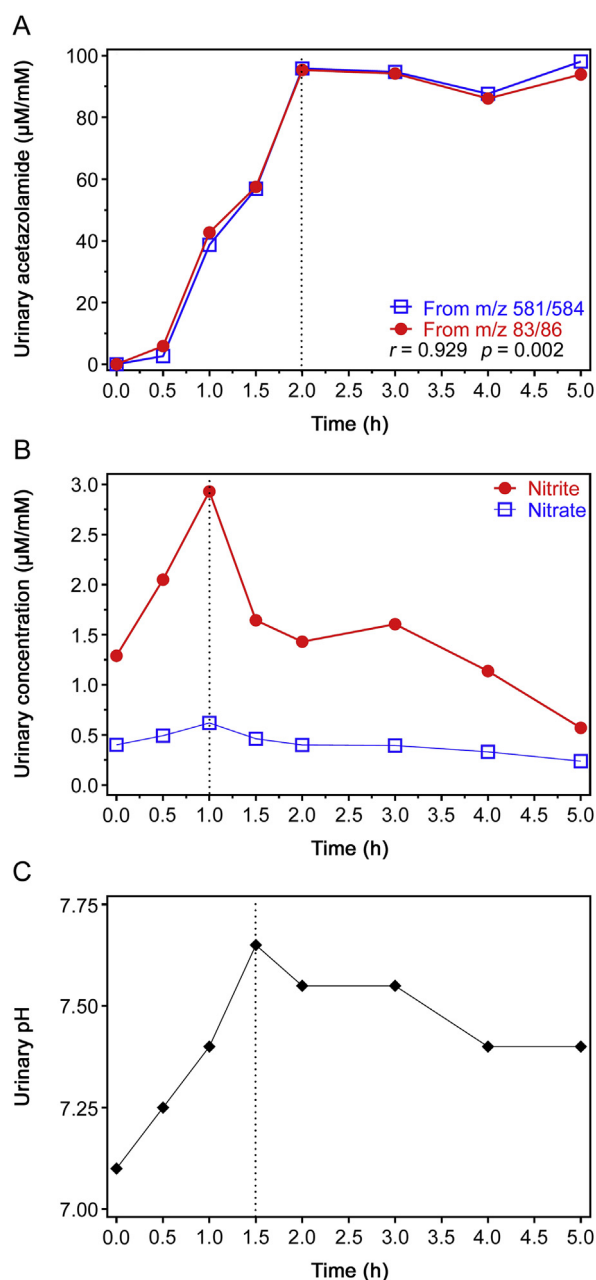


**Fig. 3.** Creatinine-corrected urinary excretion of (A) acetazolamide and (B) nitrate and nitrite, and (C) urinary pH before (0 h) and after ingestion of a 250 mg tablet acetazolamide. The arrows indicate the time point of ingestion.

with negligible labour and without analyte derivatization. This has been recently demonstrated for the measurement of acetazolamide in human plasma [6]. Historically, GC-MS was the first instrumental technique combining chromatographic with MS separation and

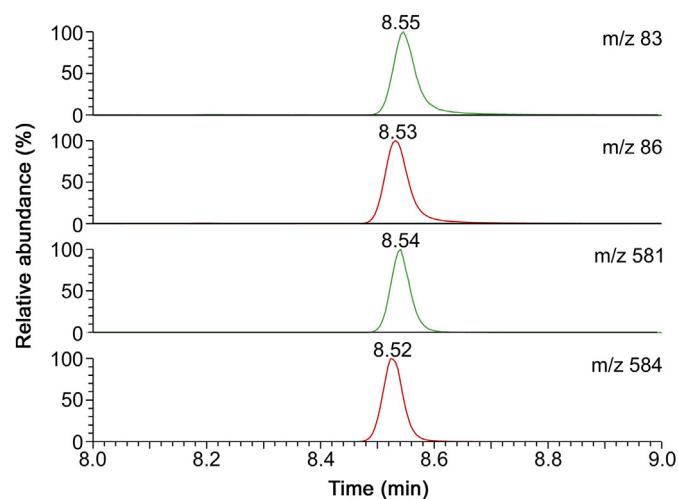


**Fig. 4.** GC-MS chromatograms from the analysis of acetazolamide in urine (50  $\mu$ L) collected 2 h after ingestion of a 250 mg acetazolamide tablet (Acemet®). SIM of  $m/z$  83, 86, 581 and 584 was performed. The concentration of the internal standard was 250  $\mu$ M. The retention time of 8.53 min is due to the use of a new GC column.

gained a wide application area in various disciplines, notably including pharmacology. Concerning acetazolamide and other sulfonamides, derivatization of the amino group is indispensable in GC-based methods. Alkylation (e.g., with iodomethane) and silylation (e.g., with MSTFA) of the amine group of sulfonamides including acetazolamide have been used for their analysis by GC-MS and GC-MS/MS using electron ionization [14,21]. In GC-MS-based methods using negative-ion chemical ionization (NICI), incorporation of fluorine (F) atoms in the analytes by using F-containing derivatization reagents such as PFB-Br, PFB-Cl and PFPFA, enhances analytical sensitivity by several orders of magnitude. In the present work, we tested these derivatization reagents and the silylation reagent BSTFA for the GC-MS analysis of acetazolamide and other sulfonamides including methazolamide and dorzolamide. For this we used derivatization procedures that have been turned out to be very useful for some analytes including creatinine [24], dimethylamine [26] and amino acids [27].

In the present work, the most useful derivatization reagent for acetazolamide was found to be PFB-Br. PFB-Br is a versatile derivatization reagent [22]. Derivatization reactions with PFB-Br can be performed directly in aqueous solutions including human plasma and urine, as has been demonstrated by us for carbonate [2], nitrite and nitrate [23], and creatinine [24]. Derivatization reactions with PFB-Br can also be performed indirectly in non-aqueous solutions such as in anhydrous acetonitrile in the presence of a base serving as the catalyst. This derivatization approach is most useful for long-chain carboxylic acids including the eicosanoids [28]. In the present study, we found that acetazolamide can be derivatized with PFB-Br in anhydrous acetonitrile to form a di-PFB derivative  $[\text{RSO}_2\text{N}(\text{PFB})_2]$  under very mild derivatization conditions (60 min, 30  $^{\circ}\text{C}$ ). For the measurement of acetazolamide in urine, urine-water is completely removed under a stream of nitrogen. The solid residue is then reconstituted in anhydrous acetonitrile. After derivatization complete removal of acetonitrile, remaining base and PFB-Br reagent is performed under a stream of nitrogen gas; the remaining charge-free PFB derivative of acetazolamide is reconstituted in toluene, which is best suited as a solvent for PFB derivatives. We found that methazolamide and dorzolamide can also be converted to their di-PFB derivatives, suggesting the general use of PFB-Br for the derivatization of the sulfonamide group of organic sulfonamides. Using sulfonamides with larger molecular weights, we found that

this derivatization reaction is limited by the size of the sulfonamide analyte rather than by the reactivity of the sulfonamide group towards PFB-Br. To our knowledge this is the first work to report on the derivatization of acetazolamide with PFB-Br.

Due to our interest in acetazolamide as a pharmacological potent carbonic anhydrase (CA) inhibitor [1], we developed and validated a straightforward GC-MS method for the precise and accurate quantitative measurement of acetazolamide in 50  $\mu$ L aliquots of human urine using a commercially available isotopically labelled internal standard,  $[\text{acetylo-}^2\text{H}_3]\text{acetazolamide}$  ( $d_3\text{-AZM}$ ). NICI of the PFB derivative of acetazolamide generates multiple ions, from which some are characteristic for acetazolamide. These anions are  $m/z$  581,  $m/z$  83 and  $m/z$  58. NICI of the PFB derivative of the internal standard  $[\text{acetylo-}^2\text{H}_3]\text{acetazolamide}$  generates multiple ions including  $m/z$  584,  $m/z$  86 and  $m/z$  58. The mass fragment at  $m/z$  58 is obtained from the PFB derivatives of both, unlabeled acetazolamide and  $[\text{acetylo-}^2\text{H}_3]\text{acetazolamide}$ . Therefore, the ion  $m/z$  58 cannot be used for quantitative measurements using  $[\text{acetylo-}^2\text{H}_3]\text{acetazolamide}$  as the internal standard. The method validation demonstrated that SIM of  $m/z$  581,  $m/z$  584,  $m/z$  83 and  $m/z$  86 is specific for acetazolamide and provides closely comparable results in human urine in a pharmacologically relevant concentration range of acetazolamide.

We applied the method to measure acetazolamide in urine samples collected before and for 5 h after ingestion of a 250 mg acetazolamide (1.11 mmol) tablet by a healthy young volunteer. Two hours after ingestion, the creatinine-corrected excretion rate reached a relative constant plateau at the value of 96  $\mu$ mol acetazolamide per mmol creatinine. This observation is in line with observations from other studies, which used HPLC with ultraviolet absorbance detection after solvent extraction of acetazolamide [5]. A similar pharmacokinetic behaviour has been reported for acetazolamide in human plasma by other groups [31,32], suggesting a fairly constant long-term equilibrium between circulating and excretory acetazolamide.

In the urine samples of the present study, we also measured the concentration of nitrite and nitrate by GC-MS as PFB derivatives [23] and the pH value of the urine samples. In confirmation of previous findings of our group, we found that the creatinine-corrected excretion rate of nitrite and nitrate reached temporary maximum values. This observation suggests that acetazolamide inhibited the CA-dependent reabsorption of nitrite and nitrate in the kidney [2–4]. In the present study, urinary pH reached its maximum value approximately 1.5 h post-ingestion. Previously, we found that ingested acetazolamide increased the excretion of bicarbonate in the urine with a kinetics resembling that of nitrite and nitrate [2,3]. All these observations suggest that excretion of nitrite and nitrate in the urine partly depends upon the CA activity in the proximal tubule of the kidney. Further, the different kinetics of urinary (and circulating) acetazolamide compared to that of nitrite, nitrate and bicarbonate suggests that acetazolamide inhibits renal CA activity in two phases. First, acetazolamide inhibits acutely and strongly the CA activity 1–2 h post-ingestion, resulting in temporary inhibition of the reabsorption of urinary nitrite, nitrate and bicarbonate in the kidney. Consecutively, acetazolamide inhibits weakly but sustainably the activity of CA; inhibition of the CA activity in this phase is presumably not associated with nitrite and nitrate reabsorption, but is apparently associated with inhibition of urinary bicarbonate reabsorption in the kidney.

Table 3 summarizes main characteristics of our GC-MS method in comparison with those of previously reported LC- and GC-based methods for the measurement of acetazolamide in human urine and other biological samples. For the quantification of acetazolamide in human urine by GC-MS, we used only 50  $\mu$ L urine volume, while others used up to 5 mL urine in the GC-MS methods (Table 3).

**Table 3**

Reported liquid chromatographic (LC) and gas chromatographic (GC) methods for the quantification of acetazolamide in human urine, plasma or serum.

Method	Matrix	Column	Derivatization	Mobile phase	Sample preparation	LOD; LOQ	Ref.
<b>Liquid chromatography</b>							
LC-MS/MS	Plasma	Hypurity advance (50 mm × 4.6 mm)	none	MeCN + 0.1% FA	100 µL plasma + IS + FA. SPE. Evaporation to dryness and reconstitution with 500 µL MeCN + 0.1% FA	n.r.; 50 ng/mL	[6]
HPLC-DAD	Urine	HP-Hypersil ODS-Cl <sub>8</sub> (250 mm × 4.0 mm)	none	A: phosphate buffer; B: MeCN	2 mL urine + 0.5 g sodium phosphate + 0.5 g NaCl. Extraction with 4 mL EA, addition of 5% lead acetate to the organic phase. Centrifugation, evaporation to dryness, reconstitution in 300 µL MeOH; 10 µL injection	8 ng/mL	[7]
HPLC-DAD	Urine	HP-LiChrospher 100 RP 18 (125 mm × 4.0 mm)	none	MeCN-H <sub>2</sub> O	native urine; column-switching technique	10 ng/mL	[8]
LC-MS/MS	Plasma (beagle)	Shimadzu VP-ODS C <sub>18</sub> (150 mm × 2.0 mm)	none	A: H <sub>2</sub> O; B: MeCN	100 µL plasma + IS. Protein precipitation with 600 µL MeCN.	n.r.; 200 ng/mL	[9]
UHPLC-HRMS	Urine	Zorbax SB-C <sub>8</sub> (2.1 mm × 50 mm)	none	A: H <sub>2</sub> O + 1 mM ammonium acetate + 0.001% AA; B: MeOH + 1 mM ammonium acetate + 0.001% AA	100 µL urine + IS; centrifugation	50 ng/mL; n.r.	[10]
LC-MS/MS	Urine	Supelco Discovery HS-C18 (50 mm × 2.1 mm)	none	A: H <sub>2</sub> O + 0.2% FA; B: MeOH + 0.2% FA	SPE. Evaporation to dryness and reconstitution with H <sub>2</sub> O + 0.2% FA. Filtration through a 0.45-µm membrane.	25 ng/mL; n.r.	[11]
UHPSFC-MS/MS	Urine	Acquity UPC2 BEH (100 mm × 3.0 mm)	none	CO <sub>2</sub> + MeOH + 10 mM FA + 2% H <sub>2</sub> O	100 µL urine and 10-fold dilution with H <sub>2</sub> O-MeCN	0.15 ng/mL; n.r.	[12]
<b>Gas chromatography</b>							
GC-ECD	Serum	Glass columns (150 cm × 0.18 cm)	CH <sub>3</sub> I	Nitrogen	100 µL serum + IS + 1 mL tetrapentylammonium + 0.2 mL NaOH + H <sub>2</sub> O. Addition of 1 mL CH <sub>2</sub> Cl <sub>2</sub> with 5% CH <sub>3</sub> I. Evaporation of the organic phase, reconstitution with 1 mL toluene washing with aqueous silver sulphate.	500 ng/mL	[13]
GC-MS	Urine	HP Ultra 1 (25 m × 0.20 mm)	CH <sub>3</sub> I	Helium	1 mL urine + 25 µL NaOH 6 M + IS + 150 µL tetrahexylammonium hydrogensulphate + 5 mL CH <sub>3</sub> I. Extraction with toluene, centrifugation. Filtration through SM-7 resin, evaporation to dryness and reconstitution in 100 µL toluene.	50 ng/mL; n.r.	[14]
GC-MS	Urine	HP (25 m × 0.20 mm)	CH <sub>3</sub> I	Helium	5 mL urine + IS, filtration through XAD-2 resin. Evaporation to dryness and reconstitution with 200 µL Me <sub>2</sub> CO. Addition of 20 µL CH <sub>3</sub> I and K <sub>2</sub> CO <sub>3</sub> . Derivatization for 3 h at 60 °C.	n.r.	[15]
GC-MS	Urine	DB1 MS (5 m × 0.10 mm)	CH <sub>3</sub> I	Helium	2 mL urine + 80 µL NaOH + 1 mL CH <sub>2</sub> Cl <sub>2</sub> -2-propanol. Reconstitution with 50 mg K <sub>2</sub> CO <sub>3</sub> + 400 µL of Me <sub>2</sub> CO/CH <sub>3</sub> I. Derivatization using microwaves for 10 min at 900 W.	3 ng/mL	[16]
GC-MS	Urine	VF-DA (12 m × 0.20 mm)	CH <sub>3</sub> I	Helium	Evaporation to dryness and reconstitution with 100 µL Me <sub>2</sub> CO. 5 mL urine + IS + 200 mg Na <sub>2</sub> SO <sub>4</sub> + NaOH + 5 mL organic solvent. Evaporation to dryness and reconstitution with CH <sub>3</sub> I.	50 ng/mL; n.r.	[17]
GC-MS	Urine	HP-1 (12 m × 0.2 mm)	CH <sub>3</sub> I	Helium	2 mL urine + 0.02 THA + 6 mL CH <sub>3</sub> I in toluene. Derivatization for 30 min at 50 °C. SPE. Evaporation to dryness and reconstitution with 50 µL EA.	10 ng/mL; n.r.	[18]
GC-MS	Urine	HP5 (18 m × 0.2 mm)	CH <sub>3</sub> I	Helium	5 mL urine + IS. SPE. Evaporation to dryness. Derivatization with CH <sub>3</sub> I in acetone + 50 mg K <sub>2</sub> CO <sub>3</sub> under microwave irradiation.	50 ng/mL	[19]
GC-MS	Urine	Agilent Ultra 1 (17 m × 0.2 mm)	MSTFA NH <sub>4</sub> I, PrSH	Helium	2.5 mL urine + acetate buffer + IS + Na <sub>2</sub> CO <sub>3</sub> . Extraction with diethylether-2-propanol (5:1, v/v) + Na <sub>2</sub> SO <sub>4</sub> . Evaporation to dryness. Two-step silylation: 1) 50 µL MSTFA + MeCN (10 min, 80 °C); 2) 50 µL MSTFA/NH <sub>4</sub> I/PrSH (10 min, 80 °C)	n.r.	[21]
GC-MS	Urine	Optima 17 (15 m × 0.25 mm)	PFB-Br	Helium	50 µL urine + IS, evaporation to dryness. Addition of 100 µL EtOH, evaporation to dryness. Reconstitution with 100 µL MeCN + 10 µL PFB-Br + 10 µL Hünig base, 60 min at 30 °C. Evaporation to dryness and reconstitution with 200 µL toluene.	0.3 pmol; 25 µM	Present study

Abbreviations. AA, acetic acid; EA, ethyl acetate; EtOH, ethanol; FA, formic acid/formate; IS, internal standard; MeCN, acetonitrile; MeOH, methanol; Me<sub>2</sub>CO, acetone; n.r., not reported; SPE, solid-phase extraction.

In the vast majority of reported GC-based methods, acetazolamide was analyzed after derivatization mostly using CH<sub>3</sub>I. In our GC-MS method we used PFB-Br for derivatization of the sulfonamide group. This allows for a highly sensitive measurement of acetazolamide with minimum urine volume and sample work up. The LOQ value of our method may be reduced by increasing the urine volume and by decreasing the toluene volume. For practical reasons we used 200 µL aliquots of toluene for reconstituting the acetazolamide derivative. Reduction of the toluene volume is limited for technical reasons. In our GC-MS system the minimum solvent volume is about 50 µL in commercially available autosampler vials including microinserts. In LC-based methods, acetazolamide is generally analyzed without any derivatization step as they utilize the UV absorbance of acetazolamide. In HPLC methods with UV absorbance detection, endogenous compounds may interfere with the measurement of acetazolamide in human urine, despite the use of extraction steps such as solvent extraction with ethyl acetate [7]. By using an HPLC system previously reported for the analysis of reduced glutathione (GSH) as *o*-phthaldialdehyde (OPA) derivative [33], we observed co-elution of unknown endogenous compound(s) with acetazolamide which may become important in the lower µM-range (Fig. S6). As the extent of such interferences is unpredictable, accurate measurement of low concentrations of acetazolamide in human urine may be seriously compromised.

## 5. Conclusion

Acetazolamide, an organic sulfonamide drug (RSO<sub>2</sub>NH<sub>2</sub>) and a potent CA inhibitor, can be derivatized with PFB-Br in anhydrous acetonitrile using an organic base as the catalyst to form RSO<sub>2</sub>N(PFB)<sub>2</sub>. Derivatization of acetazolamide of urinary origin is performed under mild conditions (30 °C, 1 h) after evaporation of the urine water to dryness without prior extraction from the urine. In routine, acetazolamide can be analyzed quantitatively in urine (50 µL urine; range, 0–1000 µM acetazolamide; 200 µL toluene) by GC-MS in NICI mode using [*acetylo*-<sup>2</sup>H<sub>3</sub>]acetazolamide as the internal standard (250 µM). Ingestion of a 250 mg acetazolamide containing tablet by a healthy volunteer resulted in constant creatinine-corrected excretion rates of acetazolamide in the urine and in reversible inhibition of the reabsorption of urinary nitrite and nitrate after about 1.5 h. The PFB-Br derivatization procedure is applicable to the measurement of methazolamide, another sulfonamide. The size of the organic moiety of the sulfonamide drug rather than the reactivity of its sulfonamide group towards PFB-Br limits the application of the GC-MS method to other larger sulfonamides.

## Acknowledgments

Olga Begou is recipient of an ERASMUS+ (ID code GTHESSAL01) studentship from the Aristotle University of Thessaloniki, Greece.

## Conflicts of interest

The authors declare that there are no conflicts of interest.

## Appendix A. Supplementary data

Supplementary data to this article can be found online at <https://doi.org/10.1016/j.jpha.2019.11.006>.

## References

- [1] C.T. Supuran, Carbonic anhydrases: novel therapeutic applications for inhibitors and activators, *Nat. Rev. Drug Discov.* 7 (2008) 168–181.
- [2] D. Tsikas, K. Chobanyan-Jürgens, Quantification of carbonate by gas chromatography-mass spectrometry, *Anal. Chem.* 82 (2010) 7897–7905.
- [3] K. Chobanyan-Jürgens, A. Schwarz, A. Böhmer, et al., Renal carbonic anhydrases are involved in the reabsorption of endogenous nitrite, *Nitric Oxide* 26 (2012) 126–131.
- [4] D. Tsikas, E. Hanff, A. Bollenbach, et al., Results, meta-analysis and a first evaluation of U<sub>NOxR</sub>, the urinary nitrate-to-nitrite molar ratio, as a measure of nitrite reabsorption in experimental and clinical settings, *Amino Acids* 50 (2018) 799–821.
- [5] A.B. Cadwallader, X. de la Torre, A. Tieri, et al., The abuse of diuretics as performance-enhancing drugs and masking agents in sport doping: pharmacology, toxicology and analysis, *Br. J. Pharmacol.* 161 (2010) 1–16.
- [6] A. Narapuseetti, LC-MS/MS assay for acetazolamide, a carbonic anhydrase inhibitor in human plasma and its clinical application, *J. Young Pharm.* 7 (2015) 438–445.
- [7] R. Herráez-Hernández, P. Campíns-Falcó, A. Sevillano-Cabeza, Determination of acetazolamide in human urine samples by reversed-phase high-performance liquid chromatography in the presence of xanthines, *J. Chromatogr.* 582 (1992) 181–187.
- [8] P. Campíns-Falcó, R. Herráez-Hernández, A. Sevillano-Cabeza, Application of column-switching techniques to the determination of medium polarity drugs: determination of acetazolamide in urine, *J. Chromatogr. B Biomed. Appl.* 654 (1994) 85–90.
- [9] X. Li, N. Li, C. Wang, et al., Development and validation of a simple and reliable LC-MS/MS method for the determination of acetazolamide, an effective carbonic anhydrase inhibitor, in plasma and its application to a pharmacokinetic study, *Drug Res.* 64 (2014) 499–504.
- [10] A.J. Girón, K. Deventer, K. Roels, et al., Development and validation of an open screening method for diuretics, stimulants and selected compounds in human urine by UHPLC-HRMS for doping control, *Anal. Chim. Acta* 721 (2012) 137–146.
- [11] K.F. Hsu, K.-Y. Chien, G.P. Chang-Chien, et al., Liquid chromatography-tandem mass spectrometry screening method for the simultaneous detection of stimulants and diuretics in urine, *J. Anal. Toxicol.* 35 (2011) 665–674.
- [12] L. Nováková, M. Rentsch, A. Grand-Guillaume Perrenoud, et al., Ultra high performance supercritical fluid chromatography coupled with tandem mass spectrometry for screening of doping agents. II: analysis of biological samples, *Anal. Chim. Acta* 853 (2015) 647–659.
- [13] C. Fagerlund, P. Hartvig, B. Lindström, Extractive alkylation of sulphonamide diuretics and their determination by electron-capture gas chromatography, *J. Chromatogr.* 168 (1979) 107–116.
- [14] A.M. Lisi, G.J. Trout, R. Kazlauskas, Screening for diuretics in human urine by gas chromatography-mass spectrometry with derivatisation by direct extractive alkylation, *J. Chromatogr.* 563 (1991) 257–270.
- [15] D. Carreras, C. Imaz, R. Navajas, et al., Comparison of derivatization procedures for the determination of diuretics in urine by gas chromatography-mass spectrometry, *J. Chromatogr. A* 683 (1994) 195–202.
- [16] V. Morra, P. Davit, P. Capra, et al., Fast gas chromatographic/mass spectrometric determination of diuretics and masking agents in human urine: development and validation of a productive screening protocol for antidoping analysis, *J. Chromatogr. A* 1135 (2006) 219–229.
- [17] O. Zaporozhets, I. Tsyurulneva, M. Ischenko, Determination of 8 diuretics and probenecid in human urine by gas chromatography-mass spectrometry: confirmation procedure, *Am. J. Anal. Chem.* 3 (2012) 320–327.
- [18] J. Beyer, A. Bieri, F.T. Peters, et al., Screening procedure for detection of diuretics and uricosurics and/or their metabolites in human urine using gas chromatography-mass spectrometry after extractive methylation, *Ther. Drug Monit.* 27 (2005) 509–520.
- [19] L. Amendola, C. Colamonicí, M. Mazzarino, et al., Rapid determination of diuretics in human urine by gas chromatography-mass spectrometry following microwave assisted derivatization, *Anal. Chim. Acta* 475 (2003) 125–136.
- [20] R. Ventura, J. Segura, Detection of diuretic agents in doping control, *J. Chromatogr. B* 687 (1996) 127–144.
- [21] P. Kioussi, Y.S. Angelis, E. Lyris, et al., Two-step silylation procedure for the unified analysis of 190 doping control substances in human urine samples by GC-MS, *Bioanalysis* 1 (2009) 1209–1224.
- [22] D. Tsikas, Pentafluorobenzyl bromide-A versatile derivatization agent in chromatography and mass spectrometry: I. Analysis of inorganic anions and organophosphates, *J. Chromatogr. B* 1043 (2017) 187–201.
- [23] D. Tsikas, Simultaneous derivatization and quantification of the nitric oxide metabolites nitrite and nitrate in biological fluids by gas chromatography/mass spectrometry, *Anal. Chem.* 72 (2000) 4064–4072.
- [24] D. Tsikas, A. Wolf, A. Mitschke, et al., GC-MS determination of creatinine in human biological fluids as pentafluorobenzyl derivative in clinical studies and biomonitoring: inter-laboratory comparison in urine with Jaffé, HPLC and enzymatic assays, *J. Chromatogr. B* 878 (2010) 2582–2592.
- [25] D. Tsikas, A.A. Kayacelebi, E. Hanff, et al., GC-MS and GC-MS/MS measurement of ibuprofen in 10-µL aliquots of human plasma and mice serum using [*α*-methyl-<sup>2</sup>H<sub>3</sub>]ibuprofen after ethyl acetate extraction and pentafluorobenzyl bromide derivatization: discovery of a collision energy-dependent H/D isotope effect and pharmacokinetic application to inhaled ibuprofen-arginine in mice, *J. Chromatogr. B* 1043 (2017) 158–166.
- [26] K. Chobanyan, A. Mitschke, F.-M. Gutzki, et al., Accurate quantification of dimethylamine (DMA) in human plasma and serum by GC-MS and GC-tandem MS as pentafluorobenzamide derivative in the positive-ion

- chemical ionization mode, *J. Chromatogr. B* 851 (2007) 240–249.
- [27] E. Hanff, S. Ruben, M. Kreuzer, et al., Development and validation of GC–MS methods for the comprehensive analysis of amino acids in plasma and urine and applications to the HELLP syndrome and pediatric kidney transplantation: evidence of altered methylation, transamidation, and arginase activity, *Amino Acids* 51 (2018) 529–547.
- [28] D. Tsikas, Application of gas chromatography-mass spectrometry and gas chromatography-tandem mass spectrometry to assess in vivo synthesis of prostaglandins, thromboxane, leukotrienes, isoprostanes and related compounds in humans, *J. Chromatogr. Biomed. Sci. Appl.* 717 (1998) 201–245.
- [29] W.A. Ritschel, C. Paulos, A. Arancibia, et al., Urinary excretion of acetazolamide in healthy volunteers after short- and long-term exposure to high altitude, *Methods Find. Exp. Clin. Pharmacol.* 20 (1998) 133–137.
- [30] A.J. Hampson, S. Babalonis, M.R. Lofwall, et al., Pharmacokinetic study examining acetazolamide as a novel adherence marker for clinical trials, *J. Clin. Psychopharmacol.* 36 (2016) 324–332.
- [31] I. Yano, A. Takayama, M. Takano, et al., Pharmacokinetics and pharmacodynamics of acetazolamide in patients with transient intraocular pressure elevation, *Eur. J. Clin. Pharmacol.* 54 (1998) 63–68.
- [32] W.A. Ritschel, C. Paulos, A. Arancibia, et al., Pharmacokinetics of acetazolamide in healthy volunteers after short- and long-term exposure to high altitude, *J. Clin. Pharmacol.* 38 (1998) 533–539.
- [33] A. Böhmer, J. Jordan, D. Tsikas, High-performance liquid chromatography ultraviolet assay for human erythrocytic catalase activity by measuring glutathione as *o*-phthalaldehyde derivative, *Anal. Biochem.* 410 (2011) 296–303.



Contents lists available at ScienceDirect

## Journal of Pharmaceutical Analysis

journal homepage: [www.elsevier.com/locate/jpa](http://www.elsevier.com/locate/jpa)

## Original Article

## Analysis of pesticide residues in commercially available chenpi using a modified QuEChERS method and GC-MS/MS determination

Shuang Li<sup>a,b</sup>, Peipei Yu<sup>a</sup>, Ceng Zhou<sup>a</sup>, Ling Tong<sup>c</sup>, Dongxiang Li<sup>c</sup>, Zhiguo Yu<sup>a</sup>, Yunli Zhao<sup>a,\*</sup><sup>a</sup> School of Pharmacy, Shenyang Pharmaceutical University, Shenyang, 110016, China<sup>b</sup> Baoding No.1 Central Hospital, Baoding, Hebei Province 071000, China<sup>c</sup> State Key Laboratory of Core Technology in Innovative Chinese Medicine, Tasy Pharmaceutical Analysis Institute, Tasy Academy, Tianjin 300402, China

## ARTICLE INFO

## Article history:

Received 2 September 2018

Received in revised form

8 January 2019

Accepted 30 January 2019

Available online 31 January 2019

## Keywords:

Pesticide residues

Chenpi

GC-MS/MS

QuEChERS

## ABSTRACT

To ensure the safety of the commercially available chenpi, a convenient and fast analytical method was developed for the determination of 133 pesticide residues in chenpi using gas chromatography-tandem mass spectrometry (GC-MS/MS). In this study, different extraction solvents, redissolution solvents and adsorbents were tested according to the recovery and purification effect to obtain a modified QuEChERS method. The samples were extracted with acetonitrile. During the clean-up step, octadecyl-modified silica (C18) and graphitized carbon black (GCB) were selected, and aminopropyl (NH<sub>2</sub>) was used instead of primary secondary amine (PSA) because of its weaker ion exchange capacity which had little effect on the recovery of ditalimfos. Samples were quantified by matrix-matched calibration with internal standards. All pesticides showed good linearity in the respective range, both with values of  $r^2 > 0.99$ . The average recoveries of the pesticides spiked samples ranged from 70.0% to 112.2% with the RSDs of 0.2%–14.4%. The modified QuEChERS method was validated and applied to twenty real samples. Five pesticides were found in eight batches, but no pesticide exceeded the maximum residue limits (MRL, MRL reference to European commission).

© 2019 Xi'an Jiaotong University. Production and hosting by Elsevier B.V. This is an open access article under the CC BY-NC-ND license (<http://creativecommons.org/licenses/by-nc-nd/4.0/>).

## 1. Introduction

Pericarpium citri Reticulatae (chenpi), the dried pericarp of the fruit of Citrus reticulata Blanco or its cultivars, is used in medicine and food [1]. As a food, chenpi has the effect of strengthening the spleen. As a traditional herb, chenpi is widely used to treat indigestion and inflammatory respiratory tract conditions [2].

Pesticide residues are detected frequently in commercially available chenpi. Relevant literature shows that pesticides pollution in chenpi is serious [3]. Pesticides are very toxic to humans and research has shown that some pesticides have teratogenic, carcinogenic and mutagenic effects [4,5]. In 2016, Peng et al. [6] used gas chromatography to determine organophosphorus pesticides in chenpi and only 11 kinds of organophosphorus pesticides were determined by this method. Therefore, it is extremely important to establish a set of convenient and fast detection techniques for the determination of multiple pesticide residues in chenpi.

Sample preparation is a crucial step in all analytical methods and an appropriate clean-up method was developed for the

extraction of pesticide residues with high selectivity, and low co-extraction. The most common sample preparation methods include solid-phase extraction (SPE) [7,8], QuEChERS [9], solid-phase micro extraction (SPME) [10,11] and gel permeation chromatography (GPC) [12–14].

The QuEChERS (Quick, Easy, Cheap, Effective, Rugged, Safe) method was developed by Anastassiades et al. in 2003 [15] and it has become one of the most commonly used methods for the determination of pesticides. A typical QuEChERS method involves an extraction with acetonitrile (and water in dry commodities), followed by a phase partitioning assisted by salting out and further clean up by d-SPE. [16–19]. The method can be used to analyze many compounds, including highly polar pesticides and highly acidic compounds. It is suitable for the detection of samples with a low fat content and a high water content. Furthermore, the method has been applied to pesticide determination of many different matrices like vegetables, fruits and tea [20–22].

In the clean-up step, sorbent C18 and primary secondary amine (PSA) are used in most published methods, and florisisil is used in some, but NH<sub>2</sub> is seldom used. NH<sub>2</sub> has a similar adsorption performance to PSA, while PSA contains two amino groups giving it a higher ion exchange capacity than NH<sub>2</sub>. However, PSA sorbents result in the pH value of the final extract solutions being more than 8, which affects the stability of base-sensitive pesticides [23]

Peer review under the responsibility of Xi'an Jiaotong University.

\* Corresponding author.

E-mail address: [yunli76@163.com](mailto:yunli76@163.com) (Y. Zhao).

and NH<sub>2</sub> can be used when PSA affects the determination of analytes.

In order to ensure food safety, in this study, a method was developed for multi-residue determination of pesticides in chenpi by GC-MS/MS and NH<sub>2</sub> sorbent was used in a modified QuEChERS method because of the pesticides influenced by PSA.

## 2. Experimental

### 2.1. Chemicals and other materials

Pesticide standards and the internal standard (IS), chlorpyrifos-d10 with a purity >98%, were provided by Dr. Ehrenstorfer (Augsburg, Germany). HPLC grade acetonitrile was obtained from Omni Chem (Schaumburg, IL, USA). HPLC grade acetone, ethyl acetate and n-hexane were obtained from Merck (Darmstadt, Germany). Anhydrous magnesium sulfate (MgSO<sub>4</sub>) was obtained from Sigma-Aldrich (St. Louis, USA). Analytical reagent grade anhydrous sodium chloride (NaCl) was obtained from Weichen Chemical Reagent Co., Ltd (Tianjin, China). PSA, octadecyl-modified silica (C18), Florisil, graphitized carbon black (GCB) and aminopropyl (NH<sub>2</sub>) were supplied by DIKMA Technologies (Beijing, China).

### 2.2. Instruments

GC-MS/MS analyses were carried out with a Shimadzu GCMS-TQ8030 (Japan). A Hitachi CF 16RN centrifuge (Japan) and an Eppendorf centrifuge 5804 (Germany) were used for the 50 mL and 10 mL centrifuge tubes, respectively, along with a BUCHI rotary evaporator (Switzerland), KQ-500DE numerical control ultrasonic cleaner (China) and Eppendorf tube (EP, China).

### 2.3. Preparation of pesticide standards and internal standard solutions

Individual stock standard solutions of each pesticide (1 mg/mL) were prepared by weighing pesticides and dissolving them in n-hexane. Mixed solutions of multiple pesticides (2.5 µg/mL) were prepared by combining appropriate volume of each stock standard solution and stored in a freezer (−20 °C). A suitable amount of mixed standard reserve solution was transferred into 10 mL volumetric flask, and was diluted into matrix-matched standard working solutions with concentrations of 1, 2, 5, 10, 20, 50, 100 and 200 ng/mL respectively by blank (pesticide-free) chenpi extract. The internal standard solution, chlorpyrifos-d10, was prepared at a concentration of 1 mg/mL, and then diluted to 2 µg/mL.

### 2.4. Sample treatment and preparation

Each batch of chenpi was obtained from different markets in China. Pesticide residues can be easily extracted from small particle samples, so before use, all samples were ground to a powder mechanically, and passed through a no. 24 mesh sieve. (The particles retained in the sieve are not included for the analysis.)

2 g samples and 100 µL internal standard (2 µg/mL) were added to 50 mL polypropylene (PP) centrifuge tubes and then 10 mL acetonitrile was used for extraction. The ultrasonic extraction was carried out for 5 min and 0.8 g anhydrous MgSO<sub>4</sub> and 0.2 g NaCl were added. Each mixture was shaken by hand for 1 min and centrifuged at 11,180 g (rcf) for 5 min. Then, 7 mL of the upper acetonitrile layer was transferred to a 10 mL EP tube containing 200 mg C18, 200 mg NH<sub>2</sub>, 200 mg anhydrous MgSO<sub>4</sub> and 30 mg GCB. The solution was subjected to vortex mixing for 1 min, and then centrifuged at 7155 g (rcf) for 5 min, and 5 mL of the upper

layer was transferred to a 50 mL round-bottom flask and evaporated to near dryness on a rotary vacuum evaporator at 40 °C. The dry residue was redissolved in 2 mL acetone for analysis by GC-MS/MS.

### 2.5. GC-MS/MS conditions

GC separation was performed on a DB-5MS IU capillary column (30 m × 0.25 mm × 0.25 µm; Agilent, America) and helium (purity ≥ 99.996%) was used as a carrier gas at a constant flow of 1.5 mL/min. The inlet temperature was set at 250 °C; the mode of inlet was splitless; the injection volume was 1 µL. The column temperature program is as follows: the initial temperature was maintained at 50 °C for 1 min, increased to 125 °C at a rate of 25 °C/min, raised to 230 °C at 4 °C/min, and then at 8 °C/min up to 310 °C, and held there for 3 min.

The mass spectrometer was operated with an electron impact (EI) source in multiple reaction monitoring (MRM) mode. The electron energy was 70 eV, and the ion and transfer line temperatures were set at 200 °C and 250 °C, respectively. In order to prevent instrument damage, the solvent delay was set at 3.5 min. Table 1 shows the optimized parameters of ion transition for 133 pesticide residues in chenpi.

## 3. Results and discussion

### 3.1. Optimization of extraction solvent

Acetonitrile, ethyl acetate and n-hexane are commonly used for extraction of multi-pesticide residues [24–27]. Fig. 1 shows the TIC chromatograms of negative samples extracted by different solvents. Those extracted with n-hexane had the lowest matrix; however, recoveries of dimethoate, metalaxyl, paraoxon, bromacil, isocarbophos, E-chlorfenvinfos, fipronil, triadimenol, trans-chlordane, cis-chlordane, fenthionsulfoxide, fensulfthion, fenthion-sulfone, and azinphos-methyl were close to zero. When extracted with ethyl acetate, the recovery of trans-chlordane and pyridaben was less than 60%. Compared with n-hexane and ethyl acetate, acetonitrile had the strong dissolving capability for the analytes, meeting the recovery requirement. Therefore, in this study acetonitrile was used as the extraction solvent.

### 3.2. Selection of solvent for redissolution

Acetonitrile possesses many advantages for extraction, but the polarity of acetonitrile is high, which can damage the gas chromatography column. For the protection of chromatographic columns, before analysis, acetonitrile should be replaced. In this study, n-hexane and acetone were selected as solvents for redissolution. The recoveries of pesticides obtained with these two solvents are shown in Fig. 2.

Compared with that of acetone, the recoveries of some pesticides were lower when redissolved with n-hexane, and approximately 42% of pesticides were outside the range of 60%–120%. Dimethoate and cis-chlordane were close to zero. When dissolved with acetone, most of analytical pesticides satisfied the recovery requirement. So acetone was chosen as the solvent for redissolution.

### 3.3. Optimization of adsorbents

The use of co-extraction leads to an unsatisfactory peak shape, and an increased or inhibited response, which adversely affects the quantification. The adsorbents PSA, C18, Florisil, GCB and NH<sub>2</sub> were investigated to choose the most appropriate purification method.

**Table 1**  
GC-MS/MS acquisition parameters for 133 pesticide residues in chenpi.

No.	Pesticides	Ion ratio (%)	$t_R$ (min)	Quantitative transition		Qualitative transition	
				Precursor > product	CE/V	Precursor > product	CE/V
15	Chlorpyrifos-D10	28.37	22.122	324.0 > 260.0	15	324.0 > 195.0	30
1	Dichlorvos	29.96	6.585	185.0 > 93.0	14	185.0 > 109.0	14
2	Mevinphos	25.09	9.585	127.0 > 109.1	9	192.0 > 127.0	9
3	Methacrifos	26.34	11.112	240.0 > 208.0	4	240.0 > 180.0	10
4	Isoprocab	20.26	13.571	136.0 > 121.0	9	121.0 > 103.1	12
5	Propoxur	12.34	13.571	152.1 > 110.1	8	152.1 > 64.0	28
6	Ethoprophos	20.32	14.228	158.0 > 97.0	18	158.0 > 114.0	6
7	Dicrotophos	28.07	14.885	127.1 > 109.0	12	127.1 > 95.0	18
8	Phorate	28.61	15.591	260.0 > 75.0	8	260.0 > 231.0	18
9	$\alpha$ -hexachlorocyclohexane	21.02	15.640	218.9 > 182.9	8	218.9 > 144.9	20
10	Hexachlorobenzene	21.31	15.762	283.8 > 248.8	24	283.8 > 213.8	28
11	2,6-dichloro-4-nitroaniline	18.89	16.227	206.0 > 176.0	10	206.0 > 160.0	16
12	Dimethoate	29.65	16.276	125.0 > 47.0	14	125.0 > 79.0	8
13	$\beta$ -hexachlorocyclohexane	29.41	16.794	218.9 > 182.9	8	218.9 > 144.9	20
14	Pentachloroanisole	30.00	16.917	265.0 > 237.0	15	280.0 > 265.0	10
15	Quintozene	22.09	16.917	294.8 > 236.8	16	294.8 > 264.8	12
16	$\gamma$ -hexachlorocyclohexane	24.30	17.188	218.9 > 182.9	8	218.9 > 144.9	20
17	Fonofos	23.98	17.656	137.0 > 109.0	6	246.0 > 137.0	6
18	Pyrimethanil	23.67	18.050	198.0 > 183.0	12	198.0 > 156.1	24
19	Diazinon	23.34	18.075	304.1 > 179.1	10	304.1 > 162.1	8
20	$\delta$ -hexachlorocyclohexane	26.83	18.542	218.9 > 182.9	10	218.9 > 144.9	20
21	Isazofos	25.67	18.542	161.0 > 119.0	9	162.0 > 120.0	9
22	Etrimfos	23.67	18.786	292.1 > 181.1	8	292.1 > 153.1	20
23	Disulfoton	10.60	18.786	153.0 > 97.0	10	153.0 > 125.0	6
24	Tefluthrin	24.13	18.859	177.0 > 127.1	16	177.0 > 137.1	16
25	Iprobenfos	24.06	19.103	204.0 > 91.0	8	204.0 > 122.0	12
26	Pirimicarb	16.69	19.128	238.1 > 166.1	12	238.1 > 72.0	24
27	Pentachloroaniline	23.80	19.128	265.0 > 194.0	25	263.0 > 192.0	25
28	Fenchlorphos-oxon	23.63	19.372	269.0 > 254.0	20	269.0 > 224.0	25
29	Dichlofenthion	26.07	19.811	279.0 > 222.9	14	279.0 > 250.9	8
30	Chlorpyrifos-methyl	27.07	20.031	285.9 > 93.0	22	285.9 > 270.9	14
31	Acetochlor	20.12	20.031	223.1 > 132.1	22	223.1 > 147.1	10
32	Vinclozolin	29.39	20.275	285.0 > 212.0	12	285.0 > 178.0	14
33	Parathion-methyl	15.15	20.299	263.0 > 109.0	14	263.0 > 136.0	8
34	Tolclofos-methyl	20.41	20.348	264.9 > 249.9	14	264.9 > 93.0	24
35	Alachlor	29.58	20.421	188.1 > 160.1	10	188.1 > 132.1	18
36	Heptachlor	7.54	20.586	271.8 > 236.9	20	271.8 > 117.0	32
37	N-desethyl-pirimiphos-methyl	28.92	20.788	277.0 > 135.0	10	277.0 > 168.0	10
38	Metalaxyl	22.46	20.788	249.2 > 190.1	8	249.2 > 146.1	22
39	Fenchlorphos	22.29	20.788	284.9 > 269.9	16	284.9 > 93.0	24
40	Paraoxon	28.72	21.028	139.0 > 109.0	10	149.0 > 102.0	25
41	Prometryn	22.61	21.028	241.2 > 199.1	6	241.2 > 58.0	14
42	Pentachlorothioanisole	30.00	21.504	296.0 > 263.0	15	246.0 > 211.0	20
43	Fenitrothion	27.21	21.552	277.0 > 260.0	6	277.0 > 109.1	14
44	Pirimiphos-methyl	20.84	21.576	305.1 > 180.1	8	305.1 > 290.1	12
45	Bromacil	28.20	21.647	204.9 > 187.9	14	204.9 > 162.0	14
46	Metolachlor	23.38	22.172	238.1 > 162.1	12	238.1 > 133.1	26
47	Aldrin	13.34	2.195	262.9 > 193.0	28	262.9 > 203.0	26
48	Clorpyrifos	20.16	22.338	313.9 > 257.9	14	313.9 > 285.9	8
49	Dacthal	23.42	22.481	300.9 > 222.9	26	300.9 > 272.9	14
50	Fenthion	24.47	22.505	278.0 > 109.0	20	278.0 > 125.0	20
51	Parathion	25.33	22.672	291.1 > 109.0	14	291.1 > 137.0	6
52	Isocarbophos	26.63	22.863	289.1 > 136.0	10	289.1 > 113.0	14
53	Bromophos	29.87	23.244	330.9 > 315.9	14	330.9 > 285.9	28
54	Pirimiphos ethyl	23.99	23.544	304.0 > 168.0	10	318.0 > 166.0	15
55	Cyprodinil	26.30	23.891	224.1 > 208.1	16	224.1 > 197.1	22
56	E-chlorfenvinphos	29.22	23.960	323.0 > 267.0	16	323.0 > 295.0	6
57	trans-heptachlorepoxyde	24.21	24.237	352.8 > 253.0	26	352.8 > 289.0	6
58	Fipronil	21.44	24.237	366.9 > 212.9	30	366.9 > 254.9	22
59	Z-chlorfenvinphos	27.49	24.422	323.0 > 267.0	16	323.0 > 295.0	6
60	Mecarbam	21.06	24.584	329.0 > 159.1	4	329.0 > 131.1	18
61	Quinalphos	25.62	24.630	298.0 > 156.0	5	298.0 > 190.0	10
62	Phenthoate	27.03	24.630	273.9 > 125.0	20	273.9 > 246.0	6
63	Procymidone	17.47	24.722	283.0 > 96.0	10	283.0 > 255.0	12
64	Triadimenol	9.37	24.791	168.1 > 70.0	10	168.1 > 112.1	4
		12.67	25.161				
65	Methodathion	22.20	25.161	145.0 > 85.0	8	145.0 > 58.0	14
66	Bromophos-ethyl	28.69	25.276	358.9 > 302.9	16	358.9 > 330.9	10
67	Methoprene	22.56	25.392	111.0 > 55.1	15	109.0 > 67.1	9
68	o,p'-DDE	15.41	25.415	246.0 > 176.0	30	246.0 > 211.0	22
69	Paclobutrazol	29.19	25.554	236.1 > 125.0	14	236.1 > 167.0	10
70	Trans-chlordane	19.56	25.754	374.8 > 263.9	28	374.8 > 336.8	10
71	Fenothiocarb KCO-3001 Panocon	7.55	25.843	160.1 > 72.0	10	160.1 > 106.1	12

(continued on next page)

Table 1 (continued)

No.	Pesticides	Ion ratio (%)	$t_R$ (min)	Quantitative transition		Qualitative transition	
				Precursor > product	CE/V	Precursor > product	CE/V
72	Ditalimfos	20.77	25.977	130.0 > 102.1	12	148.0 > 130.1	12
73	N,N-Diethyl-2-(1-naphthoxy)propanamide	22.18	26.266	128.0 > 72.1	6	271.0 > 128.1	6
74	Prothiofos	25.48	26.600	309.0 > 238.9	14	309.0 > 280.9	10
75	Cis-chlordane	27.66	26.823	374.8 > 338.8	8	372.8 > 265.9	22
76	Profenofos	24.54	26.823	336.9 > 266.9	14	336.9 > 308.9	6
77	Myclobutanil	21.15	27.179	179.0 > 125.0	18	179.0 > 90.1	27
78	Carboxin	29.42	27.290	235.0 > 143.1	12	235.0 > 87.0	21
79	Flusilazole	29.81	27.335	233.1 > 165.1	14	233.1 > 152.1	14
80	Buprofezin	21.48	27.380	172.1 > 57.0	14	172.1 > 131.1	6
81	<i>p,p'</i> -DDE	16.07	27.888	246.0 > 211.0	22	246.0 > 176.0	30
82	Dieldrin	22.21	27.888	262.9 > 193.0	34	262.9 > 228.0	24
83	Endrin	21.22	27.888	262.9 > 191.0	30	262.9 > 193.0	28
84	Nitrofen	27.28	27.995	282.9 > 162.0	24	282.9 > 253.0	12
85	Fenthionsulfoxide	20.42	28.509	279.0 > 109.0	20	294.0 > 279.0	10
86	Fensulfothion	29.20	28.595	293.0 > 125.0	14	293.0 > 153.0	8
87	Diniconazole	27.40	28.638	268.0 > 232.0	12	268.0 > 149.0	24
88	Fenthion-sulfone	24.24	28.766	310.0 > 105.0	15	310.0 > 109.0	20
89	<i>o,p'</i> -DDD	23.54	28.852	235.0 > 165.0	24	235.0 > 199.0	14
90	<i>o,p'</i> -DDT	23.54	28.766	235.0 > 165.0	24	235.0 > 199.0	16
91	Ethion	29.55	29.024	230.9 > 174.9	14	230.9 > 184.9	12
92	Fensulfothion sulfone	22.99	29.324	188.0 > 109.1	18	324.0 > 109.1	18
93	Famphur	18.34	29.902	218.0 > 109.0	16	218.0 > 79.0	24
94	Benalaxyl	24.19	29.981	148.0 > 77.1	27	148.0 > 105.1	18
95	Endosulfan sulfate	22.75	30.191	386.8 > 252.9	16	386.8 > 288.8	10
96	Propiconazole	26.54	30.325	259.0 > 69.0	14	259.0 > 191.0	8
		29.43	30.593				
97	<i>p,p'</i> -DDT	30.00	30.554	235.0 > 165.0	24	235.0 > 199.0	16
98	Tebuconazole	30.00	31.147	250.1 > 125.1	22	250.1 > 153.1	12
99	Piperonyl butoxide	27.48	31.739	176.1 > 131.1	12	176.1 > 117.1	20
100	Pyridaphenthion	26.92	32.223	340.0 > 199.2	9	199.0 > 77.1	30
101	Phosmet	25.23	32.332	160.0 > 77.0	24	160.0 > 133.0	14
102	Bromopropylate	23.50	32.612	340.9 > 182.9	18	340.9 > 184.9	20
103	Bifenthrin	5.87	32.736	181.1 > 166.1	12	183.1 > 153.1	8
104	Bifenazate	26.83	32.829	300.1 > 258.1	8	300.1 > 199.1	20
105	Methoxychlor	26.37	32.845	227.1 > 169.1	24	227.1 > 212.1	14
106	Fenpropathrin	12.20	33.016	265.1 > 210.1	12	265.1 > 172.1	14
107	Tebufenpyrad	24.61	33.187	333.0 > 171.1	21	318.0 > 131.2	21
108	Tetradifon	29.03	33.455	355.9 > 228.9	12	355.9 > 159.0	18
109	Phenothrin	24.35	33.522	183.1 > 153.1	14	183.1 > 168.1	14
		29.11	33.736				
110	Phosalone	21.89	33.682	182.0 > 111.0	14	182.0 > 138.0	8
111	Azinphos-methyl	21.74	33.736	160.1 > 132.1	6	160.1 > 77.0	20
112	Mefenacet	25.43	34.069	192.0 > 136.0	12	192.0 > 109.0	27
113	Mirex	13.20	34.216	272.0 > 237.0	15	270.0 > 235.0	5
114	Cyhalothrin	27.81	34.510	197.0 > 141.0	8	197.0 > 161.0	22
		28.81	34.900				
115	$\lambda$ -Cyhalothrin	21.73	34.510	181.0 > 152.1	21	197.0 > 141.1	9
116	Fenarimol	28.56	34.550	251.0 > 139.0	14	251.0 > 111.0	26
117	Pyrazophos	223.60	34.710	221.1 > 193.1	12	221.1 > 149.1	14
118	Acrinathrin	24.36	34.900	289.1 > 93.0	14	289.1 > 77.0	26
		24.67	35.206				
119	Bitertanol	29.26	35.548	170.0 > 141.1	18	170.0 > 115.2	27
120	Permethrin	22.70	35.713	183.1 > 168.1	14	183.1 > 165.1	14
		24.90	35.912				
121	Coumaphos	23.63	35.759	362.0 > 109.0	16	362.0 > 226.0	14
122	Flusilazole	25.80	35.807	340.0 > 298.0	14	340.0 > 313.0	14
123	Pyridaben	20.10	35.889	147.1 > 117.1	22	147.1 > 132.1	14
124	Cyfluthrin	27.68	36.556	226.1 > 206.1	6	226.1 > 199.1	14
		24.88	36.717				
		24.11	36.792				
		23.14	36.867				
125	Boscalid	26.41	37.004	342.1 > 140.1	14	342.1 > 112.1	28
126	Cypermethrin	15.11	37.024	163.1 > 127.1	6	163.1 > 109.1	22
		17.62	37.182				
		19.05	37.252				
		11.96	37.321				
127	Quinalofop-ethyl	29.31	37.242	372.0 > 299.2	12	299.0 > 91.2	24
128	Flucythrinate	22.11	37.281	199.1 > 157.1	10	199.1 > 107.1	22
		21.41	37.568				
129	Ethofenprox	25.46	37.479	163.0 > 135.1	10	163.0 > 107.1	18
130	Phenvalerate	29.21	38.261	419.1 > 225.1	6	419.1 > 125.1	26
		29.01	38.558				
131	Tua-Fluvalinate	17.50	38.465	250.1 > 55.0	20	250.1 > 208.0	20
		16.53	38.567				

(continued on next page)

Table 1 (continued)

No.	Pesticides	Ion ratio (%)	$t_R$ (min)	Quantitative transition		Qualitative transition	
				Precursor > product	CE/V	Precursor > product	CE/V
132	Difenoconazole	15.30	38.846	323.0 > 265.0	14	323.0 > 202.0	28
		19.56	38.927				
		26.41	39.015				
133	Deltamethrin	27.14	39.278	252.9 > 93.0	20	251.0 > 172.0	10

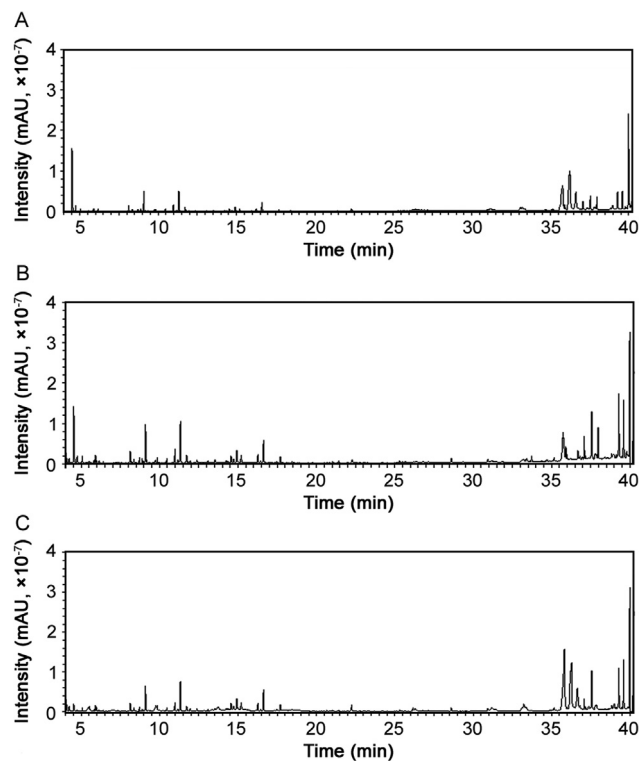


Fig. 1. Full scan chromatograms of negative samples extracted with (A) n-hexane, (B) ethyl acetate and (C) acetonitrile.

If the extraction solution was injected into the GC-MS/MS without adding adsorbents, there was clear interference of the matrix for the pesticides bitertanol, cypermethrin, flucythrinate, and difenoconazole.

The addition of Florisil for purification seemed to have no effect. C18 can be used for the reduction of lipids and non-polar interference. Because of the addition of C18, the matrices that interfered with the determination of pesticides, such as bitertanol, flucythrinate and difenoconazole, were removed.

PSA can adsorb fatty acids and pigments extracted from chenpi to improve the chromatographic peak shape of cypermethrin (Fig. 3). When the amount of PSA was 200 mg, the chromatographic peaks of cypermethrin isomers was free of interference from impurities. However, PSA clearly had an effect on the recovery of ditalimfos. This study compared the effect of the addition of 50, 100, 150, 200 mg PSA on the recovery of ditalimfos, and the results obtained are shown in Fig. 4. When the adsorbent amount was 50 mg, the recovery of ditalimfos was about 73.1%, while the recovery of ditalimfos decreased to 23.9% when the amount of PSA reached 200 mg. The main reason for this may be that PSA may increase the pH value of the final extract solutions to more than 8. According to the structure of ditalimfos (Fig. 5), ditalimfos is unstable and decomposes easily in an alkaline

environment, so as the amount of adsorbent is increased, the recovery of ditalimfos is reduced.

Fig. 5 shows the structures of  $\text{NH}_2$  and PSA. They had a similar adsorption, while PSA contains two amino groups, which resulted in a higher ion exchange capacity than  $\text{NH}_2$ . Therefore,  $\text{NH}_2$  could not only improve the chromatographic peak shape of cypermethrin, but also have small effect on ditalimfos. When the dose of  $\text{NH}_2$  reached 200 mg, the recoveries of pesticides were all between 72.4% and 118.6%.

The solution extracted with acetonitrile contained more pigments. GCB is widely used in the adsorption of pigments. The color of the extraction solution changed with an increase in the amount of GCB. In addition, GCB is well known for adsorbing pesticides with a planar structure, leading to unsatisfactory recoveries and poor precision. This study compared the effect of the addition of 10, 20, 30 and 40 mg GCB on the recovery of pesticides, and the results obtained are shown in Fig. 6. As the amount of GCB increased, the recoveries of some pesticides, such as hexachlorobenzene with a planar structure, decreased but were still in an acceptable range. Also, the extraction was improved when 30 mg GCB was added. In summary, 30 mg GCB was used as the adsorbent.

#### 3.4. Validation study

Under the modified QuEChERS method conditions, a validation study was carried out to evaluate the performance characteristics of the method for multiple pesticides in chenpi by estimating the linearity, limit of quantification (LOQ), accuracy (expressed by recovery), precision and matrix effects. Validation was performed following the European Union SANTE/11945/ 2015 guideline [28].

##### 3.4.1. Linearity

The linearity for each pesticide was assessed in matrix-matched standard solution. The calibration curves of the compounds were obtained by plotting the pesticide/IS peak area ratios against the concentration of the corresponding calibration standards at eight different levels (1, 2, 5, 10, 20, 50, 100, 200 ng/mL). The linearity results are shown in Table 2. The linearity of the method for all the pesticides was satisfactory, with correlation coefficients ( $r^2$ ) higher than 0.99.

##### 3.4.2. LOQ

The LOQ for each pesticide was defined as the lowest validated spiked level satisfying the requirement of recovery ranging from 70% to 120% and a relative standard deviation (RSD) less than 20%. Samples were spiked at two different concentrations: 0.005 and 0.01 mg/kg (6 replicates per level). The LOQ values are presented in Table 2.

##### 3.4.3. Accuracy and precision

Recovery was evaluated at three different spiked levels of 0.05, 0.1 and 0.2 mg/kg by spiking six blank samples at each level. Precision was expressed as the relative standard deviation (RSD)

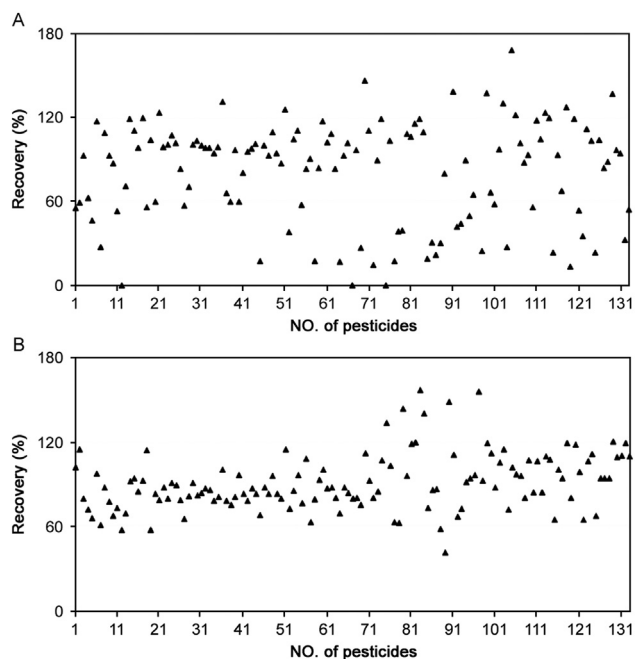


Fig. 2. Recoveries of pesticides obtained using (A) n-hexane and (B) acetone for redissolution.

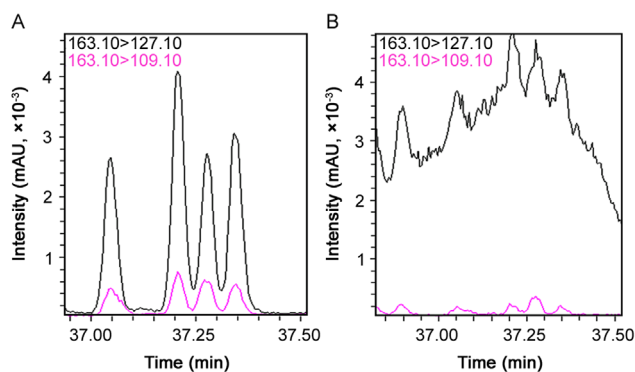


Fig. 3. Chromatogram of cypermethrin with (A) PSA adsorbent and (B) without adsorbent.

and was obtained from the six spiked samples at three spiking levels. Table 2 shows the recoveries and RSDs of all pesticides at all concentrations. The recovery of all the pesticides met the requirements of the pesticide residue determination.

#### 3.4.4. Matrix effects (ME)

In this study, some pesticides, such as mevinphos, propoxur, dicrotophos and carboxine, have better chromatographic peak shapes in matrix-matched blank solutions than in pure solvent solutions because of the ME.

The ME was evaluated by the slope of the solvent calibration curve and the matrix-matched blank extract calibration curve according to the equation:  $ME (\%) = [(slope \text{ in matrix}/slope \text{ in solvent}) - 1] * 100$  [29]. The ME results were grouped into 3 classes: a high ME (less than  $-50\%$  or higher than  $+50\%$ ), a medium ME (between  $-50\%$  and  $-20\%$  or  $+20\%$  and  $+50\%$ ) and a low ME (between  $+20\%$  and  $-20\%$ ). Fig. 7 shows the ME of each pesticide. Among 133 pesticides, 53% showed low ME, 32% showed medium ME and 16% showed high ME. In order to avoid the ME, matrix-matched calibration standards were used for quantification to compensate for the ME.

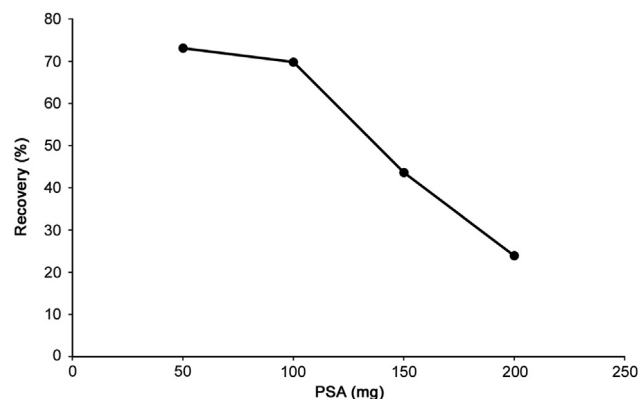


Fig. 4. Recoveries of ditalimfos with different amounts of PSA.

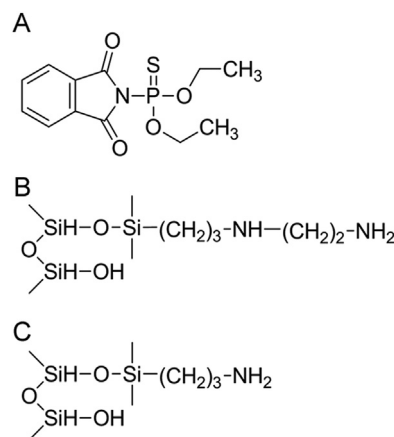


Fig. 5. The structure of (A) ditalimfos, (B) PSA and (C) NH<sub>2</sub>.

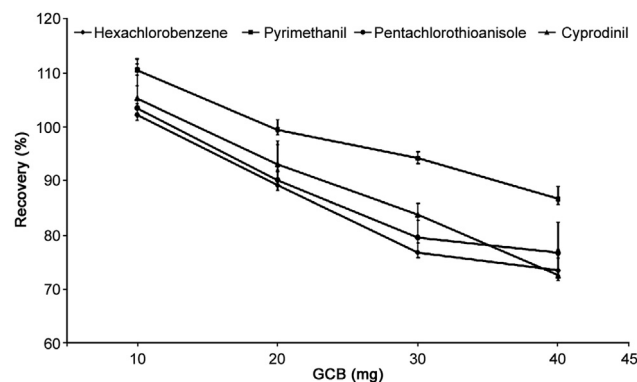


Fig. 6. Recoveries of pesticides with different amounts of GCB.

#### 3.5. Application to real samples

Once the analytical methodology was validated, it was used for monitoring pesticides in chenpi samples. The established method was used for the simultaneous determination of the pesticides in twenty real samples and the results are summarized in Table 3. Chlorpyrifos, isocarbophos, methidathion, profenofos and fenprothrin were found in eight batches, most of which were insecticides and fungicides. Insecticide clorpyrifos and methidathion were frequently detected pesticides, but no pesticide exceeded the maximum residue limits (MRL, the values of MRL for orange were taken as reference) prescribed by Regulation (EC) no. 396/2005 [30]. Clorpyrifos and methidathion are low toxicity pesticides, but the others are moderately or highly toxic pesticides, which are

**Table 2**  
Validation results of the developed method for determination of multiple pesticides in chenpi.

No.	Pesticide	Linear range (ng/mL)	$r^2$	Recovery (%RSD) (% , n = 6)			LOQ (mg/kg)	ME(%)
				0.05 mg/kg	0.1 mg/kg	0.2 mg/kg		
1	Dichlorvos	1–200	0.9992	84.0(1.4)	90.3(2.3)	90.5(3.6)	0.005	4.3
2	Mevinphos	1–200	0.9988	85.6(2.3)	94.1(2.9)	97.2(2.3)	0.005	56.2
3	Methacrifos	1–200	0.9989	88.1(1.0)	98.9(3.0)	103.5(2.9)	0.005	21.7
4	Isoprocarb	1–200	0.9988	92.8(3.9)	92.6(1.8)	93.9(2.0)	0.005	2.5
5	Propoxur	1–200	0.9989	90.7(2.0)	93.3(2.2)	93.5(1.7)	0.005	18.8
6	Ethoprophos	1–200	0.9987	92.1(3.7)	86.5(2.0)	85.4(1.7)	0.005	14.5
7	Dicrotophos	1–200	0.9986	93.9(4.0)	87.6(3.3)	92.1(2.3)	0.005	44.0
8	Phorate	1–200	0.9981	86.6(1.2)	93.4(2.2)	93.0(1.7)	0.005	18.6
9	$\alpha$ -hexachlorocyclohexane	1–200	0.9989	93.4(6.4)	91.8(2.2)	94.1(2.3)	0.005	–15.5
10	Hexachlorobenzene	1–200	0.9990	71.9(2.9)	73.0(2.2)	72.0(2.5)	0.005	–19.9
11	2,6-dichloro-4-nitroaniline	2–200	0.9970	84.2(2.4)	93.0(3.8)	97.7(2.4)	0.01	62.1
12	Dimethoate	1–200	0.9984	90.7(1.6)	91.4(2.7)	91.9(1.4)	0.01	46.9
13	$\beta$ -hexachlorocyclohexane	1–200	0.9988	95.5(5.2)	94.1(2.4)	95.3(2.0)	0.005	–13.2
14	Pentachloroanisole	2–200	0.9974	85.4(4.9)	78.0(2.9)	69.8(3.2)	0.005	17.5
15	Quintozene	2–200	0.9977	79.9(1.3)	84.5(1.6)	85.5(2.0)	0.005	32.7
16	$\gamma$ -hexachlorocyclohexane	1–200	0.9995	92.3(7.6)	90.0(5.3)	92.0(1.7)	0.01	–7.8
17	Fonofos	1–200	0.9988	88.0(1.5)	95.5(2.8)	98.4(2.0)	0.005	11.0
18	Pyrimethanil	2–200	0.9988	77.6(1.5)	78.1(3.2)	80.7(1.8)	0.005	9.1
19	Diazinon	1–200	0.9986	92.1(1.7)	89.7(1.4)	87.9(1.7)	0.01	–0.8
20	$\delta$ -hexachlorocyclohexane	1–200	0.9986	92.8(5.9)	92.2(2.3)	94.7(2.0)	0.005	–9.3
21	Isazofos	2–200	0.9982	89.8(0.4)	96.6(3.1)	99.8(2.0)	0.005	1.3
22	Etrinfos	1–200	0.9980	93.7(5.2)	89.9(2.0)	93.4(2.2)	0.01	–18.3
23	Disulfoton	1–200	0.9976	88.1(2.4)	92.5(2.5)	95.0(2.1)	0.01	–6.9
24	Tefluthrin	1–200	0.9982	87.3(0.8)	94.1(2.5)	97.1(1.8)	0.01	–4.2
25	Iprobenfos	1–200	0.9973	85.5(3.9)	98.9(3.2)	103.0(1.9)	0.01	26.9
26	Pirimicarb	1–200	0.9980	90.0(2.3)	94.4(2.8)	97.2(2.2)	0.01	–10.5
27	Pentachloroaniline	1–200	0.9982	87.0(7.0)	91.4(3.2)	70.9(2.3)	0.005	–19.9
28	Fenchlorphos-oxon	1–200	0.9978	93.4(3.5)	91.3(3.2)	96.4(2.6)	0.005	2.2
29	Dichlofenthion	1–200	0.9983	91.3(1.1)	88.1(1.5)	87.3(2.0)	0.005	0.9
30	Chlorpyrifos-methyl	1–200	0.9981	86.6(0.6)	90.3(2.0)	90.1(2.2)	0.005	2.0
31	Acetochlor	5–200	0.9980	89.6(1.6)	98.3(3.2)	102.0(1.8)	0.01	5.4
32	Vinclozolin	1–200	0.9984	93.8(4.0)	89.5(1.2)	88.4(1.7)	0.005	–4.9
33	Parathion-methyl	1–200	0.9953	85.8(5.5)	85.5(1.2)	86.8(1.6)	0.01	70.7
34	Tolclofos-methyl	1–200	0.9984	90.0(1.9)	98.5(3.0)	103.0(2.2)	0.005	–11.3
35	Alachlor	2–200	0.9980	88.4(1.0)	97.7(2.6)	101.5(1.9)	0.01	2.2
36	Heptachlor	1–200	0.9980	83.2(1.5)	76.2(2.3)	74.5(1.8)	0.005	–10.3
37	<i>N</i> -desethyl-pirimiphos-methyl	2–200	0.9981	86.9(1.9)	99.7(3.7)	104.4(1.9)	0.005	9.6
38	Metalaxyl	2–200	0.9978	93.5(5.4)	89.1(1.7)	89.2(1.3)	0.005	–12.1
39	Fenchlorphos	1–200	0.9984	87.4(1.6)	92.5(2.0)	91.7(1.2)	0.005	–4.0
40	Paraoxon	5–200	0.9934	91.1(3.8)	89.7(4.2)	92.9(3.2)	0.01	79.7
41	Prometryn	1–200	0.9984	91.3(1.6)	88.4(1.4)	86.7(1.9)	0.005	0.2
42	Pentachlorothioanisole	2–200	0.9988	77.5(7.8)	74.0(3.3)	76.4(4.4)	0.005	–20.1
43	Fenitrothion	1–200	0.9917	82.4(4.4)	84.2(0.9)	84.4(1.5)	0.01	67.3
44	Pirimiphos-methyl	2–200	0.9980	91.6(2.2)	86.9(1.7)	86.5(1.9)	0.01	–6.5
45	Bromacil	2–200	0.9990	89.2(2.0)	93.7(2.3)	94.4(2.6)	0.01	28.7
46	Metolachlor	1–200	0.9986	89.4(1.1)	100.1(3.3)	104.6(2.1)	0.005	3.3
47	Aldrin	2–200	0.9984	92.7(6.1)	87.5(2.4)	89.7(3.0)	0.005	–20.7
48	Chlorpyrifos	1–200	0.9985	88.3(3.5)	105.5(4.9)	107.3(2.4)	0.005	1.8
49	Dacthal	1–200	0.9989	97.7(6.9)	92.0(2.1)	94.3(1.7)	0.005	–21.2
50	Fenthion	1–200	0.9986	89.8(0.8)	94.1(1.5)	92.6(1.5)	0.01	1.2
51	Parathion	2–200	0.9926	88.6(2.1)	96.2(5.0)	103.6(2.2)	0.01	69.3
52	Isocarbophos	2–200	0.9979	92.5(2.2)	96.6(3.8)	102.0(2.4)	0.005	18.5
53	Bromophos	1–200	0.9986	92.2(2.9)	90.6(1.6)	94.0(2.2)	0.005	0.3
54	Pirimiphos ethyl	1–200	0.9986	86.4(1.8)	99.4(3.8)	104.9(2.6)	0.005	6.1
55	Cyprodinil	1–200	0.9978	73.3(2.0)	70.0(5.6)	73.4(2.0)	0.005	–2.1
56	<i>E</i> -chlorfenvinphos	5–200	0.9980	95.8(5.8)	92.8(3.1)	90.6(3.0)	0.01	24.8
57	<i>trans</i> -heptachlorepoxyde	5–200	0.9974	99.2(12.0)	101.1(5.0)	97.2(3.1)	0.01	–8.7
58	Fipronil	2–200	0.9970	86.5(4.1)	96.1(2.1)	95.5(1.8)	0.01	49.1
59	<i>Z</i> -chlorfenvinphos	1–200	0.9988	90.1(1.9)	88.5(1.3)	87.9(1.9)	0.01	17.3
60	Mecarbam	2–200	0.9966	86.7(6.3)	102.4(3.3)	103.2(2.4)	0.01	24.8
61	Quinalphos	2–200	0.9966	86.4(3.8)	98.5(2.7)	101.5(1.3)	0.01	4.9
62	Phenthoate	1–200	0.9976	86.4(1.0)	97.1(3.0)	102.0(2.4)	0.01	–4.4
63	Procymidone	1–200	0.9983	91.5(1.5)	92.0(1.2)	90.4(1.3)	0.01	–8.4
64	Triadimenol	1–200	0.9975	86.4(3.5)	95.3(3.5)	99.5(2.4)	0.01	29.0
65	Methidathion	1–200	0.9977	91.3(2.4)	100.4(3.4)	102.6(1.6)	0.01	29.2
66	Bromophos-ethyl	1–200	0.9984	86.9(1.4)	85.3(1.9)	84.6(1.4)	0.01	–10.1
67	Methoprene	1–200	0.9924	74.1(2.5)	96.5(4.2)	95.6(8.3)	0.01	13.0
68	<i>o,p'</i> -DDE	1–200	0.9984	87.7(2.6)	95.2(3.1)	97.2(1.7)	0.005	–14.6
69	Paclbutrazol	1–200	0.9979	84.9(2.8)	96.9(2.1)	97.7(1.4)	0.01	28.6
70	<i>Trans</i> -chlordane	5–200	0.9960	100.4(7.3)	90.1(5.5)	88.4(4.0)	0.01	–11.4
71	Fenothiocarb	1–200	0.9978	88.5(0.7)	94.1(1.9)	94.2(1.6)	0.01	51.7
72	Ditalimfos	1–200	0.9981	72.7(1.0)	83.5(4.0)	84.5(1.4)	0.005	2.5
73	Napropamid	1–200	0.9986	92.7(5.4)	92.9(2.5)	94.3(1.3)	0.005	3.6
74	Prothiofos	1–200	0.9989	90.3(2.8)	86.6(1.6)	86.1(1.7)	0.005	14.3

(continued on next page)

Table 2 (continued)

No.	Pesticide	Linear range (ng/mL)	$r^2$	Recovery (%RSD)(%, n = 6)			LOQ (mg/kg)	ME(%)
				0.05 mg/kg	0.1 mg/kg	0.2 mg/kg		
75	Cis-chlordane	5–200	0.9914	89.9(8.9)	97.9(13.1)	102.7(3.7)	0.01	24.5
76	Profenofos	1–200	0.9991	88.9(2.5)	102.1(3.9)	105.3(2.1)	0.005	34.6
77	Myclobutanil	1–200	0.9986	88.8(1.6)	96.3(2.9)	99.6(2.0)	0.01	15.8
78	Carboxin	1–200	0.9984	92.0(3.5)	93.9(2.3)	95.4(1.6)	0.01	25.4
79	Flusilazole	1–200	0.9982	88.7(1.9)	97.4(3.0)	97.8(0.9)	0.01	7.6
80	Buprofezin	1–200	0.9985	89.0(2.0)	96.8(3.5)	98.5(1.9)	0.005	1.4
81	<i>p,p'</i> -DDE	2–200	0.9992	100.0(12.3)	83.9(3.4)	79.0(2.5)	0.01	–6.7
82	Dieldrin	5–200	0.9980	92.6(6.3)	86.0(1.7)	88.2(2.8)	0.01	–9.3
83	Endrin	5–200	0.9983	94.0(7.6)	84.6(4.4)	87.0(1.3)	0.01	–8.0
84	Nitrofen	2–200	0.9933	84.6(3.2)	91.1(4.4)	97.7(2.7)	0.01	44.3
85	Fenthionsulfoxide	2–200	0.9931	89.1(1.8)	84.1(2.3)	84.2(2.2)	0.01	21.6
86	Fensulfothion	1–200	0.9997	79.2(3.6)	79.4(1.5)	81.1(2.1)	0.01	79.8
87	Diniconazole	1–200	0.9981	84.2(1.1)	83.7(2.0)	83.5(1.5)	0.005	50.0
88	Fenthion-sulfone	2–200	0.9973	90.9(2.2)	88.4(2.1)	86.3(1.4)	0.01	54.7
89	<i>o,p'</i> -DDD	1–200	0.9993	96.7(8.4)	110.8(5.1)	112.2(3.8)	0.01	69.8
90	<i>o,p'</i> -DDT	1–200	0.9964	78.8(1.1)	72.6(2.5)	77.7(1.8)	0.005	–17.8
91	Ethion	1–200	0.9971	88.9(1.6)	91.0(2.7)	92.2(1.6)	0.01	16.9
92	Fensulfothion sulfone	1–200	0.9970	88.8(1.1)	97.7(3.8)	101.6(1.9)	0.01	34.9
93	Famphur	1–200	0.9977	90.7(2.9)	92.8(3.0)	95.4(2.0)	0.005	99.3
94	Benalaxyl	1–200	0.9978	90.4(3.5)	90.6(2.2)	91.3(1.9)	0.005	8.7
95	Endosulfan sulfate	5–200	0.9979	93.4(4.9)	91.7(2.0)	87.0(1.6)	0.01	10.3
96	Propiconazole	1–200	0.9975	84.3(2.6)	96.2(3.9)	98.0(1.9)	0.005	39.9
97	<i>p,p'</i> -DDT	1–200	0.9948	75.3(4.7)	71.6(2.3)	74.6(1.7)	0.01	–9.6
98	Tebuconazole	1–200	0.9980	88.3(3.1)	90.5(2.4)	89.9(1.4)	0.005	49.1
99	Piperonyl butoxide	1–200	0.9980	85.1(2.6)	94.8(3.1)	96.7(1.8)	0.01	45.6
100	Pyridaphenthion	1–200	0.9964	83.9(4.7)	99.6(3.3)	102.7(2.0)	0.01	49.2
101	Phosmet	1–200	0.9952	85.2(1.3)	91.6(3.6)	96.1(2.2)	0.01	–2.8
102	Bromopropylate	1–200	0.9983	89.5(1.7)	90.8(1.8)	91.7(1.6)	0.005	27.1
103	Bifenthrin	1–200	0.9983	86.0(1.8)	96.8(3.8)	99.2(1.8)	0.005	26.3
104	Bifenazate	1–200	0.9962	83.3(2.9)	94.6(2.8)	95.9(1.8)	0.01	50.3
105	Methoxychlor	1–200	0.9941	78.0(3.3)	72.4(2.5)	75.2(1.7)	0.01	–10.9
106	Fenpropathrin	1–200	0.9973	91.3(2.4)	88.1(3.4)	89.8(2.0)	0.01	6.7
107	Tebufenpyrad	1–200	0.9975	88.4(1.2)	91.1(2.6)	92.9(1.9)	0.01	13.5
108	Tetradifon	2–200	0.9974	92.5(4.8)	90.1(2.8)	94.5(1.6)	0.005	–3.9
109	Phenothrin	1–200	0.9979	83.0(2.5)	91.8(4.2)	95.3(2.9)	0.01	48.3
110	Phosalone	1–200	0.9959	84.9(2.2)	94.3(3.5)	98.7(2.1)	0.01	51.8
111	Azinphos-methyl	1–200	0.9945	84.9(1.8)	80.5(1.9)	82.4(1.9)	0.01	–28.7
112	Mefenacet	1–200	0.9982	85.6(1.4)	97.2(3.8)	101(1.7)	0.005	72.8
113	Mirex	1–200	0.9985	85.0(4.9)	88.2(9.4)	86.6(4.1)	0.005	–16.1
114	Cyhalothrin	1–200	0.9950	82.5(0.2)	88.8(3.7)	93.2(1.5)	0.01	26.4
115	$\lambda$ -Cyhalothrin	1–200	0.9943	81.8(2.3)	86.8(3.6)	91.2(2.3)	0.01	35.6
116	Fenarimol	1–200	0.9979	84.7(0.8)	94.0(2.5)	94.6(1.8)	0.01	23.8
117	Pyrazophos	1–200	0.9965	81.7(2.3)	86.4(4.6)	92.1(2.3)	0.01	60.3
118	Acrinathrin	2–200	0.9922	83.0(2.7)	83.0(2.4)	88.0(1.3)	0.01	–50.9
119	Bitertanol	1–200	0.9977	85.6(1.7)	90.0(3.3)	93.1(1.8)	0.01	88.7
120	Permethrin	1–200	0.9988	86.7(3.4)	94.3(4.5)	97.7(3.3)	0.005	–47.8
121	Coumaphos	1–200	0.9974	83.8(2.1)	79.4(3.6)	80.8(1.8)	0.01	59.4
122	Fluquinconazole	1–200	0.9984	86.8(2.1)	90.5(2.1)	90.2(2.0)	0.005	29.3
123	Pyridaben	1–200	0.9976	83.0(1.8)	91.6(3.2)	94.1(1.9)	0.005	28.4
124	Cyfluthrin	2–200	0.9960	80.4(2.0)	92.0(4.7)	98.6(2.6)	0.01	–49.4
125	Boscalid	1–200	0.9973	82.9(1.3)	92.3(2.2)	89.0(1.0)	0.005	64.4
126	Cypermethrin	1–200	0.9938	88.6(1.8)	92.8(5.0)	97.7(1.7)	0.01	–22.7
127	Quizalofop-ethyl	1–200	0.9964	82.7(0.9)	91.3(4.9)	95.4(2.6)	0.01	56.4
128	Flucythrinate	1–200	0.9945	81.3(1.4)	90.6(4.0)	96.4(2.0)	0.01	–39.5
129	Ethofenprox	1–200	0.9948	74.4(14.4)	85.2(10.8)	93.9(3.4)	0.01	1.3
130	Phenvalerate	2–200	0.9935	79.0(2.6)	82.8(2.7)	80.9(2.0)	0.01	–46.7
131	Tua-Fluvalinate	1–200	0.9911	79.5(0.9)	78.8(2.2)	80.1(1.4)	0.01	–36.4
132	Difenoconazole	1–200	0.9979	72.2(10.5)	90.2(7.2)	85.2(2.0)	0.01	–68.5
133	Deltamethrin	1–200	0.9905	75.5(3.8)	82.6(2.8)	86.6(2.2)	0.01	–34.3

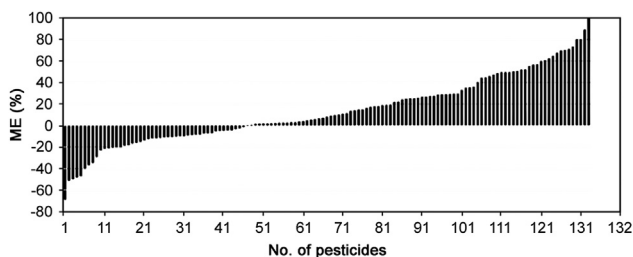


Fig. 7. Matrix effect of pesticides in chenpi.

harmful to human health. Therefore, it is important to pay attention to the appropriate use of pesticides.

#### 4. Conclusions

A modified QuEChERS method for the determination of multiple pesticides by GC-MS/MS was developed. Several sorbents were evaluated in order to reduce the ME as much as possible. C18 and PSA were mainly used in the Original QuEChERS method. In our

**Table 3**  
Pesticide residues found in different batches of chenpi samples and their concentrations (mg/kg).

No.	Pesticide found (mg/kg)				
	Chlorpyrifos	Isocarbophos	Methidathion	Profenofos	Fenpropathrin
2	< LOQ	n.d.	0.016	n.d.	n.d.
5	n.d.	n.d.	0.014	n.d.	n.d.
10	< LOQ	n.d.	0.016	n.d.	< LOQ
14	0.007	< LOQ	n.d.	n.d.	n.d.
16	0.008	< LOQ	< LOQ	0.007	0.221
17	0.007	0.009	0.017	0.006	0.025
18	< LOQ	< LOQ	0.013	< LOQ	0.117
20	< LOQ	< LOQ	< LOQ	n.d.	0.042
MRL	0.01	0.01	0.02	0.01	2

Note: n.d.: no residues detected. MRL: maximum residue limit.

study, PSA had an effect on the pesticide ditalimfos, which showed an unsatisfactory recovery on increasing the amount of PSA. NH<sub>2</sub>, with a similar adsorption performance to PSA, is a substitute product of PSA for base-sensitive pesticides or pesticides which could be affected by PSA. The addition of GCB can remove pigment extracted with acetonitrile. A validation procedure was performed, which showed good results for suitability, recovery and repeatability. The developed method was applied to the determination of real samples, and some pesticides were detected, which demonstrated that it is essential to constantly monitor pesticide residues in chenpi.

### Acknowledgments

The authors wish to thank the management of Tasly Academy for supporting this research.

### Conflicts of interest

The authors declare that there are no conflicts of interest.

### References

- [1] Chinese Pharmacopoeia Commission, Pharmacopoeia of the People's Republic of China, China Medical Science Press, Beijing, China, 2015.
- [2] Z.B. Yi, Y. Yu, Y. Liang, et al., In vitro antioxidant and antimicrobial activities of the extract of pericarpium citri reticulatae of a new citrus cultivar and its main flavonoids, *LWT-Food Sci. Technol.* 41 (2018) 597–603.
- [3] X.J. Peng, W.H. Liang, M. Peng, et al., Determination of 8 organophosphorus pesticides in pericarpium citri Reticulatae and its products by solid phase extraction/gas chromatography, *J. Instrum. Anal.* 10 (2016) 1267–1272.
- [4] M. Ma, C. Chen, G. Yang, et al., Combined cytotoxic effects of pesticide mixtures present in the Chinese diet on human hepatocarcinoma cell line, *Chemosphere* 159 (2016) 256–266.
- [5] G. Babayeva, R. Issayeva, A. Zhumadilova, et al., Organochlorine pesticides and female puberty in South Kazakhstan, *Reprod. Toxicol.* 65 (2016) 67–75.
- [6] X.J. Peng, H. Qin, Q.J. Wen, et al., Application of homemade double solid phase extraction column for determination of 11 organophosphorus pesticides in Xinhui dried orange peel and its pproducts, *Chin. J. Chromatogr.* 34 (2016) 817–822.
- [7] M. Pelajic, G. Pecek, D.M. Pavlovic, et al., Novel multiresidue method for determination of pesticides in red wine using gas chromatography–mass spectrometry and solid phase extraction, *Food Chem.* 200 (2016) 98–106.
- [8] X. Yang, H. Zhang, Y. Liu, et al., Multiresidue method for determination of 88 pesticides in berry fruits using solid-phase extraction and gas chromatography–mass spectrometry: determination of 88 pesticides in berries using SPE and GC–MS, *Food Chem.* 127 (2011) 855–865.
- [9] I. Machado, N. Gerez, M. Piston, et al., Determination of pesticide residues in globe artichoke leaves and fruits by GC–MS and LC–MS/MS using the same QuEChERS procedure, *Food Chem.* 227 (2017) 227–236.
- [10] M. Sajid, C. Basheer, M. Daud, et al., Evaluation of layered double hydroxide/graphene hybrid as a sorbent in membrane-protected stir-bar supported micro-solid-phase extraction for determination of organochlorine pesticides in urine samples, *J. Chromatogr. A* 1489 (2017) 1–8.
- [11] N. Zhang, J. Gao, C. Huang, et al., In situ hydrothermal growth of ZnO/gC<sub>3</sub>N<sub>4</sub> nanoflowers coated solid-phase microextraction fibers coupled with GC–MS for determination of pesticides residues, *Anal. Chim. Acta* 934 (2016) 122–131.
- [12] F. David, C. Devos, E. Dumont, et al., Determination of pesticides in fatty matrices using gel permeation clean-up followed by GC–MS/MS and LC–MS/MS analysis: a comparison of low-and high-pressure gel permeation columns, *Talanta* 165 (2017) 201–210.
- [13] W. Lian, F. Ren, L. Tang, et al., Analysis of polycyclic aromatic hydrocarbons in cigarette samples using gel permeation chromatography clean-up by gas chromatography–tandem mass spectrometry, *Microchem. J.* 129 (2016) 194–199.
- [14] G. Wu, X. Bao, S. Zhao, et al., Analysis of multi-pesticide residues in the foods of animal origin by GC–MS coupled with accelerated solvent extraction and gel permeation chromatography cleanup, *Food Chem.* 126 (2011) 646–654.
- [15] M. Anastassiades, S.J. Lehotay, D. Stajnbaher, et al., Fast and easy multiresidue method employing acetonitrile extraction/partitioning and “dispersive solid-phase extraction” for the determination of pesticide residues in produce, *J. AOAC Int.* 86 (2003) 412–431.
- [16] Z. He, L. Wang, Y. Peng, et al., Multiresidue analysis of over 200 pesticides in cereals using a QuEChERS and gas chromatography–tandem mass spectrometry-based method, *Food Chem.* 169 (2015) 372–380.
- [17] Y. Yang, W. Kong, L. Zhao, et al., A multiresidue method for simultaneous determination of 44 organophosphorus pesticides in Pogostemon cablin and related products using modified QuEChERS sample preparation procedure and GC–FPD, *J. Chromatogr. B* 974 (2015) 118–125.
- [18] P. Georgakopoulos, R. Zachari, M. Mataragas, et al., Optimisation of octadecyl (C18) sorbent amount in QuEChERS analytical method for the accurate organophosphorus pesticide residues determination in low-fatty baby foods with response surface methodology, *Food Chem.* 128 (2011) 536–542.
- [19] O. Golge, B. Kabak, Evaluation of QuEChERS sample preparation and liquid chromatography–triple–quadrupole mass spectrometry method for the determination of 109 pesticide residues in tomatoes, *Food Chem.* 176 (2015) 319–332.
- [20] E. Boes, R.T. Rosmalina, Y.S. Ridwan, et al., Pesticide residues in vegetable, *Procedia Chem.* 16 (2015) 229–236.
- [21] R.P. Carneiro, F.A.S. Oliveira, Madureira, et al., Development and method validation for determination of 128 pesticides in bananas by modified QuEChERS and UHPLC–MS/MS analysis, *Food Control.* 33 (2013) 413–423.
- [22] G. Martinez-Dominguez, A.J. Nieto-García, R. Romero-González, et al., Application of QuEChERS based method for the determination of pesticides in nutraceutical products (Camellia sinensis) by liquid chromatography coupled to triple quadrupole tandem mass spectrometry, *Food Chem.* 177 (2015) 182–190.
- [23] S.J. Lehotay, Determination of pesticide residues in foods by acetonitrile extraction and partitioning with magnesium sulfate: collaborative study, *J. AOAC Int.* 90 (2007) 485–520.
- [24] P.S. Tette, F.A. da Silva Oliveira, E.N. Pereira, et al., Multiclass method for pesticides quantification in honey by means of modified QuEChERS and UHPLC–MS/MS, *Food Chem.* 211 (2016) 130–139.
- [25] A. Palenikova, G. Martinez-Dominguez, F.J. Arrebola, et al., Multifamily determination of pesticide residues in soya-based nutraceutical products by GC/MS–MS, *Food Chem.* 173 (2015) 796–807.
- [26] X. Liu, Y. Li, W. Meng, et al., A multi-residue method for simultaneous determination of 74 pesticides in Chinese material medica using modified QuEChERS sample preparation procedure and gas chromatography tandem mass spectrometry, *J. Chromatogr. B.* 1015 (2016) 1–12.
- [27] E.P. Costa, S.S. Caldas, E.G. Primel, Comparison of QuEChERS sample

- preparation methods for the analysis of pesticide residues in canned and fresh peach, *Food Chem.* 165 (2014) 587–593.
- [28] EC-European Commission, Guidance document on analytical quality control and method validation procedures for pesticides residues analysis in food and feed. SANTE/11945/2015.
- [29] B. Lozowicka, G. Ilyasova, P. Kaczynski, et al., Multi-residue methods for the determination of over four hundred pesticides in solid and liquid high sucrose content matrices by tandem mass spectrometry coupled with gas and liquid chromatograph, *Talanta* 151 (2016) 51–61.
- [30] EC-European Commission, Regulation (EC) No 396/2005 of the European Parliament and of the Council of 23 February 2005 on maximum residue levels of pesticides in or on food and feed of plant and animal origin and amending Council Directive 91/414/EEC, *Official Journal of the European Union*, L70, 2005, 1–16.



## Original Article

# Determination of L-norvaline and L-tryptophan in dietary supplements by nano-LC using an O-[2-(methacryloyloxy)-ethylcarbamoyl]-10,11-dihydroquinidine-silica hybrid monolithic column

Dongsheng Xu <sup>a, b, c</sup>, Elena Sánchez-López <sup>a, d</sup>, Qiqin Wang <sup>b, c</sup>, Zhengjin Jiang <sup>b, c, \*\*</sup>,  
María Luisa Marina <sup>a, d, \*</sup>

<sup>a</sup> Departamento de Química Analítica, Química Física e Ingeniería Química, Universidad de Alcalá, Ctra. Madrid-Barcelona Km. 33.600, 28871, Alcalá de Henares (Madrid), Spain

<sup>b</sup> Institute of Pharmaceutical Analysis, College of Pharmacy, Jinan University, Guangzhou, 510632, China

<sup>c</sup> Department of Pharmacy and Guangdong Province Key Laboratory of Pharmacodynamic Constituents of Traditional Chinese Medicine & New Drug Research, Jinan University, Guangzhou, 510632, China

<sup>d</sup> Instituto de Investigación Química "Andrés M. del Río" (IQAR), Universidad de Alcalá, Ctra. Madrid-Barcelona Km. 33.600, 28871, Alcalá de Henares (Madrid), Spain

## ARTICLE INFO

## Article history:

Received 11 August 2019

Received in revised form

19 October 2019

Accepted 19 October 2019

Available online 23 October 2019

## Keywords:

9-Fluorenylmethoxycarbonyl

Amino acids

Chiral separation

Nano-LC

Quinidine-silica hybrid monolithic column

## ABSTRACT

An analytical methodology based on an O-[2-(methacryloyloxy)-ethylcarbamoyl]-10,11-dihydroquinidine (MQD)-silica hybrid monolithic column was developed for the enantioseparation of 9-fluorenylmethoxycarbonyl (Fmoc) derivatized amino acids by nano-liquid chromatography. The mobile phase was optimized including the apparent pH, content of ACN, and concentration of the buffer to obtain a satisfactory enantioresolution performance. 27 Fmoc derivatized amino acids including 19 protein and 8 non-protein amino acids were tested, and 19 out of them were enantiomerically discriminated obtaining baseline separation for 11 of them. Analytical characteristics of the method were evaluated for norvaline and tryptophan in terms of linearity, precision, accuracy, limits of detection (LOD) and quantitation (LOQ) showing good performance to be applied to the enantiomeric determination of these amino acids in dietary supplements. LOD and LOQ values were 9.3 and 31  $\mu\text{M}$  for norvaline enantiomers and 7.5 and 25  $\mu\text{M}$  for tryptophan enantiomers, respectively. The contents of D-norvaline and D-tryptophan were below their respective LODs in all the analyzed samples. Quantitation of L-tryptophan and L-norvaline showed good agreement with the labeled contents except for one sample which did not show presence of L-norvaline, contrary to the label indication.

© 2019 Xi'an Jiaotong University. Production and hosting by Elsevier B.V. This is an open access article under the CC BY-NC-ND license (<http://creativecommons.org/licenses/by-nc-nd/4.0/>).

## 1. Introduction

Amino acids are essential and ubiquitous compounds playing a vital role in many living organisms. Differences in the properties of D- and L-enantiomers have been widely reported, both for protein and non-protein amino acids [1]. For instance, the L-enantiomer of the non-protein amino acid norvaline enhances the nitric oxide

production, which is an important regulator and mediator in physiological and pathophysiological events such as vasodilatation [2]. Moreover, it can be used to treat artificial metabolic syndrome in a rat model [3], and it has been proven to be effective in Alzheimer's disease (AD) [4,5]. However, to the best of our knowledge, D-norvaline has not been reported as an effective substance. On the other hand, L-tryptophan is a protein amino acid which is the precursor of important neurotransmitters, hormones and other relevant biomolecules [6]. The level of L-tryptophan in humans has been reported to act as a biomarker of certain diseases [7,8]. At the pharmacological level, L-tryptophan is used as antidepressant agent [9], whereas D-tryptophan is considered as an impurity because of its low biological activity [10,11]. In addition, only the L-enantiomer of tryptophan is involved in the synthesis of proteins and, additionally, it can cross the blood-brain, being the precursor of the

Peer review under responsibility of Xi'an Jiaotong University.

\* Corresponding author at: Departamento de Química Analítica, Química Física e Ingeniería Química, Universidad de Alcalá, Ctra. Madrid-Barcelona Km. 33.600, 28871, Alcalá de Henares (Madrid), Spain.

\*\* Corresponding author at: Institute of Pharmaceutical Analysis, College of Pharmacy, Jinan University, Guangzhou, 510632, China.

E-mail addresses: [jzjackson@hotmail.com](mailto:jzjackson@hotmail.com) (Z. Jiang), [mluisa.marina@uah.es](mailto:mluisa.marina@uah.es) (M.L. Marina).

<https://doi.org/10.1016/j.jpha.2019.10.001>

2095-1779/© 2019 Xi'an Jiaotong University. Production and hosting by Elsevier B.V. This is an open access article under the CC BY-NC-ND license (<http://creativecommons.org/licenses/by-nc-nd/4.0/>).

important neurotransmitter serotonin [12]. Amino acids can be used as ingredients in dietary supplements where the presence of the D-enantiomer is not allowed by legal regulations [13]. Therefore, the enantiomeric determination of DL-amino acids in real samples remains a very important challenge.

In order to obtain satisfactory chiral separation of amino acids, various chiral stationary phases (CSPs) have been developed, including those based on cyclodextrins [14], polysaccharides [15], 3,5-dinitrobenzamide-naphthylglycine derivatives [16], macrocyclic antibiotics [17] and cinchona alkaloids [18–21]. Cinchona alkaloids, especially quinine and quinidine have attracted much attention owing to their excellent enantioselectivity for amino acids. Usually, because of the low detection sensitivity and weak interaction between the chiral selector and analytes, different derivatization groups were used to react with the amino acids, such as 4-fluoro-7-nitro-2,1,3-benzoxadiazole (NBD-F) [22–24], 9-fluorenylmethoxycarbonyl (FMOC) fluoride [25,26], 2,4-dinitrofluorobenzene (DNFB) [27], dansyl chloride (DNS-Cl) [28], and carbazole-9-carbonyl chloride (CC-Cl) [18]. Among the different derivatization reagents, FMOC not only allows the amino acids to achieve satisfactory enantioresolution, but also has the advantage of reacting with primary and secondary amines in just 3 min.

Over the past several decades, monolithic columns have exhibited high separation efficiency and sensitivity, low sample and elution solvent consumption, as well as the ease of coupling to MS [29–32]. So far, the use of quinine or quinidine functionalized monolithic columns has been reported in the enantioresolution of amino acids in capillary electrochromatography (CEC) and nano-liquid chromatography (nano-LC). For instance, Lämmerhofer et al. [18,33] separated some N-derivatized amino acid standards with high efficiency and enantioresolution on the quinine and quinidine silica-based monolithic column by CEC. On the other hand, Wang et al. [25,29] developed several quinidine polymer-based monolithic columns which were also successful in enantio-separating N-derivatized amino acid standards by nano-LC. However, the silica or polymer based monolithic column was limited by the cumbersome and multi-step preparation method, or low mechanical strength and poor stability. On the other hand, they focused on the development of the novel monolithic columns, but their application in the real sample was not reported.

Silica-hybrid monolithic columns offer great advantages such as high surface, little shrinkage, excellent pH stability and good permeability [34–36]. However, they have scarcely been employed for the enantioresolution of amino acids. Thus, Tran et al. [19] only separated dinitrobenzoyl-leucine on the quinidine-silica/zirconia hybrid monolithic column by CEC and Kato et al. [37] tried to enantioresolve DL-tryptophan on a new-type bovine serum albumin (BSA)-encapsulated hybrid monolithic column. Unfortunately, the enantioresolution was very limited. In a previous work, our research group prepared an O-[2-(methacryloyloxy)-ethyl-carbamoyl]-10,11-dihydroquinidine (MQD)-silica hybrid monolithic column and the enantiomeric separation of protein and non-protein amino acids was investigated using up to 8 different derivatization reagents including 3,5-dinitrobenzoyl chloride, 3,5-dichlorobenzoyl chloride, *p*-nitrobenzoyl chloride, 3,5-dimethoxybenzoyl chloride, *m*-chlorobenzoyl chloride, *p*-chlorobenzoyl chloride, benzoyl chloride, and FMOC chloride [38]. Nevertheless, from the 8 FMOC-amino acids tested, only 2 of them were baseline separated in the reversed phase mode (valine ( $R_s$  1.55) and isoleucine ( $R_s$  1.71)) and none of them was baseline separated in the polar organic phase mode [38]. Moreover, the applicability of quinidine silica-hybrid monolithic column to the quantitative analysis of amino acids in real samples has not been

demonstrated yet. In this work, the enantiomeric separation of protein and non-protein FMOC derivatized amino acids was achieved by nano-LC using the above-mentioned MQD-silica hybrid monolithic column. In order to obtain satisfactory enantio-resolution performance in the reversed phased mode, the mobile phase was systematically optimized, including the apparent pH, content of ACN, and buffer concentration. Under the optimized conditions, 27 FMOC-derivatized amino acids consisting of 19 protein and 8 non-protein amino acids were tested. Finally, the analytical characteristics of the developed method were evaluated for norvaline and tryptophan and the method was applied to the quantitation of L-norvaline and L-tryptophan in dietary supplements.

## 2. Materials and methods

### 2.1. Reagents and samples

All reagents were of analytical grade. Methanol (MeOH), acetonitrile (ACN), and acetic acid (HAc) were acquired from Scharlau Chemie (Barcelona, Spain). Triethylamine (TEA) and 9-fluorenylmethoxycarbonyl (FMOC) chloride were obtained from Fluka (Buchs, Switzerland). Ammonium hydroxide ( $\text{NH}_3 \cdot \text{H}_2\text{O}$ ), boric acid ( $\text{H}_3\text{BO}_3$ ) and pentane were from Sigma (St. Louis, Missouri, USA), and ammonium acetate was from Merck (Darmstadt, Germany). 10,11-dihydroquinidine, 2,2'-azobisisobutyronitrile (AIBN), 3-(trimethoxysilyl)-propylmethacrylate ( $\gamma$ -MAPS), vinyltrimethoxysilane (VTMS), cetyltrimethylammonium bromide (CTAB), tetramethoxysilane (TMOS) and ethylene glycol (EG) were acquired from Aladdin Chemicals (Shanghai, China). DL-arginine, DL-histidine, DL-lysine, DL-serine, DL-threonine, DL-asparagine, DL-glutamine, DL-cysteine, DL-proline, DL-alanine, DL-valine, DL-leucine, DL-methionine, DL-phenylalanine, DL-tyrosine, D-tryptophan, L-tryptophan, DL-ornithine, DL-citrulline standards were from Fluka (Buchs, Switzerland), while DL-isoleucine, DL-carnitine, DL-aspartic acid, DL-glutamic acid, DL-norvaline, L-norvaline, DL-norleucine, DL-DOPA, DL-pyroglyutamic acid and DL-methionine sulfone were obtained from Sigma (St. Louis, Missouri, USA). FMOC-amino acids were synthesized as reported previously [29,30]. The dietary supplements were obtained in capsule form from online sources.

### 2.2. Instrumentation

All nano-LC experiments were conducted on a laboratory self-assembled nano-LC instrument. The system consisted of a Shimadzu LC-20AD pump (Kyoto, Japan), a Linear Instruments UV-Vis 200 detector (California, USA), and a Valco four-port injection valve with 20 nL internal loop (Houston, USA). In order to reduce the flow and pressure, a stainless-steel tee (Cheminert, Valco Instruments Houston, Texas, USA) with flow split capillary (150 mm  $\times$  25  $\mu\text{m}$  I.D.) was employed before the injection valve. The data acquisition and data handling were performed using the software Chromatostation N200 (Zhejiang University, China). All chromatograms were converted to a text file and redrawn using Microcal Origin 8.5. pH values of buffer solutions were measured in a 744 pH meter (Herisau, Switzerland).

### 2.3. Chromatographic conditions

Mobile phase was prepared by mixing the 3 mM ammonium acetate solution with ACN (35/65, v/v), and adjusting the apparent pH to the desired value (pH 4.8) with acetic acid. In the beginning,

the mobile phase was subjected to filtration through a 0.22  $\mu\text{m}$  membrane and sonication degas prior to be employed. The total flow rate was 10  $\mu\text{L}/\text{min}$ , total backpressure was 23 bar, injection volume was 20 nL, and the UV detection wavelength was 254 nm.

#### 2.4. Preparation of the MQD-silica hybrid monolithic column

Synthesis of the MQD-silica hybrid monolithic column was conducted as previously reported [38]. Briefly, anchoring sites for the bulk polymer on the inner capillary walls were generated using  $\gamma$ -MAPS/MeOH (50/50, v/v). The pre-polymerizable mix for the MQD column was prepared as follows: MQD (6.0 mg), MeOH (100  $\mu\text{L}$ ), EG (30  $\mu\text{L}$ ), CTAB (1.6 mg),  $\text{H}_2\text{O}$  (30  $\mu\text{L}$ ),  $\text{NH}_3 \cdot \text{H}_2\text{O}$  (0.02 M, 30  $\mu\text{L}$ ), TMOS (60  $\mu\text{L}$ ), VTMS (80  $\mu\text{L}$ ), and AIBN (1 mg) were mixed in

a 2 mL vial and sonicated during 5 min at room temperature. The obtained homogeneous solution was introduced into the 30 cm pre-treated capillary. Both ends of the capillary column were sealed using GC septa and capillary was placed in a water bath at 40  $^\circ\text{C}$  during 12 h first, then at 60  $^\circ\text{C}$  for another 12 h. Non-reacted CTAB and other waste products were rinsed out by flushing the column with MeOH. The monolithic column was cut to 15 cm for further use.

#### 2.5. Preparation of the standard and dietary supplements solutions

FMOC-amino acids standard solutions were prepared by dissolving the corresponding amino acid standards into 1 mL of 200 mM  $\text{H}_3\text{BO}_3$  (pH 9.0) to obtain a 10 mM solution, and were

**Table 1**  
Effect of the mobile phase composition and pH on the enantioseparation data for FMOC derivatized amino acids.

Mobile phase	Sample	$k_1$	$k_2$	$\alpha$	$R_s$	$N_1$ (m)	$N_2$ (m)
<b>Apparent pH<sup>a</sup></b>							
pH=4.3	FMOC-methionine	0.83	1.00	1.21	0.73	14700	13600
	FMOC-valine	0.52	0.69	1.33	0.93	17200	17000
	FMOC-methionine sulfone	0.88	1.08	1.22	0.76	14000	12000
	FMOC-norvaline	0.53	0.64	1.20	0.54	14900	12800
pH=4.8	FMOC-methionine	1.65	2.00	1.21	1.20	14200	13000
	FMOC-valine	1.11	1.47	1.33	1.45	14500	14300
	FMOC-methionine sulfone	1.54	1.90	1.23	1.10	11900	11500
	FMOC-norvaline	1.13	1.37	1.21	0.97	14700	14200
pH=5.3	FMOC-methionine	3.42	4.06	1.19	0.84	13200	8900
	FMOC-valine	2.57	3.35	1.30	1.55	12000	9700
	FMOC-methionine sulfone	1.91	2.33	1.22	0.81	13400	8500
	FMOC-norvaline	2.56	3.14	1.23	0.88	11000	8200
<b>Buffer concentration<sup>b</sup></b>							
1.0 mM	FMOC-methionine	7.85	9.52	1.21	1.58	7500	6000
	FMOC-valine	5.25	7.12	1.36	1.87	5600	4600
	FMOC-methionine sulfone	8.01	10.16	1.27	1.46	5800	4800
	FMOC-norvaline	5.77	7.09	1.23	1.46	5900	4600
3.0 mM	FMOC-methionine	4.26	5.15	1.21	1.52	13200	12700
	FMOC-valine	2.82	3.78	1.34	1.74	12500	11800
	FMOC-methionine sulfone	4.06	4.99	1.23	1.46	10100	9600
	FMOC-norvaline	2.85	3.48	1.22	1.44	12500	11200
5.0 mM	FMOC-methionine	2.59	3.16	1.22	1.44	13600	13100
	FMOC-valine	1.75	2.32	1.33	1.56	13500	12800
	FMOC-methionine sulfone	2.58	3.20	1.24	1.44	12000	11000
	FMOC-norvaline	1.89	2.28	1.21	1.37	15800	15000
10 mM	FMOC-methionine	1.65	2.00	1.21	1.20	14200	13000
	FMOC-valine	1.11	1.47	1.33	1.45	14500	14300
	FMOC-methionine sulfone	1.54	1.90	1.23	1.10	11900	11500
	FMOC-norvaline	1.13	1.37	1.21	0.97	14900	14200
<b>ACN content<sup>c</sup></b>							
60%	FMOC-methionine	8.78	10.75	1.23	1.61	12500	11000
	FMOC-valine	6.07	8.05	1.33	1.95	12100	11800
	FMOC-methionine sulfone	6.46	7.91	1.23	1.54	12300	11000
	FMOC-norvaline	6.24	7.58	1.21	1.52	11700	10200
65%	FMOC-methionine	6.11	7.40	1.21	1.58	13000	11800
	FMOC-valine	4.13	5.54	1.34	1.92	12400	11500
	FMOC-methionine sulfone	4.95	6.07	1.23	1.52	8400	7100
	FMOC-norvaline	4.26	5.25	1.23	1.52	14400	11500
70%	FMOC-methionine	4.26	5.15	1.21	1.52	13200	12700
	FMOC-valine	2.82	3.78	1.34	1.74	12500	11800
	FMOC-methionine sulfone	4.06	4.99	1.23	1.46	10100	9600
	FMOC-norvaline	2.85	3.48	1.22	1.44	12500	11200
75%	FMOC-methionine	2.98	3.60	1.21	1.45	13600	13300
	FMOC-valine	1.99	2.63	1.32	1.59	12700	11700
	FMOC-methionine sulfone	3.27	4.01	1.23	1.39	11700	10100
	FMOC-norvaline	1.99	2.41	1.22	1.41	12500	11100
80%	FMOC-methionine	1.89	2.27	1.20	1.24	15800	15100
	FMOC-valine	1.21	1.60	1.32	1.51	15400	14200
	FMOC-methionine sulfone	2.48	3.01	1.21	1.29	13200	12800
	FMOC-norvaline	1.21	1.46	1.21	1.01	16100	15800

Experimental conditions as in Fig. 1.

<sup>a</sup> 10 mM ammonium acetate/ACN (30/70, v/v) (at the desired apparent pH values).

<sup>b</sup> Ammonium acetate/ACN (at the desired concentration of the buffer) (30/70, v/v) (apparent pH=4.8).

<sup>c</sup> 3 mM ammonium acetate/ACN (at the desired ratio of ACN and buffer, v/v) (apparent pH=4.8).

sonicated for 2 min. Then, 1 mL of a 220 mM FMOCl solution in acetonitrile was added and it was made to react at room temperature for 3 min. Afterwards, 2 mL of pentane was added into the solution and it was vortexed. After 5 min of resting, the lower layer solution was diluted at the desired concentration using the mobile phase.

FMOCl-dietary supplement solutions were prepared by dissolving the powder within the capsules (200 mg norvaline or 2 mg tryptophan) into 1 mL of 200 mM  $H_3BO_3$  (pH 9.0) and were sonicated for 2 min, then they were filtered and 1 mL of 220 mM FMOCl in acetonitrile was then added into the filtrate. Reaction took place for 3 min at room temperature. Afterwards, 2 mL of pentane was added into the solution and it was vortexed. Finally, after 5 min of resting, the lower layer solution was diluted at the desired concentration using the mobile phase.

### 3. Results and discussion

#### 3.1. Enantioseparation of FMOCl-amino acids by nano-LC using a MQD-silica hybrid monolithic column

The MQD-silica hybrid monolithic column was prepared as detailed in Section 2.4. In a previous work from our research group, the enantiomeric separation of protein and non-protein amino acids was investigated using up to 8 different derivatization reagents [38]. However, when using FMOCl as derivatizing reagent, from the eight amino acids tested, only two of them were baseline separated in the reversed phase mode (10 mM ammonium acetate/ACN (30/70, v/v)(apparent pH 5.3))(valine ( $R_s$  1.55) and isoleucine ( $R_s$  1.71)) and none of them was baseline separated in the polar organic phase mode (0.05% HAC, 0.005% TEA in ACN/MeOH (60/40, v/v)) [38]. As shown in Fig. S1, when comparing the polar organic-phase and reversed-phase modes for some FMOCl-amino acids, the latter enabled obtaining better peak shapes [38]. Thus, the reversed phase mode was selected in order to obtain a good

enantioresolution for the FMOCl derivatized amino acids. With this aim, in this work, the mobile phase was optimized using four FMOCl derivatized amino acids, i.e. two protein amino acids (methionine and valine) and two non-protein amino acids (methionine sulfone and norvaline).

First, the effect of apparent pH on the retention factors ( $k_1$  and  $k_2$ ), enantioselectivity ( $\alpha$ ), enantioresolution ( $R_s$ ) and efficiency ( $N_1$  and  $N_2$ ). As shown in Table 1, the apparent pH values were evaluated from 4.3 to 5.3 in the mobile phase 10 mM ammonium acetate/ACN (30/70, v/v), while other conditions were kept constant. On the one hand, when increasing the apparent pH value from 4.3 to 5.3, the enantioselectivity kept constant but the retention factors increased for the four analytes. This can be explained that the chiral selector is positively charged when the pH of the mobile phase is between 4.3 and 5.3, while the four FMOCl-derivatized amino acids are negatively charged, thus leading to a stronger electrostatic interaction between the analytes and the CSP. On the other hand, the enantioresolution significantly increased when the apparent pH value changed from 4.3 to 4.8, while the efficiency gradually decreased. Further increasing in the apparent pH value to 5.3 led to similar values of enantioresolution, while the efficiency decreased significantly. Considering the retention factors, enantioresolution and efficiency, an apparent pH of 4.8 was selected for the following experiments.

Second, the influence of the buffer concentration was investigated while keeping constant the mobile phase apparent pH at 4.8 and composition as ammonium acetate/ACN (30/70, v/v). As shown in Table 1, the retention factors, analysis time and enantioresolution values decreased when increasing the concentration of the ammonium acetate buffer from 1 to 10 mM, meanwhile the efficiency increased. Comparing the efficiency, analysis time, and enantioresolution obtained in 1 and 3 mM of ammonium acetate buffer, the efficiency was significantly higher when the buffer concentration increased, but the analysis time increased from 35 min to 60 min (such as in the case of methionine and methionine

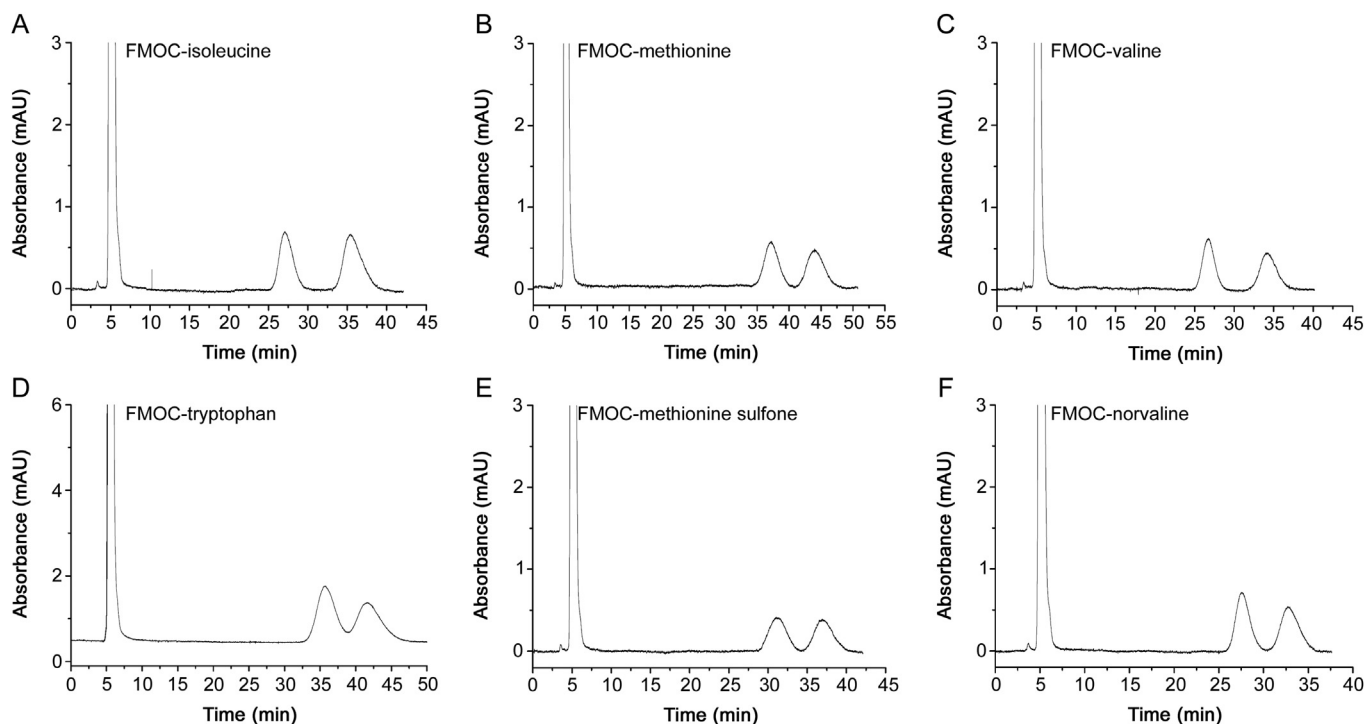


**Fig. 1.** Enantioseparation of some FMOCl-derivatized amino acids. Experimental conditions: column dimensions: 15 cm  $\times$  100  $\mu$ m I.D.; mobile phase: ACN/3 mM ammonium acetate (65/35, v/v) (apparent pH=4.8); UV detection wavelength: 254 nm; flow rate: 10  $\mu$ L/min; backpressure: 23 bar; injection volume: 20 nL.

sulfone), whereas the enantioresolution did not significantly change. Hence, a buffer concentration of 3 mM was selected as a compromise between the analysis time and efficiency.

Third, the ACN content was investigated by varying its percentage from 60 to 80%. As can be seen in Table 1, the retention factor and enantioresolution decreased when increasing the ACN content from 60 to 80%, while apparent pH=4.8 and 3 mM ammonium acetate were kept constant. The hydrophobic interaction between the FMOc derivatized amino acids and MQD-silica hybrid monolithic column is weakened when the organic solvent content in the mobile phase is increased because the elution ability of the mobile phase increases. Considering the analysis time, enantioresolution and efficiency, 65% ACN was selected as the optimum condition in the mobile phase.

Finally, using a 3 mM ammonium acetate/ACN (35/65, v/v) (apparent pH=4.8) mobile phase, 27 FMOc-labeled amino acids (19 protein and 8 non-protein) were assayed. Chiral discrimination for 19 amino acids was observed and a total of 11 FMOc-derivatized amino acids (9 protein and 3 non-protein) were baseline or almost baseline enantioseparated ( $R_s$  1.46 was obtained for tryptophan) (see Table S1). Fig. 1 displays the chiral separation of some representative amino acids.

**Table 2**

Analytical characteristics of the developed method for the enantiomeric determination of norvaline in dietary supplements.

Method and parameter	L-norvaline First enantiomer	D-norvaline Second enantiomer
External standard calibration method <sup>a</sup>		
Range	0.031–12.5	0.031–1.25
Slope $\pm$ t · S <sub>slope</sub>	479786 $\pm$ 5243	478792 $\pm$ 7646
Intercept $\pm$ t · S <sub>intercept</sub>	20902 $\pm$ 24051	–363 $\pm$ 4295
R <sup>2</sup>	0.9993	0.9991
Standard addition calibration method <sup>b</sup>		
Study of matrix interferences (P-value of ANOVA)	0.625	0.779
Accuracy <sup>c</sup>		
Mean recovery (%)	109 $\pm$ 3	105 $\pm$ 6
Precision		
Instrumental repeatability <sup>d</sup>		
t,RSD (%)	0.45	0.38
A,RSD (%)	0.91	1.10
Method repeatability <sup>e</sup>		
t,RSD (%)	1.01	1.14
A,RSD (%)	4.86	5.74
Intermediate precision <sup>f</sup>		
t,RSD (%)	2.14	2.03
A,RSD (%)	5.68	5.45
LOD <sup>g</sup>	9.3 $\mu$ M	
LOQ <sup>h</sup>	31 $\mu$ M	

Experimental conditions as in Fig. 1.

<sup>a</sup> Six standard solutions at different concentration levels injected in triplicate (Concentration of L-norvaline: 12.5, 5.0, 2.5, 1.25, 0.5 and 0.25 mM; concentration of D-norvaline: 1.25, 0.5, 0.25, 0.125, 0.05, and 0.025 mM).

<sup>b</sup> Addition of six known amounts of D- and L-norvaline (Concentration of added L-norvaline: 0.167, 0.250, 0.333, 0.417, 0.500, and 0.583 mM; concentration of added D-norvaline: 0.033, 0.050, 0.067, 0.083, 0.100, and 0.117 mM) to a dietary supplement sample 1 containing a constant concentration of L-norvaline.

<sup>c</sup> Accuracy was evaluated as the recovery obtained from three dietary supplements spiked with standard D,L-norvaline at three different percentages (80, 100, and 120 %) of the labeled content ( $n = 3$ ).

<sup>d</sup> Consecutive injections of a D,L-norvaline standard solution (0.125 mM) ( $n = 6$ ).

<sup>e</sup> 200 mg dietary supplement sample 1 containing 1 mg of L-norvaline (as labeled amount) spiked with 2 mg of L and 2 mg of D-norvaline ( $n = 6$ ).

<sup>f</sup> 200 mg dietary supplement sample 1 containing 1 mg of L-norvaline (as labeled amount) spiked with 2 mg of L-norvaline and 2 mg of D-norvaline in three days ( $n = 9$ ).

<sup>g</sup> LOD obtained for a S/N equal to 3.

<sup>h</sup> LOQ obtained for a S/N equal to 10.

### 3.2. Application of the developed method to the enantiomeric determination of tryptophan and norvaline in dietary supplements

Based on the interest of tryptophan and norvaline as ingredients in dietary supplements, the developed method was applied to the enantiomeric determination of these two amino acids in different dietary supplements. With this aim, the analytical characteristics of the method were evaluated in terms of selectivity, linearity, precision, accuracy and limits of detection (LOD) and quantitation (LOQ) both for norvaline (Table 2) and for tryptophan (Table 3). The selectivity was suitable for tryptophan and norvaline enantiomers because they were separated and there were no interfering peaks which originated from the sample matrices. The linearity results were obtained from six standard solutions at different concentration levels, injected in triplicate. As shown in Tables 2 and 3, the linearity for the two analytes was demonstrated to be adequate in all cases as R<sup>2</sup> values were  $\geq 99.0\%$ , and confidence intervals for the slope did not include the zero value, meanwhile confidence interval for the intercept included the zero value for a 95% confidence level. In order to assess whether there were matrix interferences, slopes of the calibration curves obtained from the external standard and standard additions calibration methods were compared using analysis of variance (ANOVA) test. Both for tryptophan and norvaline, the p-values of ANOVA were above 0.05 which means that there were no matrix interferences for a 95% confidence level. Therefore, the external standard calibrations method was considered appropriate

**Table 3**

Analytical characteristics of the developed method for the enantiomeric determination of tryptophan in dietary supplements.

Method and parameter	L-tryptophan First enantiomer	D-tryptophan Second enantiomer
External standard calibration method <sup>a</sup>		
Range	0.025–12.5	0.025–1.25
Slope $\pm$ t · S <sub>slope</sub>	599205 $\pm$ 1696	598197 $\pm$ 16093
Intercept $\pm$ t · S <sub>intercept</sub>	7267 $\pm$ 7782	3259 $\pm$ 9041
R <sup>2</sup>	0.9995	0.9996
Standard addition calibration method <sup>b</sup>		
Study of matrix interferences (P-value of ANOVA)	0.821	0.887
Accuracy <sup>c</sup>		
Mean recovery (%)	98 $\pm$ 2	101 $\pm$ 3
Precision		
Instrumental repeatability <sup>d</sup>		
t,RSD (%)	0.48	0.56
A,RSD (%)	0.50	1.11
Method repeatability <sup>e</sup>		
t,RSD (%)	1.10	1.30
A,RSD (%)	4.71	4.00
Intermediate precision <sup>f</sup>		
t,RSD (%)	4.15	4.44
A,RSD (%)	6.15	6.69
LOD <sup>g</sup>	7.5 $\mu$ M	
LOQ <sup>h</sup>	25 $\mu$ M	

Experimental conditions as in Fig. 1.

<sup>a</sup> Six standard solutions at different concentration levels injected in triplicate (Concentration of L- and D-tryptophan same as norvaline in Table 2).

<sup>b</sup> Addition of six known amounts of D- and L-tryptophan (Concentration of added L-tryptophan: 0.139, 0.167, 0.208, 0.278, 0.417, and 0.833 mM; concentration of added D-tryptophan: 0.028, 0.033, 0.042, 0.056, 0.083, and 0.167 mM) to a dietary supplement sample 1 containing a constant concentration of L-tryptophan.

<sup>c</sup> Accuracy was evaluated as in Table 2.

<sup>d</sup> Consecutive injections of a D,L-tryptophan standard solution (0.333 mM) ( $n = 6$ ).

<sup>e</sup> 2 mg dietary supplement sample 1 containing 2 mg of L-tryptophan (as labeled amount) spiked with 2 mg of D-tryptophan ( $n = 6$ ).

<sup>f</sup> 2 mg dietary supplement sample 1 containing 2 mg of L-tryptophan (as labeled amount) spiked with 2 mg of D-tryptophan in three days ( $n = 9$ ).

<sup>g</sup> LOD obtained for a S/N equal to 3.

<sup>h</sup> LOQ obtained for a S/N equal to 10.

to perform the quantitation of the analytes in the dietary supplements. Accuracy was evaluated as the recovery obtained from both spiked solutions of norvaline and tryptophan at different labeled content percentages (80, 100 and 120%) injected in triplicate. As shown in Tables 2 and 3, recovery values for the two analytes were satisfactory as all of them were near the 100%. Precision was evaluated as the instrumental repeatability, method repeatability and intermediate precision. As Tables 2 and 3 show, regarding the instrumental repeatability, the RSD values (%) for areas and retention times were lower than 1 and 2%, respectively. For the method repeatability, the RSD values (%) for areas and retention times were also adequate, with values lower than 2 and 6%, respectively.

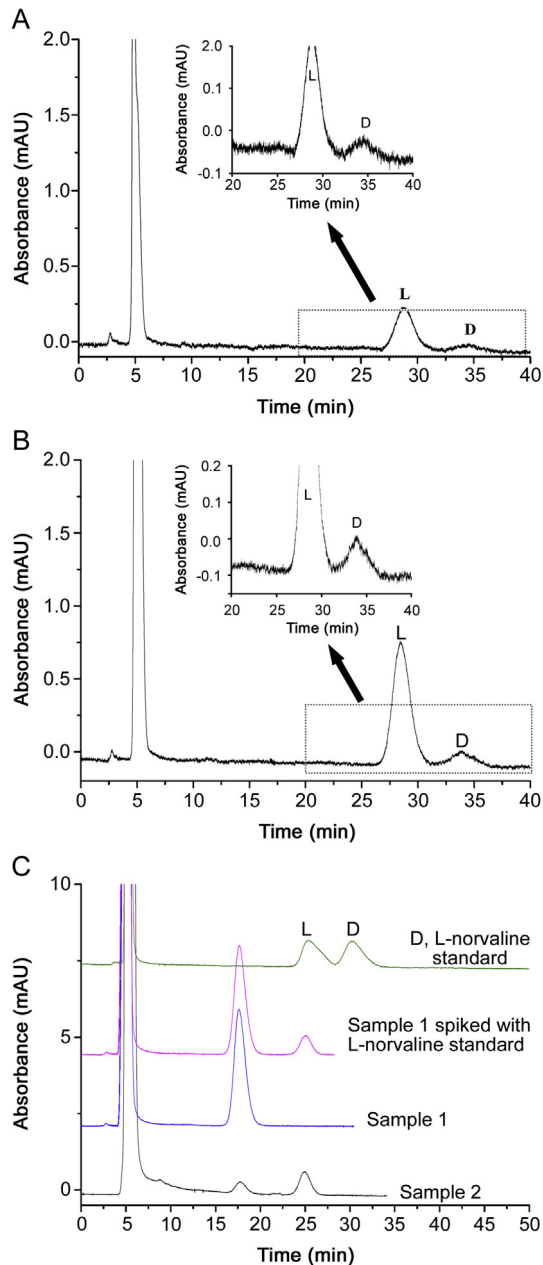


**Fig. 2.** Chromatograms corresponding to (A) the LOD (9.3  $\mu\text{M}$ ) and (B) the LOQ (31  $\mu\text{M}$ ) of D-norvaline; (C) FMOC-derivatized racemic norvaline standard solution (0.5 M) and analyzed dietary supplements whose label indicated presence of L-norvaline (samples 1 and 2). Experimental conditions: 15 cm  $\times$  100  $\mu\text{m}$  I.D.; mobile phase: ACN/3 mM ammonium acetate (65/35, v/v) (apparent pH=4.8); UV detection wavelength: 254 nm; flow rate: 10  $\mu\text{L}/\text{min}$ ; backpressure: 23 bar; injection volume: 20 nL.

Moreover, in the case of intermediate precision, the RSD values (%) were lower than 10% for both the areas and retention times.

Regarding LOD and LOQ values, as can be seen in Tables 2 and 3, these values were 9.3 and 31  $\mu\text{M}$  for norvaline enantiomers, and 7.5 and 25  $\mu\text{M}$  for tryptophan enantiomers. Figs. 2A and B, and 3A and 3B display the chromatograms corresponding to the enantiomeric separation of norvaline and tryptophan, respectively, at concentrations corresponding to their LOD and LOQ.

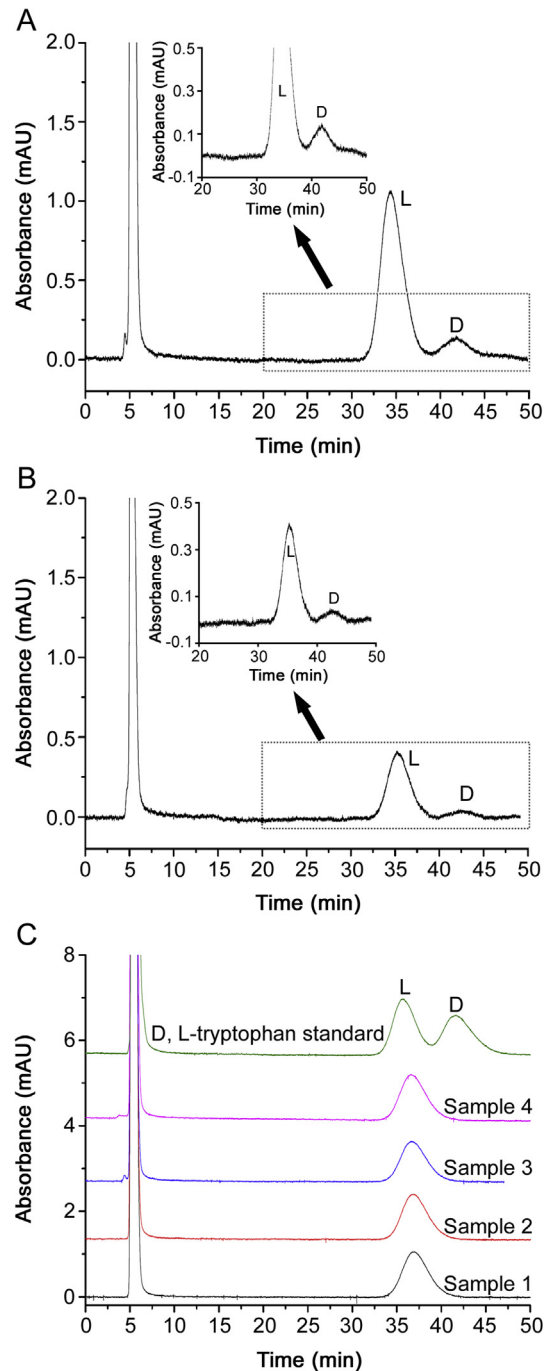


**Fig. 3.** Chromatograms corresponding to (A) the LOD (7.5  $\mu\text{M}$ ) and (B) the LOQ (25  $\mu\text{M}$ ) of D-tryptophan; (C) FMOC-derivatized racemic tryptophan standard solution and analyzed dietary supplements whose label indicates presence of L-tryptophan (samples 1–4). Experimental conditions: 15 cm  $\times$  100  $\mu\text{m}$  I.D.; mobile phase: ACN/3 mM ammonium acetate (65/35, v/v) (apparent pH=4.8); UV detection wavelength: 254 nm; flow rate: 10  $\mu\text{L}/\text{min}$ ; backpressure: 23 bar; injection volume: 20 nL.

**Table 4**

The results obtained in the analysis of norvaline and tryptophan in dietary supplements.

Sample	D-enantiomer content (%)	L-enantiomer content (%)
Norvaline-sample 1	<LOD	<LOD
Norvaline-sample 2	<LOD	104 ± 4
Tryptophan-sample 1	<LOD	103 ± 4
Tryptophan-sample 2	<LOD	97 ± 3
Tryptophan-sample 3	<LOD	110 ± 4
Tryptophan-sample 4	<LOD	106 ± 2

Experimental conditions as in Fig. 1.

Once the developed method was proven to be adequate for the enantiomeric determination of tryptophan and norvaline, it was applied to the analysis of four dietary supplements containing L-tryptophan and two containing L-norvaline. As can be seen in Fig. 2C, D-norvaline content was below the LOD (9.3 µM) in samples 1 and 2, while the content of L-norvaline in sample 2 was above the LOQ value and the amount quantified by the standard external calibration method was in agreement with the labeled content (Table 4). Regarding sample 1, content of L-norvaline did not match the labeled content, since it was below the LOD. Preconcentrating 4 times sample 1 still led to no detection of L-norvaline. Spiking sample 1 with 125 µM of L-norvaline resulted in the detection of this peak being the calculated concentration equal to the added one. A second batch of sample 1 was also injected (data not shown) and the outcome was the same as with the first batch that L-norvaline could not be detected. Consequently, it could be concluded that L-norvaline was not present in this sample in spite of the fact that the label declared its presence.

As in the case of L-norvaline dietary supplements, the content of D-tryptophan in the four supplements analyzed was below the LOD value (Fig. 3C). Content of L-tryptophan was in agreement with the label in all cases (Table 4).

#### 4. Conclusions

The enantiomeric separation of FMOC-derivatized protein and non-protein amino acids was achieved by nano-LC using an MQD-silica hybrid monolithic column. First, the FMOC was selected as the derivatization reagent which has the simplest sample preparation and satisfactory enantioresolution. Second, the effect of the apparent pH, buffer concentration and content of the ACN in the mobile phase was investigated for a group of FMOC-derivatized amino acids. Third, under the optimized conditions, the MQD-silica hybrid monolithic column provided good enantio-recognition for 19 analytes, enabling baseline enantioseparation for 11 out of 27 assayed FMOC-amino acids. Finally, the method was proven to be adequate in terms of selectivity, linearity, precision, accuracy and LODs and LOQs for the enantiomeric determination of L-norvaline and L-tryptophan in dietary supplements. From the analyzed dietary samples, none of them presented detectable amounts of the D-enantiomers while the content of the L-enantiomers was in agreement with the label content in all cases, except for one L-norvaline sample whose presence was completely missing although the label indicated its presence. This demonstrates the applicability of the developed strategy in the quality control of dietary supplements in a fast and accurate manner. It is also the first report showing the application of the MQD silica-hybrid monolithic column to analysis of real samples.

#### Acknowledgments

M. L. Marina and E. Sánchez-López thank the Ministry of

Economy and Competitiveness (Spain) for research projects CTQ2013-48740-P and CTQ2016-76368-P. They also thank the Comunidad of Madrid (Spain) and European funding from FEDER program for research project S2018/BAA-4393 (AVANSECAL-II-CM). D. Xu and E. Sánchez-López thank the Comunidad of Madrid (Spain) and European funding from FEDER program (S2013/ABI-3028, AVANSECAL-CM) for their contracts.

#### Conflicts of interest

The authors declare that there are no conflicts of interest.

#### Appendix A. Supplementary data

Supplementary data to this article can be found online at <https://doi.org/10.1016/j.jpha.2019.10.001>.

#### References

- [1] L.P. Zhao, J. Qiao, K. Zhang, et al., Construction of chiral ligand exchange capillary electrochromatography for D,L-amino acids enantioseparation and its application in glutaminase kinetics study, *J. Chromatogr. A* 1548 (2018) 104–110. <https://doi.org/10.1016/j.chroma.2018.03.031>.
- [2] C.I. Chang, J.C. Liao, L. Kuo, Arginase modulates nitric oxide production in activated macrophages, *Am. J. Physiol. Cell. Physiol.* 274 (1998) 342–348. <https://doi.org/10.1152/ajpcell.1998.274.1.H342>.
- [3] H.M. El-Bassossy, R. El-Fawal, A. Fahmy, et al., Arginase inhibition alleviates hypertension in the metabolic syndrome, *Br. J. Pharmacol.* 169 (2013) 693–703. <https://doi.org/10.1111/bph.12144>.
- [4] X.F. Ming, A.G. Rajapakse, J.M. Carvas, et al., Inhibition of S6K1 accounts partially for the anti-inflammatory effects of the arginase inhibitor L-norvaline, *Bmc Cardiovasc Disor* 9 (2009) 1–7. <https://doi.org/10.1186/1471-2261-9-12>.
- [5] B. Polis, K.D. Srikanth, E. Elliott, et al., L-norvaline reverses cognitive decline and synaptic loss in a murine model of Alzheimer's disease, *Neurotherapeutics* 15 (2018) 1036–1054. <https://doi.org/10.1007/s13311-018-0669-5>.
- [6] X.F. Tang, Y. Liu, H.Q. Hou, et al., Electrochemical determination of L-Tryptophan, L-Tyrosine and L-Cysteine using electrospun carbon nanofibers modified electrode, *Talanta* 80 (2010) 2182–2186. <https://doi.org/10.1016/j.talanta.2009.11.027>.
- [7] A. Agazzi, F. De Ponti, R. De Giorgio, et al., Review of the implications of dietary tryptophan intake in patients with irritable bowel syndrome and psychiatric disorders, *Dig. Liver Dis.* 35 (2003) 590–595. [https://doi.org/10.1016/S1590-8658\(03\)00277-9](https://doi.org/10.1016/S1590-8658(03)00277-9).
- [8] J.B. Raoof, R. Ojani, H. Karimi-Maleh, Carbon paste electrode incorporating 1-[4-(ferrocenyl ethynyl) phenyl]-1-ethanone for electrocatalytic and voltammetric determination of tryptophan, *Electroanalysis* 20 (2008) 1259–1262. <https://doi.org/10.1002/elan.200704176>.
- [9] J. Yang, D.S. Hage, Characterization of the binding and chiral separation of D- and L-tryptophan on a high-performance immobilized human serum albumin column, *J. Chromatogr. A* 645 (1993) 241–250. [https://doi.org/10.1016/0021-9673\(93\)83383-4](https://doi.org/10.1016/0021-9673(93)83383-4).
- [10] R.R. Langner, C.P. Berg, Metabolism of D-tryptophan in the normal human subject, *J. Biol. Chem.* 214 (1955) 699–707. <http://www.jbc.org/content/214/2/699>.
- [11] W.C. Rose, G.F. Lambert, M.J. Coon, The amino acid requirements of min. 7. General procedures; the tryptophan requirement, *J. Biol. Chem.* 211 (1954) 815–827. <http://www.jbc.org/content/211/2/815.citation>.
- [12] D.W. Richard, M.A. Dawes, C.W. Mathias, et al., L-tryptophan: basic metabolic functions, behavioral research and therapeutic indications, *Int. J. Tryptophan Res.* 2 (2009) 45–60. <https://doi.org/10.4137/IJTR.S2129>.
- [13] Commission Decision 2001/15/EC, *Off. J. Eur. Commun.*, L52, 2001, pp. 19–25.
- [14] X.B. Yao, T.T.Y. Tan, Y. Wang, Thiol-ene click chemistry derived cationic cyclodextrin chiral stationary phase and its enhanced separation performance in liquid chromatography, *J. Chromatogr. A* 1326 (2014) 80–88. <https://doi.org/10.1016/j.chroma.2013.12.054>.
- [15] Y.H. Li, C.S. Baek, B.W. Jo, et al., Direct chiral separation of N-fluorenylmethoxycarbonyl α-amino acids by HPLC for determination of enantiomeric purity, *Bull. Korean Chem. Soc.* 26 (2005) 998–1000. <https://doi.org/10.5012/bkcs.2005.26.6.998>.
- [16] M. Kato, T. Fukushima, N. Shimba, et al., A study of chiral recognition for NBD-derivatives on a Pirkle-type chiral stationary phase, *Biomed. Chromatogr.* 15 (2001) 227–234. <https://doi.org/10.1002/bmc.47>.
- [17] I. Ilisz, R. Berkecz, A. Peter, HPLC separation of amino acid enantiomers and small peptides on macrocyclic antibiotic-based chiral stationary phases: a review, *J. Sep. Sci.* 29 (2006) 1305–1321. <https://doi.org/10.1002/jssc.200600046>.
- [18] M. Lämmerhofer, E. Tobler, E. Zarbl, et al., Macroporous monolithic chiral

- stationary phases for capillary electrochromatography: new chiral monomer derived from cinchona alkaloid with enhanced enantioselectivity, *Electrophoresis* 24 (2003) 2986–2999, <https://doi.org/10.1002/elps.200305527>.
- [19] L.N. Tran, J.H. Park, Enantiomer separation of acidic chiral compounds on a quinine-silica/zirconia hybrid monolith by capillary electrochromatography, *J. Chromatogr. A* 1396 (2015) 140–147, <https://doi.org/10.1016/j.chroma.2015.03.085>.
- [20] M. Lämmerhofer, F. Svec, J.M.J. Frechet, Chiral monolithic columns for enantioselective capillary electrochromatography prepared by copolymerization of a monomer with quinidine functionality. 2. Effect of chromatographic conditions on the chiral separations, *Anal. Chem.* 72 (2000) 4623–4628, <https://doi.org/10.1021/ac000323d>.
- [21] Q.X. Zhang, V. Gil, E. Sánchez-López, et al., Evaluation of the potential of a quinidine-based monolithic column on the enantiomeric separation of herbicides by nano-liquid chromatography, *Microchem. J.* 123 (2015) 15–21, <https://doi.org/10.1016/j.microc.2015.05.011>.
- [22] H.H. Wu, Q.Q. Wang, M. Ruan, et al., Enantioseparation of N-derivatized amino acids by micro-liquid chromatography/laser induced fluorescence detection using quinidine-based monolithic columns, *J. Pharm. Biomed. Anal.* 121 (2016) 244–252, <https://doi.org/10.1016/j.jpba.2015.12.011>.
- [23] H. Han, Q.Q. Wang, H.H. Wu, et al., Establishment and application of an automated chiral two-dimensional high performance liquid chromatography method for bio-analysis of D-acidic amino acids, *Chin. J. Anal. Chem.* 42 (2014) 891–895, [https://doi.org/10.1016/S1872-2040\(14\)60746-5](https://doi.org/10.1016/S1872-2040(14)60746-5).
- [24] K. Hamase, A. Morikawa, S. Etoh, et al., Analysis of small amounts of D-amino acids and the study of their physiological functions in mammals, *Anal. Sci.* 25 (2009) 961–968, <https://doi.org/10.2116/analsci.25.961>.
- [25] Q.Q. Wang, J. Feng, H. Han, et al., Enantioseparation of N-derivatized amino acids by micro-liquid chromatography using carbamoylated quinidine functionalized monolithic stationary phase, *J. Chromatogr. A* 1363 (2014) 207–215, <https://doi.org/10.1016/j.chroma.2014.06.039>.
- [26] E. Dominguez-Vega, A.L. Crego, K. Lomsadze, et al., Enantiomeric separation of FMOC-amino acids by nano-LC and CEC using a new chiral stationary phase, cellulose tris(3-chloro-4-methylphenylcarbamate), *Electrophoresis* 32 (2011) 2700–2707, <https://doi.org/10.1002/elps.201000701>.
- [27] L. Chen, Q. Chen, Z.Z. Zhang, et al., A novel colorimetric determination of free amino acids content in tea infusions with 2,4-dinitrofluorobenzene, *J. Food Compos. Anal.* 22 (2009) 137–141, <https://doi.org/10.1016/j.jfca.2008.08.007>.
- [28] F.J. Márquez, A.R. Quesada, F. Sánchez-Jiménez, et al., Determination of 27 dansyl amino acid derivatives in biological fluids by reversed-phase high-performance liquid chromatography, *J. Chromatogr. B* 380 (1986) 275–283, [https://doi.org/10.1016/S0378-4347\(00\)83656-7](https://doi.org/10.1016/S0378-4347(00)83656-7).
- [29] Q.Q. Wang, P.J. Zhu, M. Ruan, et al., Chiral separation of acidic compounds using an O-9-(tert-butylcarbamoyl)quinidine functionalized monolith in micro-liquid chromatography, *J. Chromatogr. A* 1444 (2016) 64–73, <https://doi.org/10.1016/j.chroma.2016.03.047>.
- [30] Q.Q. Wang, E. Sánchez-López, H. Han, et al., Separation of N-derivatized di- and tri-peptide stereoisomers by micro-liquid chromatography using a quinidine-based monolithic column—Analysis of L-carnosine in dietary supplements, *J. Chromatogr. A* 1428 (2016) 176–184, <https://doi.org/10.1016/j.chroma.2015.09.016>.
- [31] J.L. Guo, Y. Xiao, Y.J. Lin, et al., Effect of the crosslinker type on the enantio-separation performance of  $\beta$ -cyclodextrin functionalized monoliths prepared by the one-pot approach, *J. Chromatogr. A* 1467 (2016) 288–296, <https://doi.org/10.1016/j.chroma.2016.05.078>.
- [32] Q.Q. Duan, C.S. Liu, Z.H. Liu, et al., Preparation and evaluation of a novel monolithic column containing double octadecyl chains for reverse-phase micro high performance liquid chromatography, *J. Chromatogr. A* 1345 (2014) 174–181, <https://doi.org/10.1016/j.chroma.2014.04.036>.
- [33] M. Lämmerhofer, F. Svec, J.M.J. Frechet, et al., Monolithic stationary phases for enantioselective capillary electrochromatography, *J. Microcolumn Sep.* 12 (2000) 597–602, [https://doi.org/10.1002/1520-667X\(2000\)12:12<597:AID-MCS1005>3.0.CO;2-6](https://doi.org/10.1002/1520-667X(2000)12:12<597:AID-MCS1005>3.0.CO;2-6).
- [34] H. Lin, J.J. Ou, Z.B. Zhang, et al., Facile preparation of zwitterionic organic-silica hybrid monolithic capillary column with an improved “one-pot” approach for hydrophilic-interaction liquid chromatography (HILIC), *Anal. Chem.* 84 (2012) 2721–2728, <https://doi.org/10.1021/ac3001429>.
- [35] J.J. Ou, H. Lin, Z.B. Zhang, et al., Recent advances in preparation and application of hybrid organic-silica monolithic capillary columns, *Electrophoresis* 34 (2013) 126–140, <https://doi.org/10.1002/elps.201200344>.
- [36] H.Y. Zhang, J.J. Ou, Z.S. Liu, et al., Preparation of hybrid monolithic columns via “one-pot” photoinitiated thiol-acrylate polymerization for retention-independent performance in capillary liquid chromatography, *Anal. Chem.* 87 (2015) 8789–8797, <https://doi.org/10.1021/acs.analchem.5b01707>.
- [37] M. Kato, H. Saruwatari, K. Sakai-Kato, et al., Silica sol-gel/organic hybrid material for protein encapsulated column of capillary electrochromatography, *J. Chromatogr. A* 1044 (2004) 267–270, <https://doi.org/10.1016/j.chroma.2004.04.056>.
- [38] D.S. Xu, E. Sánchez-López, Q.Q. Wang, et al., Preparation of an O-[2-(methacryloyloxy)-ethylcarbamoyl]-10,11-dihydroquinidine-silica hybrid monolithic column for the enantioseparation of amino acids by nano-liquid chromatography, *J. Chromatogr. A* 1593 (2019) 63–72, <https://doi.org/10.1016/j.chroma.2019.01.065>.



## Original Article

## Thermodynamics of clay–drug complex dispersions: Isothermal titration calorimetry and high-performance liquid chromatography

Ana-Maria Totea <sup>a</sup>, Juan Sabin <sup>b</sup>, Irina Dorin <sup>c</sup>, Karl Hemming <sup>d</sup>, Peter R. Laity <sup>e</sup>, Barbara R. Conway <sup>a</sup>, Laura Waters <sup>a</sup>, Kofi Asare-Addo <sup>a,\*</sup><sup>a</sup> School of Applied Sciences, Department of Pharmacy, University of Huddersfield, Queensgate, Huddersfield, HD1 3DH, UK<sup>b</sup> AFFINmeter, Edificio Emprendia, Campus Vida, Santiago de Compostela, Spain<sup>c</sup> Malvern Panalytical Ltd., Malvern, UK<sup>d</sup> School of Applied Sciences, Department of Chemistry, University of Huddersfield, Queensgate, Huddersfield, HD1 3DH, UK<sup>e</sup> Department of Materials Science and Engineering, University of Sheffield, Sir Robert Hadfield Building, Mappin Street, Sheffield, S1 3JD, UK

## ARTICLE INFO

## Article history:

Received 23 May 2019

Received in revised form

3 December 2019

Accepted 4 December 2019

Available online 5 December 2019

## Keywords:

Clay–drug complex dispersions

Magnesium aluminium silicate

Diltiazem hydrochloride

Isothermal titration calorimetry

High performance liquid chromatography

## ABSTRACT

An understanding of the thermodynamics of the complexation process utilized in sustaining drug release in clay matrices is of great importance. Several characterisation techniques as well as isothermal calorimetry were utilized in investigating the adsorption process of a model cationic drug (diltiazem hydrochloride, DIL) onto a pharmaceutical clay system (magnesium aluminium silicate, MAS). X-ray powder diffraction (XRPD), attenuated total reflectance Fourier transform infrared spectroscopy (ATR-FTIR) and optical microscopy confirmed the successful formation of the DIL-MAS complexes. Drug quantification from the complexes demonstrated variable behaviour in the differing media used with DIL degrading to desacetyl diltiazem hydrochloride (DC-DIL) in the 2 M HCl media. Here also, the authors report for the first time two binding processes that occurred for DIL and MAS. A competitor binding model was thus proposed and the thermodynamics obtained suggested their binding processes to be enthalpy driven and entropically unfavourable. This information is of great importance for a formulator as care and consideration should be given with appropriate media selection as well as the nature of binding in complexes.

© 2019 Xi'an Jiaotong University. Production and hosting by Elsevier B.V. This is an open access article under the CC BY-NC-ND license (<http://creativecommons.org/licenses/by-nc-nd/4.0/>).

## 1. Introduction

Minerals have a variety of applications in the pharmaceutical industry and in medicine which date back since prehistory [1]. Minerals have desirable physicochemical properties such as chemical inertness, high adsorption capacity and specific area, swelling, water solubility and dispersivity, plasticity, acid-absorbing capacity, as well as colour, opacity and low or no toxicity in patients, which makes them suitable for medical and pharmaceutical applications [1,2]. In the formulation of pharmaceutical dosage forms, minerals are used as excipients as carriers of active ingredients to achieve modified release, or as binders, fillers, disintegrants, lubricants, thickening agents, anticaking agents, flavouring correctors and emulsifying agents [2].

Magnesium aluminium silicate (MAS or VEEGUM®) is a mixture of natural smectite montmorillonite and saponite clays (Fig. 1). MAS has a layered silicate structure, formed of one alumina or magnesia octahedral sheet, sandwiched between two tetrahedral silicate sheets [3,4]. The high surface area and good affinity with cationic drugs, as well as its non-toxic properties make MAS a suitable material for use in drug formulation. MAS has previously been shown to be able to adsorb cationic drugs such as propranolol hydrochloride and form complexes that are able to retard drug release [5–7]. Controlling drug release is of high interest as it has been demonstrated to show many benefits compared with conventional drug release. By maintaining a constant drug–plasma concentration for extended periods of time, it is possible to achieve optimal efficacy in chronic conditions where medication must be administered at constant levels, and reduce the side effects [8]. The use of a model drug such as diltiazem hydrochloride (DIL), in combination with magnesium aluminium silicate to achieve controlled drug release, adds value to the importance of using clay minerals as drug carriers [5,6,9].

Peer review under responsibility of Xi'an Jiaotong University.

\* Corresponding author.

E-mail address: [k.asare-addo@hud.ac.uk](mailto:k.asare-addo@hud.ac.uk) (K. Asare-Addo).

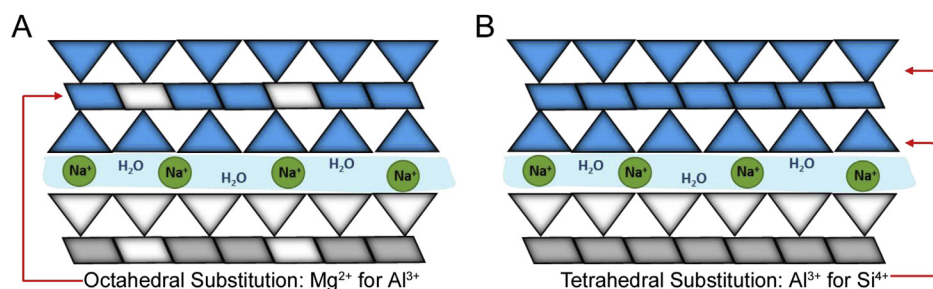


**Fig. 1.** Montmorillonite (A) and saponite (B) clay structure showing the magnesia or alumina octahedral sheet trapped between two tetrahedral silicate sheets: adapted from [4].

DIL is a non-dihydropyridine calcium channel blocker. It inhibits the calcium channels in the blood vessels, which leads to vasodilatation and, hence, to a lower blood pressure. Furthermore, DIL inhibits calcium channels in the heart, leading to a reduced cardiac contractility and a slower atrioventricular conduction velocity [10,11]. Therefore, DIL represents an efficient treatment for patients suffering from stable chronic angina, due to its ability to reduce myocardial oxygen demand, as it lowers blood pressure, heart rate and cardiac contractility. The drug can also be efficiently used in treating arterial fibrillation due to its ability to control heart rate through its capability to reduce atrioventricular node conduction. DIL's critical drawbacks include an elimination half-life of  $3.2 \pm 1.3$  h following oral administration, and a bioavailability of  $(42 \pm 18)\%$  following first pass metabolism [12]. Therefore, in order to acquire its therapeutic effects and to maintain adequate drug plasma levels, it needs to be administered frequently (3–4 times/day) [13,14]. This model drug therefore represents a suitable target for an extended release formulation. Using clay, instead of the traditionally adopted polymers to control drug release, brings multiple benefits such as overall reduced costs and antibacterial effects, as well as improved kinetics of drug release. This study therefore aims to understand and fully characterise the complexes that are formed between the MAS and DIL that provide the controlled release effect as well as using complex software in understanding the thermodynamics associated with this process.

## 2. Experimental

### 2.1. Materials

VEEGUM F EP® (MAS) was a kind gift from R. T. Vanderbilt Company, Norwalk, CT (USA). DIL (MW = 450.98, pKa =  $7.8 \pm 0.4$ ) was purchased from TCI (Tokyo Chemical Industry), Tokyo. Acetonitrile (HPLC grade) and sodium phosphate, dibasic hydrate, 99+% (HPLC grade), 2 M sodium hydroxide and 2 M hydrochloric acid were purchased from Fisher Scientific, UK.

### 2.2. Methods

#### 2.2.1. Microscopy studies and formulation of MAS-DIL complex particles

Digital microscopy was used to observe the formation of flocs upon the addition of dilute DIL solution to dilute MAS dispersion (ratio 0.5:1, w/v). The drug to clay ratio used in this study was chosen based on the assay studies presented in Section 3.1. This showed the amount of DIL adsorbed onto the clay was maximum 0.26 g DIL/1 g of MAS. Studies were performed using a VHX2000 Digital Microscope from KEYENCE using a blue daylight filter to enhance the contrast between the flocculated particles and the dispersion media. Pictures were recorded at different mixing time

points (2 min, 30 min, 60 min, 120 min, 180 min and 24 h) and were compared. Images of the MAS dispersion prior to DIL addition were also acquired.

For the formulation process, MAS-DIL complex particles were prepared by loading the MAS with DIL twice in order to ensure a high drug adsorption. For the first drug loading, separate DIL solution (2%, w/v) and MAS dispersion (2%, w/v) were prepared under continuous stirring for 24 h at 500 rpm (25 °C). The pH of the prepared MAS dispersion and DIL solution was adjusted to pH 5 using 2 M hydrochloric acid and 2 M sodium hydroxide. After 24 h, the MAS dispersion and DIL solution were combined (1:1, w/w) and the mixture was incubated at 37 °C with shaking for 24 h. Flocculates were observed in the mixture. The MAS-DIL complex dispersions obtained were then filtered using a Buchner filtration apparatus with vacuum. For the second drug loading, previously filtered single drug loaded MAS-DIL complex particles were redispersed into a fresh DIL solution (2%, w/v) and incubated at 37 °C with shaking for 24 h. The MAS-DIL flocculated complexes formed were filtered and dried in the oven at 50 °C for 48 h. The dried double drug loaded MAS-DIL complex particles were ground (10 min) using a Retsch® PM 100 ball mill set at 350 rpm to particle sized at 123–65 μm. The use of the ball mill led to a faster breakdown of the hard particulates to the desired particle size.

#### 2.2.2. Characterisation of MAS-DIL complex dispersions and particles

**2.2.2.1. Attenuated total reflectance Fourier transform infrared spectroscopy (ATR-FTIR).** ATR-FTIR was used to study the interaction between MAS and DIL at the molecular level. MAS, DIL and MAS-DIL complex particles were analysed from 4000 to 400 cm<sup>-1</sup> on a Smart Orbit ATR-FTIR machine, using diamond as the ATR crystal.

**2.2.2.2. Powder X-ray diffractometry (PXRD).** Experiments were performed on a D2 PHASER XRD from BRUKER and sample preparation involved the placement of sample powder onto a transmitter holder and conducted using a similar methodology as reported [15]. Analysis was performed at an angular range 2.5–70° (2θ) and a step angle of 0.02° (2θ) s<sup>-1</sup>. The X-ray source was generated as a Cu radiation at 30 kV and 10 mA. Experiments were performed in triplicate for reproducibility.

#### 2.2.3. High performance liquid chromatography (HPLC)

An HPLC method was developed and validated for the determination and quantification of both DIL and its main degradant, desacetyldiltiazem (DC-DIL) which was observed in samples. Linearity range, precision, limit of quantitation (LOQ) and limit of detection (LOD) were separately determined for both compounds (DIL and DC-DIL) to validate the method used. The peak area of the standards along with the corresponding drug concentration was used to generate a calibration graph to evaluate linearity (slope,

intercept and coefficient of determination  $R^2$ ) and determine LOD and LOQ. All experiments were conducted in triplicate. An assay of freshly prepared standard DIL and DC-DIL solutions at four different concentrations (1.00, 10.00, 50.00 and 100.00  $\mu\text{g}/\text{mL}$  and 0.83, 8.25, 41.26, 82.52  $\mu\text{g}/\text{mL}$  respectively) repeatedly run on the same day or on three different days was used to evaluate the intra- and inter-day precision in terms of standard deviation RSD %.

DIL stock solution and standard solutions in the range 100 to 0.1  $\mu\text{g}/\text{mL}$  were prepared in purified water. DC-DIL was formed from DIL via hydrolysis (Fig. 2). DIL stock solution was prepared in dilute acid (2 M HCl) and standard solutions in the range 75 to 0.1  $\mu\text{g}/\text{mL}$  were prepared from the stock solution using purified water. Samples were left for 72 h at room temperature until complete hydrolysis occurred (confirmed by HPLC). The concentration of DC-DIL present in the standards was determined from the equilibrated hydrolysis reaction assuming that 100% of the drug hydrolysed was observed, as no traces of the parent drug were observed in solution.

The calibration graphs generated for DIL and DC-DIL were found to be linear over the concentration range studied (1.00, 10.00, 50.00 and 100.00  $\mu\text{g}/\text{mL}$  and 0.83, 8.25, 41.26 and 82.52  $\mu\text{g}/\text{mL}$ , respectively) ( $R^2 \geq 0.9999$  and  $R^2 \geq 0.9998$ , respectively). Linearity was defined by an equation that was further used in the recovery studies. The method was shown to be precise for the detection of both DIL and DC-DIL, the intermediate and intra-assay precision at four different concentrations on three different days being lower than 2% RSD (Table 1) which complies with the acceptable criteria for quality control of pharmaceutical preparations [16,17]. LOQ (the lowest drug concentration that can be recovered within acceptable limits of precision and accuracy) was found to be 1.72  $\mu\text{g}/\text{mL}$  for DIL and 1.65  $\mu\text{g}/\text{mL}$  for DC-DIL, indicating the high sensitivity of the proposed method at low concentrations of DIL and DC-DIL. LOD (the lowest detectable amount of drug distinguishable from the blank) was 0.57  $\mu\text{g}/\text{mL}$  for DIL and 0.55  $\mu\text{g}/\text{mL}$  for DC-DIL, confirming the sensitivity of the method proposed.

#### 2.2.4. Isothermal titration calorimetry (ITC)

ITC was used to investigate the binding between MAS and DIL. Single injections experiment (SIM) and multiple injection experiments (MIM) were performed. The fast titration and versatile SIM experiments were used to initially confirm binding and determine the nature of the interaction, while MIM experiments were used further to characterise the reaction in detail and determine the thermodynamic parameters. Studies were carried out on a Microcal VP ITC micro-calorimeter. The instrument was used in high-gain mode, applying a reference power of 20  $\mu\text{cal s}^{-1}$  whilst stirring the sample cell contents at 307 rpm. The MAS dispersion was added into the sample cell and DIL solution into the syringe for all the experiments.

SIM experiments were performed at three different pH values, i.e., 5, 7 and 9 (25 °C). DIL solution was added in one injection into

the sample cell. The SIM experiments were fast titration experiments and the real time binding isotherm observed was analysed using Origin 7.0 (MicroCal, Inc) by comparing the reaction rate at the pH values studied [18].

0.010% (w/v) MAS dispersion was prepared under continuous stirring for 24 h, at 25 °C and 200 rpm and was used to fill the sample cell. A 1 mM DIL solution was also prepared separately under stirring for 30 min at 25 °C and 200 rpm prior to the experiments and was independently used to fill the syringe. The drug solution was added as 1 injection of 250  $\mu\text{L}$  into the sample cell containing MAS. The pH of the prepared solutions and dispersions were adjusted using 2 M hydrochloric acid and 2 M sodium hydroxide to 5, 7 and 9. All experiments were conducted in triplicate.

MIM ITC studies were carried out at 25 °C and pH 5, at two different DIL and MAS concentrations. The binding isotherm was studied in 120–140 injections of 2  $\mu\text{L}$  each into the sample cell every 260 s. MAS dispersion (0.036% and 0.010%, w/v) and DIL solution (3.2 mM and 0.45 mM) were prepared. A competitor binding model (Fig. 3) was fitted to the data to get thermodynamic parameters which best reproduce the experimental data using AFFINImeter (AFFINImeter, Spain). The total molar concentration of MAS was estimated and the relative molar fractions of each kind of clay ( $r_b$ ,  $r_m$ ) were considered unknown and set as fitted parameter in the analysis.

$$r_b \cdot [B] + r_m \cdot [M] = [\text{MAS}]$$

### 3. Results and discussion

#### 3.1. Observation of floc formation and drug content analysis from MAS-DIL double drug loaded complex particles

The initial analysis of the MAS dispersion using digital microscopy (Fig. 4) allowed the observation of small clay particles dispersed in water forming a colloidal structure, described in literature as the 'house of cards' [4] through the attraction between the negatively charged faces and the partially positive edges of the clay platelets (Fig. 4 A). Following the addition of DIL, the initially monodispersed particles started aggregating as flocs (forming after only 2 min) (Fig. 4 D). With time, flocs were observed to increase in size, became more porous and spread out as the particles clustered together (Figs. 4E–G). After 24 h, a decrease in the size of the flocculated clustered particles was observed as loosely bound aggregates separated away and reattached to other aggregates in a more stable form (Figs. 4H–J) [19]. This process allows the intercalation process to occur after which drug entrapment can be determined.

Determination of drug content in the MAS-DIL double drug loaded complex particles prepared as described in Section 2.2.1 showed discrepancies between the different media used for the dispersion of the complex particles (Table 2). The difference can be related to the behaviour of DIL and MAS in the dissolution media, as well as to the mechanism of adsorption of DIL onto MAS. Results showed that only DC-DIL was recovered by dispersing the MAS-DIL particles in 2 M HCl (Table 2). The degradant was identified following a shift in the retention time on the chromatograms from approx. 7 min (DIL standard solution), to approx. 3.8 min (recovered DIL) (Fig. 5). This behaviour was attributed to the hydrolysis of DIL under acidic conditions and the peak was identified as being DC-DIL, the main degradant of DIL [16,20,21]. A reduction in the exposure time of the MAS-DIL complex to the acid solution from 24 h to 30 min allowed the observation of the two peaks belonging to DIL and DC-DIL on the same chromatogram (Fig. 5B).

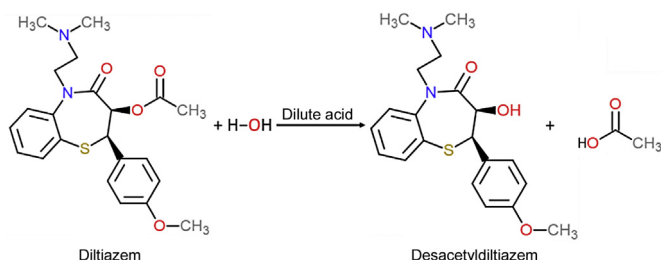
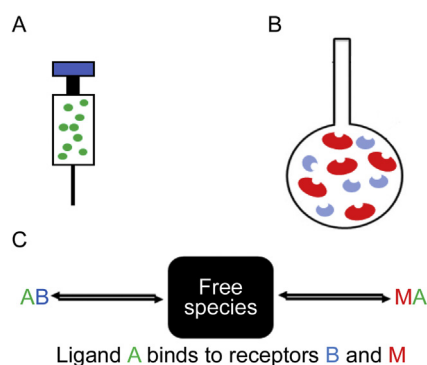


Fig. 2. DIL undergoing dilute acid hydrolysis and product desacetyldiltiazem.

**Table 1**  
HPLC method validation for DIL and DC-DIL showing intermediate and intra assay precision at four different concentrations.

Compound	Concentration ( $\mu\text{g/mL}$ )	Intermediate precision (RSD, %)	Intra-assay precision (RSD, %)
DIL	1.00	5.32	1.67
	10.00	0.85	0.48
	50.00	0.65	0.17
	100.00	0.55	0.16
DC-DIL	0.83	1.26	0.63
	8.25	0.52	0.91
	41.26	0.25	0.39
	82.52	0.38	0.63



**Fig. 3.** Competitive ligand binding where A is the ligand in the syringe (DIL) (A), and M and B are the macromolecule and competitive ligand respectively (montmorillonite and saponite making up the MAS), both present in the sample cell (B) and (C) proposes the how ligand A binds to receptors B and M.

Further studies evaluating DIL content in MAS-DIL double drug loaded complex particles by dispersing the particles in ultra-pure water (pH 5) and phosphate buffer (pH 6.8) showed a considerable reduction of DIL degradation. The results showed less than 10% of DIL recovered from the complexes hydrolysed over 24 h in water and phosphate buffer, hence confirming the effect of 2 M HCl on DIL leading to degradant DC-DIL.

**Table 2**  
DIL and DC-DIL content in double drug loaded MAS-DIL complex particles.

Media	Recovered DIL (% w/w)	Recovered DC-DIL (% w/w)
2 M HCl	n/a <sup>§</sup>	25.78 $\pm$ 0.32*
Ultra-pure water	16.48 $\pm$ 0.42*	1.31 $\pm$ 0.03*
pH 6.8 phosphate buffer	17.61 $\pm$ 0.22*	1.55 $\pm$ 0.02*

Note: <sup>§</sup>DIL completely degraded, hence only degradant DC-DIL recovered. \*values are reported as mg of drug per g MAS.

### 3.2. Solid state characterisation

#### 3.2.1. ATR-FTIR

ATR-FTIR was used to study the adsorption of DIL onto MAS based on the vibration of chemical bonds formed (Fig. 6). Characteristic peaks were observed on the spectrum of MAS such as the hydroxyl group belonging to Si–OH at 3625  $\text{cm}^{-1}$  and the Si–O–Si stretching at 980  $\text{cm}^{-1}$ , as well as peaks related to water residues (O–H stretching 3415  $\text{cm}^{-1}$ ) and water of crystallisation (O–H group bending at 1640  $\text{cm}^{-1}$ ) [6,7].

The spectrum of MAS-DIL double drug loaded complexes was very different from that of DIL alone, but similar to that of MAS. The presence of the Si–O–Si stretching belonging to the clay was still observed as a broad peak at 980  $\text{cm}^{-1}$ . A peak attributed to the hydroxyl stretching of the Si–OH group was observed at 3631  $\text{cm}^{-1}$ . The C=O carbonyl groups belonging to DIL at 1680  $\text{cm}^{-1}$  and 1740  $\text{cm}^{-1}$  and C=C aromatic ring stretching belonging to DIL at

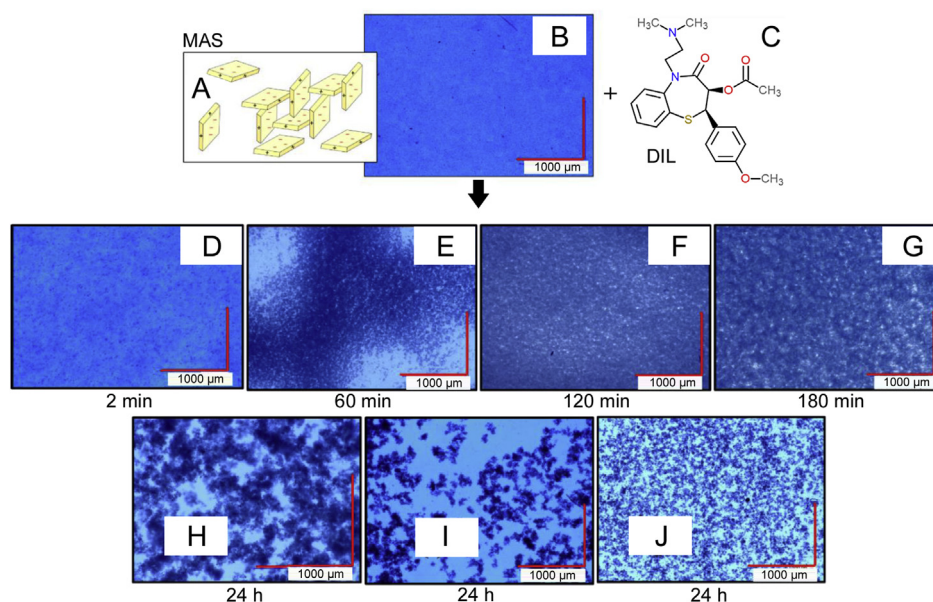


**Fig. 4.** Scheme of the 'house of cards' formed upon MAS dispersion in water: adapted from Ref. [4] (A); Digital microscopy images of MAS (B); Chemical representation of DIL structure (C); and complexes formed between MAS and DIL at different time points of aggregation (D–J).

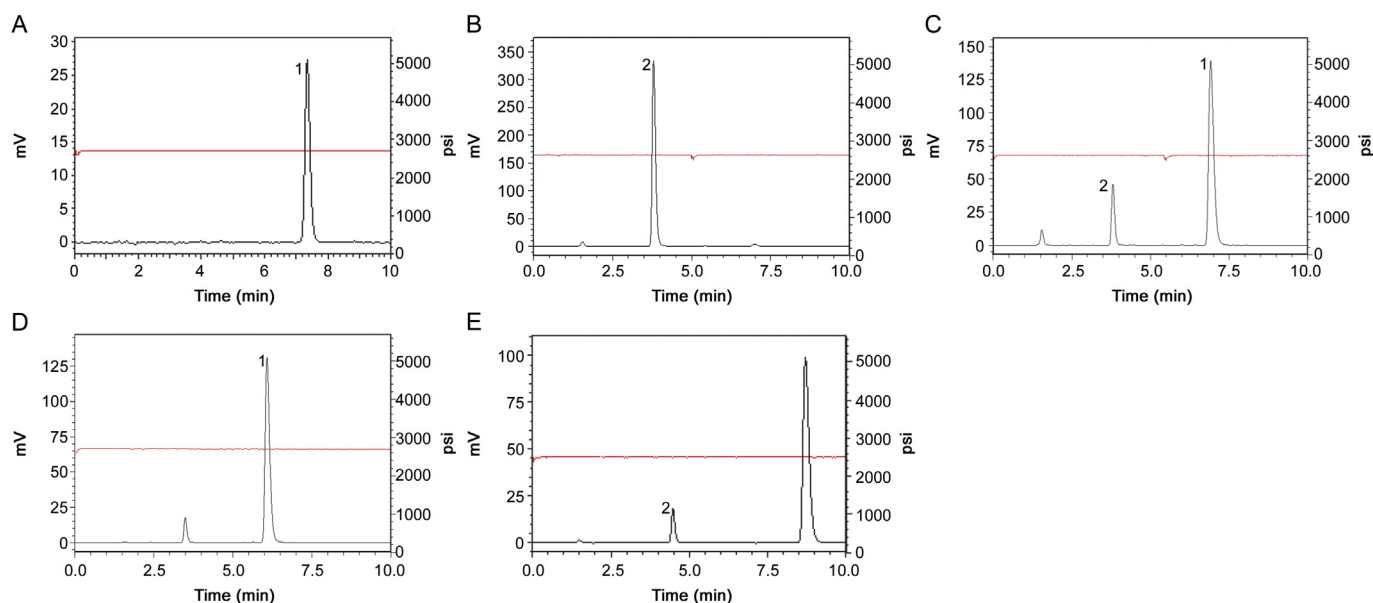


**Fig. 5.** Typical HPLC chromatograms of DIL standard solution at 25 °C (A) and DIL recovered from MAS-DIL complex using 2 M HCl (24 h exposure) (B), 2 M HCl (30 min exposure) (C), ultra – pure water (D) and pH 6.8 phosphate buffer (E) showing the presence of DIL (1) and degradant desacetyl diltiazem (2).

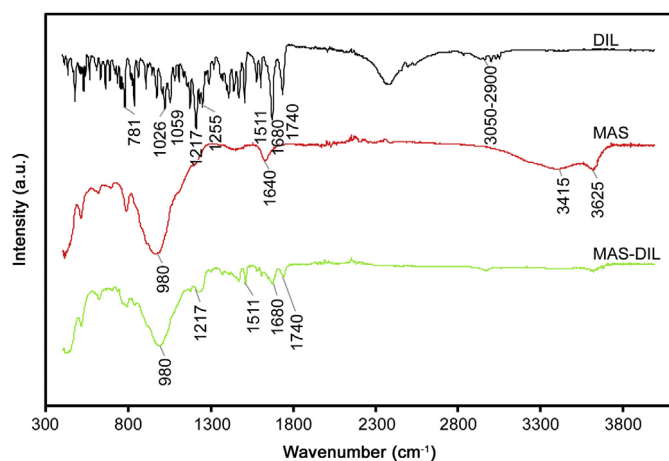


**Fig. 6.** ATR-FTIR for DIL, MAS and MAS-DIL double drug loaded complex.

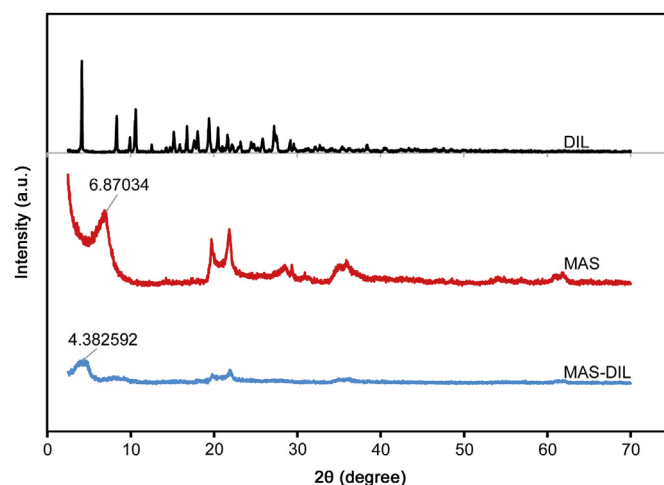


**Fig. 7.** PXRD patterns of MAS, DIL and MAS-DIL double drug loaded complexes.

1511 cm<sup>-1</sup> were still observed but all became smaller. The peak belonging to the amine group on the DIL structure observed at 1217 cm<sup>-1</sup> was still present but became broader. The peaks attributed to R–O–R stretching at 1026 cm<sup>-1</sup> and C–O ester stretching at 1059 cm<sup>-1</sup> on DIL structure were not observed on the spectrum of MAS – DIL complex particles. The change and disappearance of some of the peaks characteristic to both DIL and MAS demonstrated the potential interaction between them by the formation of hydrogen bonds between the silanol groups of MAS with the amine and hydroxyl groups of DIL [6,7].

### 3.2.2. PXRD

The diffractogram acquired for MAS (Fig. 7) displays a distinctive reflection at 6.87034° (2θ) representing the thickness of the basal spacing between the platelets, calculated using Bragg's Law as being 1.28 nm, a value similar to those suggested in the literature [6,9]. The prepared MAS-DIL complex particles were shown to be in amorphous form and did not follow the PXRD pattern of DIL or MAS alone. The amorphous characteristic of the MAS-DIL sample

suggests the molecular dispersivity of the drug in the prepared complexes. Furthermore, the reflection at 6.87034° (2θ) on the MAS diffractogram representing the basal spacing was shifted to 4.382592° (2θ) on the MAS-DIL diffractogram and showed a reduced intensity. The peak shift means an increase in basal spacing of MAS from 1.28 nm up to ≈2.016 nm upon intercalation of DIL into the clay platelets, hence confirming the complexation [6,22].

### 3.3. ITC

#### 3.3.1. Binding between MAS and DIL: single injection experiments

SIM experiments confirmed that binding occurred between MAS and DIL. The binding isotherm between MAS and DIL was shown to be highly exothermic at the pH values studied (Fig. 8). The power signal returned to baseline faster at pH 9 compared with pH 5 and 7, indicating therefore a more rapid interaction. Considering the ionisation of DIL, a more favourable interaction at pH 9 implies that DIL is more readily adsorbed onto MAS via hydrogen bonding

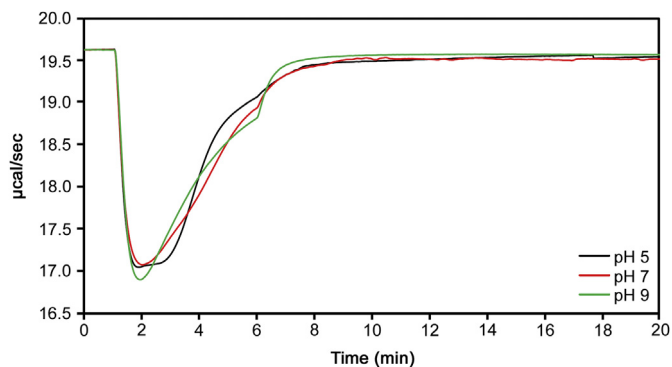


**Fig. 8.** Titration of DIL solution (pH 5) into MAS dispersion (pH 5) (black), pH 7 (red) and pH 9 (green) at 25 °C.

and water bridging, the drug being mainly present in solution in its unionised form at this pH. This may be explained by the increased length of the alkyl ammonium chain and large molecular weight of DIL, which were shown to result in a greater contribution to adsorption onto the clay via van der Waals forces in previous studies [23,24].

### 3.3.2. Binding between MAS and DIL: multiple injection experiments

The binding between MAS and DIL was further explored using MIM stepwise experiments at pH 5 and 25 °C. The working pH was chosen based on drug ionisation, DIL being mostly ionised in solution at pH 5 ( $pK_a$  7.8) and hence, expected to interact with the negatively charged faces of MAS platelets [4,25]. Experiments confirmed the binding and showed the presence of more than one binding event at both higher and lower concentrations (Figs. 9 A and B). The experiment at low concentration (Fig. 9 B) allowed the

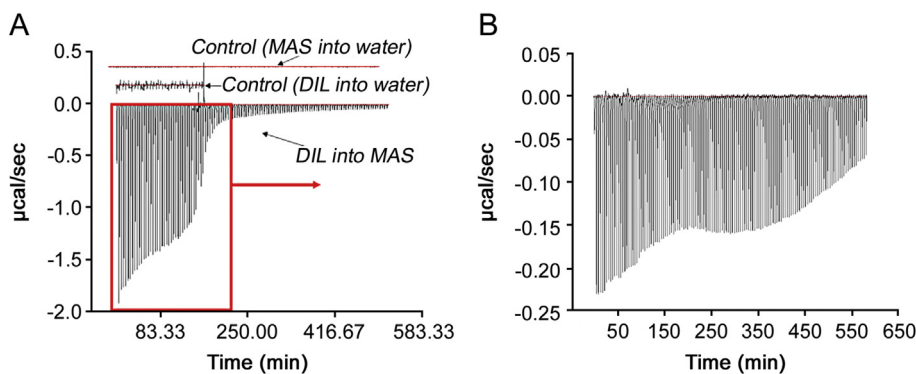


**Fig. 9.** ITC raw data showing: titration of 3.2 mM DIL into 0.036% MAS and blank titrations (water into MAS 0.036% (w/v) and DIL 3.2 mM into water) (A); titration of 0.45 mM DIL into 0.010% (w/v) MAS (B). All experiments were undertaken at pH 5 and 25 °C.

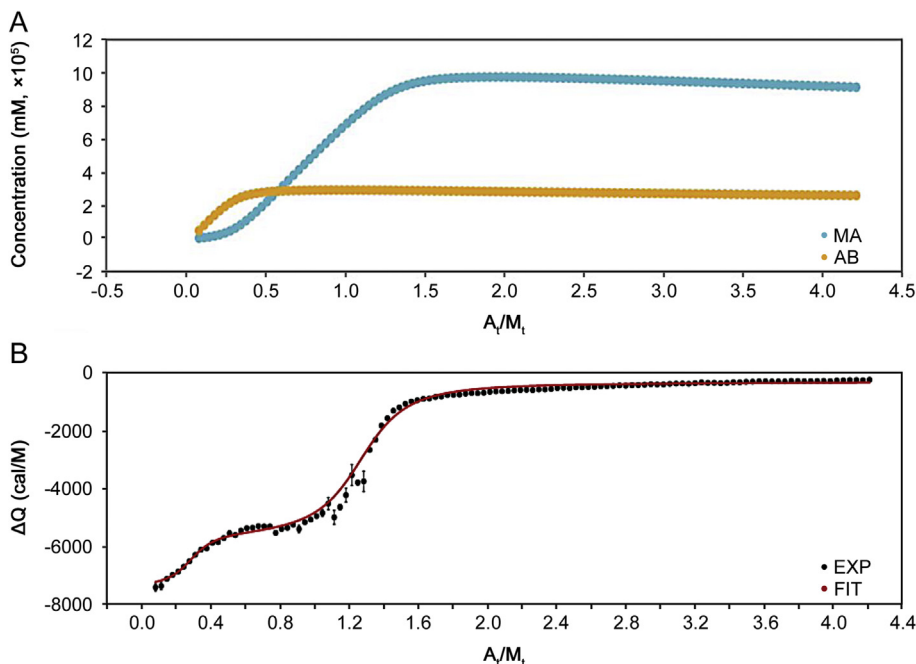


**Fig. 10.** Species distribution plot showing the binding between ligand A (DIL) and macromolecules M and B (MAS mixture of montmorillonite and saponite) reaching saturation point (A); Thermodynamic profile through a competitive curve fitting model for adsorption of DIL solution (3.2 mM) pH 5 onto MAS dispersion (0.036%, w/v) pH 5 at 25 °C (B).

**Table 3**  
Multiple injection mode calorimetric binding studies studying the adsorption of DIL (3.2 mM) onto MAS (0.036%, w/v) at 25 °C (pH 5). Data analysed through a competitive curve fitting model to calculate affinity ( $K_a$ ) and changes in enthalpy ( $\Delta H$ ) and entropy ( $-\Delta S$ ).

Reaction	r	$K_a$ ( $M^{-1}$ )	$\Delta H$ (cal/mol)	$-\Delta S$ (cal/mol)
$M + A \leftrightarrow MA$	0.76	$4.80 E+5 \pm 7.59 E+3$	$-6.71 E+3 \pm 1.29 E+1$	$-9.28E+2$
$A + B \leftrightarrow AB$	0.24	$2.54 E+7 \pm 1.10 E+6$	$-8.94 E+3 \pm 2.18 E+1$	$-1.02E+3$

highly detailed observation of the binding events, confirming that there were no other additional processes taking place. Control binding experiments showed no interaction between MAS dispersion and water, and between DIL solution and water at pH 5 and 25 °C. The presence of multiple binding events following MAS-DIL binding was not observed in the ITC SIM experiments, hence emphasising the importance of MIM stepwise experiments in describing chemical interactions in detail.

A competitor binding model (Fig. 10) was fitted to the data to determine the thermodynamic parameters of the reaction. For this analysis it was assumed that the two different types of clay within MAS (montmorillonite and saponite) placed into the sample cell may potentially interact differently upon the addition of DIL. This assumption was made based on the isomorphic substitution of a limited amount of octahedral  $Al^{3+}$  with  $Mg^{2+}$  in montmorillonite and the substitution of a limited amount of tetrahedral  $Si^{4+}$  by  $Al^{3+}$  in saponite, naturally balanced by exchangeable  $Na^+$  ions that can be easily displaced and replaced, giving the clay the ability to act like a reservoir. Initially the concentrations of both clays were considered equal to total MAS, that is,  $[B] = [M] = [MAS]$  and AFFINImeter was used to fit the data with the competitive model using  $rb$  and  $rm$  (the correction of the nominal concentration of the compounds in the cell) as fitted parameters with the following constraint  $rb + rm = 1$ . The fitting of  $rb$  and  $rm$  allows the calculation of the real concentration of both kinds of clay. The analysis revealed that approximately 24% of the MAS interacts strongly with DIL ( $K_a = 2.54 E+7 \pm 1.10 E+6 M$ ) and 76% of MAS interacts weakly with DIL ( $K_a = 4.80 E+5 \pm 7.59 E+3 M$ ) (Table 3). The binding events had similar negative enthalpies ( $-6.71 E+3 \pm 1.29 E+1$  cal/mol and  $-8.94 E+3 \pm 2.18 E+1$  cal/mol) and negative entropies  $-9.28E+2$  cal/mol and  $-1.02E+3$  cal/mol (Table 3), suggesting that in both cases the binding was enthalpy driven and entropically unfavourable, as high energy resulted from broken and created hydrogen bonds as well as electrostatic van der Waals interactions. This implies that montmorillonite and saponite are able to adsorb DIL through a similar mechanism due to their similar structure. The presence of the two binding events upon the adsorption of a cationic compound onto MAS has not been reported in the literature before.

#### 4. Conclusions

DIL and MAS complexes which can be used in providing oral controlled release formulation or strategies were successfully made and characterised. The process of binding revealed two binding processes that are being reported for the first time for DIL and MAS. The thermodynamics suggested that the binding processes for these two events were enthalpy driven and entropically unfavourable. The quantification of these complexes also revealed variable behaviour in the various media tested which can inform a formulator decision in appropriate media for testing due to drug degradation in acidic media.

#### Acknowledgments

The authors acknowledge the University of Huddersfield for

funding A.M. Totea. Authors declare that there are no conflicts of interest.

#### Conflicts of interest

The authors declare that there are no conflicts of interest.

#### References

- [1] M.I. Carretero, M. Pozo, Clay and non-clay minerals in the pharmaceutical industry. Part I. Excipients and medical applications, *Appl. Clay Sci.* 46 (2009) 73–80.
- [2] M.I. Carretero, Clay minerals and their beneficial effects upon human health. A review, *Appl. Clay Sci.* 21 (2002) 155–163.
- [3] W. Kanjanakawinkul, T. Rades, S. Puttipipatkachorn, et al., Nicotine-magnesium aluminum silicate microparticle surface modified with chitosan for mucosal delivery, *Mater. Sci. Eng. C* 33 (2013) 1727–1736.
- [4] Vanderbilt Minerals, VEEGUM® Magnesium aluminum silicate Vanatural® Bentonite clay for personal care and pharmaceuticals. [https://www.vanderbiltminerals.com/assets/uploads/documents/technical/VEEGUM\\_VANATURAL\\_P\\_C\\_Pharma\\_Web.pdf](https://www.vanderbiltminerals.com/assets/uploads/documents/technical/VEEGUM_VANATURAL_P_C_Pharma_Web.pdf).
- [5] T. Pongjanyakul, S. Rojtanatanya, Use of propranolol-magnesium aluminum silicate intercalated complexes as drug reservoirs in polymeric matrix tablets, *Indian J. Pharm. Sci.* 74 (2012) 292–301.
- [6] S. Rojtanatanya, T. Pongjanyakul, Propranolol-magnesium aluminum silicate complex dispersions and particles: characterization and factors influencing drug release, *Int. J. Pharm.* 383 (2010) 106–115.
- [7] A.M. Totea, I. Dorin, G. Gavrilo, et al., Real time calorimetric characterisation of clay – drug complex dispersions and particles, *Int. J. Pharm.* X 1 (2019) 100003, <https://doi.org/10.1016/j.ijpx.2018.100003>.
- [8] M.E. Aulton, *Aulton's Pharmaceutics*, third ed., Churchill Livingstone, Edinburgh, 2007.
- [9] T. Pongjanyakul, W. Khunawattanukul, S. Puttipipatkachorn, Physicochemical characterizations and release studies of nicotine-magnesium aluminum silicate complexes, *Appl. Clay Sci.* 44 (2009) 242–250.
- [10] L. Rodríguez Padial, G. Barón-Esquivias, A. Hernández Madrid, et al., Clinical experience with diltiazem in the treatment of cardiovascular diseases, *Cardiol. Ther.* 5 (2016) 75–82.
- [11] D. Abernethy, J. Schwartz, Calcium-antagonist drugs, *N. Engl. J. Med.* 341 (1999) 1447–1457.
- [12] P. Hermann, S.D. Rodger, G. Remones, et al., Pharmacokinetics of diltiazem after intravenous and oral administration, *Eur. J. Clin. Pharmacol.* 24 (1983) 349–352.
- [13] F. Qazi, M.H. Shoaib, R.I. Yousuf, et al., Formulation development and evaluation of diltiazem HCl sustained release matrix tablets using HPMC K4M and K100M, *Pak. J. Pharm. Sci.* 26 (2013) 653–663.
- [14] J. Li, C. Luo, D. Zhang, et al., Formulation and development of ternary hybrid matrix tablets of diltiazem hydrochloride, *Powder Technol.* 294 (2016) 66–70.
- [15] P.R. Laity, K. Asare-Addo, F. Sweeney, et al., Using small-angle X-ray scattering to investigate the compaction behaviour of a granulated clay, *Appl. Clay Sci.* 108 (2015) 149–164.
- [16] V.A. Chatpalliwar, P.K. Porwal, N. Upmanyu, Validated gradient stability indicating HPLC method for determining diltiazem hydrochloride and related substances in bulk drug and novel tablet formulation, *J. Pharm. Anal.* 2 (2012) 226–237.
- [17] J. Ermer, H.J. Ploss, Validation in pharmaceutical analysis: Part II: central importance of precision to establish acceptance criteria and for verifying and improving the quality of analytical data, *J. Pharm. Biomed. Anal.* 37 (2005) 859–870.
- [18] MicroCal, VP-ITC user's manual, Northampton (1998). [https://ctrstbio.org.uic.edu/manuals/vp-itc\\_manual.pdf](https://ctrstbio.org.uic.edu/manuals/vp-itc_manual.pdf).
- [19] R. Chakraborty, Effects of floc size and shape in particle aggregation, in: G. Droppo, G.G. Leppard, S.N. Liss, T.G. Milligan (Eds.), *Flocculation in Natural and Engineered Environmental Systems*, CRC Press, Boca Raton, Florida, 2005, pp. 95–120.
- [20] F. Sadeghi, L. Navidpour, S. Bayat, et al., Validation and uncertainty estimation of an ecofriendly and stability-indicating HPLC method for determination of diltiazem in pharmaceutical preparations, *J. Anal. Methods Chem.* (2013), <https://doi.org/10.1155/2013/353814>. Article ID 353814.
- [21] G. Holloway, H. Rowe-Joyce, S. Waha, A stability-indicating HPLC procedure for determination of diltiazem hydrochloride in extemporaneously

- compounded oral liquids, *Pharm. Technol. Eur.* 20 (2008) 38–45, in: <http://www.pharmtech.com/stability-indicating-hplc-procedure-determination-diltiazem-hydrochloride-extemporaneously-compounde>.
- [22] S.S. Ray, P. Maiti, M. Okamoto, et al., New polylactide/layered silicate nanocomposites. 1. Preparation, characterization, and properties, *Macromolecules* 35 (2002) 3104–3110.
- [23] S. Yariv, C. Harold, *Organo-Clay Complexes and Interactions*, CRC Press, 2001.
- [24] B.K.G. Theng, Formation, properties, and practical applications of clay–organic complexes, *J. R. Soc. N. Z.* 2 (1972) 437–457.
- [25] ACD I-Lab. <https://ilab.acdlabs.com/iLab2/>.



## Original Article

## Trace determination and characterization of ginsenosides in rat plasma through magnetic dispersive solid-phase extraction based on core-shell polydopamine-coated magnetic nanoparticles

Ningning Zhao<sup>a, b</sup>, Shu Liu<sup>a, \*</sup>, Junpeng Xing<sup>a</sup>, Zifeng Pi<sup>a</sup>, Fengrui Song<sup>a</sup>, Zhiqiang Liu<sup>a, b, c</sup><sup>a</sup> National Center of Mass Spectrometry in Changchun and Jilin Province Key Laboratory of Chinese Medicine Chemistry, Changchun Institute of Applied Chemistry, Chinese Academy of Sciences, Changchun 130022, China<sup>b</sup> University of Science and Technology of China, Hefei 230029, China<sup>c</sup> State Key Laboratory of Electroanalytical Chemistry, Changchun Institute of Applied Chemistry, Chinese Academy of Sciences, Changchun 130022, China

## ARTICLE INFO

## Article history:

Received 22 March 2019

Received in revised form

2 September 2019

Accepted 4 September 2019

Available online 5 September 2019

## Keywords:

Fe<sub>3</sub>O<sub>4</sub>@SiO<sub>2</sub>@PDA NPs

Multiple recognition sites

Magnetic dispersive solid-phase extraction

Enrichment

Ginsenosides

## ABSTRACT

Enrichment of trace bioactive constituents and metabolites from complex biological samples is challenging. This study presented a one-pot synthesis of magnetic polydopamine nanoparticles (Fe<sub>3</sub>O<sub>4</sub>@SiO<sub>2</sub>@PDA NPs) with multiple recognition sites for the magnetic dispersive solid-phase extraction (MDSPE) of ginsenosides from rat plasma treated with *white ginseng*. The extracted ginsenosides were characterized by combining an ultra-high-performance liquid chromatography coupled to a high-resolution mass spectrometry with supplemental UNIFI libraries. Response surface methodology was statistically used to optimize the extraction procedure of the ginsenosides. The reusability of Fe<sub>3</sub>O<sub>4</sub>@SiO<sub>2</sub>@PDA NPs was also examined and the results showed that the recovery rate exceeded 80% after recycling 6 times. Furthermore, the proposed method showed greater enrichment efficiency and could rapidly determine and characterize 23 ginsenoside prototypes and metabolites from plasma. In comparison, conventional methanol method can only detect 8 ginsenosides from the same plasma samples. The proposed approach can provide methodological reference for the trace determination and characterization of different bioactive ingredients and metabolites of traditional Chinese medicines and food.

© 2019 Xi'an Jiaotong University. Production and hosting by Elsevier B.V. This is an open access article under the CC BY-NC-ND license (<http://creativecommons.org/licenses/by-nc-nd/4.0/>).

## 1. Introduction

Many traditional Chinese medicines (TCMs), which are homologous to food and medicine, have been widely used in daily food and disease treatment [1]. However, their pharmacodynamic material basis or food nutrients remain unclear. The matrix effect of complex biological samples seriously limits the research on active ingredients and metabolites of TCMs [2,3]. Thus, trace bioactive constituents and metabolites from biological samples with highly abundant endogenous interference should be enriched to better investigate the pharmacodynamic material basis. At present, the ultra-high-performance liquid chromatography coupled with high-resolution mass spectrometry (UPLC-MS) has been widely used to

enrich and detect the complex biological samples [4,5]. In addition, new acquisition modes that can obtain good data of all precursors and fragment ions for the determination of targeted molecules are developed by the development of data-dependent acquisition (DDA) and data-independent acquisition (MS<sup>E</sup>) [6,7]. Moreover, the analytical sensitivity and capacity are remarkably enhanced [8]. Thus, these superiorities have provided an advanced analytical platform to gain comprehensive information for the separation and characterization of metabolites.

Despite the presence of advanced analytical instrumental platforms, there is an urgent need to develop pretreatment methods in conjunction with UPLC-MS for better analysis. At present, traditional solvent extraction methods [9–13], liquid–liquid extraction (LLE) and solid-phase extraction (SPE) [14] are widely used to extract ginsenosides. But these methods require high temperature, long hours, and lots of efforts and solvent. And SPE method needs expensive commercial cartridges and fussy procedures. Although our previously proposed eco-friendly deep eutectic solvent (DES)

Peer review under responsibility of Xi'an Jiaotong University.

\* Corresponding author.

E-mail address: [m5lab20@ciac.ac.cn](mailto:m5lab20@ciac.ac.cn) (S. Liu).

[2] for extraction of ginsenosides showed high efficiency and solubility, sample concentration is still limited by negligible volatility of DES. The development of magnetic solid-phase extraction (MSPE) and magnetic dispersion solid-phase extraction (MDSPE) [15] has provided a new potential value for the efficient extraction of ginsenosides, but it is a challenge to synthesize functional adsorbents. Table S1 summarizes the advantages and drawbacks of extraction techniques for ginsenosides.

Recently, magnetic nanoparticles (MNPs) have attracted considerable attention due to their outstanding properties, such as good dispersion, controllable core-shell structure, fast and efficient separation, sustainable usage and no need to pack columns. MNPs have been widely used as adsorbents for enriching small molecules [16,17]. However, MNPs cannot form other interactions except for hydrogen bonds between most TCMs or food bioactive constituents due to the lack of specific functional groups. Moreover, the syntheses of materials require complex procedures and harmful solvents in the preparation process, and few are applied to complex biological samples.

Dopamine (DA), a small molecule that mimics the adhesive proteins of mussels, has been confirmed to play a unique role in the interfacial adhesion of numerous material surfaces by self-polymerization under sufficient mild conditions (weak alkaline medium) [18–20]. For example, self-polymerization of DA has been used for the extraction of estrogenic compounds from cow, goat, sheep and human milk [21]. Unfortunately, the reported core-shell-based polydopamine NPs (PDA NPs) still have some limitations. The first limitation is that PDA possesses strong interfacial adhesion, which results in blocking cavities of buried substance in molecular imprinted materials (MIPs). Moreover, few studies report the detection of targeted molecules from complex matrix samples.

In this study, a novel strategy was developed to enrich and detect ginsenosides from complex biological samples by introducing UNIFI<sup>TM</sup> libraries assisted with Fe<sub>3</sub>O<sub>4</sub>@SiO<sub>2</sub>@PDA NPs as adsorbents of MDSPE. The strategy incorporated the advantages of the three approaches: (1) MDSPE with Fe<sub>3</sub>O<sub>4</sub>@SiO<sub>2</sub>@PDA NPs for fast and efficiently capturing trace bioactive constituents from biological samples without packing column; (2) UPLC-MS technology for fast and accurate detection of trace constituents; (3) Supplemental UNIFI libraries for fast, high-throughput and automatic match of data and identification of compounds. This strategy achieved a promote platform including pre-treatment, sample analysis based on MS and data analysis. For experiments, the conditions were statistically optimized by response surface methodology (RSM) with total ginsenosides to obtain the best extraction process. Subsequently, the strategy was applied for the fast detection and determination of metabolites from rat plasma, which eliminated the interference of several endogenous substances. Moreover, the synergetic strategy was accomplished in compliance to 9 of the 12 green chemistry principles with green analytical chemistry's (GAC) [22]. The proposed method was proven to be a promising strategy to improve the enrichment capability and sensitivity of MS for tracing the targeted molecules in biological samples.

## 2. Experimental

### 2.1. Chemicals

White ginseng (WG), total ginsenosides (extract of WG) and all the standards of ginsenosides Rb1, Rb2, Rb3, Rc, Rd, Re, Rg1, PPD, Rf, Rg2, Rg3, Rh1, Rh2 and compound K were obtained from the College of Pharmacy, Jilin University. Dioscin as an internal standard (IS) was purchased from National Institutes for Food and Drug Control (Beijing, China). HPLC-grade acetonitrile and methanol

were acquired from Fisher Scientific (Loughborough, UK). Ultrapure water was prepared by a Milli-Q water (18.2 M $\Omega$ ) purification system (Milford, MA, USA). Tris (hydroxyl methyl amino methane) (Tris), dopamine hydrochloride (DA·HCl), heparin, ammonium sulfate (NH<sub>4</sub>)<sub>2</sub>SO<sub>4</sub>, aminopropyl triethoxy silane (APTES), tetraethoxysilane (TEOS) and Fe<sub>3</sub>O<sub>4</sub> nanoparticles (20–30 nm) were obtained from Aladdin Industrial Corporation (Shanghai, China). HCl, acetic acid and methanol were provided by Sinopharm Chemical Reagent Co (Shenyang, China). A 5 mM Tris-HCl buffer solution (pH 7–9) was prepared by us.

### 2.2. Instrumentations

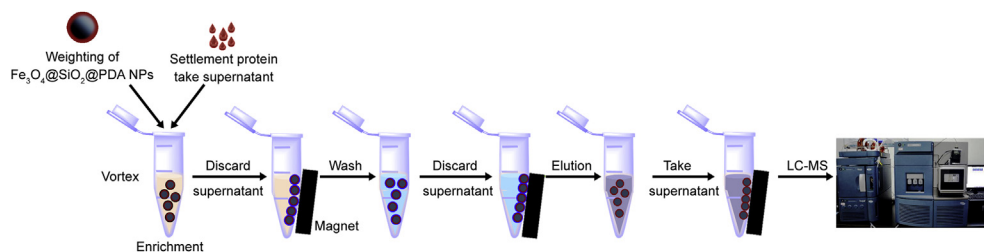
The morphology and Energy Dispersive X-Ray (EDX) spectroscopies of MNPs were obtained by the scanning electron microscopy (SEM, JSM-6460LV, Japan). Fourier transform infrared spectroscopy (FT-IR, IFS 66 V/S, Germany) was performed to identify the materials with KBr. Other characteristics were measured by vibrating sample magnetometry (VSM, MPMS XL, USA) at room temperature and a D8 advance X-ray diffractometer (XRD, D8, Germany) with Cu K $\alpha$  radiation ( $\lambda = 1.5406 \text{ \AA}$ ). The UPLC-MS/MS analyses were performed by a Waters ACQUITY UPLC system (Waters Corp., Milford, USA) coupled to a triple quadrupole (TQ) mass spectrometer equipped with the electrospray ionization (ESI) source in multiple reactions monitoring (MRM) mode. A Q-TOF SYNAPT G2-S High Definition Mass Spectrometer coupled to ESI (Waters Corp., Manchester, UK) was adopted for detection of ginsenosides metabolites before and after treatment with Fe<sub>3</sub>O<sub>4</sub>@SiO<sub>2</sub>@PDA NPs. The C18 column (50 mm  $\times$  2.1 mm, 1.9  $\mu$ m; Thermo scientific) was employed in the entire experiments. MassLynxV4.1 and MarkerLynx Application Manager (Waters Corporation, Milford, USA) and UNIFI 1.8 (Waters, USA) were carried out to process the collected data. And all detailed steps of mass spectrometry analyses were described in Supplementary data (Methods section), including UPLC-MS/MS analysis, Q-TOF analysis and mass spectral data analysis with UNIFI<sup>TM</sup>.

### 2.3. Synthesis of the Fe<sub>3</sub>O<sub>4</sub>@SiO<sub>2</sub>, Fe<sub>3</sub>O<sub>4</sub>@SiO<sub>2</sub>@APTES and Fe<sub>3</sub>O<sub>4</sub>@SiO<sub>2</sub>@PDA NPs

The Fe<sub>3</sub>O<sub>4</sub>@SiO<sub>2</sub> NPs were synthesized by the previous method [23]. The Fe<sub>3</sub>O<sub>4</sub>@SiO<sub>2</sub>@APTES NPs were synthesized through the modified method [24]. The synthesis strategy of Fe<sub>3</sub>O<sub>4</sub>@SiO<sub>2</sub>@PDA NPs based on the modified method [25] through one-pot synthesis is as follows: briefly, the Fe<sub>3</sub>O<sub>4</sub> NPs (100 mg) were dispersed into an ethanol solution (95% ethanol : water, v/v). Then, ammonium hydroxide was added into the mixture solvents (pH = 8.5). Ultrasound 10 min later, 0.2 mL of TEOS was added dropwise into the system for 6 h at 40 °C. After that, 90 mg of DA·HCl was added into the bottle, followed by stirring for 1 h. Subsequently, the obtained product was isolated by the external magnetic field and washed by water and ethanol. Eventually, the product was dried under vacuum at 40 °C for 24 h.

### 2.4. Animals

Six male rats, weighting 200  $\pm$  20 g, were obtained by Jilin Medical University (Jilin, China). After a week of adjustable feeding, they were administered WG (7 g/kg) once a day for 5 days. The rats were sacrificed 2 h after the last gavage, and the blood was collected and centrifuged. The supernatants were stored at -80 °C. All animals' experiments and the procedures followed the Guide for the Care and the Use of Laboratory Animals of Jilin University.



**Scheme 1.** Schematic presentation of the proposed strategy for capture and characterization of ginsenosides by  $\text{Fe}_3\text{O}_4@SiO_2@PDA$  NPs based on UPLC-MS method.

## 2.5. Enrichment of ginsenosides from total ginsenosides

During MNPs screening and tailoring, 5 mg of the MNPs were mixed with 1 mL of the total ginsenosides in water (500  $\mu\text{g}/\text{mL}$ ). The mixture was vortexed and shaken for 2 h. Later, the MNPs were isolated by external magnetic field, followed by ultrasound-assisted cleaning with 1 mL of methanol-acetic acid (9:1, v/v) and then direct mass spectrometry analysis.

The adsorption capacity of  $\text{Fe}_3\text{O}_4@SiO_2@PDA$  NPs for ginsenosides was investigated at different concentrations of total ginsenosides while other conditions remained unchanged. Meanwhile, the dynamic adsorption capacity was evaluated by varied time from 10 min to 360 min. Desorption time was estimated at varied time from 10 min to 120 min. The adsorption amounts ( $Q$ , mg/g) of MNPs were calculated according to Eq (1) [26].

$$Q = (C_0 - C_e) \times \frac{V}{m} \quad (1)$$

where,  $C_0$  ( $\mu\text{g}/\text{mL}$ ),  $C_e$  ( $\mu\text{g}/\text{mL}$ ),  $V$  (mL) and  $m$  (g) represent the initial and equilibrium concentration of ginsenosides, the volume of the total ginsenosides solutions and the mass of the MNPs, respectively.

To investigate the maximum adsorption properties of  $\text{Fe}_3\text{O}_4@SiO_2@PDA$  NPs, the adsorption isotherm was calculated by using a series of total ginsenosides solutions with different concentrations. The kinetic tests were calculated by varied different adsorption time. The Langmuir and Freundlich isotherm models, and the pseudo-first-order and pseudo-second-order models were adopted to evaluate the equilibrium and kinetic data, respectively [27].

## 2.6. Experimental design and statistical analysis for total ginsenosides

The screening experiments, including synthetic species of magnetic materials, content of dopamine, pH of the solvent system, concentrations of the total ginsenosides, enrichment time and desorption time were carried out. According to the above obtained result of single factor experiments, the appropriate variable range in extraction process (shown in Table S2) was employed for experimental design using RSM. The Box-behnken design (BBD) combined with RSM was performed as follows: pH (7–9), concentrations of the total ginsenosides (100–700  $\mu\text{g}/\text{mL}$ ), enrichment time (30–80 min), and elution time (10–80 min) at levels (-1, 0, 1). Here, the reason for choosing such pH range was that the extraction efficiency was better at weak alkalinity for ginsenosides [15]. The extraction recoveries of ginsenosides in 29 experiments (three replicates) were estimated by BBD in Table S3.

Design-Expert 8.0.6 software [28] was operated to evaluate the statistical significance in design experiment. Based on analysis of variance (ANOVA), the quadratic multiple regression models were built to investigate model quality according to the square of correlation coefficient ( $R^2$ ) and the lack of fit which evaluated the failure of the model.

## 2.7. Real samples extraction procedure

The real plasma samples after lavage WG were analyzed by our synergetic strategy in Scheme 1. The 200  $\mu\text{L}$  plasma samples were divided into conventional methanol group and  $\text{Fe}_3\text{O}_4@SiO_2@PDA$  NPs enrichment group (six replicates). First, all plasma samples were dealt with 3 folds methanol. After centrifugation, the supernatants were dried under nitrogen in methanol group. However, in

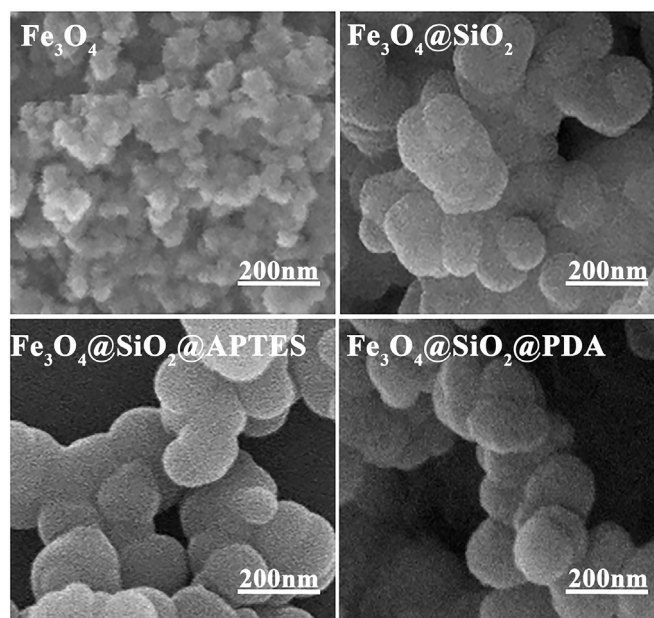


**Fig. 1.** SEM images of  $\text{Fe}_3\text{O}_4$ ,  $\text{Fe}_3\text{O}_4@SiO_2$ ,  $\text{Fe}_3\text{O}_4@SiO_2@APTES$  and  $\text{Fe}_3\text{O}_4@SiO_2@PDA$  NPs.

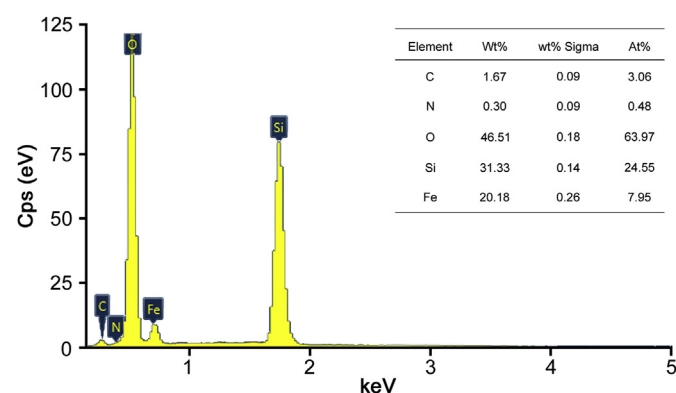


**Fig. 2.** The EDX spectrum and element compositions of  $\text{Fe}_3\text{O}_4@SiO_2@PDA$  NPs.

the PDA group, 5 mg  $\text{Fe}_3\text{O}_4@\text{SiO}_2@\text{PDA}$  NPs were added into 1 mL Tris-HCl buffer system containing the supernatants of the same volume (final pH = 8.78). After vortexing for 2 min, the system was shaken for 80 min. Later, the obtained supernatant was removed by external magnetic field. And the MNPs were eluted with 1 mL of methanol-acetic acid (9:1, v/v) by ultrasound for 68.25 min. Finally, the eluted solvents were also dried under nitrogen. All both dried samples were re-dissolved with 50  $\mu\text{L}$  methanol for TOF analysis.

## 2.8. Method validation and measurement uncertainty

A series of working solutions of Rb1, Rb2, Rb3, Rc, Rd, Re, Rg1, PPD, Rf, Rg2, Rg3, Rh1, Rh2 and compound K were obtained by stepwise dilution of the stock solutions in methanol. The calibration was created in the form of  $y = ax + b$ . The limits of detection (LODs) and limits of quantification (LOQs) were recognized at a signal-to-noise ratio (S/N) of 3 and 10 times. For quality control (QC) samples, fourteen ginsenosides were operated at low, medium, and high concentrations in WG powder and plasma, respectively. The IS was prepared at a concentration of 0.1  $\mu\text{g}/\text{mL}$  in each sample. Intra- and inter-day accuracy and precision were assessed by QC samples at concentration levels of low, middle and high for 14 ginsenosides in 3 days. The relative standard deviation (RSD) and relative error (RE) represented the precision and accuracy, respectively. To investigate the matrix effect, the analyses of total ginsenosides and drug-free plasma samples spiked with the 14 analytes were carried out. To further estimate the extraction recovery, the samples of WG powder and drug-free plasma samples spiked with the 14 analytes were directly analyzed using our proposed method.

Proper quality assurance/quality control (QA/QC) procedures are

vital for the measurement results, which provide reliable analytical information. According to Konieczka and Namieśnik [29], amount of sample, analyte concentration, calibration step, repeatability of results and recovery determination (trueness) of the uncertainty components were estimated. The uncertainty of results was calculated based on Karimi et al. [30] and Borecka et al. [31]. Expanded uncertainty was determined by the Eq (2).

$$U = k \sqrt{(u_{r(\text{sample})})^2 + (u_{r(\text{cal})})^2 + (u_{r(\text{true})})^2 + (u_{r(\text{rep})})^2 + (u_{r(\text{MDL})})^2} \cdot 100\% \quad (2)$$

The meaning of each element in the Eq (2) is as follows:  $U$ —expanded uncertainty (%),  $k$ —coverage factor ( $k = 2$  for  $P = 95\%$ ),  $u_{r(\text{sample})}$ —relative standard uncertainty of sample,  $u_{r(\text{cal})}$ —relative standard uncertainty of calibration step,  $u_{r(\text{true})}$ —relative standard uncertainty of trueness,  $u_{r(\text{rep})}$ —relative standard uncertainty of repeatability, and  $u_{r(\text{MDL})}$ —relative standard uncertainty of MDL determination. Meanwhile,  $u_{r(\text{cal})}$ ,  $u_{r(\text{true})}$ ,  $u_{r(\text{rep})}$  and  $u_{r(\text{MDL})}$  were calculated by the following Eqs (3)–(6), respectively.

The sensitivity of the method is expressed by method detection limit (MDL) and method quantitation limit (MQL) for the entire procedure. And the MDL and MQL were calculated by the Eq (7) and Eq (8).

$$u_{r(\text{cal})} = \frac{SD_{xy} \sqrt{\frac{1}{p} + \frac{1}{m} + \frac{(X_{\text{sample}} - X_m)^2}{\sum_{i=1}^m (X_i - X_m)^2}}}{b \cdot X_{\text{sample}}} \quad (3)$$

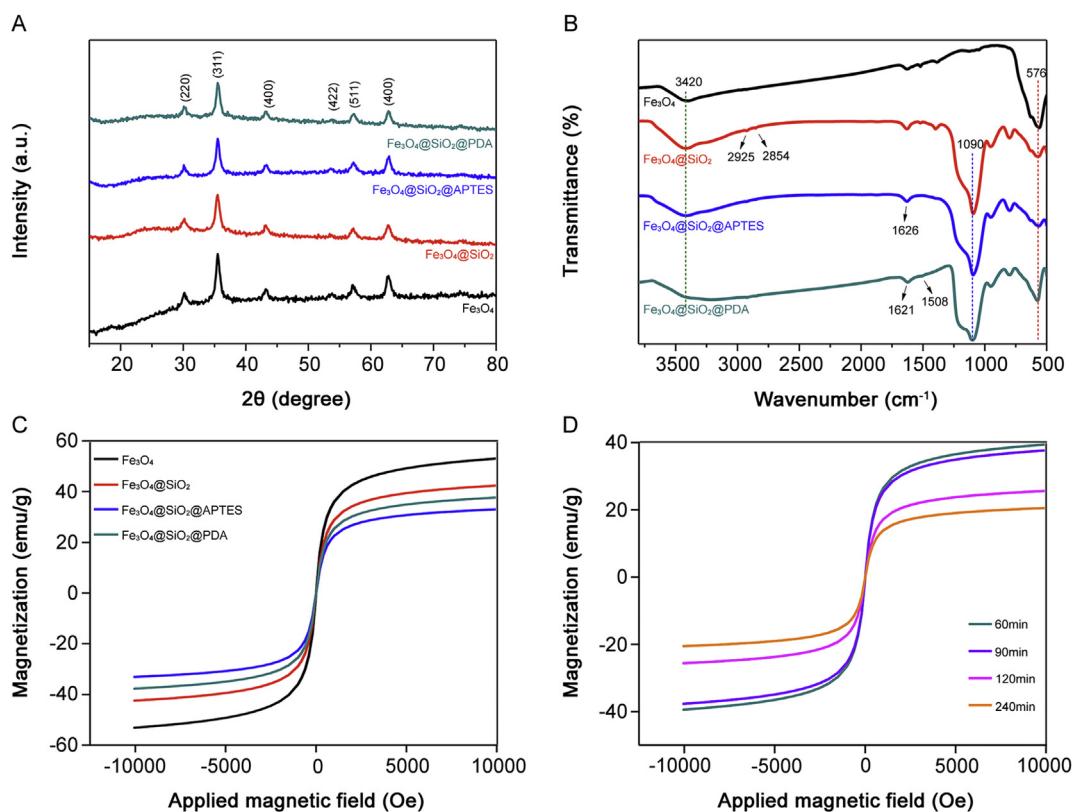


**Fig. 3.** (A) X-Ray diffraction patterns of  $\text{Fe}_3\text{O}_4$ ,  $\text{Fe}_3\text{O}_4@\text{SiO}_2$ ,  $\text{Fe}_3\text{O}_4@\text{SiO}_2@\text{APTES}$  and  $\text{Fe}_3\text{O}_4@\text{SiO}_2@\text{PDA}$  NPs. (B) FT-IR spectra of all the NPs. (C) VSM magnetization curves of all the NPs. (D) VSM magnetization curves of synthetic  $\text{Fe}_3\text{O}_4@\text{SiO}_2@\text{PDA}$  NPs at different reaction times.

$$u_{r(true)} = RSD_R \quad (4)$$

$$u_{r(rep)} = \frac{RSD_{results}}{\sqrt{n}} \quad (5)$$

$$u_{r(MDL)} = \frac{MDL}{c_m} \quad (6)$$

$$MDL = \frac{3.3SD_{xy}}{b} \quad (7)$$

$$MQL = \frac{10 SD_{xy}}{b} \quad (8)$$

where  $SD_{xy}$  is the standard deviation of the calibration curve,  $p$  is the repetition number of measurements for a given sample,  $m$  is the total number of standard samples used for plotting the calibration curve,  $X_{sample}$  is the concentration of sample,  $X_m$  is the mean value of all concentrations of a standard solution for which the measurement was made to plot a calibration curve,  $X_i$  is the calculated concentration,  $b$  is the slope of the calibration curve,  $RSD_R$  is the RSD derived from the recovery,  $RSD_{results}$  is the RSD in real samples and  $C_m$  is the mean concentration of analyte. The analytical result is expressed as mean  $\pm$  expanded uncertainty.

### 3. Results and discussions

#### 3.1. Characterization of the magnetic nanoparticles

##### 3.1.1. SEM and EDX characterizations

All MNPs were characterized through SEM. As shown in Fig. 1, the diameters of  $Fe_3O_4$ ,  $Fe_3O_4@SiO_2$ ,  $Fe_3O_4@SiO_2@PDA$  and  $Fe_3O_4@SiO_2@APTES$  NPs were about 25 nm, 130 nm, 180 nm, and 220 nm, respectively. The results revealed that the size of particles increased with the layer-by-layer modification on the  $Fe_3O_4$  core, and the order is expressed as follows:  $Fe_3O_4$  NPs <  $Fe_3O_4@SiO_2$  NPs <  $Fe_3O_4@SiO_2@PDA$  NPs <  $Fe_3O_4@SiO_2@APTES$  NPs. In addition, the enrichment capability of different MNPs for ginsenosides was also estimated through MS analysis (MRM conditions, calibration curves and analytical results are shown in Tables S4 and S5 and Fig. S1). The order of enrichment capability was in consistent with the order of MNPs size. Although the specific surface areas of  $Fe_3O_4$  and  $Fe_3O_4@SiO_2$  NPs were larger than the other two, the enrichment capabilities of bare MNPs and hydroxyl-containing  $Fe_3O_4@SiO_2$  NPs were weaker than the other two amino-containing MNPs. It is obvious that the effect of amino groups was greater than hydroxyl groups, and the effect of functional groups was relatively more important than specific surface area in this experiment. Moreover, the higher enrichment capability for  $Fe_3O_4@SiO_2@PDA$  NPs compared with  $Fe_3O_4@SiO_2@APTES$  NPs was obtained due to two reasons: (1) PDA possessed multiple recognition sites, such as

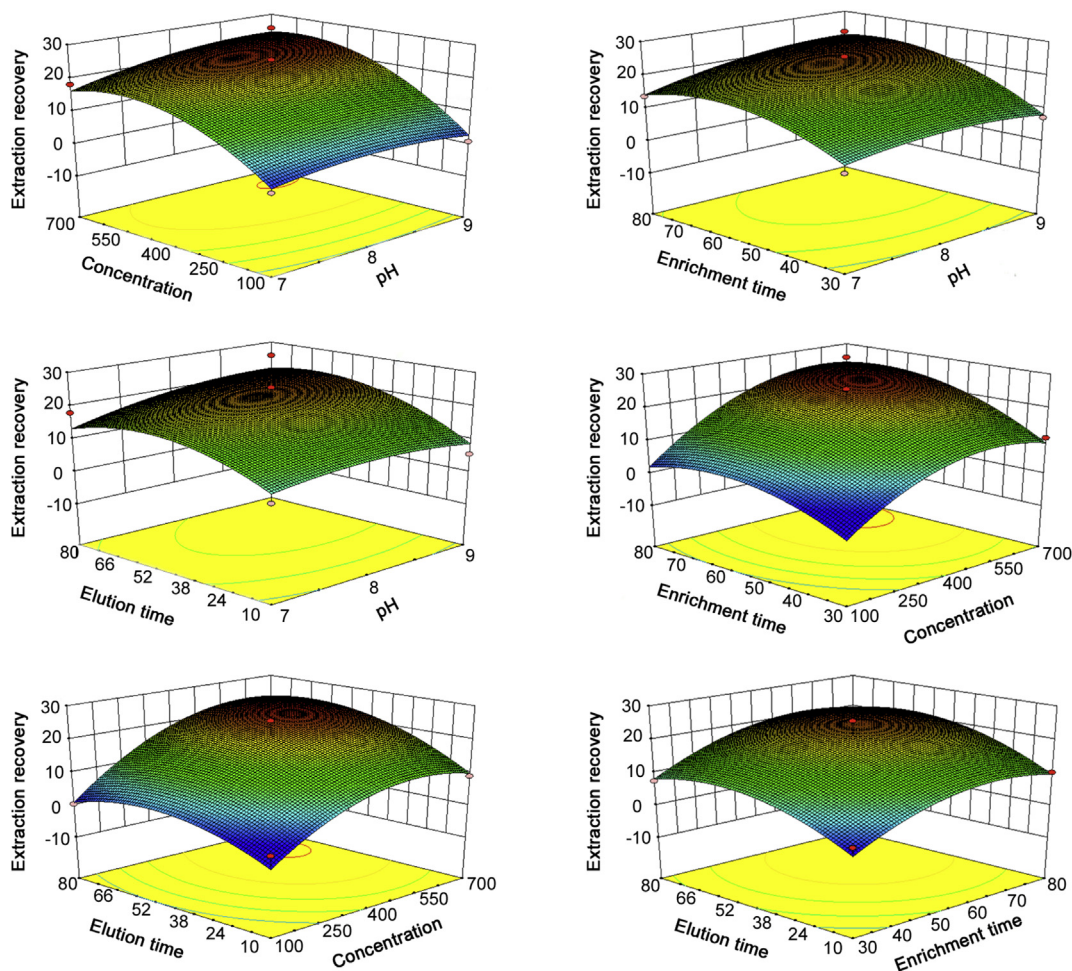


Fig. 4. RSM response surface plots of the model for extraction of ginsenosides.

amino and hydroxyl groups; (2) Fe<sub>3</sub>O<sub>4</sub>@SiO<sub>2</sub>@PDA NPs with small size had relatively high surface areas.

Furthermore, the EDX spectrum and main elemental composition analysis for Fe<sub>3</sub>O<sub>4</sub>@SiO<sub>2</sub>@PDA NPs are presented in Fig. 2. The contents of N elements were further validated the existence of PDA. All the results suggested that PDA was successfully grafted to the Fe<sub>3</sub>O<sub>4</sub>@SiO<sub>2</sub> NPs.

### 3.1.2. XRD characterization

The XRD patterns are shown in Fig. 3A. It was obviously observed that six major characteristic diffraction peaks of Fe<sub>3</sub>O<sub>4</sub> NPs appeared at 2θ = 30.2° (220), 35.5° (311), 43.2° (400), 53.4° (422), 57.2° (511), and 62.9° (440). Although the Fe<sub>3</sub>O<sub>4</sub> NPs were gradually modified, the spectra of modified MNPs were similar to the XRD spectrum of Fe<sub>3</sub>O<sub>4</sub> NPs at the six major peaks, revealing that the modification had not been destroyed on the crystal structure of Fe<sub>3</sub>O<sub>4</sub> particles. The peaks attributed to SiO<sub>2</sub> and PDA were not observed, because SiO<sub>2</sub> or PDA coating on the surface of Fe<sub>3</sub>O<sub>4</sub> mainly existed as amorphous forms [32].

### 3.1.3. FT-IR characterization

The Fe<sub>3</sub>O<sub>4</sub>, Fe<sub>3</sub>O<sub>4</sub>@SiO<sub>2</sub>, Fe<sub>3</sub>O<sub>4</sub>@SiO<sub>2</sub>@APTES and Fe<sub>3</sub>O<sub>4</sub>@SiO<sub>2</sub>@PDA NPs were further validated by FT-IR (Fig. 3B). The typical peaks located at approximately 576 cm<sup>-1</sup> and 1090 cm<sup>-1</sup> were attributed to the stretching vibration of Fe–O and Si–O bonds, respectively [33]. The peak at approximately 1626 cm<sup>-1</sup> was assigned to the N–H vibration in APTES [34]. The peaks for PDA at approximately 1621 cm<sup>-1</sup> and 1508 cm<sup>-1</sup> were assigned to C=C stretching vibrations in the aromatic ring and N–H bending vibration, respectively [35]. Moreover, in the entire spectrum, a broad band at approximately 3420 cm<sup>-1</sup> corresponded to the –NH or –OH stretching vibration [32]. These results reaffirmed the formation of PDA shell on Fe<sub>3</sub>O<sub>4</sub>@SiO<sub>2</sub>@PDA NPs.

### 3.1.4. VSM analysis

As observed in Fig. 3C, the saturation magnetizations of Fe<sub>3</sub>O<sub>4</sub> and Fe<sub>3</sub>O<sub>4</sub>@SiO<sub>2</sub> NPs were 53.08 emu/g and 42.40 emu/g, which reduced to 33.07 and 37.71 emu/g after coating with APTES and PDA, respectively. Although the saturation magnetization declined clearly, the MNPs still met the experimental requirements. The saturation magnetization of Fe<sub>3</sub>O<sub>4</sub>@SiO<sub>2</sub>@PDA NPs was stronger than that of Fe<sub>3</sub>O<sub>4</sub>@SiO<sub>2</sub>@APTES, which proved its efficient separation in the adsorption of ginsenosides. As shown in Fig. 3D, saturation magnetization reduced with the increase of polymerization time. And the intensity was the highest when the polymerization time was 60 min. This optical condition demonstrated the existence of critical values for polymerization time.

## 3.2. Effect of content of DA

The content of DA was estimated for the synthesis of Fe<sub>3</sub>O<sub>4</sub>@SiO<sub>2</sub>@PDA NPs to improve their enrichment capability (Q). As shown in Fig. S2A, Q was the strongest when DA·HCl was 90 mg. Excess amounts of DA·HCl caused the decrease of extraction capacity for ginsenosides. The results showed that superfluous DA·HCl promoted self-aggregation of DA, or the shell of MNPs thickened and resulted in the decrease of specific surface area [36].

## 3.3. Effect of reaction time

The polymerization time was also estimated for the synthesis of Fe<sub>3</sub>O<sub>4</sub>@SiO<sub>2</sub>@PDA NPs. As displayed in Fig. S2B, Fe<sub>3</sub>O<sub>4</sub>@SiO<sub>2</sub>@PDA NPs exhibited the highest extraction efficiencies of ginsenosides when the polymerization time was 60 min, which resulted from the increasement of recognition sites, a stepwise suitable thickness and

**Table 1** Calculated values of relative standard uncertainties, combined standard uncertainties and expanded uncertainties for the determination of 14 analytes in real plasma.

Parameter	Analyte													
	Rg1	Re	Rf	Rh1	Rg2	Rb1	Rc	Rb2	Rb3	Rd	Rg3	CK	PPD	Rh2
Concentration (mg/g)	3.33	2.17	1.75	0.23	1.88	1.94	1.43	0.63	0.33	4.38	6.48	–	–	–
LOD (mg/g)	0.005	0.005	0.006	0.005	0.003	0.002	0.006	0.002	0.004	0.006	0.005	0.002	0.003	0.003
LOQ (mg/g)	0.01	0.01	0.02	0.02	0.01	0.01	0.02	0.01	0.01	0.02	0.02	0.01	0.01	0.01
Repeatability–RSD (%)	2.89	7.15	4.73	0.83	2.03	2.26	2.89	1.74	2.17	5.80	2.38	2.11	9.99	2.52
Trueness – recovery (%)	95.30 ± 5.06	93.88 ± 7.12	88.80 ± 6.3	91.61 ± 10.06	98.94 ± 4.02	86.54 ± 3.22	85.30 ± 10.12	87.47 ± 6.1	86.22 ± 2.1	95.15 ± 10.5	91.27 ± 4.06	94.47 ± 12.2	93.77 ± 8.22	95.61 ± 15.78
Uncertainty														
Mass of sample –u <sub>r</sub> (adsorbent)	0.0099	0.0099	0.0099	0.0099	0.0099	0.0099	0.0099	0.0099	0.0099	0.0099	0.0099	0.0099	0.0099	0.0099
Volume of sample –u <sub>r</sub> (sample)	0.0087	0.0087	0.0087	0.0087	0.0087	0.0087	0.0087	0.0087	0.0087	0.0087	0.0087	0.0087	0.0087	0.0087
Calibration – u <sub>r</sub> (cal)	0.0004	0.0006	0.0042	0.0011	0.0378	0.0149	0.0107	0.0036	0.0037	0.0006	0.0042	–	–	–
Recovery –u <sub>r</sub> (true)	0.027	0.038	0.035	0.055	0.020	0.019	0.059	0.035	0.012	0.055	0.027	0.065	0.044	0.083
Repeatability –u <sub>r</sub> (rep)	0.012	0.029	0.019	0.003	0.008	0.009	0.012	0.007	0.009	0.024	0.010	0.009	0.041	0.010
LOD –u <sub>r</sub> (LOD)	0.0014	0.0022	0.0034	0.0230	0.0017	0.0012	0.0042	0.0029	0.0116	0.0013	0.0008	–	–	–
Combined uncertainty	3.2%	5.0%	4.2%	6.1%	4.5%	2.9%	6.3%	3.8%	2.3%	6.1%	3.3%	–	–	–
Expanded uncertainty (k = 2)	6.5%	9.9%	8.5%	12.2%	9.1%	5.8%	12.5%	7.7%	4.7%	12.3%	6.5%	–	–	–
Re-sult														
Concentration ± U (mg/g)	3.33 ± 0.22	2.17 ± 0.22	1.75 ± 0.15	0.23 ± 0.03	1.88 ± 0.17	1.94 ± 0.11	1.43 ± 0.18	0.63 ± 0.05	0.33 ± 0.02	4.38 ± 0.54	6.48 ± 0.42	–	–	–

the above-mentioned strong saturation magnetization. However, the enrichment effect became relatively low with long polymerization time. The low enrichment effect was caused by the reduction of magnetism and specific surface area due to the thickened shell of the MNPs as time went by, and this finding was consistent with the characterization data in Fig. 3D.

#### 3.4. Optimization for ginsenosides extraction using RSM

Single-factor experiments were implemented to obtain the suitable value ranges for statistical analysis (Fig. S3). In Fig. S3A, when pH ranged from 7 to 9, the values of adsorption capacities increased. It is confirmed that the adsorption capacities for ginsenosides were better at weak alkalinity for the following two reasons: (1) ginsenosides formed more hydrogen bonds with the multiple recognition sites of PDA at weak alkalinity; (2) hydrophobic interaction was better at weak alkalinity. For the isotherm test, Langmuir model ( $R^2 = 0.94$ ) was more successful and suitable than Freundlich model ( $R^2 = 0.89$ ) at 10–1000  $\mu\text{g/mL}$  (Total ginsenosides solutions), and the fitting  $Q$  was greater by Langmuir model (Fig. S3B). For the adsorption kinetic test (Fig. S3C), the  $Q$  was coincided with the pseudo-first-order model, and the pseudo-first-order model ( $R^2 = 0.99$ ) was more suitable than pseudo-second-order model ( $R^2 = 0.86$ ). As shown in Fig. S3D, the desorption capacity remained unchanged after about 60 min. All those results suggested that the single-factor experiment could provide certain ranges for RSM analysis. Furthermore, Design-Expert 8.0.6 was used to evaluate the statistical relevance in the suitable range (Fig. 4). Second-order polynomial quadratic equations between extraction yields ( $Y$ ) and coded variables ( $A$ ,  $B$ ,  $C$  and  $D$ ) were calculated and expressed as follows:

$$Y = 21.25 + 2.21A + 8.94B + 5.19C + 4.45D + 1.83AB + 1.93A + 1.94AD + 2.08BC + 2.25BD + 0.48CD - 2.30A^2 - 7.59B^2 - 5.84C^2 - 6.02D^2$$

The data of ANOVA analysis and 3D response plots indicated the relevant variables for  $Y$  of ginsenosides and the interaction effect between the variables (Table S6). In the model, extraction

concentrations ( $B$ ), enrichment time ( $C$ ), and elution time ( $D$ ) exhibited significant difference at  $p < 0.05$ . pH displayed an insignificant efficiency ( $p = 0.0856$ ). The results indicated that  $B$ ,  $C$  and  $D$  presented remarkable effects, and no obvious interactions with each other were observed during the enrichment process. A predicted optimal  $Y$  of 29.63 mg/g was obtained when the extraction system pH was 8.78, concentration was 576.32  $\mu\text{g/mL}$ , enrichment time was 80 min, and elution time was 68.25 min. Meanwhile, the highest  $Y$  of  $28.32 \pm 0.82$  mg/g was achieved and the result reflected the repeatability of the model obtained. Generally, a good methodological result was obtained. In addition, the recovery exceeded 80% after recycling  $\text{Fe}_3\text{O}_4@/\text{SiO}_2@/\text{PDA}$  NPs 6 times (data are shown in Fig. S4), and this finding revealed that the MNPs were efficient and sustainable for the enrichment of ginsenosides.

#### 3.5. Application to plasma samples and metabolite identification

From BBD experiments, the best extraction process was optimized and the recovery was extremely close to predicted values. The LODs and LOQs of analytes were obtained through the verification of methodology, and good linearities were higher than 0.99 and wide linear ranges were obtained. In Table S7, the accuracy and precision of all the analytes were evaluated. All values conformed to methodological standard. In Table S8, mean accuracies of extraction recoveries and matrix effects of all the analytes ranged from 85% to 115% at three QC levels ( $n = 6$ ). The high extraction recovery and less matrix effect of 14 analytes indicated that the  $\text{Fe}_3\text{O}_4@/\text{SiO}_2@/\text{PDA}$  NPs extraction method was viable. The method was feasible when ginsenosides were enriched from blank plasma spiked with standard mixtures of ginsenosides (in methanol) by the  $\text{Fe}_3\text{O}_4@/\text{SiO}_2@/\text{PDA}$  NPs. In addition, the QA/QC procedures were successfully applied to the measurement and analytical results. Finally, uncertainties of all measurement and analytical results were calculated and the final expanded uncertainty results are shown in Table 1. To further evaluate whether the proposed method has high sensitivity for Q-TOF MS analysis in real complex samples, the proposed approach was implemented to the rat plasma-administered WG, and UNIFI™ libraries were supplemented to automatically assist the separation and characterization of

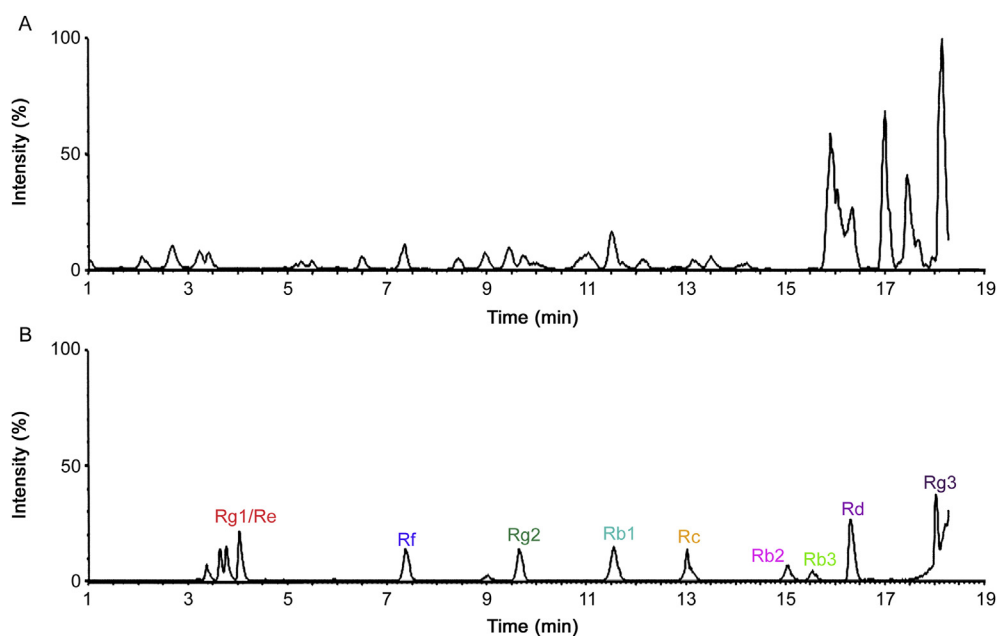


Fig. 5. The BPI chromatograms acquired by conventional methanol extraction method (A) and  $\text{Fe}_3\text{O}_4@/\text{SiO}_2@/\text{PDA}$  NPs enrichment method (B).

compounds. The base peak ion (BPI) chromatograms of conventional methanol group and Fe<sub>3</sub>O<sub>4</sub>@SiO<sub>2</sub>@PDA NPs enrichment group are summarized in Fig. 5. As shown in BPI chromatograms, ion suppressions from plasma had a severe effect on the mass spectrum of ginsenosides, although the signal intensity was slightly high for the conventional methanol method.

Compound 3 (recognized as ginsenosides Re) was taken as examples to illustrate the structural identification of ginsenosides based on mass spectral fragmentation pathways [15] and UNIFI™ libraries. As shown in Fig. 6, characteristic ions of compound 3 were  $m/z$  945.5379 [M – H]<sup>–</sup> and 991.5471 [M + HCOOH – H]<sup>–</sup> in the negative ion mode. For the high-energy function, the main fragmentation ions were at  $m/z$  799.4739, 783.4918, 637.4239, 475.3763, 391.2855 and 161.0451, which corresponded to [M – Rha]<sup>–</sup>, [M – Glc]<sup>–</sup>, [M – Glc – Rha]<sup>–</sup>, [M – Glc – Rha – Glc]<sup>–</sup>, [M – Glc – Rha – Glc – C<sub>6</sub>H<sub>12</sub>]<sup>–</sup> and [C<sub>6</sub>H<sub>9</sub>O<sub>5</sub>]<sup>–</sup>, respectively. These fragmentation ions were identical to those of Re in the UNIFI™ libraries. Moreover, the liquid retention time of compound 3 was the

same as the Re in UNIFI™ libraries. So, compound 3 was identified to ginsenoside Re through constant comparison and confirmation. All the prototypes and metabolites *in vivo* were matched through the above characterization and confirmation steps, the results are listed in Table 2. The combination of MS<sup>E</sup> and UNIFI showed a huge potential in the separation and determination of compounds.

### 3.6. Comparison of the proposed method with other methods

Table S9 shows the distribution information of each ginsenoside in the biological samples detected by different enrichment methods. Surprisingly, 23 compounds were detected and determined using our proposed method, whereas only 8 ginsenosides were determined by the methanol method. For the proposed enrichment method, the ion signal enhancement effect of targeted compounds was obvious. Moreover, the proposed strategy can rapidly separate and identify many targets in the spectrum, which avoided several endogenous substances. This finding proved that

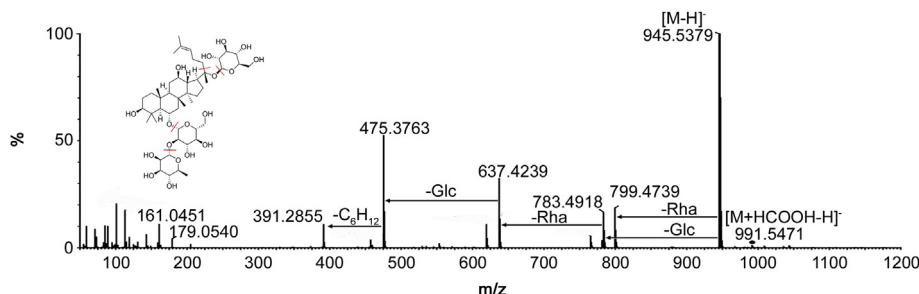


Fig. 6. The major fragmentation pathways of ginsenoside Re.

Table 2

The major prototypes and metabolites of enrichment and identification using Fe<sub>3</sub>O<sub>4</sub>@SiO<sub>2</sub>@PDA NPs extraction method in the biological samples in the negative ion mode.

NO.	RT (min)	Molecular formula	Neutral mass (Da)	Observed $m/z$	Mass error (ppm)	MS/MS (–)	Identified
1	4.02	C <sub>48</sub> H <sub>82</sub> O <sub>18</sub>	946.5501	991.5466	–1.2	945.5379, 341.1087, 339.1293, 161.0456, 149.0452	Cyenoside XDII
2	4.04	C <sub>42</sub> H <sub>72</sub> O <sub>14</sub>	800.4922	845.4857	–5.0	799.4792, 637.4305, 619.4229, 475.3728, 391.2855, 179.0540, 161.0461	Ginsenoside Rg1
3	4.05	C <sub>48</sub> H <sub>82</sub> O <sub>18</sub>	946.5501	991.5466	–1.2	945.5379, 783.4918, 765.4668, 637.4239, 619.4229, 475.3763, 457.3649, 391.2855, 179.0540, 161.0451	Ginsenoside Re
4	7.39	C <sub>42</sub> H <sub>72</sub> O <sub>14</sub>	800.4922	845.4857	–5.0	799.4792, 619.4229, 475.3824, 457.3679, 391.2855, 161.0461	Ginsenoside Rf
5	9.33	C <sub>36</sub> H <sub>62</sub> O <sub>9</sub>	638.4394	683.4355	–2.3	637.4387, 619.4215, 437.3419, 389.2689	Ginsenoside Rh1(s)
6	9.63	C <sub>42</sub> H <sub>72</sub> O <sub>13</sub>	784.4973	829.4974	2.9	783.4918, 637.4305, 619.4229, 475.3824, 161.0461	Ginsenoside Rg2
7	11.57	C <sub>54</sub> H <sub>92</sub> O <sub>23</sub>	1108.6029	1153.5989	–1.5	1107.5934, 945.5379, 783.4918, 621.4341, 459.3784, 323.0989, 179.0540	Ginsenoside Rb1
8	13.05	C <sub>53</sub> H <sub>90</sub> O <sub>22</sub>	1078.5924	1123.5879	–2.0	1077.5831, 915.5270, 783.4917, 311.0969, 293.0834, 149.0437, 131.0334	Ginsenoside Rc
9	14.78	C <sub>53</sub> H <sub>90</sub> O <sub>22</sub>	1078.5924	1123.5880	–1.9	1077.5831, 915.5270, 783.4918, 311.0967, 293.0834, 149.0437, 131.0330	Ginsenoside Rb2
10	15.16	C <sub>53</sub> H <sub>90</sub> O <sub>22</sub>	1078.5924	1123.5877	–2.1	1077.5831, 783.4918, 765.4789, 621.4341, 603.4291, 459.3878, 149.0435, 131.0331	Ginsenoside Rb3
11	15.55	C <sub>56</sub> H <sub>92</sub> O <sub>25</sub>	1164.5928	1163.5871	1.8	1119.5947, 1029.5271, 929.5473, 897.5217, 781.4746, 769.4740, 753.4785	Mal–Ginsenoside Rc
12	15.79	C <sub>56</sub> H <sub>92</sub> O <sub>25</sub>	1164.5928	1163.5873	1.9	1119.5951, 1059.5742, 1047.5737, 1029.5640, 927.5334, 835.4485, 783.4904, 765.4787	Mal–Ginsenoside Rb2
13	16.31	C <sub>48</sub> H <sub>82</sub> O <sub>18</sub>	946.5501	991.5446	–3.2	945.5379, 783.4918, 621.4341, 459.38478, 179.0440, 161.0441	Ginsenoside Rd
14	16.62	C <sub>36</sub> H <sub>62</sub> O <sub>10</sub>	654.4343	653.4253	–1.8	493.3555, 477.3589, 391.2877	Compound K+2O –2H <sub>2</sub>
15	17.12	C <sub>42</sub> H <sub>72</sub> O <sub>13</sub>	784.4973	829.4969	2.3	783.4919, 621.4372, 537.3433, 475.3793, 375.2905, 159.0299	Ginsenoside F2
16	18.02	C <sub>36</sub> H <sub>60</sub> O <sub>11</sub>	668.4136	667.4039	–2.9	387.2613, 305.1830, 303.1609, 297.2203	Ginsenoside F1+2O –H <sub>2</sub>
17	18.37	C <sub>42</sub> H <sub>72</sub> O <sub>13</sub>	784.4973	829.4969	2.3	783.4917, 621.4341, 537.3466, 459.3784, 161.0461	Ginsenoside Rg3
18	18.62	C <sub>36</sub> H <sub>60</sub> O <sub>11</sub>	668.4136	667.4074	2.4	489.2759, 463.3458, 457.3338, 407.2841, 391.2879	Compound K+3O –H <sub>2</sub>
19	18.99	C <sub>30</sub> H <sub>52</sub> O <sub>4</sub>	476.3866	475.3795	1.4	445.3646, 439.3549, 293.2081, 373.2738, 407.3216	Protopanaxadiol + O
20	19.51	C <sub>30</sub> H <sub>52</sub> O <sub>5</sub>	492.3815	491.3749	2.4	473.3639, 387.3271, 361.2752, 347.2959, 245.1548	Protopanaxadiol+2O
21	20.25	C <sub>30</sub> H <sub>52</sub> O <sub>5</sub>	492.3815	491.3752	3.1	475.3433, 443.3533, 441.3736, 403.3221, 401.3063	Protopanaxadiol+2O
22	22.25	C <sub>30</sub> H <sub>50</sub> O <sub>5</sub>	490.3658	489.3589	1.8	437.3058, 423.3264, 393.3013, 371.2183, 343.2645, 331.2283, 305.2491	Protopanaxadiol+2O –H <sub>2</sub>
23	22.81	C <sub>30</sub> H <sub>50</sub> O <sub>5</sub>	490.3658	489.3593	2.7	475.3463, 427.3569, 387.2906, 375.2903, 373.2743, 361.2386, 343.2983, 331.2632	Protopanaxadiol+2O –H <sub>2</sub>

**Table 3**  
Comparison of adsorption capability of pre-concentration methods for determination of ginsenosides.

Pre-concentration method	Analytes	Techniques	Separation	Temperature	Capacity (mg/g)	LOQ (ng/mL)	Matrix	Reference
70% aqueous methanol	Ginsenosides	UAE	Centrifugation		7.48 <sup>#</sup>		Panax ginseng	[9]
Methanol	Ginsenosides	Refluxing	Centrifugation	60–65 °C	6.46 <sup>#</sup>		American ginseng	[10]
Methanol	Ginsenosides	Refluxing	Centrifugation	60–65 °C	7.26 <sup>#</sup>		Panax quin-quefolius	[11]
MeOH-ACN	Ginsenosides	Vortex	Centrifugation			0.12–8.12	Plasma	[12]
Acetonitrile	Ginsenosides	Vortex	Centrifugation			1–5	Plasma	[13]
Methanol	Ginsenosides	LLE	Centrifugation		19.37 <sup>*</sup>	0.25–1	Plasma	This work
DES	Ginsenosides	LLE	Centrifugation		36.65 <sup>#</sup>	0.4–40	White ginseng	[2]
MIPs	Rg1	SPE	Centrifugation		27.74 <sup>*</sup>		Total ginsenosides	[14]
PDA-MMIPs	Anemoside B4	MSPE	Magnetic separation		5.65 <sup>*</sup>		Feces	[15]
PDA-MNPs	Ginsenosides	MDSPE	Magnetic separation		28.32 <sup>*</sup>	0.25–1	Total ginsenosides	This work
					24.56 <sup>*</sup>	1–2	Plasma	

UAE: Ultrasound-assisted extraction.

<sup>#</sup> mg of extracted ginsenosides from per g of white ginseng powder.

<sup>\*</sup> mg of extracted ginsenosides from per g of adsorbent.

Fe<sub>3</sub>O<sub>4</sub>@SiO<sub>2</sub>@PDA NPs had a huge potential for the enrichment of ginsenosides from a wide range of samples.

As shown in Table 3, the proposed strategy was compared with previous extraction methods for the determination of ginsenosides [2,9–15]. The proposed strategy had several advantages over normal methods. Compared with conventional solvent extraction and LLE, MDSPE did not require centrifugation and can perform rapid separation. Moreover, the adsorption capability of Fe<sub>3</sub>O<sub>4</sub>@SiO<sub>2</sub>@PDA NPs for ginsenosides was the highest (28.32 mg/g in total ginseng and 24.56 mg/g in plasma). All these results demonstrated that the proposed method was a fast, sensitive and reusable technique that could be used for the enrichment and determination of ginsenosides in biological samples.

As for green aspects, the above-mentioned techniques for the enrichment of ginsenosides are comprehensively assessed in Table S10. The proposed strategy was accomplished in compliance to 9 of the 12 GAC principles, which stood for reduction of the use of chemical substances and the recycle of them. All other methods met no more requirements of the principles than the one used in this work.

#### 4. Conclusions

In summary, Fe<sub>3</sub>O<sub>4</sub>@SiO<sub>2</sub>@PDA NPs with multiple recognition sites in PDA were synthesized through a green one-pot procedure. It is easy to synthesize and there is no need to pack columns for sample analysis. Importantly, the materials could recycle at least 6 times, conforming to the GAC principles. Moreover, the fast separation and characterization of 23 ginsenoside prototypes and metabolites from plasma were achieved by combining UPLC-MS with UNIFI libraries. In comparison, conventional methanol method can only detect 8 ginsenosides from the same plasma samples. This new synergetic strategy for the accurate characterization of trace ginsenosides using an easy, fast, economical, automated and eco-friendly way shows potential applications. The integration of facile and one-pot materials, advanced analytical platforms and automatically high-throughput post data-processing softwares will promote the research on the pharmacodynamic material basis of related food and TCMs.

#### Acknowledgments

This work was supported by grants from the National Natural Science Foundation of China Key Program (NO. 81530094) and General Program (NO. 81573574, 81873193), and the Science and Technology Development Project of Jilin Province (20190201283JC).

#### Conflicts of interest

The authors declare that there are no conflicts of interest.

#### Appendix A. Supplementary data

Supplementary data to this article can be found online at <https://doi.org/10.1016/j.jpha.2019.09.001>.

#### References

- D. Xiao, X. Yang, H. Yue, et al., A comparative study on chemical composition of total saponins extracted from fermented and white ginseng under the effect of macrophage phagocytotic function, *J. Ginseng Res.* 41 (2017) 379–385.
- N. Zhao, S. Liu, J. Xing, et al., Enhanced one-step sample pretreatment method for extraction of ginsenosides from rat plasma using tailor-made deep eutectic mixture solvents, *Anal. Methods* 11 (2019) 1035–1042.
- H. Xu, C. Wang, Y. Wei, A boronate affinity restricted-access material with external hydrophilic bottlebrush polymers for pretreatment of cis-diols in biological matrices, *Chin. Chem. Lett.* 29 (2018) 521–523.
- W. Song, X. Qiao, K. Chen, et al., Biosynthesis-based quantitative analysis of 151 secondary metabolites of licorice to differentiate medicinal glycyrrhiza species and their hybrids, *Anal. Chem.* 89 (2017) 3146–3153.
- C. Sun, J. He, H. Wu, et al., A rapid and sensitive UPLC-MS/MS method for quantitative determination of arformoterol in rat plasma, lung and trachea tissues, *Chin. Chem. Lett.* 29 (2018) 1284–1286.
- C.L. Yao, H.Q. Pan, H. Wang, et al., Global profiling combined with predicted metabolites screening for discovery of natural compounds: characterization of ginsenosides in the leaves of *Panax notoginseng* as a case study, *J. Chromatogr. A* 1538 (2018) 34–44.
- S. Qiu, W.Z. Yang, C.L. Yao, et al., Nontargeted metabolomic analysis and “commercial-homophyletic” comparison-induced biomarkers verification for the systematic chemical differentiation of five different parts of *Panax ginseng*, *J. Chromatogr. A* 1453 (2016) 78–87.
- H. Ouyang, J. Li, B. Wu, et al., A robust platform based on ultra-high performance liquid chromatography quadrupole time of flight tandem mass spectrometry with a two-step data mining strategy in the investigation, classification, and identification of chlorogenic acids in *Ainsliaea fragrans* Champ, *J. Chromatogr. A* 1502 (2017) 38–50.
- X.Q. Ma, X.M. Liang, Q. Xu, et al., Identification of ginsenosides in roots of panax ginseng by HPLC-APCI/MS, *Phytochem. Anal.* 16 (2005) 181–187.
- E.M. Schlag, M.S. McIntosh, Ginsenoside content and variation among and within American ginseng (*Panax quinquefolius* L.) populations, *Phytochemistry* 67 (2006) 1510–1519.
- R.M. Corbit, J.F.S. Ferreira, S.D. Ebbs, et al., Simplified extraction of ginsenosides from American ginseng (*Panax quinquefolius* L.) for high-performance liquid chromatography-ultraviolet analysis, *J. Agric. Food Chem.* 53 (2005) 9867–9873.
- Q.L. Zhou, D.N. Zhu, Y.F. Yang, et al., Simultaneous quantification of twenty-one ginsenosides and their three aglycones in rat plasma by a developed UPLC-MS/MS assay: application to a pharmacokinetic study of red ginseng, *J. Pharm. Biomed. Anal.* 137 (2017) 1–12.
- J. Chen, M. Li, L. Chen, et al., Effects of processing method on the pharmacokinetics and tissue distribution of orally administered ginseng, *J. Ginseng Res.* 42 (2018) 27–34.
- Q.S. Liu, J. He, W.B. Zhou, et al., Innovative method for the enrichment of high-polarity bioactive molecules present at low concentrations in complex matrices, *J. Sep. Sci.* 40 (2017) 744–752.

- [15] Y.Z. Zhang, J.W. Zhang, C.Z. Wang, et al., Polydopamine-coated magnetic molecularly imprinted polymers with fragment template for identification of pulsatilla saponin metabolites in rat feces with UPLC-Q-TOF-MS, *J. Agric. Food Chem.* 66 (2018) 653–660.
- [16] N. Jalilian, H. Ebrahimzadeh, A.A. Asgharinezhad, Dispersive micro-solid phase extraction of aromatic amines based on an efficient sorbent made from poly (1,8-diaminonaphthalen) and magnetic multiwalled carbon nanotubes composite, *J. Chromatogr. A* 1499 (2017) 38–47.
- [17] Y. Wang, Y. Wu, H. Ge, et al., Fabrication of metal-organic frameworks and graphite oxide hybrid composites for solid-phase extraction and preconcentration of luteolin, *Talanta* 122 (2014) 91–96.
- [18] X. Li, X. Niu, W. Zhang, et al., One-pot anchoring of Pd nanoparticles on Nitrogen-doped Carbon through dopamine self-polymerization and activity in the electrocatalytic methanol oxidation reaction, *ChemSusChem* 10 (2017) 976–983.
- [19] E. Yavuz, S. Tokalioglu, S. Patat, Core-shell Fe<sub>3</sub>O<sub>4</sub> polydopamine nanoparticles as sorbent for magnetic dispersive solid-phase extraction of copper from food samples, *Food Chem.* 263 (2018) 232–239.
- [20] Y. Yin, L. Yan, Z. Zhang, et al., Polydopamine-coated magnetic molecularly imprinted polymer for the selective solid-phase extraction of cinnamic acid, ferulic acid and caffeic acid from radix scrophulariae sample, *J. Sep. Sci.* 39 (2016) 1480–1488.
- [21] B. Socas-Rodríguez, J. Hernández-Borges, A.V. Herrera-Herrera, et al., Multi-residue analysis of oestrogenic compounds in cow, goat, sheep and human milk using core-shell polydopamine coated magnetic nanoparticles as extraction sorbent in micro-dispersive solid-phase extraction followed by ultra-high-performance liquid chromatography tandem mass spectrometry, *Anal. Bioanal. Chem.* 410 (2018) 2031–2042.
- [22] A. Gałuszka, Z. Migaszewski, J. Namieśnik, The 12 principles of green analytical chemistry and the significance mnemonic of green analytical practices, *Trends Anal. Chem.* 50 (2013) 78–84.
- [23] K. Molaie, H. Bagheri, A.A. Asgharinezhad, et al., SiO<sub>2</sub>-coated magnetic graphene oxide modified with polypyrrole–polythiophene: a novel and efficient nanocomposite for solid phase extraction of trace amounts of heavy metals, *Talanta* 167 (2017) 607–616.
- [24] J. Zhang, S. Zhai, S. Li, et al., Pb (II) removal of Fe<sub>3</sub>O<sub>4</sub>@SiO<sub>2</sub>-NH<sub>2</sub> core-shell nanomaterials prepared via a controllable sol-gel process, *Chem. Eng. J.* 215 (2013) 461–471.
- [25] N. Lu, M. Zhang, L. Ding, et al., Yolk-shell nanostructured Fe<sub>3</sub>O<sub>4</sub>@C magnetic nanoparticles with enhanced peroxidase-like activity for label-free colorimetric detection of H<sub>2</sub>O<sub>2</sub> and glucose, *Nanoscale* 9 (2017) 4508–4515.
- [26] F. Guo, Q. Wen, Y. Peng, et al., Simple one-pot approach toward robust and boiling-water resistant superhydrophobic cotton fabric and the application in oil/water separation, *J. Mater. Chem.* 5 (2017) 21866–21874.
- [27] H. Zhu, H. Yao, K. Xia, et al., Magnetic nanoparticles combining teamed boronate affinity and surface imprinting for efficient selective recognition of glycoproteins under physiological pH, *Chem. Eng. J.* 346 (2018) 317–328.
- [28] L. Duan, L.L. Dou, L. Guo, et al., Comprehensive evaluation of deep eutectic solvents in extraction of bioactive natural products, *ACS Sustain. Chem. Eng.* 4 (2016) 2405–2411.
- [29] P. Konieczka, J. Namieśnik, Estimating uncertainty in analytical procedures based on chromatographic techniques, *J. Chromatogr. A* 1217 (2010) 882–891.
- [30] M. Karimi, S. Dadfarnia, A.M.H. Shabani, et al., Deep eutectic liquid organic salt as a new solvent for liquid-phase microextraction and its application in ligandless extraction and preconcentration of lead and cadmium in edible oils, *Talanta* 144 (2015) 648–654.
- [31] M. Borecka, A. Białk-Bielińska, G. Siedlewicz, et al., A new approach for the estimation of expanded uncertainty of results of an analytical method developed for determining antibiotics in seawater using solid-phase extraction disks and liquid chromatography coupled with tandem mass spectrometry technique, *J. Chromatogr. A* 1304 (2013) 138–146.
- [32] S. Shi, J. Yang, S. Liang, et al., Enhanced Cr (VI) removal from acidic solutions using biochar modified by Fe<sub>3</sub>O<sub>4</sub>@SiO<sub>2</sub>-NH<sub>2</sub> particles, *Sci. Total Environ.* 628 (2018) 499–508.
- [33] H. Zeng, Y. Wang, C. Nie, et al., Preparation of magnetic molecularly imprinted polymers for separating rutin from Chinese medicinal plants, *Analyst* 137 (2012) 2503–2512.
- [34] D. Gao, D.D. Wang, Q.F. Fu, et al., Preparation and evaluation of magnetic molecularly imprinted polymers for the specific enrichment of phloridzin, *Talanta* 178 (2018) 299–307.
- [35] W. Cai, J. Wang, Y. Pan, et al., Mussel-inspired functionalization of electrochemically exfoliated graphene: based on self-polymerization of dopamine and its suppression effect on the fire hazards and smoke toxicity of thermoplastic polyurethane, *J. Hazard Mater.* 352 (2018) 57–69.
- [36] Y. Hao, R. Gao, D. Liu, et al., A facile and general approach for preparation of glycoprotein-imprinted magnetic nanoparticles with synergistic selectivity, *Talanta* 153 (2016) 211–220.